

Wednesday September 16, 2009

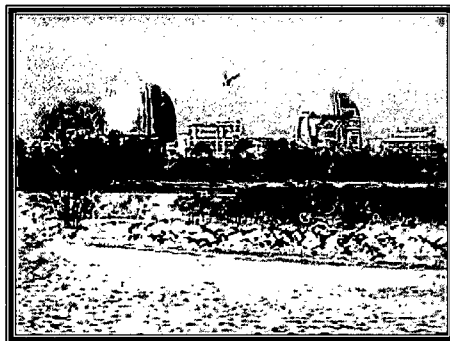
Subject: Technical Letter Report with Open
Items for the South Texas Project FSAR Section
2.4.6 Tsunami



**Technical Letter Report
to the U.S. Nuclear Regulatory Commission
JCN Q-4151, Task Order No. 2**

**Technical Evaluation Report with Open Items for the
South Texas Project FSAR Section 2.4.6 Tsunami**

By Eric L. Geist (USGS, Menlo Park), Patrick J. Lynett (Texas A&M University), David C. Twichell (USGS, Woods Hole), Uri S. ten Brink (USGS, Woods Hole), Bruce Jaffe (USGS, Santa Cruz), and Jason Chaytor (USGS, Woods Hole)



Any use of trade, firm, or product names is for descriptive purposes only and does not imply endorsement by the U.S. Government

Administrative Report, 2009

**U.S. Department of the Interior
U.S. Geological Survey**

2.4S.6 PROBABLE MAXIMUM TSUNAMI

2.4S.6.1 Introduction/Overview/General

Section 2.4S.6, "Probable Maximum Tsunami," of the FSAR addresses the hydrological design basis developed to ensure that any potential tsunami hazards to the SSCs important to safety are considered in the plant design. This section includes the description of probable maximum tsunami, historical tsunami record, source generator characteristics, tsunami analysis, tsunami water levels, hydrography and harbor or breakwater influences on tsunami, and effects on safety-related facilities.

The applicant bases the Probable Maximum Tsunami (PMT) for South Texas Project Units 3 & 4 on the historical record of tsunamis and previously published tsunami assessments for the Gulf of Mexico. Wave heights from offshore landslide sources were not considered in the establishment of the PMT. The source for the PMT that the applicant used is the 1755 Lisbon earthquake. For this event, the applicant uses an offshore wave height estimate of less than 1 m in the Gulf of Mexico as estimated by Mader (2001). The applicant then establishes a maximum surge water level at the STP site of approximately 16.3 feet (5.0 m) above MSL, by applying a runup amplification factor and taking into account 10% exceedance spring high tide and global sea-level rise within the next century considering the maximum life span of the proposed plants. The applicant concludes that the PMT will not affect safety-related facilities and will not be the controlling design basis flood.

2.4S.6.2 Summary of Application

2.4S.6.2.1 Probable Maximum Tsunami

To determine the maximum probable tsunami, the applicant considers several potential source scenarios that are available from the published literature. These include four seismogenic sources discussed in the short paper by Knight (2006): three in the Caribbean and one in the Gulf of Mexico located offshore Veracruz, Mexico. The applicant also considers the tsunami scenario from the 1755 Lisbon earthquake presented by Mader (2001), and one landslide-tsunami scenario presented by Trabant et al. (2001). The applicant discounts the landslide scenario as being highly unlikely. Following a review of published reports, tsunami databases and historical accounts, the applicant considers the 1755 Lisbon tsunami representative of the probable maximum tsunami for the STP site.

Technical Letter Report
South Texas Project Hydrology TER w/ OIs
Section 2.4.6

JCN Q-4151
Task Order No. 2
U.S. Geological Survey

The applicant identifies seismic seiche wave heights of 3.3 feet to 6.6 feet along the Texas coast generated from the 1964 Alaska earthquake as representing the maximum possible seismic seiche for the STP site.

2.4S.6.2.2 Historical Tsunami Record

The applicant has reviewed four primary sources of information to establish the historical record of tsunamis affecting the U.S. Gulf Coast: (a) NOAA/NGDC Historical Tsunami Database (internet), (b) USGS Fact Sheet 2006-3012 summarizing tsunami generating earthquakes in the Caribbean; (c) Recent tsunami events and simulation results posted on the NOAA/PMEL web site; and (d) various published journal articles and the O'Laughlin and Lander (2006) Caribbean tsunami catalog.

Three tsunami events are discussed by the applicant: (1) October 11, 1918 seismogenic tsunami originating NW of Puerto Rico; (2) May 2, 1922 seismogenic tsunami originating near the U.S. Virgin Islands; and (3) March 27, 1964 seiche in the Gulf of Mexico triggered by a M=9.2 earthquake in the Gulf of Alaska.

For event (1), the causative event was a M=7.3 earthquake near the Mona Rift that separates Puerto Rico and Hispaniola. A small wave with undefined amplitude is reported in the NGDC database at the Galveston tide gauge station. For event (2) an undetermined magnitude earthquake apparently caused a tsunami with a 64 cm amplitude reading at the Galveston tide gauge station (Parker, 1922; O'Laughlin and Lander, 2006), although the causative relationship is disputed by Campbell (1991). For event (3), long-period seismic waves set up local seiches along the Gulf Coast, with maximum wave heights in the 3.3-6.6 ft (1-2 m) range.

Modeling results included by the applicant in this section are summarized and discussed in Section 2.4S.6.5

2.4S.6.2.3 Source Generator Characteristics

The applicant summarizes several source regions that may generate tsunami waves potentially affecting the U.S. Gulf Coast. Offshore earthquakes regions considered by the applicant include the Azores-Gibraltar fracture zone and the northern and southern Caribbean plate boundaries. For volcanogenic tsunamis, they consider the Canary Island region. For landslides, the applicant includes one local landslide that occurred in the Gulf of Mexico.

For seismogenic tsunamis, the applicant focuses on the propagation characteristics described by Knight (2006) for Atlantic and Caribbean sources. The applicant cites

Knight (2006) who indicates that seismogenic sources located outside the Gulf of Mexico are not expected to generate a tsunami that would significantly affect the U.S. Gulf Coast.

For volcanogenic tsunamis, the applicant summarizes the hypothesis that a transoceanic tsunami was generated by a prehistoric catastrophic flank collapse of La Palma Island (Ward and Day, 2001), with estimated trans-Atlantic wave heights of 10-25 m. The applicant cites more recent studies that indicate the nature of volcanic flank failures in this region are made up of distinct subevents, each of which generates smaller tsunamis than the catastrophic scenario suggested by Ward and Day (2001).

For landslide-generated tsunamis, the applicant indicates that although the occurrence of submarine landslides in the Gulf of Mexico are relatively common, no tsunamis appear to have been generated by this type of event as evidenced by the geologic and historic record. The applicant specifically identifies the East Breaks slump in the northwestern Gulf of Mexico. Although one modeling study (Trabant et al., 2001) indicates a tsunami with an offshore wave height of 24.9 ft (7.6 m) may have been generated from this event, the applicant indicates that because there is a lack of geologic evidence or subsequent confirmatory analysis to validate this wave height, this is not a probable source for tsunamis that may affect the STP site. However, an independent evaluation of the validity of this assessment has not been completed.

For seismic seiches, the applicant indicates that the only documented event along the Texas coast is from seismic wave generated by the 1964 M=9.2 Gulf of Alaska earthquake. The applicant indicates that the 1960 M=9.5 Chile earthquake did not generate any seiche recorded on tide gauges along the Gulf of Mexico coast. The 1812 New Madrid earthquake generated seismic seiches in the Mississippi River and the Texas state boundary, but not along the Texas coast.

2.4S.6.2.4 Tsunami Analysis

Based on the review of tsunami sources presented in Section 2.4S.6.4, the applicant indicates that modeling of tsunami wave height and periods at the site is not warranted and was not performed.

2.4S.6.2.5 Tsunami water levels

The applicant estimates a maximum tsunami wave height at the site based on a previously published study (Mader, 2001) for the 1755 Lisbon seismogenic tsunami. This scenario is considered by the applicant to be the worst-case tsunami source. The applicant takes the sub-meter estimate in the Gulf of Mexico from Mader (2001) and then applies a runoff amplification factor to obtain a conservative maximum wave height estimate of about 10 ft (3 m). To account for tidal stages according to Regulatory Guide 1.59 (1977), the applicant indicates that the 10% exceedance of astronomical spring high tide is 2.2

Technical Letter Report
South Texas Project Hydrology TER w/ OIs
Section 2.4.6

JCN Q-4151
Task Order No. 2
U.S. Geological Survey

feet (0.67 m) above MLW, with an initial rise of 2.4 feet (0.73 m). To account for sea level rise from global climate change, the applicant uses a sea level increase trend of 5.87 mm/year. From this analysis, the applicant concludes that the maximum water level from the probable maximum tsunami is on the order of 16.3 feet (5.0 m) above present MSL within the next century and therefore will not be the controlling design basis flood.

2.4S.6.2.6 Hydrography and Harbor or Breakwater Influences on Tsunami

The applicant states that from the tsunami water level analysis presented in Section 2.4S.6.5, the maximum water level from tsunamis is less than the grade elevations for the plant. Therefore, they conclude that there will be no on-site effects from breaking waves or seiches caused by resonance.

2.4S.6.2.7 Effects on Safety-related Facilities

The applicant's analysis indicates that the maximum water level from tsunamis is less than the grade elevations for the plant. Therefore, the applicant concludes that there will be no on-site tsunami waves affecting safety-related facilities.

2.4S.6.3 Regulatory Basis

Chapter 2 of the Standard Review Plan (SRP) discusses the site characteristics that could affect the safe design and siting of nuclear power plants. In Section 2.4S.6 of the Safety Evaluation Report (SER), the staff reviews information presented by the applicant regarding the determining the probable maximum tsunami water levels and tsunami generating mechanisms applicable to the site. RG 1.206 specifies that the staff's review of FSAR 2.4.6 covers the following areas: Probable Maximum Tsunami, Historical Tsunami Record, Source Generator Characteristics, Tsunami Analysis, Tsunami water levels, Hydrography and Harbor or Breakwater Influences on Tsunami, and Effects on Safety-related Facilities.

The regulatory requirements to establish the acceptance criteria for reviewing this section are as following:

1. Pursuant to 10 CFR Part 50, Appendix A, General Design Criterion (GDC) 2, COL applicants should consider the most severe of the natural phenomena that have been historically reported for the site and surrounding area, with sufficient margin for the limited accuracy, quantity, and period of time in which the historical data have been accumulated.

Technical Letter Report
South Texas Project Hydrology TER w/ OIs
Section 2.4.6

JCN Q-4151
Task Order No. 2
U.S. Geological Survey

2. Pursuant to 10 CFR 52.79(a)(1)(iii), COL applicants should identify hydrologic site characteristics with appropriate consideration of the most severe of the natural phenomena that have been historically reported for the site and surrounding areas and with sufficient margin for the limited accuracy, quantity, and period of time in which the historical data have been accumulated.

3. 10 CFR Part 100.20 specifies the factors to be considered when evaluating sites. The requirements to consider the physical characteristics of a site (including seismology, meteorology, geology, and hydrology) to determine its acceptability to host a nuclear unit(s) are specified in 10 CFR 100.20(c).

4. 10 CFR 100.23(d) sets forth the criteria to determine the siting factors for plant design bases with respect to seismically induced floods and water waves at the site. Section IV(c) of Appendix A to Part 100, Section IV(c) specifies the required information for seismically induced floods and water waves, including distantly and locally generated tsunami runup and drawdown, local coastal topography that affect tsunami runup and drawdown, geologic and seismic evidence for evaluating seismically induced flood and water wave, and probable slip characteristics of offshore or near lake and rivers.

Appropriate sections of the following Regulatory Guides are used by the staff for the identified acceptance criteria:

Regulatory Guide 1.27 describes the applicable ultimate heat sink capabilities.

Regulatory Guide 1.29 identifies seismic design bases for safety-related SSCs.

Regulatory Guide 1.59, as supplemented by best current practices, provides guidance for developing the design flood bases.

Regulatory Guide 1.102 describes acceptable flood protection to prevent the safety-related facilities from being adversely affected.

To judge whether the applicant has met the requirements of 10 CFR Part 52, 10 CFR Part 100, and 10 CFR 100.23 with respect to tsunamis and the analysis thereof, the NRC staff uses the criteria described in Section C.1.2.4.6 of RG 1.206.:

2.4S.6.4 Technical Evaluation

2.4S.6.4.1 Probable Maximum Tsunami

Summary of FSAR contents: The applicant evaluated several different tsunami sources from published scientific literature to establish the Probable Maximum Tsunami. Approximate tsunami wave heights were indicated by Knight (2006) for four seismogenic sources located in the Caribbean and Gulf of Mexico and by Mader (2001) for the 1755 Lisbon earthquake located in the Atlantic Ocean. The wave height estimate from Trabant et al. (2001) from the East Breaks submarine landslide is considered highly unlikely by the applicant. The applicant revises the potential for tsunamis from the East Breaks landslide in their response to RAI 2.4S.6.1-1.

Brief description of staff's review: We comment in detail on the applicant's response to RAI 2.4S.6.1-1 (below). We then summarize the PMT determination from our independent confirmatory analysis and compare our results with the results contained within applicant's response to RAI 2.4S.6.1-1.

Request for Additional Information (RAI) 2.4S.6.1-1: Section C.1.2.4.6.1 of Regulatory Guide 1.206 (RG 1.206) provides specific guidance with respect to the establishment of the PMT. This includes how the orientation of the site relative to the generating mechanism, shape of the coastline, offshore land areas, hydrography, and stability of the coastal area (proneness of sliding) were considered in the analysis. [Item 1] Provide tsunami modeling analysis of the East Breaks landslide to clarify whether the 7.6 m offshore wave height indicated by Trabant et al. (2001) can be discounted. [Item 2] In addition, provide additional tsunami analysis of other regions in the Gulf of Mexico prone to landslides. [Item 3] To independently validate whether no tsunami hazard exists for the proposed site, provide geologic methods and tsunami identification criteria used to justify the determination that no tsunami deposit was found at the site. [Item 4] Provide excavation photos from Units 1 & 2. [Item 5] Indicate if there are geologically conducive locations for the deposition and preservation of tsunami deposits at the STP site or nearby regions.

Resolution of the RAI and issuance of Open Items: RAI 2.4S.6.1-1 has been separated into five items, as indicated in the applicant's response to the RAI.

[Item 1] East Breaks Landslide: In their response to the RAI, the applicant provides geologic background and four possible source scenarios for landslide tsunamis in the East Breaks region. The geologic background for the East Breaks landslide is taken primarily from published literature and, in general, presents a reasonable summary. With regard to the source scenarios, however, several questions arose. First, it is unclear why the applicant chose a factor of 20x applied to the Palos Verdes debris avalanche to obtain a

source scenario for East Breaks (140 m leading depression wave). Second, the applicant estimates a slide thickness of 100 m from a mid-slope profile across the slide. Along this part of the slide, there appears to be quite a bit of post-slide debris/sedimentation within the scar, so the true thickness of the slide during failure might be somewhat thicker. The slide thickness near the headwall, which may be more representative of the slide thickness, is closer to 160 m. Third, it is unclear how the initial depth of the slump center-of-mass is determined. A source depth closer to the depth of the headwall scarp (i.e. 200 m) maybe more appropriate. In general, what is needed is a comparison of the size of these failures to the East Breaks failure as examples of waves generated by smaller, larger, and equal sized failures. It would also be helpful if the applicant stated the landslide volume they used for East Breaks slide and compared it to published volume estimates.

For this Item [1], the applicant also provides the theoretical basis of the tsunami propagation used (MOST) and its verification, but conservatism of input parameters was not thoroughly discussed. The physics errors incurred by using MOST for the landslide tsunami problem are not likely to be too significant, although the applicant did not directly address this issue. They also used a large (but physically reasonable) bottom roughness coefficient (i.e., 0.01 on pg. 4 of the response) that may not give the most conservative water-level estimate. The generation phase of the applicant's simulations is based on a slump center-of-mass motion model (Grilli and Watts, 2005; Watts and others, 2005), in which the time history of slide movement is specified only for the center of mass of a slide with a prescribed geometry (e.g., Gaussian shape). This contrasts with using the full time-varying displacement field for submarine mass failures as initial conditions for tsunami generation. The center-of-mass motion model may be adequate during the early stages of post-failure slide movement, but does not account for lateral changes in deformation as landslide fully mobilizes down slope.

The tsunami analysis procedure the applicant describes (MOST) is used to determine the "runup" for each of the four scenarios, relative to MSL. Although runup is the maximum inland elevation inundated by the tsunami, as the applicant indicates on pg. 5 of the response, it appears from the figures that the applicant's runup estimates are actually maximum nearshore water surface elevations (i.e., not considering the effects of overland flow). The applicant then computes the maximum water level from an East Breaks event by using the maximum runup from among the four scenarios, adjusted for the 10% exceedance high tide and long-term sea level rise. We performed an independent confirmatory analysis to validate the applicant's estimates.

[Item 2] Other Gulf of Mexico Landslides: The applicant provides a descriptive justification why other Gulf of Mexico landslide provinces are not considered in establishing the PMT for the site. These provinces are the Mississippi Canyon, Florida Escarpment, and Campeche Escarpment (ten Brink and others, 2008). The applicant maintains that because there is significant diffusion and energy dissipation associated with submarine landslide tsunamis, landslides that are more distant than the East Breaks

landslide will have a lower-potential runup. It is unclear whether further tsunami analysis was performed by the applicant for the more distant landslides to make this conjecture.

The applicant's discussion of landslide ages also implies that some landslide provinces are not further considered because of present-day inactivity. With regard specifically to the West Florida Slope region and the applicant's statement that "most of the sediments were removed before mid-Miocene", it is unclear (a) whether the sediments were removed by landslides and (b) whether the material removed was a cover of clastic sediments over the carbonate platform. It is likely the applicant is referring to a landslide from the area above the Florida Escarpment. They dismiss it in part because of its age, however there are younger failures on the slope above the Escarpment that they do not address. Landslides have occurred (and may well still be occurring) in the carbonate material of the West Florida Slope, not just the sediment cover. In general, the applicant makes reference to the age of the slides in relationship to the last glacial maximum as grounds for implying that slides in the Gulf of Mexico are no longer active because the triggering conditions are no longer active. At 16 ka, sea level had already started to rise and by ~7 ka, the time of the last known landslide occurring in the Mississippi Canyon region (Twichell and others, in press), sea level was close to today's levels (Peltier and Fairbanks, 2006). Saying that the forcing mechanisms for the slides such as the East Breaks are no longer active seems to be more assumption than a conclusion backed by evidence.

Issuance of Open Items: From our confirmatory analysis, it is likely that the applicant is correct in concluding the more distant landslides in the Gulf of Mexico with propagation paths oblique to the site are likely not to have potential runup heights greater than that from the East Breaks Landslide. However, the applicant does not provide sufficient justification to dismiss the possibility that the Campeche Escarpment region may be a potential source region that determines the PMT water levels. This is Open Item 2.4-1.

[Item 3] Paleotsunami Deposits: The applicant provides geologic criteria for identifying tsunami deposits (from González and others, 2007). The applicant indicates that no evidence of tsunami deposits according to criteria they list have been found at the site. Furthermore, the applicant provides a description of the depositional environment for near-surface stratigraphy at the site, indicating depositional processes other than from tsunamis.

As stated in González and other (2007) that the applicant cites, the combination of both the facies and sedimentology approach has resulted in an often-used, if not universally approved, set of criteria for understanding how sandy tsunami deposits might be distinguished in the stratigraphic record.

These include:

- Sand layers in continuous sheets usually <25 cm thick and laterally continuous over 100s of meters
- The sand sheet generally thins landward
- The sand layer typically cuts across stratigraphy and represents an

isochronous surface

- The sands contain marine microfossils, often from a range of depths and environments
- Sands are often massive or plane laminated, and may have flame structures at the base. Ripples and other bedload structures are rare, although they have been reported in modern deposits
- The underlying sediments may show evidence of erosion, including ripup clasts of the underlying sediment incorporated into the tsunami deposit. This does not happen in every case however, and many tsunami deposits show no evidence for strong erosion. Rather, plants rooted in the pre-tsunami surface can be well preserved in the deposit, often appearing to have grown through it
- Grain size of the deposit tends to decrease landward and upward, although recent research suggests that inverse grading (that is, layers that increase in size upward) is more prominent in the deposits of large tsunamis
- Relative abundance of marine geochemical tracers such as bromine. In some cases, the presence of marine microfossils and geochemical tracers alone has been used to infer the passage of tsunami—sand need not necessarily be present.

We accept the applicants interpretation of geologic sand that was observed during the excavation of STP 1 & 2 as described in FSAR Section 2.5 and have closed this item. The applicant has provided tsunami deposit identification criteria and a determination that no tsunami deposit was found at the site from available geologic data.

[Item 4] Excavation Photos: The applicant provided excavation photos for STP 1&2 that were requested to determine the near-surface stratigraphy at the site. These photos indicates the presence of sand layer(s), for which the applicant provides a geologic interpretation in Item 3. Therefore, we recommend that an Open Item is not needed for Item [4].

[Item 5] Possible Locations of Nearby Tsunami Deposits: The applicant indicates that because the age of the most recent landslides in the Gulf of Mexico occurred during a sea-level lowstand, any deposits within a few kilometers of the paleo-coastline would now be submerged. However, the applicant does not mention older tsunami deposits that occur during sea-level highstands, such as the Falls County tsunami deposit (Bourgeois and others, 1988) described in our confirmatory analysis in Section 2.4S.6.4.2. Local sea-level lowstands and highstands are caused by a combination of eustatic (global) sea level changes (e.g., from glacial cycles) and local changes in sediment supply and tectonics.

Confirmatory analysis and major findings: Our independent confirmatory analysis to determine the PMT at the STP site is described in detail in the sections that follow. In summary, we consider both far-field seismogenic and near-field (Gulf of Mexico) landslide sources as potential generators for the PMT. Initial analysis indicates that submarine landslides broadside (i.e., directly across) from the site are the likely sources that determine the PMT (refer to subsection 2.4S.6.4.3 for further details). This includes

Technical Letter Report
South Texas Project Hydrology TER w/ OIs
Section 2.4.6

JCN Q-4151
Task Order No. 2
U.S. Geological Survey

the East Breaks landslide and potential landslides along the Campeche Escarpment. Each of these landslide sources have unique hydrodynamic behavior described in Section 2.4S.6.4.5. Within the uncertainty of tsunamigenic source data, either could be the PMT source.

Because the applicant provides a detailed tsunami analysis for the East Breaks landslide in their response to RAI 2.4S.6.1-1, we can attempt to compare our results. It appears that the applicant does not explicitly compute overland flow, so a comparison to our confirmatory analysis of overland flow (cf., Figure 2.4S.6.4.5-16) cannot be made. However, we can approximately compare tsunami time series results at offshore locations. The applicant computes tsunami time series at an 8.1 m water depth ("Buoy Record" in Figure 2.4S.6.4.1-1 below). We compute tsunami time series at a 50 m water depth ("50m Station" in Figure 2.4S.6.4.1-1). From 50 m to 8.1 m toward the site there will be shoaling amplification counteracted by energy dissipation from non-linear propagation effects.

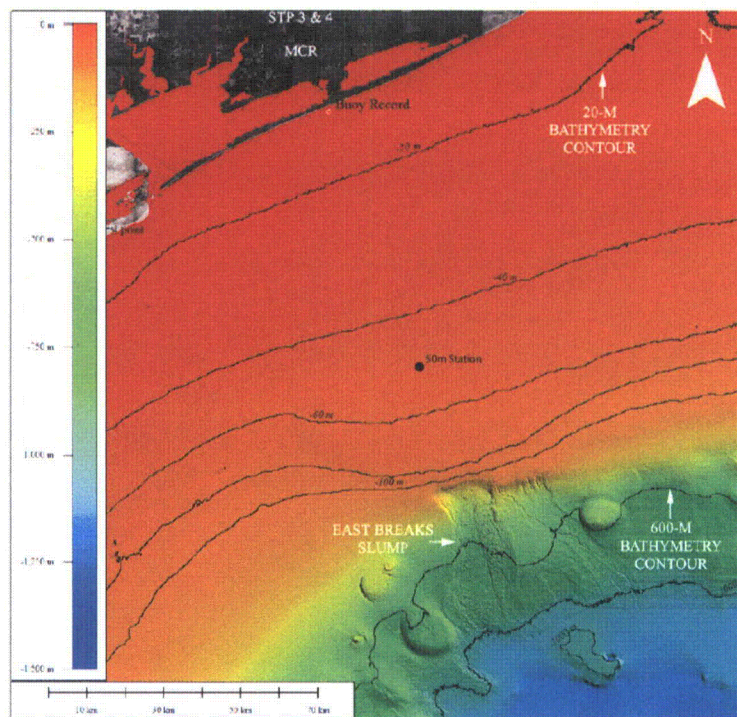


Figure 2.4S.6.4.1-1: Bathymetry near the STP site and location for synthetic tsunami time series ("Buoy Record") from applicant's RAI response (their Figure 1) and from our independent analysis ("50m Station").

Two of the applicants four source scenarios for the East Breaks landslide have approximately the same maximum offshore amplitude; the PNG and Monster scenarios as termed by the applicant. The PNG scenario uses source parameters from the 1998 tsunamigenic landslide, off the northern shore of Papua New Guinea, whereas the hypothetical Monster scenario is designed to be very wide source (approx. 50 km taken from Figure 11 of the applicant's RAI response) with less vertical seafloor displacement, compared to the observed East Breaks landslide. The time series for each of these scenarios are shown in Figures 2.4S.6.4.1-2 and 2.4S.6.4.1-3. The maximum amplitude for these two scenarios is similar.

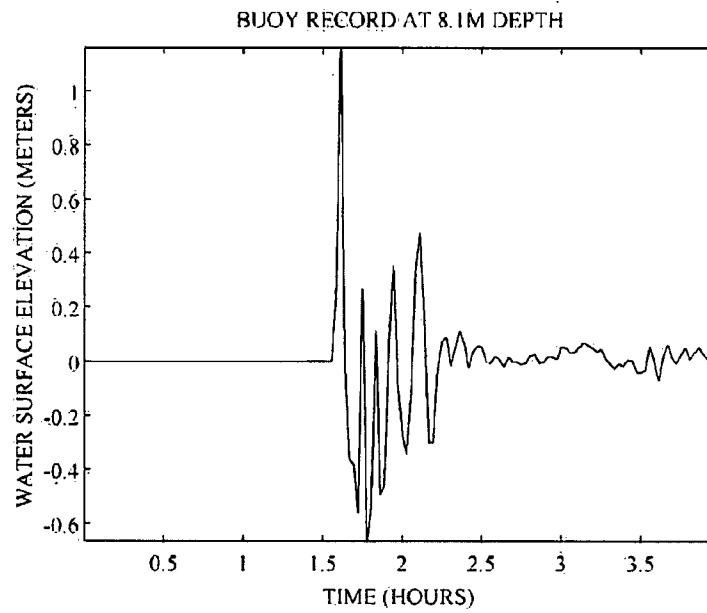


Figure 2.4S.6.4.1-2: Synthetic tsunami time series for the applicant's PNG source scenario at the location indicated in Figure 2.4S.6.4.1-1 ("Buoy Record") from applicant's RAI response (their Figure 18).

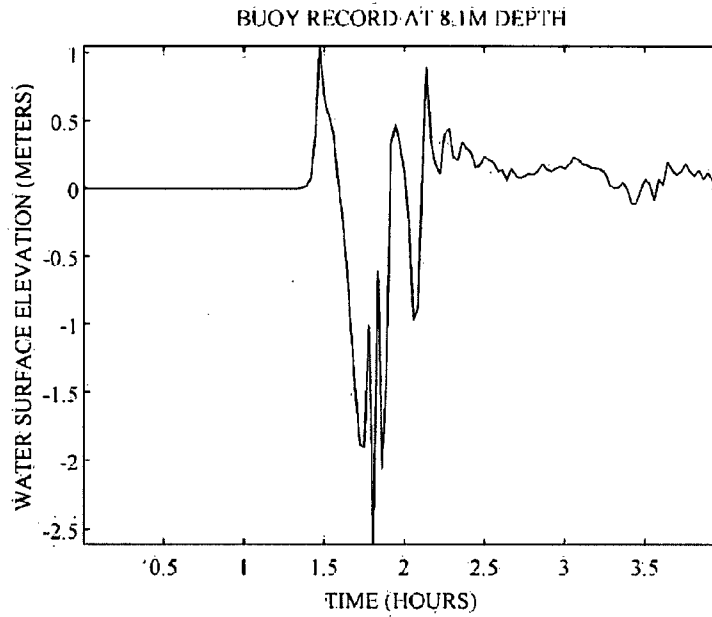


Figure 2.4S.6.4.1-3: Synthetic tsunami time series for the applicant's Monster source scenario at the location indicated in Figure 2.4S.6.4.1-1 ("Buoy Record") from applicant's RAI response (their Figure 20).

In comparison, we show offshore tsunami time series for both the East Breaks and Campeche source scenarios in Figure 2.4S.6.4.1-4 (also Figure 2.4S.6.4.5-20). Note the change in scale for the y-axis.

Figure 2.4S.6.4.1-4: Synthetic tsunami time series simulated by a 2-D model for the Campeche hypothetical landslide scenario and the East Breaks landslide scenario at the location indicated in Figure 2.4S.6.4.1-1 ("50m Station").

As is evident by comparing Figure 2.4S.6.4.1-2 and Figure 2.4S.6.4.1-3 with Figure 2.4S.6.4.1-4, there is approximately an order of magnitude difference in the maximum wave amplitudes between the applicant's and the staff's estimates (1+ meters versus 10+ meters). It is unlikely that this difference can solely be ascribed to differences owing to the station location and energy dissipation during propagation across the continental shelf. As indicated in Figure 2.4S.6.4.5-8 (1HD propagation) and Figure 2.4S.6.4.5-12 (2HD propagation) there is at most a three-fold reduction in amplitude during cross-shelf propagation, still suggesting a significant difference in the results using the applicant's methodology and our confirmatory analysis. The difference is likely caused by (1) a difference in source parameters; (2) the applicant using a center-of-mass generation model as opposed to our hot-start conditions using a cross-sectional profile of landslide motion and (3) lower bottom friction values used in our confirmatory analysis. For all of these differences, it is likely that the approach used in our confirmatory analysis is more conservative than the applicant's. Tsunami amplitudes decrease greatly during overland flow toward the plant as described in Section 2.4S.6.4.5, using conservative values of bottom friction onshore.

Independent confirmation of the 10% exceedance high tide and long-term sea level rise contribution to the PMT water levels is discussed in Section 2.4S.6.4.5.

Conclusion: There are significant differences in how the PMT is determined as described in the applicant's response to RAI 2.4S.6.1-1 and our confirmatory analysis. However, the applicant's PMT water level estimate (3.52 m) that represents a nearshore/coastal location is only slight less than our PMT water level estimate of 5 m for an inland location closer to the STP site, taking account the effect of overland flow. Moreover, the PMT surge level estimates by both the applicant and the staff are far below the bounding MCR breach water level of 47.5 ft MSL or the plant grade of 34 ft MSL, thus the NRC staff concluded that the postulated PMT would not affect the proposed STP site.

2.4S.6.4.2 Historical Tsunami Record

Summary of FSAR contents: After reviewing published and internet-based tsunami catalogs, databases, and historical accounts, the applicant identifies three historical tsunami events for the STP site. These include (1) an October 11, 1918 seismogenic tsunami originating west of Puerto Rico, (2) a May 2, 1922 seismogenic tsunami originating near the Virgin Islands, and (3) seismic seiche waves originating from the March 27, 1964 Gulf of Alaska earthquake (not a tsunami event in the Gulf of Mexico).

Brief description of staff's review: We examine the primary sources for the historical observations and measurement for Gulf Coast tsunamis and tsunami-like waves (i.e., seismic seiches) cited by the applicant. We review the applicant's response to RAI 2.4S.6.1-1 in terms of possible evidence of paleotsunami at the site. Finally, we discuss the paleotsunami located in Falls County, Texas, near the Cretaceous-Tertiary Gulf Coast shoreline.

Confirmatory analysis and major findings: A review of this historical record is conducted to confirm whether the three events listed by the applicant are the primary tsunamis and seismic seiches measured and observed along the Gulf Coast. An additional entry in the NGDC tsunami database for the Gulf of Mexico is an event that occurred at Grand Isle, Louisiana on September 22, 1909. As indicated in the database, this event was likely caused by a hurricane, not a tsunami.

(1) The primary observation of October 1918 seismogenic tsunami originating west of Puerto Rico is a small wave of indeterminate amplitude recorded at the Galveston tide gauge station. The original reference for this observation appears from the International Seismological Summary epicenter catalog (see http://earthquake.usgs.gov/research/data/iss_summ.php) as cited by Heck (1947). However, there is confusion regarding the date of the event. The date is listed as October 24, 1918 in the NGDC Tsunami Database, cross-referenced to the date of a large aftershock following the devastating October 11, 1918 Puerto Rico earthquake and a tsunami observed at the Mona lighthouse (Puerto Rico) from that aftershock. In Heck (1947), Berninghausen (1968), and Lockridge et al. (2002), the date is listed as October 25, 1918. It appears that the October 24, 1918 NGDC date is a local date (Lockridge and others, 2002). All of the aforementioned reports clearly note that the waves recorded at Galveston did not occur on October 11, 1918 (date of the Puerto Rico mainshock) as indicated by the applicant in the FSAR.

(2) The primary observation of the May 2, 1922 event is a 0.64 m amplitude recorded at the Galveston tide gauge station. The original reference for this observation appears to be Parker (1922). The record is shown in Figure 2.4S6.4.2-1 below.

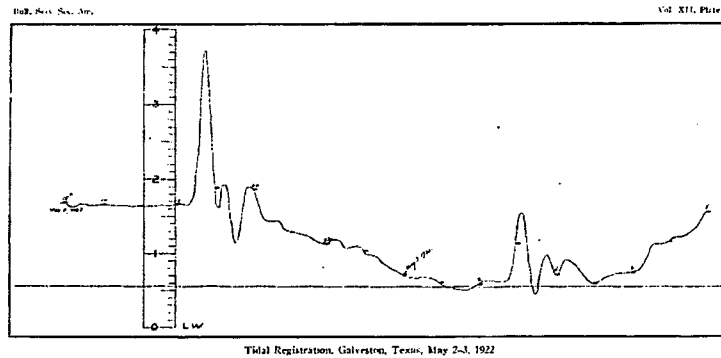


Figure 2.4S6.4.2-1: Galveston tide gauge record of the May 2, 1922 event (Parker, 1922). Scale in feet.

The 1922 tidal disturbance is linked to an earthquake in Vieques only because of the unfortunate note by Parker (1922) with regard to a single seismograph station. The NEIC historical catalog for the Caribbean and for the world, which lists earthquakes estimated to be larger than 6, does not mention any earthquake in Vieques. The Centennial catalog of Engdahl and Villaseñor (2002), which is complete for magnitudes approximately 6.5 and greater, does not list this earthquake either. Finally, Bill McCann's unpublished, local catalog for Puerto Rico does not mention an earthquake at that time. It is more likely that the tidal disturbance was the result of a source local to the Gulf of Mexico and Galveston. If it was a landslide or a slow earthquake offshore Galveston, it would not have been felt. This event does emphasize the potential hazard from local sources.

(3) The primary references of seismic seiche waves originating from the March 27, 1964 Gulf of Alaska earthquake are reports by Donn (1964) and Berninghausen (1968) who indicated that the waves reached maximum height (peak-trough) of 0.18 m (7 in.) at the Freeport tide gauge station in Texas. These reports also refer to eyewitness observations of wave heights up to 2 m from this event.

The applicant did not address possible evidence for paleotsunami deposits in the FSAR. In response the RAI 2.4S.6.1-1, the applicant provides three photos of the subsurface geology during excavation of Units 1 and 2. Two of the photos were taken a distance such that the stratigraphy is not discernable. The photo shown in Figure 2.4S6.4.2-2 (applicant's Figure 23 of the RAI response) indicates layers of different sediment: sand, silt and clay (according to the caption of the applicant's RAI response, Figure 23). The applicant indicates that the presence of sand is consistent with deposits emplaced in a "low-energy overbank floodplain adjacent to a meandering and avulsion-based deltaic river system" (pg. 23 of the response). Without additional details of these layers according to the specific sedimentological criteria for identifying tsunami deposits, the

applicant's statement that no evidence of tsunami deposits in these excavations cannot be independently confirmed.

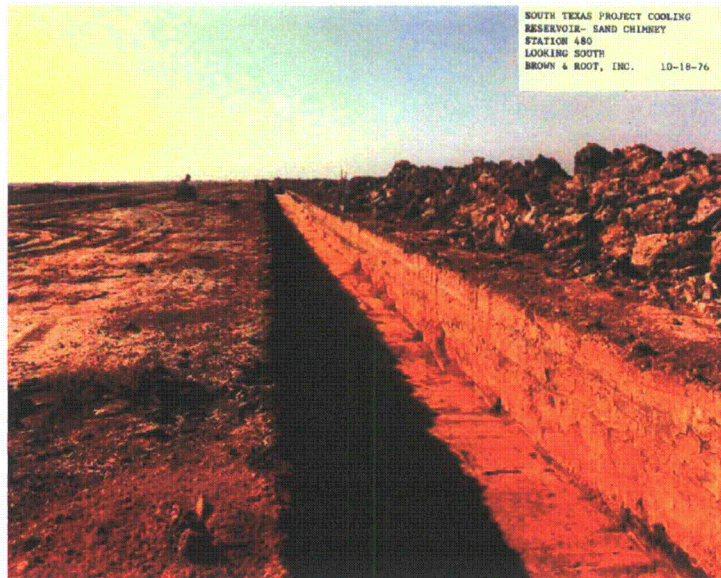


Figure 2.4S6.4.2-2: Excavation photo from applicant's RAI response (their Figure 23).

North of the site, a deposit located in Falls County, Texas near the Brazos River was originally interpreted by Bourgeois et al. (1988) as caused by a paleotsunami. This deposit, known as the Brazos deposit, has since been widely discussed in the scientific literature. It consists of a coarse-grained sandstone bed with indicators of a high-energy wave environment (e.g., rip-up clasts). The strata above and below the deposit indicate a quiet water depositional environment. The Brazos deposit is dated from nanno-, micro- and macro-fossils (Jiang and Gartner, 1986; Bourgeois and others, 1988; Schulte and others, 2006) near the time of the Cretaceous-Tertiary boundary and is located at the paleo-shoreline for the time period (Figure 2.4S6.4.2-3). Since this time, the Gulf Coast shoreline has transgressed southward to its current geographic position (outline in Figure 2.4S6.4.2-3).

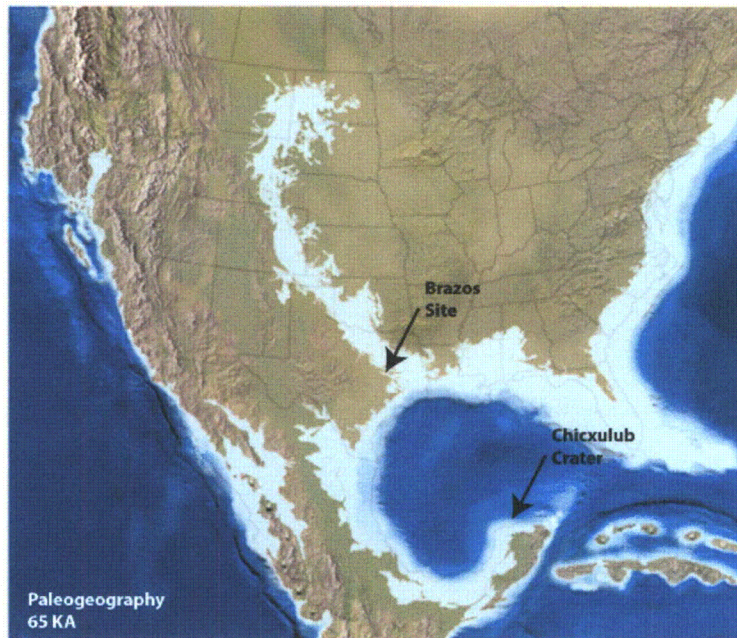


Figure 2.4S6.4.2-3: Paleogeography (Blakey, 2005) at the time when the Brazos tsunami deposit was emplaced (approx. 65 Ka). Locations of the Brazos site and Chicxulub impact crater also shown.

The common interpretation of this deposit is that it was emplaced by a tsunami generated from Chicxulub asteroid impact, owing to its date and the existence of impact ejecta at the Brazos site. However, the tsunami deposit was discovered by Bourgeois et al. (1988) prior to the discovery of the Chicxulub impact crater (Hildebrand and others, 1991). An important alternate hypothesis related to possible tsunamigenic sources in the Gulf of Mexico for determining the PMT at the site is provided by Bourgeois et al. (1988):

“If the tsunami were produced by a major submarine landslide, it should not occur precisely at the K-T boundary unless the landslide were caused by an earthquake related to boundary events, which is a possibility”
(pg. 569)

Bourgeois et al. (1988) suggested that a tsunami wave 50-100 m high was necessary to explain this deposit. The published wave heights and flow speeds of the Brazos tsunami deposit are reasonable, representing order-of-magnitude estimates. It is not conceivable

that the wave that created these deposits was generated by any landslide source that would be of relevance to the present-day PMT determination. As we demonstrate in our independent analysis, any landslide wave generated at the present-day continental shelf break would not be able to maintain a large wave height across such a long propagation distance over very shallow water. The depth-limiting dissipation effect, in which large amplitude waves are dissipated much faster than small amplitude waves during long propagation over shallow depth, would necessarily reduce any landslide generated wave located at the shelf break to a minimal event at the shoreline. It is still possible that this deposit was generated by a paleo-landslide source, but this landslide event would have been local to the Brazos site. It is considerably more likely that a wave of the estimated height would be caused by a relatively nearby large impact event. Waves emanating from such a source would have the needed extreme wave heights and long periods to be able to propagate significant wave energy this far inland.

Over the last 20 years, the deposit has been extensively sampled from out crops and subsurface cores at sites near the banks of the Brazos River. Recently, studies have both corroborated and disputed whether the Brazos deposit was emplaced by a tsunami, whether it occurred exactly at the geologic boundary between the Cretaceous and Tertiary periods (i.e., at the K-T boundary), and whether the trigger was the Chicxulub impact (e.g., Smit and others, 1996; Gale, 2006; Schulte and others, 2006; Keller and others, 2007). Therefore, the exact age and hydrologic process that formed the Brazos deposit remain controversial. However, in light of these studies over the last 20 years, the lead author of original study identifying the deposit maintains that it was emplaced by a tsunami (J. Bourgeois, pers. comm., 2009).

Conclusion: Primary references of historical observations and measurements of tsunami and seismic seiche waves occurring along the Gulf Coast were examined. Except for the date of the 1918 hydrologic event and the source for the 1922 hydrologic event, our assessment of the historical record is consistent with that of the applicant's.

The applicant did not provide evidence that an adequate investigation was conducted for tsunami deposits at or near the proposed site. Additionally, the applicant does not consider the existence of a possible paleotsunami (Bourgeois and others, 1988) that occurred along the ancient Gulf Coast shoreline, currently located along the Brazos River in Falls County, Texas. The common interpretation of this deposit is that it was emplaced by a tsunami generated by the Chicxulub impact or by landslide or earthquake activity associated with the impact. Although arguments have been presented against this interpretation, this deposit, along with the historical record, should be considered as possible evidence of tsunami occurrence along the Gulf Coast. It is unlikely, however, that the flow speeds and wave heights inferred from the deposit are relevant to determination of the present-day PMT.

2.4S.6.4.3 Source Generator Characteristics

Summary of FSAR contents: The applicant examines published information to determine the source generator characteristics for several different types of tsunamis: seismogenic, volcanogenic, and landslide generated. For seismogenic tsunamis, the applicant discusses the propagation characteristics into the Gulf of Mexico for earthquakes located in the Caribbean and Atlantic (Knight, 2006). For volcanogenic tsunamis (catastrophic flank failures), the applicant cites recent studies to discount the La Palma, Canary Islands transoceanic tsunami scenario published by Ward and Day (2001). For landslide-generated tsunamis, the applicant discounts the East Breaks landslide tsunami scenario published by Trabant et al. (2001) as being highly unlikely, though the applicant revisits this scenario in their response to RAI 2.4S.6.1-1

Brief description of staff's review: We comment on the applicant's response to RAI 2.4S.6.3-1 (below). For the remainder of this section, we describe potential tsunamigenic sources and specific source parameters used in the independent confirmatory analysis. In addition, we briefly discuss seismic seiche waves from the 1964 Gulf of Alaska earthquake.

Request for Additional Information (RAI) 2.4S.6.3-1: Section C.1.2.4.6.3 of Regulatory Guide 1.206 (RG 1.206) provides specific guidance with respect to the source characteristics needed to determine the PMT. These characteristics include detailed geo-seismic descriptions of the controlling local and distant tsunami generators, including location, source dimensions, fault orientation, and maximum displacement. Provide these characteristics for seismogenic tsunamis originating in the Caribbean and Gulf of Mexico as used in the analysis. Also provide the location, source volume and dimensions, and maximum displacement information for landslides in the Gulf of Mexico used in the analysis.

Resolution of the RAI and issuance of Open Items: The applicant provides earthquake source parameters used by Knight (2006) for a hypothetical earthquake located offshore Veracruz, Mexico, in the Gulf of Mexico (Knights source #4). The applicant does not provide source parameters for seismogenic tsunamis originating in the Caribbean.

In response to RAI 2.4S.6.1-1, the applicant provides a description of the East Breaks landslide and possible source parameters for four failure scenarios. For other landslide provinces in the Gulf of Mexico, the applicant provides a description for each of the provinces, but does not consider specific source parameters nor provides further examination (in terms of model simulations). The applicant reasons that the longer propagation distance to the site implies much greater wave attenuation such that the tsunami amplitudes from landslides in other regions will not exceed the amplitude of the tsunami from the four East Break landslide scenarios.

Issuance of Open Items: From our independent confirmatory analysis, we determine that either a local landslide similar to the East Breaks landslide or a landslide along the Campeche escarpment is the source for the PMT. Because the applicant provides their estimate of the location, source volume and dimensions, and maximum displacement information for the East Breaks landslide and because this information is likely not available for the Campeche escarpment, we recommend that an Open Item is not needed following the resolution of RAI 2.4S.6.3-1.

Confirmatory analysis and major findings: In this section, tsunami sources used for the independent confirmatory analysis are described in terms of their identification, characteristic, and tsunami generation parameters. Potential tsunamigenic sources are first discussed below, including parameters associated with the maximum submarine landslides in the Gulf of Mexico. At the end of this section, we briefly discuss seismic seiches.

Potential Tsunamigenic Sources

Potential tsunami sources that are likely to determine the PMT at the South Texas Project (STP) site are submarine landslides in the Gulf of Mexico. Subaerial landslides, volcanogenic sources, near-field intra-plate earthquakes and inter-plate earthquakes along Caribbean plate boundary faults are unlikely to be the causative tsunami generator for the PMT at the South Texas Project site as discussed below.

Subaerial Landslides

With regard to subaerial landslides, there are no major coastal cliffs near the site that would produce tsunami-like waves that exceed the amplitude of those generated by other sources.

Volcanogenic Sources

According to the Global Volcanism Program of the Smithsonian Institution (<http://www.volcano.si.edu/>), there are three general regions of volcanic activity that have the potential to generate localized wave activity in the Gulf of Mexico and Caribbean Sea: (1) two Mexican volcanoes near the Gulf of Mexico coastline; (2) two volcanoes in the western Caribbean; and (3) volcanic activity along the Lesser Antilles island arc. Two Mexican volcanoes, (Cerro el Abra and San Martin) associated with the eastern Trans-Mexican Volcanic Belt, are located near the Gulf of Mexico coastline. In addition, basaltic flows associated with another nearby volcano (Los Atlixcos) have reached as far as the coast. Capra et al. (2002) provides an inventory of major debris avalanches associated with the Trans-Mexican Volcanic Belt. In that study, there does not appear to be any major catastrophic failures that would reach the Gulf of Mexico Coast. In the eastern Caribbean, Utila Island, located offshore Honduras, is composed of primarily pyroclastic cones and rises only 74 m above sea level. However, any flank failures are unlikely to generate any significant wave activity in the Gulf of Mexico, owing to the size of the failures and obstructed propagation paths around the Yucatan Peninsula. Also in the eastern Caribbean, Volcán Azul on the coast of Nicaragua is composed of three small cinder cones, but these are unlikely to generate significant failures. There are many

active volcanoes along the Lesser Antilles island arc, some of which have historically caused local tsunamis (Pelinovsky and others, 2004). Because of their distance to the STP site, however, tsunami amplitudes from these volcanoes are unlikely to be significant (e.g., Smith and Shepherd, 1995). Similarly, tsunamis generated by volcanic processes in the eastern Atlantic Ocean (e.g., Canary Islands sector collapse) would be greatly attenuated because of the propagation distance (approx. 8,000 km) and scattering caused by obstructions through the Caribbean. In summary, catastrophic failures associated with volcanoes along the eastern coasts of Mexico and Central American are either too far inland or too small in size to generate significant wave activity in the Gulf of Mexico near the STP site. Based on existing evidence, volcanoes along the Lesser Antilles or in the eastern Atlantic Ocean are too far away to generate significant wave activity in the Gulf of Mexico.

Intra-Plate Earthquakes

Because there are no tectonic plate boundaries in the Gulf of Mexico region, earthquakes *local* to the STP site occur in an intra-plate tectonic environment, limiting the maximum magnitude these earthquakes can attain. According to the documentation for the 2008 update of the United States National Seismic Hazard Maps (Petersen and others, 2008), the maximum magnitude (M_{max}) for the south Texas coast is estimated to be approximately $M_{max}=7.5$ (see Petersen and others, 2008, for analysis details). Because the maximum slip, and consequently the maximum sea floor displacement, associated with an earthquake scales with its magnitude, the initial tsunami wave amplitude associated with an intra-plate earthquake would therefore be less than that used for local, submarine landslides under the conservative hot-start conditions as described in Section 2.4S.6.4.5. The tsunami amplitudes predicted by Knight (2006) for an arbitrary intra-plate earthquake in the Gulf of Mexico are consistent with this inference.

Inter-Plate Earthquakes

In the far-field, offshore tsunami amplitudes from Caribbean inter-plate earthquakes are estimated in Chapter 8 of ten Brink and others (2008), using the linear-long wave equations. The description of major plate boundary faults and specific source parameters are described in that study. The tsunami propagation model presented in ten Brink and others (2008) has been refined during our confirmatory analysis for two of the principal sources (the northern South America Convergent Zone and the northern Caribbean Subduction Zone) using the COMCOT tsunami model discussed in Sections 2.4S.6.4.4 and 2.4S.6.4.5. Tsunami amplitudes at the Texas coast from these seismogenic sources are generally small (i.e., < 1 m) compared to tsunami amplitudes determined for submarine landslides in establishing the PMT. Tsunami amplitudes from earthquakes along the Azores-Gibraltar oceanic convergence boundary are also likely to be small (i.e., < 1 m) in the Gulf of Mexico (Mader, 2001; Barkan and others, in press). For the remainder of this section, we focus on submarine landslide sources as the principal generator for the PMT at the STP site.

Local Submarine Landslides

Submarine landslides in the Gulf of Mexico are considered a potential tsunami hazard for the STP site for two reasons: (1) some dated landslides in the Gulf of Mexico have post-glacial ages (Coleman and others, 1983), suggesting that triggering conditions for these landslides are still present and (2) analysis recent seismicity suggest the presence of small-scale energetic landslides in the Gulf of Mexico.

With regard to (1), the Mississippi Canyon landslide is dated 7,500-11,000 years before present (ybp) (Coleman and others, 1983; Chapter 3 in ten Brink and others, 2007) and the East Breaks landslide is dated $15,900 \pm 500$ ybp (Piper and Behrens, 2003). Both landslides, which are among the largest landslides in the Gulf of Mexico, occurred after the end of the last glacial maximum, during post-glacial transgression. Although landslide activity along the passive margins of North America may be decreasing with time since the last glacial period, the 1929 Grand Banks landslide is a historic example of such an event that produced a destructive tsunami (Fine and others, 2005). In addition, the Mississippi River continues to deposit large quantities of water-saturated sediments on the continental shelf and slope, making them vulnerable to over-pressurization and slope failure

With regard to (2), seismograms of an event that occurred on February 10, 2006 (i.e., the Green Canyon event, Figure 2.4S.6.4.3-1) that occurred offshore southern Louisiana (Dewey and Dellinger, 2008) suggest that energetic landslides continue to occur in the Gulf of Mexico (Nettles, 2007). Most landslides affected by salt tectonics are small in size (e.g., in comparison to the East Breaks landslide; Chapter 3 of ten Brink and others, 2007) and unlikely to be tsunamigenic. However, in terms of the failure duration, the 2006 event must have occurred rapidly enough to generated seismic energy. While source analyses of this event cannot definitively distinguish between a fault and landslide source, this event reveals the potential for present-day slope failure. Shown below is the multibeam bathymetry near the event (Figure 2.4S.6.4.3-1) and three seismograms and accompanying spectrograms (P. Whitmore, personal communication). The first seismogram is for a typical earthquake (Figure 2.4S.6.4.3-2), showing a sudden onset of the seismic waves (body waves) and significant high frequency energy indicative of fault slip. The second seismogram is for a known subaerial landslide that occurred in SE Alaska (Figure 2.4S.6.4.3-3), showing a gradual (emergent) build up of seismic waves, no obvious P-waves, and a deficiency in high-frequency energy. The third seismogram is for the 2006 Gulf of Mexico event (Figure 2.4S.6.4.3-4) and share many of the same characteristics as the SE Alaska landslide (emergent, lack of high-frequency energy).

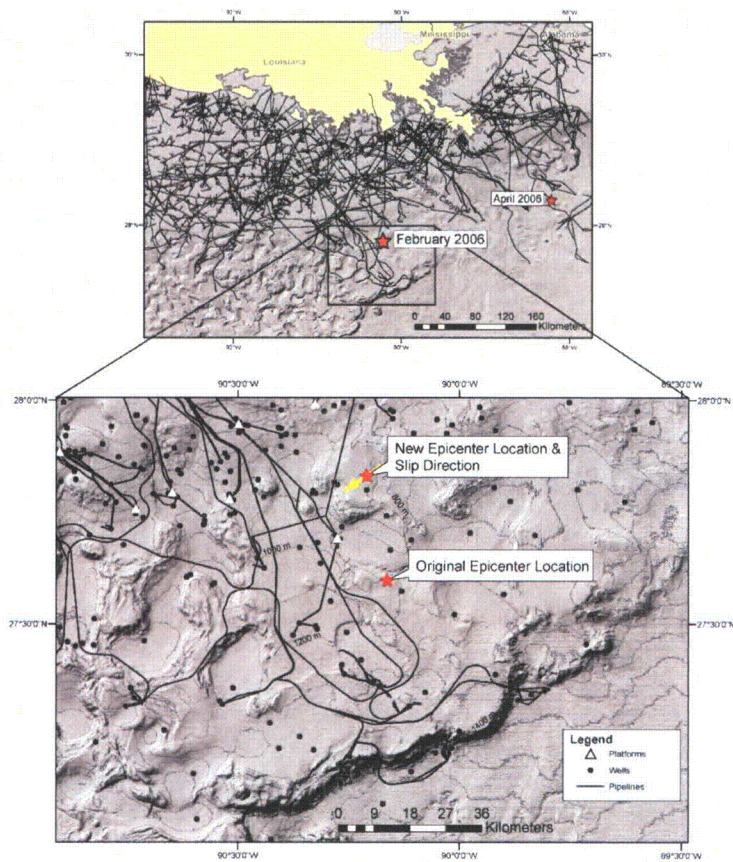


Figure 2.4S.6.4.3-1: Multibeam bathymetry showing the area around the February 10, 2006 Green Canyon event in the Gulf of Mexico that was seismically recorded.

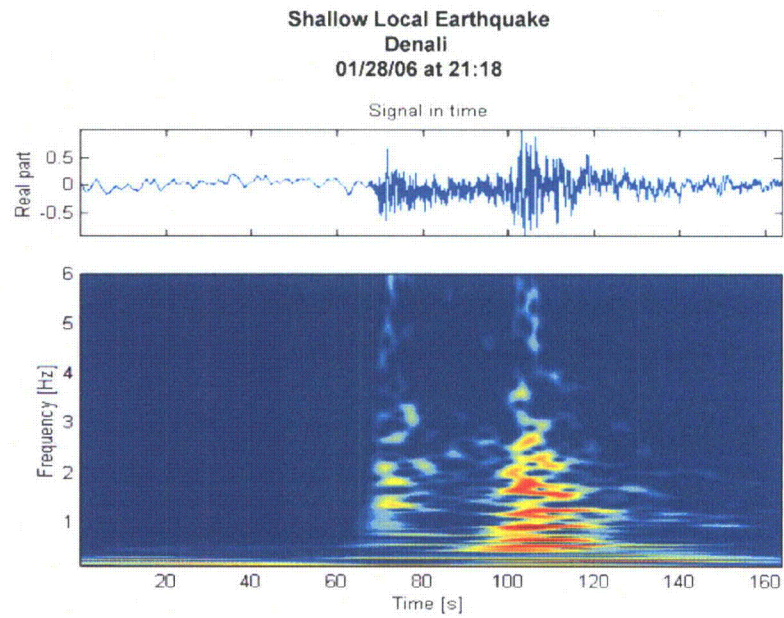


Figure 2.4S.6.4.3-2: Seismogram (top) and spectrogram of a typical shallow earthquake (M 3.9 January 27, 2006 Denali earthquake)

**Landslide Event
Station MCK
09/14/05 at 19:58**

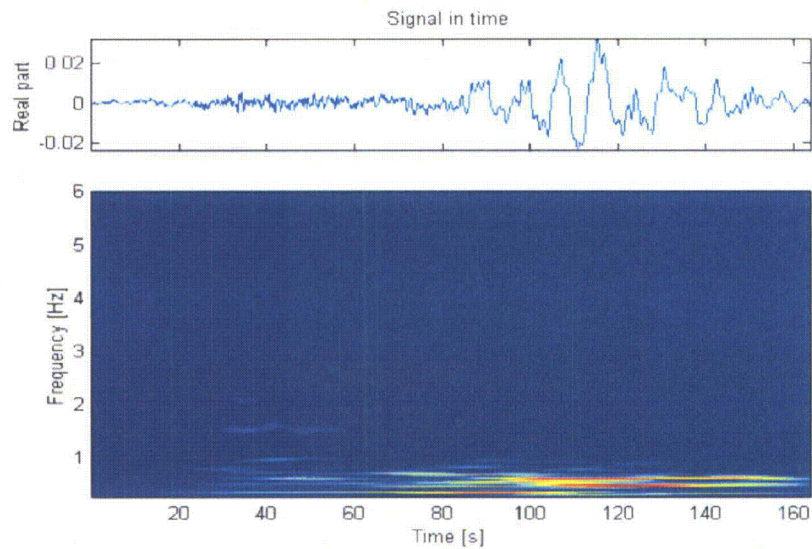


Figure 2.4S.6.4.3-3: Seismogram (top) and spectrogram of a known subaerial landslide in SE Alaska. MCK: McKinley Park seismic station.

**Gulf of Mexico Event
02/10/06 at 04:14**

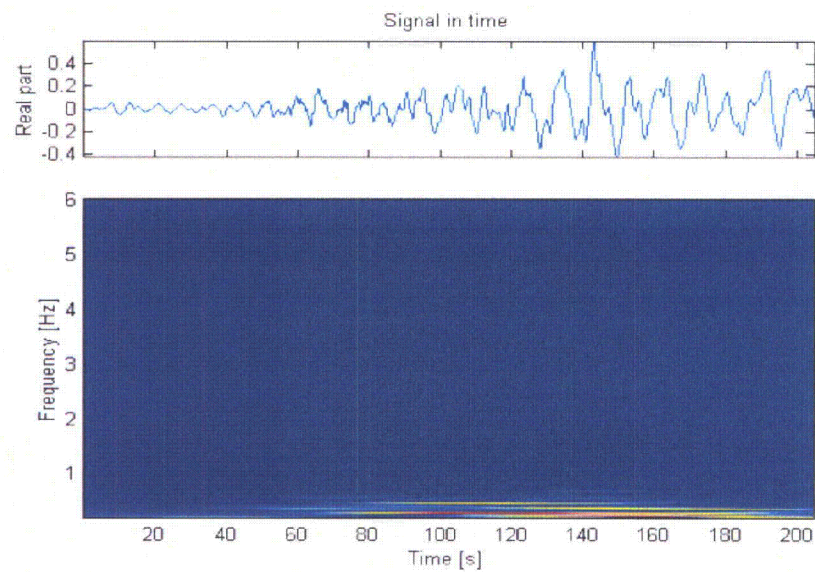


Figure 2.4S.6.4.3-4: Seismogram (top) and spectrogram of the February 10, 2006 Gulf of Mexico Green Canyon event (see Fig. 1 for location). Note the similarity with Fig. 3 (landslide) and the dissimilarity with Fig. 2 (earthquake).

Maximum Submarine Landslides

We define four geological provinces in the Gulf of Mexico that are likely to be the origin of submarine landslides that control the determination of the PMT. Three additional provinces defined in Chapter 3 of ten Brink and others (2007) are not likely to be sites of major tsunamigenic landslides. The four provinces defined for PMT analysis are the Northwest Gulf of Mexico (immediately off the STP site), Mississippi Canyon, Florida Escarpment, and Campeche Escarpment. The first is a mixed canyon/fan and salt province involving failure of terrigenous and hemipelagic sediment, the second a canyon/fan province and the third and fourth are carbonate provinces formed from reef structures and characterized by having steep slopes (i.e., escarpments).

Tsunamis propagating to the South Texas coast would be the back-going tsunamis emanating from the Northwest Gulf of Mexico (East Breaks) and Mississippi Canyon landslides (the latter being highly oblique to the STP site), whereas the site would be affected primarily by the outgoing tsunami from a landslide sourced from above the Campeche or Florida Escarpments. For the outgoing tsunami, there is a significant directivity effect that scales with the speed of downslope motion of the landslide (up to the phase speed of the tsunami). Because the Mississippi Canyon and Florida Escarpment landslides are oblique to the STP site, the length of continental shelf that the wave must travel over is much greater than for the East Breaks landslide or landslides along the Campeche escarpment that are broadside from the STP site. This would result in much greater energy dissipation during propagation associated with tsunamis from the Mississippi Canyon and Florida Escarpment source regions. The characteristics and the parameters that define the maximum landslide are given below for the East Breaks Landslide in the Northwest Gulf of Mexico and the Mississippi Canyon and Florida Escarpment provinces.

The primary landslide parameters that are used in the tsunami models include the excavation depth and slide width, which can be directly measured from sea floor mapping of the largest observed slide in the four geologic provinces. The other necessary parameter is downslope landslide length, interpreted from the runout distance. The runout distance measured from sea floor mapping is a combination of fast plug flow (low viscosity, non-turbulent), creeping plug flow (high viscosity/viscoplastic, non-turbulent) and turbidity currents (turbulent boundary layer fluid). The latter two likely have little to no tsunami-generating potential. Also, turbidity currents often involves entrainment of material during flow, such that the deposition volume may be greater than the excavation volume. Finally, hydroplaning may increase the runout of submarine landslides. The landslide lengths indicated below are intended to represent the main tsunami-generating phase. The amplitude of the initial negative wave above the excavation region is linked to the maximum excavation depth. The amplitude of the initial positive wave above the deposition region is determined from a conservation of landslide volume. The excavation volume can be well determined using GIS techniques (see below). Setting the deposition volume equal to the excavation volume, the positive amplitude is determined for a given landslide length. For a fixed volume, increasing the landslide length decreases the initial positive amplitude of the landslide tsunami.

Landslide volume calculations are based on measuring the volume of material excavated from the landslide source area using a technique similar to that applied by ten Brink and others (2006) and Chaytor and others (2009). Briefly stated, the approach involves using multibeam bathymetry to outline the extent of the excavation area, interpolating a smooth surface through the polygons that define the edges of the slide to provide an estimate of the pre-slide slope surface, and subtracting this surface from the present seafloor surface.

The maximum observed landslide from multibeam surveys is taken as the maximum landslide for a given region. It may be possible that larger landslides could occur in a given region, however this determination of the maximum landslide is consistent with the overall definition of PMT as “the most severe of the natural phenomena that have been historically reported or determined from geological and physical data for the site and surrounding area”. In this case, the maximum landslide is taken from geologic observations spanning tens of thousands of years. Moreover, because landslide volumes appear follow a power-law or log-normal distribution (ten Brink and others, 2006; Chaytor and others, 2009), there may be no mathematical or physical constraints on the definition of the theoretical maximum landslide (other than the dimensions of the entire continental slope). These calculations were only completed for part of the East Breaks landslide, the Mississippi Canyon landslide, and a landslide from the slope above the Florida Escarpment. No calculations were made for failures above the Campeche Escarpment because currently available bathymetric data are inadequate.

East Breaks Landslide

Geologic Setting: River delta that formed at the shelf edge during the early Holocene (Figure 2.4S.6.4.3-5)

Post Failure Sedimentation: Landslide source area appears to be partially filled (predominantly failure deposits with some post-failure sedimentation)

Age: 10,000 – 25,000 years (Piper, 1997; Piper and Behrens, 2003)

Maximum Single Event (East Breaks landslide): Maximum and minimum parameters are taken from different interpretations of the digitized failure scar surrounding the excavation region (Chaytor and others, 2009).

Max

- Volume: 21.95 km³
- Area: 519.52 km²

Min

- Volume: 20.80 km³
- Area: 420.98 km²

Width: ~ 12 km

Length: ~ 50 km

Excavation depth: ~160 m (shelf to base of headwall scarp)

Run out distance: 91 km from end of excavation and 130 km from headwall based on GLORIA mapping (Rothwell and others, 1991) (See Figure 2.4S.6.4.3-6). Multibeam bathymetry is not available for the entire run-out area

Trabant and others (2001) have reported volumes of 50-60 and a run-out distance of 160 km. Trabant and others (2001) derived their volume estimate from the size of debris lobes in the deposition region, using a 3D seismic reflection dataset that is proprietary. We cannot confirm their result for that reason and because we lack the necessary bathymetry coverage that far downslope to identify the extent of the debris lobes. Debris lobes are often the result of multiple events that are difficult to distinguish (Chaytor and others, 2009; Twichell and others, 2009) and may include sediment entrainment during flow. Our volume estimate above is for the amount excavated at the source (within the landslide scarp) and is more representative of a single failure event.

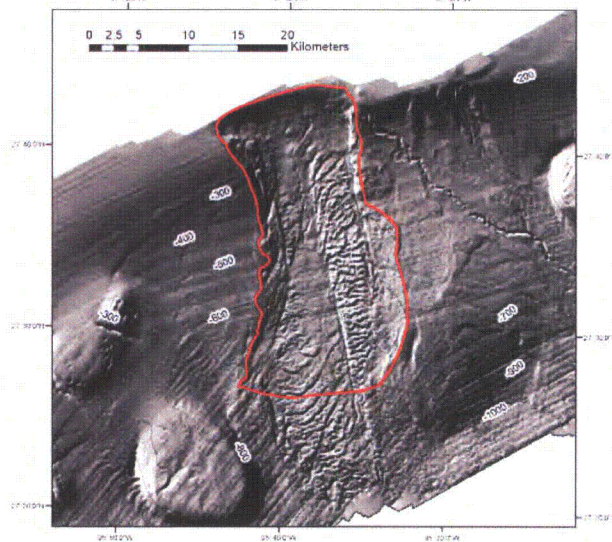


Figure 2.4S.6.4.3-5: Outline (red) of excavation area for the East Breaks landslide based on available multibeam bathymetric data.

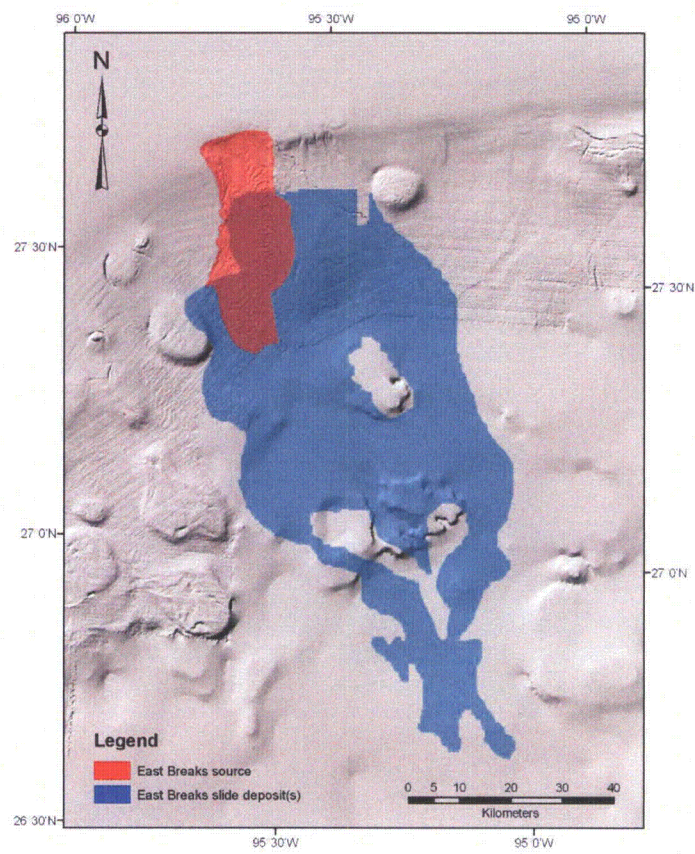


Figure 2.4S.6.4.3-6: Comparison of excavation area (red) and depositional area (blue) for the East Breaks landslide. The extent of the landslide deposit was mapped using GLORIA sidescan sonar imagery (Rothwell and others, 1991).

Technical Letter Report
South Texas Project Hydrology TER w/ OIs
Section 2.4.6

JCN Q-4151
Task Order No. 2
U.S. Geological Survey

Mississippi Canyon

Geologic Setting: River delta and fan system (Figure 2.4S.6.4.3-7).

Post Failure Sedimentation: Canyon appears to be partially filled with failure deposits that are capped by hemipelagic sediments.

Age: 7,500 to 11,000 years (Coleman and others, 1983; Chapter 3 in ten Brink and others, 2007)

Maximum Single Event

- Volume: 425.54 km³
- Area: 3687.26 km²
- Excavation depth: ~300 m (in the upper canyon)
- Runout distance: 297 km from toe of excavation area and 442 km from the headwall scarp (see Figure 2.4S.6.4.3-8).

Other reported volumes are 1500-2000 km³ (Coleman and others, 1983). As with the East Breaks landslide, this estimate is from landslide deposits that most likely represent multiple failure episodes. The volume given above is our best estimate of a maximum single-event volume.

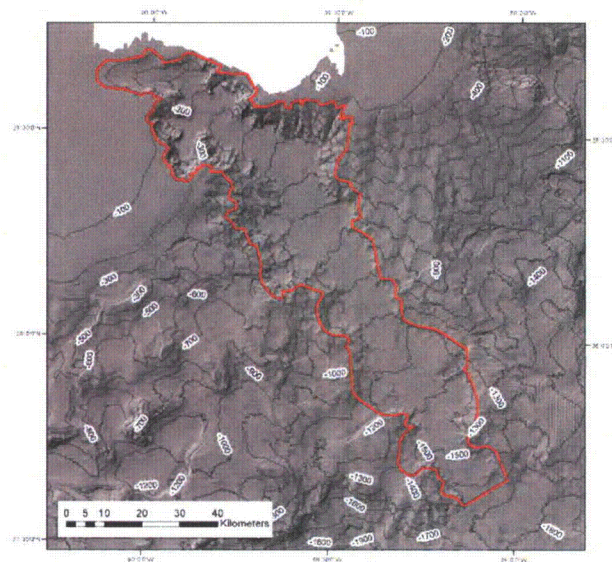


Figure 2.4S.6.4.3-7: Outline (red) of excavation area for the Mississippi Canyon landslide based on multibeam bathymetric data and reports by Coleman and others (1983) and Goodwin and Prior (1989).

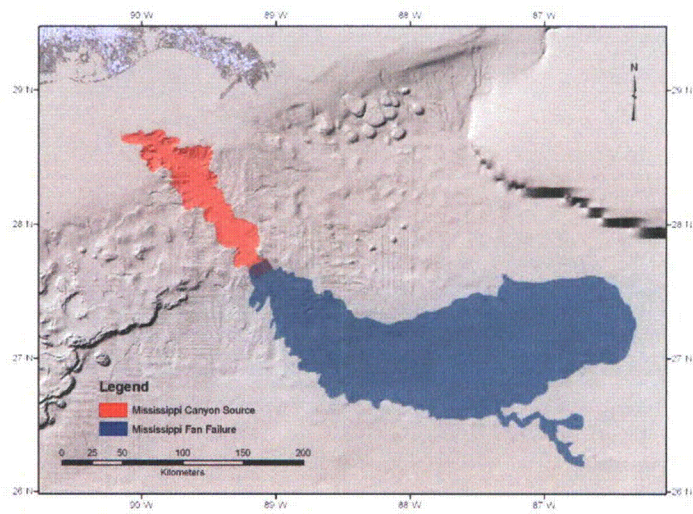


Figure 2.4S.6.4.3-8: Comparison of excavation area (red) and depositional area (blue) for the Mississippi Canyon landslide. The extent of the landslide deposit is based on GLORIA sidescan sonar imagery (Twichell and others, 1991).

Technical Letter Report
South Texas Project Hydrology TER w/ OIs
Section 2.4.6

JCN Q-4151
Task Order No. 2
U.S. Geological Survey

Florida Escarpment

Geologic Setting: Edge of a carbonate platform (Figure 2.4S.6.4.3-9).

Post Failure Sedimentation: None visible on multibeam images or on available high-resolution seismic profiles (Twichell and others, 1993).

Age: Early Holocene or older (Doyle and Holmes, 1985). Because Florida Escarpment carbonate failures are buried by Mississippi Fan deposits, the Florida Escarpment failures are older than the youngest fan deposits dated at about 11,500 years old.

Maximum Single Event

- Volume: 16.2 km³
- Area: 647.57 km²
- Excavation depth: ~150 m, but quite variable
- Runout distance: Uncertain. The landslide deposit is at the base of the Florida Escarpment buried under younger Mississippi Fan deposits.

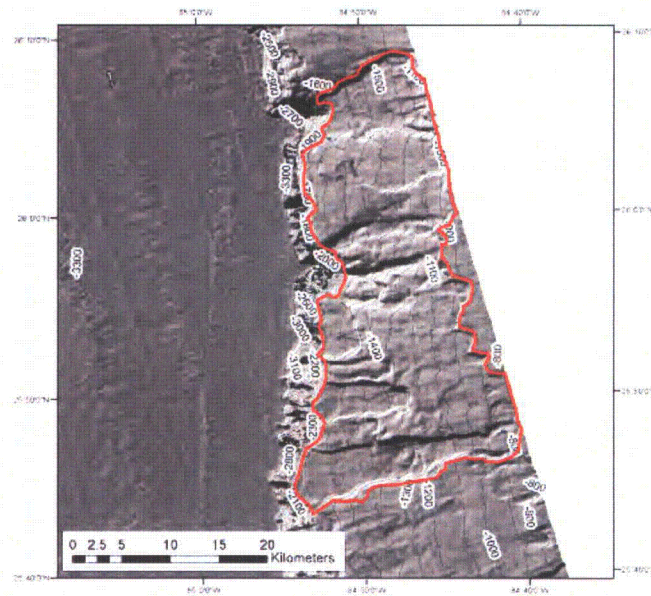


Figure 2.4S.6.4.3-9: Outline (red) of excavation area for the maximum landslide above the Florida Escarpment from multibeam bathymetric data.

Technical Letter Report
South Texas Project Hydrology TER w/ OIs
Section 2.4.6

JCN Q-4151
Task Order No. 2
U.S. Geological Survey

Campeche Escarpment

Geologic Setting: Carbonate platform

One of the persistent issues during the independent confirmatory analysis is acquiring sufficient geologic information about the Campeche Escarpment with which to estimate the maximum landslide parameters as with the other Gulf of Mexico landslide provinces. Plans to conduct multibeam bathymetry surveys are pending. Presently, there is no published information showing the detailed bathymetry or distribution of landslides on or above the Campeche Escarpment.

Seismic Seiches

Seismic seiches are fundamentally a different type of wave than tsunamis. Rather than being impulsively generated by displacement of the sea floor, seismic seiches occur from resonance of seismic surface waves (continental Rayleigh and Love waves) within enclosed or semi-enclosed bodies of water. The harmonic periods of the oscillation are dependent on the dimensions and geometry of the body of water. In 1964, seiches were set up along the Gulf Coast from seismic surface waves emanating from the M=9.2 Gulf of Alaska earthquake. The efficiency at which the seiches occurred at great distance from the earthquake is primarily explained by amplification of surface wave motion from the thick sedimentary section along the Gulf Coast (McGarr, 1965). Because the propagation path from Alaska to the Gulf Coast is almost completely continental (McGarr, 1965) and because the magnitude of the 1964 earthquake is close to the maximum possible for that subduction zone (e.g., Bird and Kagan, 2004), it is likely that the historical observations of 1964 seiche wave heights are the maximum possible and less than the PMT amplitudes from landslide sources.

Conclusion: In summary, we list the following findings of our independent confirmatory analysis of the tsunami source characteristics below:

- There is sufficient evidence to consider submarine landslides in the Gulf of Mexico as a present-day tsunami hazard for the purpose of defining the PMT at the South Texas Project Site.
- Four geologic landslide provinces are defined in the Gulf of Mexico that are applicable for determining the PMT: Northwest Gulf of Mexico, Mississippi Canyon, Florida Escarpment, and Campeche Escarpment. The propagation paths that result in the least attenuation of potential tsunamis are for the East Breaks and Campeche provinces.
- Parameters for the maximum submarine landslide were determined for each of the provinces, except for the Campeche Escarpment where we are awaiting additional data.
- It is likely that seismic seiche waves resulting from the 1964 Gulf of Alaska earthquake are nearly the highest possible, owing to a predominantly continental ray path for seismic surface waves from Alaska to the Gulf Coast.

2.4S.6.4.4 Tsunami Analysis

Summary of FSAR contents: Based on the review of tsunami sources, the applicant indicates that modeling of tsunami wave height and periods at the site is not warranted and was not performed. However, tsunami analysis was conducted by the applicant in response to RAI 2.4S.6.1-1.

Brief description of staff's review: We comment on the applicant's response to RAI 2.4S.6.4-1 (below). For most of this section we provide background information on tsunami analysis techniques and specifically describe the technical approach used in the independent confirmatory analysis. The latter includes aspects related to tsunami propagation, wave breaking, runup and inundation, and overtopping of sloping structures.

Request for Additional Information (RAI) 2.4S.6.4-1: Section C.I.2.4.6.4 of Regulatory Guide 1.206 (RG 1.206) provides specific guidance with respect to tsunami analysis. This includes providing a complete description of the analysis procedure used to calculate tsunami wave height and period at the site. Provide available high-resolution processed LIDAR (Light Detection and Ranging) data at and near the site as well as the source for the bathymetric dataset used for tsunami analysis.

Resolution of the RAI and issuance of Open Items: The applicant responded to RAI 2.4S.6.4-1 by indicating that a bathymetric and topographic elevation model is the US Coastal Relief Model that is available from NOAA/NGDC. The applicant did not indicate whether they acquired and/or processed lidar data for the STP site. The applicant did not revise the COLA as a result of this RAI.

Issuance of Open Items: At this time, our staff has a Gulf of Mexico bathymetric and topographic grid created by the U.S. Army Corps of Engineers for use with the storm surge model ADCIRC data. It is of sufficient resolution and accuracy with which to conduct our independent confirmatory analysis. We recommend that an Open Item is not needed following the resolution of RAI 2.4S.6.4-1.

Confirmatory analysis and major findings: In this section, tsunami analyses procedures for propagation and coastal effects used for the independent confirmatory analysis are described.

Background

Numerical simulations of tsunami propagation have made great progress in the last thirty years. Several tsunami computational models are currently used in the National Tsunami Hazard Mitigation Program, sponsored by the National Oceanic and Atmospheric Administration, to produce tsunami inundation and evacuation maps for the states of Alaska, California, Hawaii, Oregon, and Washington. The computational models include MOST (Method Of Splitting Tsunami), developed originally by researchers at the University of Southern California (Titov and Synolakis, 1998); COMCOT (Cornell

Multi-grid Coupled Tsunami Model), developed at Cornell University (Liu and others, 1995); and TSUNAMI2, developed at Tohoku University in Japan (Imamura, 1996). All three models solve the same depth-integrated and 2D horizontal (2DH) nonlinear shallow-water (NSW) equations with different finite-difference algorithms. There are a number of other tsunami models as well, including the finite element model ADCIRC (ADvanced CIRCulation Model For Oceanic, Coastal And Estuarine Waters) (e.g., Myers and Baptista, 1995).

For a given source region condition, existing models can simulate propagation of a tsunami over a long distance with sufficient accuracy, provided that accurate bathymetry data exist. Figure 2.4S6.4.4-1 shows the snapshots of free surface elevations at one hour and 44 minutes after the 2004 Sumatra earthquake occurred.

Figure 2.4S6.4.4-1: Snapshots of free surface elevations at one hour and forty four minutes after the 2004 Sumatra earthquake occurred. Yellow and red colors denote positive elevation blue denotes negative depression (Numerical results based on COMCOT).

The shallow-water equation models commonly lack the capability of simulating dispersive waves, which, however, could well be the dominating features in landslide-generated tsunamis and for tsunamis traveling a long distance. Several high-order depth-integrated wave hydrodynamics models (Boussinesq models) are now available for simulating nonlinear and weakly dispersive waves, such as COULWAVE (Cornell University Long and Intermediate Wave Modeling Package) (Lynett and Liu, 2002) and FUNWAVE (Kennedy and others, 2000). The major difference between the two is their treatment of moving shoreline boundaries. Lynett, et al. (2003) applied COULWAVE to the 1998 PNG tsunami with the landslide source; the results agreed with field survey data well. Recently, several finite element models have also been developed based on Boussinesq-type equations (e.g., Woo and Liu, 2004). Boussinesq models require higher spatial and temporal resolutions, and therefore are more computationally intensive. Moreover, most of model validation work was performed for open-ocean or open-coast problems. In other words, the models have not been carefully tested for wave propagation and oscillations in semi-enclosed regions – such as a harbor or bay – especially under resonant conditions.

Being depth-integrated and horizontally 2D, NSW and Boussinesq models lack the capability of simulating the details of many coastal effects, such as wave overturning and the interaction between tsunamis and coastal structures, which could be either stationary or movable. At present, stationary coastal structures are parameterized as bottom roughness and contribute to frictional effects in these 2DH models. Although by adjusting the roughness and friction parameter satisfactory results can be achieved for maximum runup and delineation of the inundation zone (e.g., Liu and others, 1995), these models cannot provide adequate information for wave forces acting on coastal structures, nor can they estimate bottom stress, which is essential in determining sediment erosion and deposition.

As a tsunami propagates into the nearshore region, the wave front undergoes a nonlinear transformation while it steepens through shoaling. If the tsunami is large enough, it can break at some offshore depth and approach land as a bore – the white wall of water commonly referenced by survivors of the Indian Ocean tsunami. Wave breaking in traditional NSW tsunami models has not been handled in a satisfactory manner. Numerical dissipation is commonly used to mimic breaking, and thus results become grid dependant. Numerical dissipative approaches most notably include shock capturing schemes. In these schemes, energy dissipation is related to the local smoothness of the solution, which is of course strongly related to the grid length near the shock. With shock capturing methods, the numerical results tend to be very smooth. However, the dissipation is entirely numerical, and although the general form of the dissipative terms may be of the proper physical form, the dissipation will inevitably be related to the grid length and time step. In Boussinesq models, this breaking is still handled in an approximate manner due to the fact that the depth-integrated derivation does not allow for an overturning wave; however these breaking schemes have been validated for a wide range of nearshore conditions (e.g., Lynett, 2006).

Being depth-integrated, NSW and Boussinesq models lack the capability of simulating the vertical details of many coastal effects, such as strong wave breaking/overturning and the interaction between tsunamis and irregularly shaped coastal structures. To address this deficiency, several 2D and 3D computational models based on Navier-Stokes equations have been developed, with varying degrees of success. For example, the co-P.I. Liu and his students developed a 2D computational model, COBRAS (Cornell Breaking waves and Structures model) (Lin and Liu, 1998a, b; Lin and others, 1999), which is capable of describing the interactions between breaking waves and structures that are either surface piercing or submerged (Chang and others, 2001; Hsu and others, 2002). COBRAS adopted the Volume of Fluid (VOF) method to track free surface movement along with a turbulence closure model; several other computational models using different free surface tracking methods are also in use, such as the micro surface cell technique developed by Johnson et al. (1994).

While a moving shoreline is readily included in VOF-type models, due to the computational costs of these models it is often not practical to use them for large-scale inundation problems like tsunami runup. The NSW and Boussinesq models are conventionally used for this purpose. Researchers generally use a fixed grid, finite difference or finite element method to solve these depth-integrated equations. Using a fixed grid numerical model to solve a moving boundary problem can lead to difficulties related to the loss of mass conservation and instabilities in the computations (Leendertse, 1987) as a result of imposing discrete fixed increments to the extent of wetting and drying areas (Balzano, 1998).

To eliminate the difficulties related to shoreline location being locked onto a grid, Zelt (1991) used a Lagrangian model to simulate shoreline movement due to solitary wave runup. This model produced maximum runup values that compared well with experimental values, but the shape of the wave as it traveled up the slope did not compare

as favorably. A handful of others have utilized Lagrangian techniques with depth-integrated equation models to simulate a moving shoreline (e.g., Gopalakrishnan, 1989; Petera and Nassehi, 1996). Another treatment of moving boundary problem is employing a slot or permeable-seabed technique (Tao, 1983, 1984). The first application of the permeable slot with a Boussinesq-type model (Madsen and others, 1997) yielded runup errors on the order of ten percent of the maximum. Modifications have been made to this permeable slot technique (Kennedy and others, 2000), increasing the accuracy, but it was also shown that the empirical coefficients that govern the technique can not be universally determined, due to numerical stability problems (Chen and others, 2000). Lynett et al (2002) developed an extrapolation method runup scheme, allowing for the shoreline to exist at any arbitrary location in-between grid points and negating the major drawback of using fixed grids. This method is shown to be accurate for a wide range of 1HD and 2HD problems including the shoreline motion due to breaking and non-breaking waves (e.g., Pedrozo-Acuña and others, 2006). using fixed grids. This method is shown to be accurate for a wide range of 1HD and 2HD problems including the shoreline motion due to breaking and non-breaking waves (e.g., Pedrozo-Acuña and others, 2006).

Technical Approach Used in Confirmatory Analysis

Earthquake generated tsunamis, with their very long wavelengths, are ideally matched with NSW for transoceanic propagation. Models such as Titov & Synolakis (1995) and Liu et al. (1995) have been shown to be reasonably accurate throughout the evolution of a tsunami, and are in widespread use today. However, when examining the tsunamis generated by submarine mass failures, the NSW can lead to significant errors (Lynett and others, 2003). The length scale of a submarine failure tends to be much less than that of an earthquake, and thus the wavelength of the created tsunami is shorter. To correctly simulate the shorter wave phenomenon, one needs equations with excellent shallow to intermediate water properties, such as the Boussinesq equations. While the Boussinesq model too has accuracy limitations on how deep (or short) the landslide can be (Lynett and Liu, 2002), it is able to simulate the majority of tsunami generating landslides. Thus, for the work proposed here, the Boussinesq-based numerical model COULWAVE (Lynett and Liu, 2002) will be used. (See Appendix for reprints of peer-reviewed papers that form the foundation of COULWAVE.) This model solves the fully nonlinear extended Boussinesq equations on a Cartesian grid. COULWAVE has the capability of accurately modeling the wind waves with both nonlinear and dispersive properties. A particular advantage of the model is the use of fully non-linear equations for both deep and shallow water. This avoids the common problem of "splitting" the analysis when the wave reaches shallow water. Applications for which COULWAVE has proven very accurate include wave evolution from intermediate depths to the shoreline, including parameterized models for wave breaking and bottom friction.

Wave Propagation

COULWAVE is based on the Boussinesq-type equations, which are known to be accurate for inviscid wave propagation from fairly deep water (wavelength/depth ~ 2) all the way to the shoreline (Wei and others, 1995). The equation model consists of a fairly

complex set of partial differential equations which are integrated in time to solve for the free surface elevation and the horizontal velocity vector, \mathbf{u} . A 4th order Adams-Bashforth-Moulton predictor-corrector time integration scheme is required, and the spatial derivatives are approximated with 4th order, centered finite differences. The high order scheme is required due to the inclusion of first to third order derivatives in the model equations. Waves are generated in the numerical domain with an internal source (Wei and others, 1999), which can use as input a wave energy spectrum to create a directional, random wave field. In conjunction with the internal source generator, sponge layers are placed along the outgoing lateral boundaries, and provide excellent wave absorption across a wide range of frequencies and amplitudes. Fundamentally, the Boussinesq equations are inviscid. To accommodate frictional effects, viscous submodels are integrated into COULWAVE. Bottom friction is calculated with the quadratic friction equation:

$$R_{BottomFriction} = f \frac{\mathbf{u}_b |\mathbf{u}_b|}{H}$$

where \mathbf{u}_b is the velocity evaluated at the seafloor, and f is a bottom friction coefficient, typically in the range of 0.001 to 0.01. As noted in Lynett et al (2002), maximum runoff is sensitive to the value of f , particularly for very large, breaking waves. (See Appendix for further explanation of the theory described above.)

Wave Breaking

The wave breaking model has received much attention and has undergone numerous validation exercises. The wave breaking model is based on the "eddy-viscosity" scheme, where energy dissipation is added to the momentum equation when the wave slope exceeds some threshold value, and continues to dissipate until the wave slope reaches some minimum value when the dissipation is turned off.

One set of comparisons is shown in Figure 2.4S6.4.4-2 for a number of regular waves breaking and running up a slope. As can be seen, COULWAVE captures the mean values of height and water level to a high degree of accuracy.

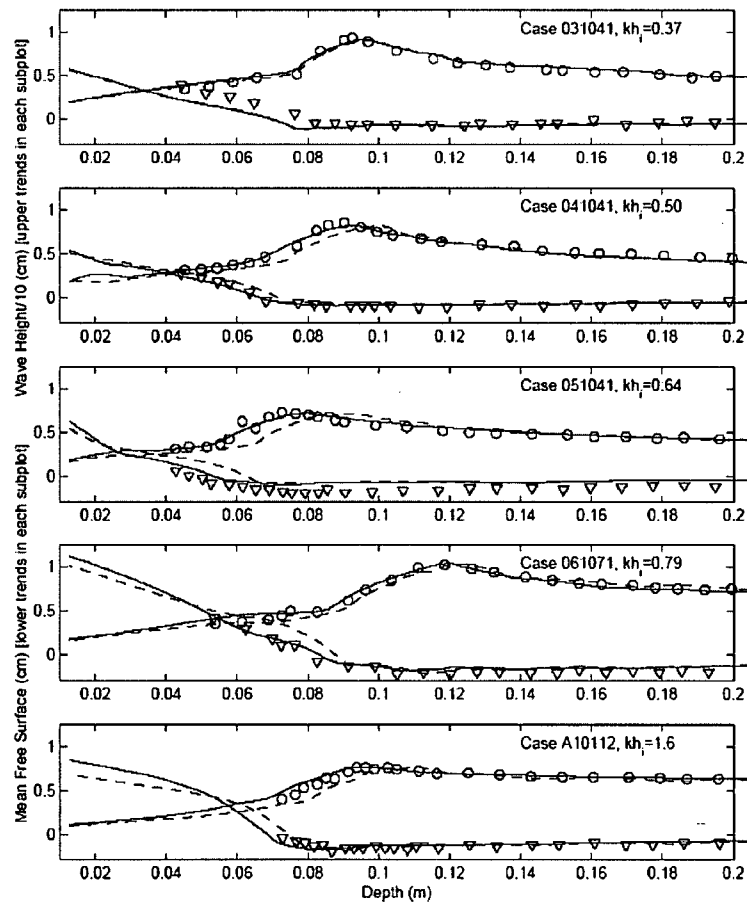


Figure 2.4S6.4.4-2: Wave height and mean free surface measurements from the experiments of Hansen and Svenson (1979) symbols, the traditional Boussinesq model (dashed-line), and COULWAVE (solid line). Trials are for monochromatic waves breaking on a planar 1/20 slope.

While these comparisons show that the model is capable of capturing a simplified, laboratory setup, it is also necessary to gauge the accuracy against real, field conditions.

COULWAVE has been compared with a number of field sites; one such comparison is given in Figure 2.4S6.4.4-3. As can be seen, the model captures the spectral transformation of random waves through the surf zone. Note that the breaking model uses a single set of parameters (eddy viscosity, etc.) for all trials, so there is no individual case optimization.

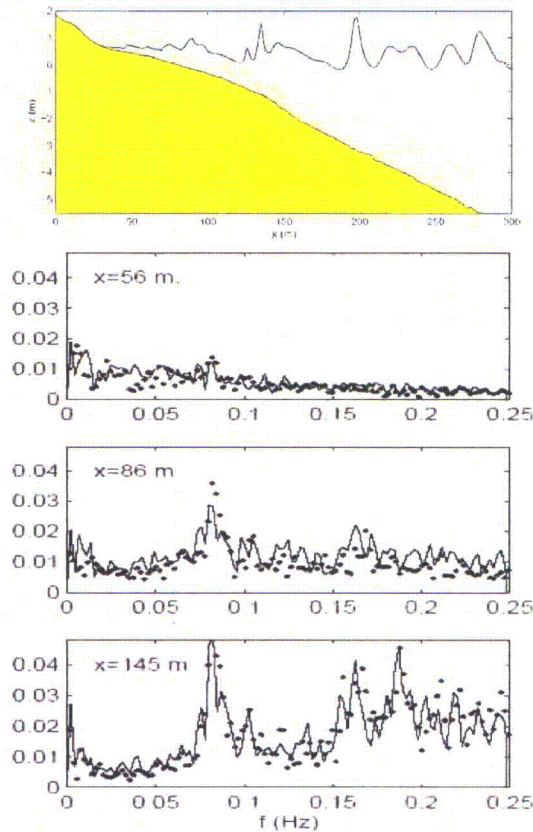


Figure 2.4S6.4.4-3: COULWAVE random wave comparison with field data. The lower subplots show the spectrum comparisons at three different locations. Dots are the field data from Raubenheimer (2002); solid lines are the COULWAVE results.

The horizontal velocity profile under breaking waves is a necessary component to capture accurately for transport-related physics. Using a process of superposition of velocity profiles (Lynett, 2006), instantaneous and mean profiles under breaking waves in predicted well (see Figure 2.4S6.4.4-4.)

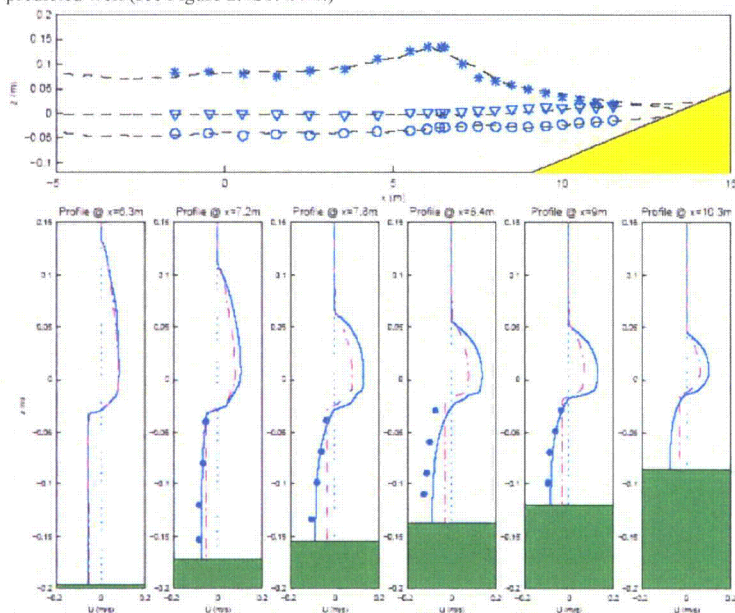


Figure 2.4S6.4.4-4: Comparison with data of Ting and Kirby (1995) spiller. The top plot shows the mean crest level (stars), mean water level (triangles), and mean trough level (circles) for the experiment as well as the numerical simulation. The lower subplots are the time-averaged horizontal velocities, where the experimental values are shown with the dot, COULWAVE results by the solid line, and the standard Boussinesq results by the dashed-dotted line.

Publications which specifically use COULWAVE to simulate wave breaking include Lynett and Liu (2002), Lynett et al (2003), Korycansky and Lynett (2005), Cheung et al (2003), (Lynett and Liu, 2006; Lynett, 2006), Lynett (2007), and Korycansky et al (2007).

Wave Runup and Inundation

The moving shoreline condition has shown to capture shoreline motion due to a wide range of wave frequencies, wave heights, and beach slopes. The shoreline algorithm was

originally developed to simulate the important motion of tsunami runup (Lynett and others, 2002), and uses a variation of the so-called "extrapolation" technique. The extrapolation method has its roots in Sielecki and Wurtele (1970), with extensions by Hibberd and Peregrine (1979), Kowalik and Murty (1993), and Lynett et al. (2002). The basic idea behind this method is that the shoreline location can be extrapolated using the nearest wet points, such that its position is not required to be locked onto a fixed grid point; it can move freely to any location. The numerical results evaluated at the extrapolated waterline are used to update the solution for the next time step. This moving-boundary technique is numerically stable and does not require any artificial dissipation mechanisms.

Recently (Korycansky and Lynett, 2005), extensive comparisons have been made with empirical runup laws and existing experimental data for runup due to regular waves. Figure 2.4S6.4.4-5 shows how COULWAVE compares with the so-called Iribarren scaling for runup, an established coastal engineering relation based on deep water properties of the waves.

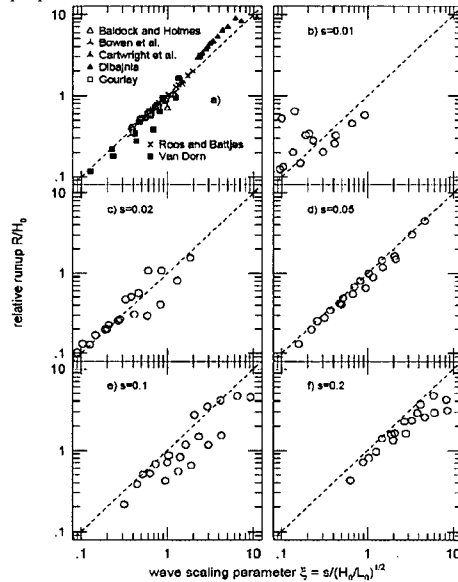


Figure 2.4S6.4.4-5: Wavetank experimental measurements of runup from the literature and COULWAVE runup results (open circles).

Publications which specifically use COULWAVE for runup or the moving shoreline algorithm developed by Lynett include Lynett et al (2002), Lynett et al (2003),

Korycansky and Lynett (2005), Cheung et al (2003), Pedrozo-Acuña et al. (2006),
(Lynett and Liu, 2006; Lynett, 2006), Lynett (2007), and Korycansky and Lynett (2007).

Overtopping of Sloping Structures

Quality, time-dependent data for wave overtopping of levees and dikes is sparse. Thus, as with existing published numerical models (e.g., Dodd, 1998), the large majority of comparisons provided here will use time-averaged experimental data. First, a comparison is made with the data of Saville (1955). This data set is one of the standard comparisons found in the literature (e.g., Kobayashi and Wurjanto, 1989; Dodd, 1998; Hu and others, 2000). An example of the physical setup for these trials is given in Figure 2.4S6.4.4-6, a spatial snapshot for a numerical simulation.

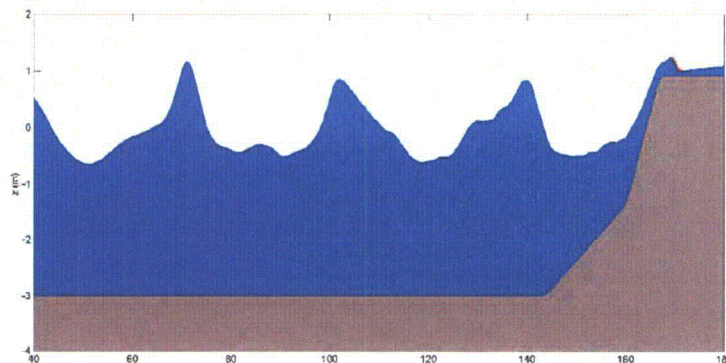


Figure 2.4S6.4.4-6: COULWAVE snapshot from a recreation of the Saville (1955) experiments. The general setup is a wavemaker depth ~ 3 m, a flat portion leading up to a $1/10$ slope, which connects to the “structure”. In these experiments, the structure has either a $1/3$ or $1/1.5$ slope.

A range of freeboard and wave conditions were tested. A summary of the comparisons is given in Table 2.4S6.4.4-1.

Run	Ho (m)	T (s)	Htoe (m)	R (m)	d _{toe} (m)	slope	Q _{meas} (m ² /s)	Q _{K&W} (m ² /s)	Q _{Bous} (m ² /s)
1	1.83	6.39	1.74	0.91	1.37	3	0.51	0.21	0.35
2	1.83	6.39	1.74	1.83	1.37	3	0.32	0.02	0.21
3	1.83	6.39	1.74	0.91	2.74	3	0.50	0.41	0.49
4	1.83	6.39	1.74	1.83	2.74	3	0.28	0.11	0.16
5	1.37	7.67	1.36	0.92	2.74	3	0.45	0.41	0.44
6	1.83	10.8	1.94	0.91	1.37	3	0.47	0.42	0.42
7	1.83	10.8	1.9	1.83	1.37	3	0.13	0.12	0.12
8	1.83	10.8	1.94	2.74	1.37	3	0.31	0.02	0.04
9	1.83	10.8	1.94	0.91	2.74	3	0.73	0.71	0.68
10	1.83	10.8	1.94	1.83	2.74	3	0.31	0.35	0.35
11	1.83	10.8	1.94	2.74	2.74	3	0.06	0.12	0.11
12	1.37	14.97	1.62	0.92	1.37	3	0.46	0.49	0.46
13	1.37	14.97	1.62	0.92	2.74	3	0.65	0.57	0.63
14	1.37	14.97	1.62	1.62	2.74	3	0.39	0.26	0.33
15	1.37	14.97	1.62	2.74	2.74	3	0.13	0.08	0.09
16	1.37	14.97	1.62	3.66	2.74	3	0.06	0.08	0.03
17	1.83	10.8	1.88	0.91	1.37	3	0.38	0.51	0.44
18	1.83	10.8	1.88	2.74	1.37	1.5	0.10	0.06	0.09
19	1.83	10.8	1.88	0.91	0	1.5	0.30	0.31	0.31
20	1.83	10.8	1.88	1.83	0	1.5	0.16	0.05	0.03

Table 2.4S6.4.4-1: Numerical comparisons with data from the Saville (1955) experiments. Ho is the wave height at the wavemaker, T is the wave period, Htoe is the wave height at the toe of the structure, R is the distance between the structure crest and the still water level, d_{toe} is the water depth at the toe, slope is the 1/slope of the structure, Q_{meas} is the measured overtopping flux, Q_{K&W} is the simulated overtopping by Kobayashi & Wurjanto (1989), and Q_{Bous} is the COULWAVE simulated flux.

Overall, the agreement between the Boussinesq simulations and the experiments is quite good. Where the two diverge, the Boussinesq results tend to agree with the published numerical results of Kobayashi & Wurjanto (1989).

The Boussinesq model results must also exhibit agreement with well established empirical formulas such as those given by Owen (1980) and Van der Meer & Janssen (1995). For these tests, a wide range of wave and levee configurations are tested. Ranges of parameters are: levee slope from 1/3 – 1/8, freeboard from 1' to 4', wave height at the structure toe from 2'-8', and wave period from 8s-16s. The incident wave condition is a shallow water TMA spectrum using a gamma value of 3.0. Approximately 500 Boussinesq simulations were performed, and the comparisons with the formula of van der Meer & Janssen (1995) are shown in Figure 2.4S6.4.4-7. Agreement is quite good.

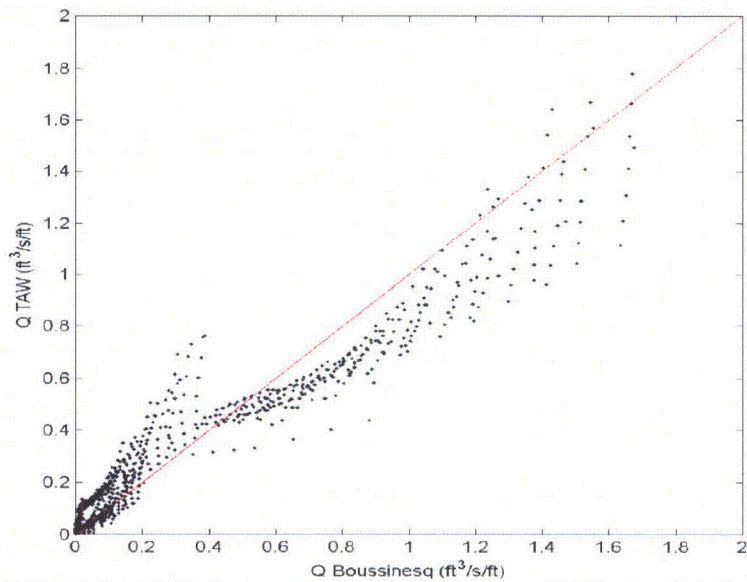


Figure 2.4S6.4.4-7: Comparison of Boussinesq overtopping rates with the formula given in the TAW design guidance.

Conclusion: As indicated in the FSAR, the applicant did not perform modeling of tsunami wave height and periods at the site. In response to RAI 2.4S.6.1-1, the applicant performed modeling of a tsunami from the East Breaks landslide using a nonlinear shallow-water wave model (MOST). In contrast, in our confirmatory analysis, we used a higher-order, depth-integrated wave hydrodynamics model (COULWAVE), more specifically suited to landslide tsunamis.

2.4S.6.4.5 Tsunami Water Levels

Summary of FSAR contents: To determine the maximum tsunami water levels, the applicant uses an estimate of the tsunami in the Gulf of Mexico from the 1755 Lisbon event (Mader, 2001) and then applies (1) a runup amplification factor, (2) 10% exceedance of astronomical high tide according to Regulatory Guide 1.59 (1977), and (3) sea-level rise from global climate change. The applicant determines the maximum water level for the PMT as 16.3 feet (5.0 m) above MSL which includes the effects of the exceedance of high tide and sea level rise within the next century at the site. Because the water levels computed for landslide sources described in the applicant's response to RAI

RAI 2.4S.6.1-1 are less than this level, it is assumed that the 5.0 m above MSL remains the PMT water level as determined by the applicant

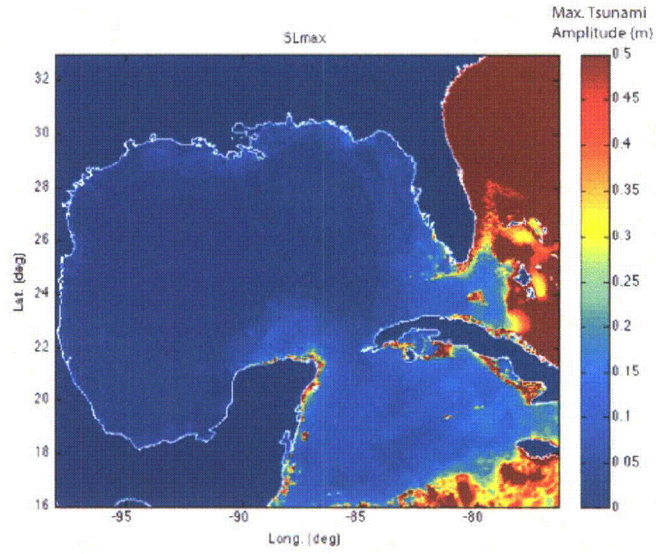
Brief description of staff's review: We conduct a confirmatory analysis to determine the PMT water levels using the tsunami analysis procedure described in 2.4S.6.4.4. After an initial screening of potential tsunami sources (2.4S.6.4.3), we develop tsunami models for distant earthquake and local landslide sources. Tsunami water levels for maximum earthquakes along Caribbean plate boundaries were less than 1 m near the site. Detailed tsunami analysis was conducted on Gulf of Mexico landslide sources to determine the PMT. Conservatism was imposed by using instantaneous displacement of the sea-surface (i.e., the so-called hot-start initial conditions for tsunami generation), without taking into account the decreased efficiency of tsunami generation related to the finite process time for landslide movement. Conservative bottom friction values were also used representing turbulent dissipation of energy during overland flow. Simulations were conducted in one and two horizontal dimensions.

Confirmatory analysis and major findings: Independent confirmatory analysis of tsunami water levels at the STP site focuses on distant earthquake tsunami sources and landslide sources local to the Gulf of Mexico.

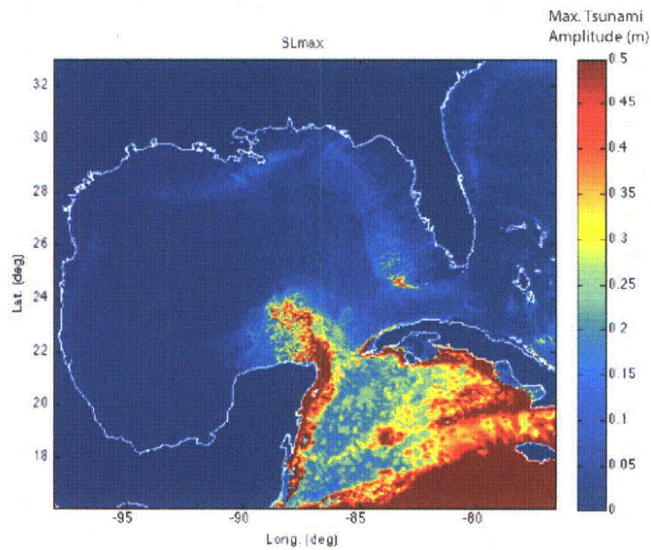
Distant Earthquake Sources

Regional tsunami propagation patterns in the Gulf of Mexico have been computed for a number of distant earthquake sources located in the Caribbean as reported in ten Brink et al. (2008). In Chapter 8 of that study, earthquake scenarios along five fault systems were examined: (1) west Cayman oceanic transform fault (OTF); (2) east Cayman OTF; (3) northern Caribbean subduction zone; (4) north Panama Oceanic Convergence Boundary; and (5) the northern South America convergent zone. In that report, tsunami propagation was modeled using the leap-frog, finite-difference approximation to the linear-long wave equations computed using Cartesian coordinates. Bottom friction, wave breaking, and runup were not modeled—computations were restricted to water depths of 250 m or greater. Results for the western Gulf of Mexico indicate that offshore tsunami amplitudes were less than 1.0 m for each earthquake scenario.

For comparative purposes, we re-compute here the offshore tsunami water levels for earthquake scenarios (3) and (5) using the COMCOT model. The COMCOT model is more accurate than the model used in ten Brink et al. (2008) since it includes non-linear terms in the propagation equations (hence, the computations can be carried into shallower water than in ten Brink et al., 2008), a moving boundary condition at the shoreline, and is computed in spherical coordinates. Bottom friction is also included, but is set at a low, conservative value ($f = 10^{-4}$) in this case. Figures 2.4S.6.4.5-1 and 2.4S.6.4.5-2 show the peak tsunami amplitude for M-9 earthquakes along the northern Caribbean subduction zone and northern South America convergent zone, respectively.



Figures 2.4S.6.4.5-1: Peak tsunami amplitude over 12 hours of propagation time for a M-9 earthquake along the northern Caribbean subduction zone. Amplitudes are clipped at 0.5 m.



Figures 2.4S.6.4.5-2: Peak tsunami amplitude over 12 hours of propagation time for a M-9 earthquake along the northern South America convergent zone. Amplitudes are clipped at 0.5 m.

These results confirm that tsunami amplitudes from distant Caribbean earthquakes are less than 1.0 m near the STP site. Tsunami amplitudes from earthquakes along the Azores-Gibraltar oceanic convergence boundary are also likely to be less than 1 m in the Gulf of Mexico (Mader, 2001; Barkan and others, in press).

Local Landslide Sources

Detailed tsunami analysis is performed for two local landslide scenarios: (1) a scenario fashioned after the East Breaks landslide and (2) a hypothetical landslide along the Campeche escarpment. For each case, tsunami propagation, runup, and inundation was computed using COULWAVE (see section 2.4S.6.4.4 Tsunami Analysis).

Numerical Grid Development

The bathymetry/topography grid required by the hydrodynamic model is created via two main sources: 1) the Smith and Sandwell (SS) 2-minute global elevation database, and 2) a recent Gulf of Mexico grid created by the U.S. Army Corps of Engineers for use with the storm surge model ADCIRC. The ADCIRC grid is a blend of numerous sources including recent lidar surveys and digitized elevation maps. The ADCIRC grid was used

for bathymetry and topography at locations with bottom elevations greater than -500 m. For depths greater than this (or elevations lower), the SS database was primarily used.

Figure 2.4S.6.4.5-3 shows the entire GOM grid coverage, with the three tsunami landslide source locations outlined. The high level of detail along the Texas coast is not evident in this image.

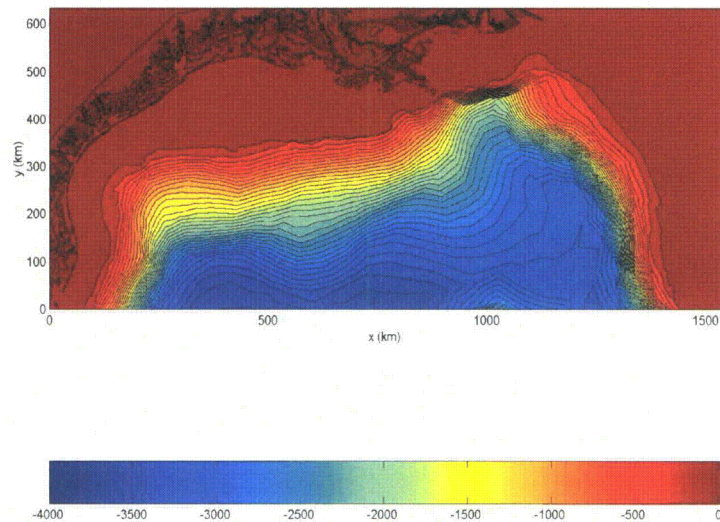
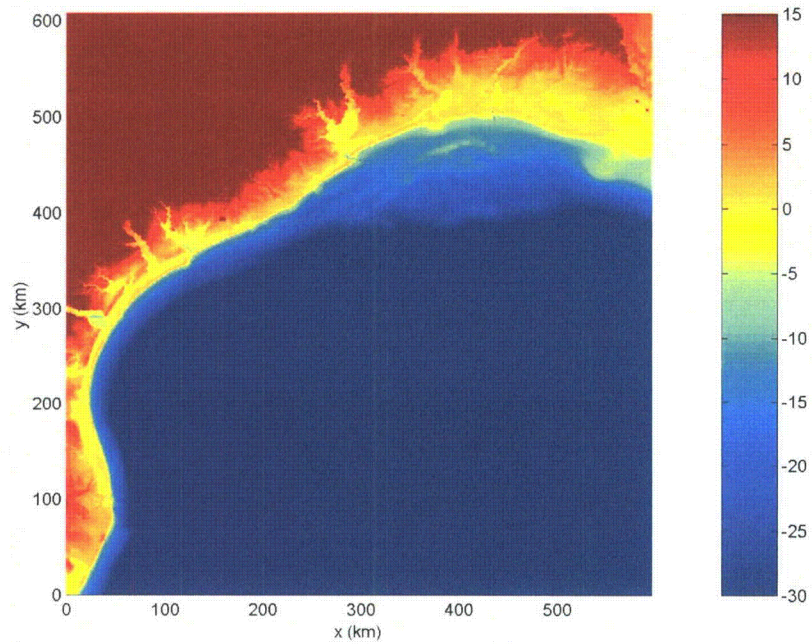
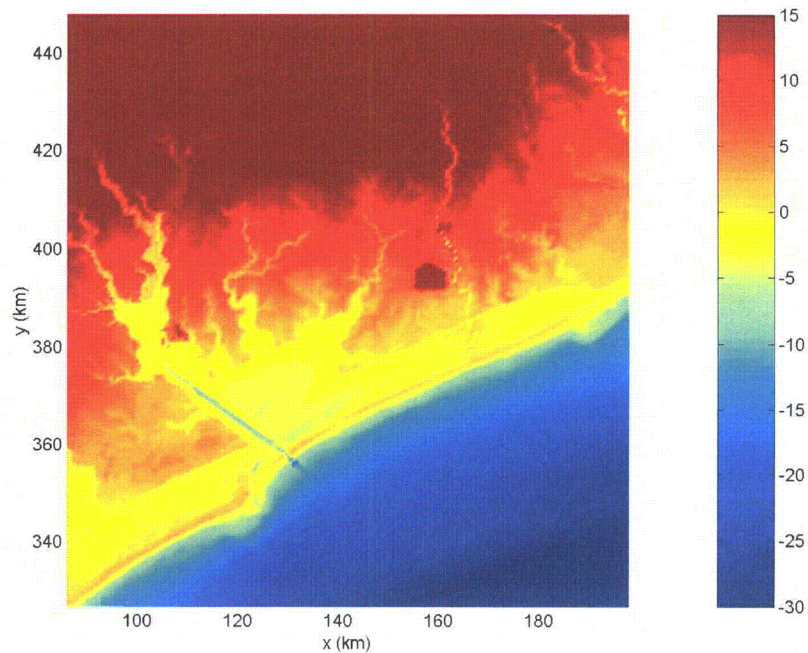


Figure 2.4S.6.4.5-3: Bathymetry/topography contour surface of the Gulf of Mexico domain used for the tsunami hydrodynamic modeling. General locations of the East Breaks landslide is shown by the white circle and the STP site by the green circle. Bottom elevations are indicated by colors following the colorbar, with units in meters.

In Figures 2.4S.6.4.5-4 and 2.4S.6.4.5-5, nearshore bathymetric detail can be seen. Figure 2.4S.6.4.5-4 shows the entire Texas coastline, whereas Figure 2.4S.6.4.5-5 is magnified near the STP site location. Barrier islands, coastal waterways, and rivers are all well resolved. Also note that the existing STP main cooling reservoir (MCR) and surrounding levee wall structure is also included in the grid, at an elevation of approximately +22m. The horizontal datum used for all model simulations is MSL.



Figures 2.4S.6.4.5-4: Detail of the bathymetry/topography contour surface on the Texas coastline, where again the STP site is given by the green circle. Bottom elevations are indicated by colors following the colorbar, with units in meters.



Figures 2.4S.6.4.5-5: Detail of the bathymetry/topography contour surface on the STP site. Bottom elevations are indicated by colors following the colorbar, with units in meters.

Initial Numerical Simulations – Physical Limits

The purpose of these initial simulations is to provide an upper limit of the tsunami wave height that could be generated by Gulf of Mexico landslide scenario. Source parameters for the simulation include landslide width, length, and excavation depth. Although landslide volume is not a direct parameter used in the model, the volumes of excavation and deposition are conserved and are used in determining the amplitude of the initial positive wave. Note that these limiting simulations use physical assumptions that are arguably unreasonable; the results of these simulations will be used to filter out tsunami sources that are incapable of adversely impacting the STP site under even the most conservative assumptions. Specifically, these assumptions are:

1. Time scale of submarine landslide motion is very small (i.e., instantaneous) compared the period of the generated tsunami

2. Bottom roughness, and the associated energy dissipation, is negligible in locations that are initially wet (i.e. locations with negative bottom elevation, offshore) Assumption 1 simplifies the numerical analysis considerably. With this assumption, the free water surface response matches the change in the seafloor profile exactly. This type of approximation is used commonly for subduction-earthquake-generated tsunamis, but is known to be very conservative for landslide tsunamis (Lynett and Liu, 2002). The modeling simplification arises because of the need to include the landslide time evolution, which is associated with a high degree of uncertainty, is removed. The initial pre-landslide bathymetry profile, as estimated by examination of neighboring depth contours, is subtracted by the post (existing) landslide bathymetry profile. This difference surface is smoothed and then used directly as a “hot-start” initial free surface condition in the hydrodynamic model.

Assumption 2 does not simplify the analysis significantly. However it does prevent the use of an overly high bottom roughness coefficient, which could artificially reduce the tsunami energy reaching the shoreline. Note that while the offshore regions are assumed to be without bottom friction, such an assumption is too physically unrealistic to accept for the inland regions where the roughness height may be the same order as the flow depth. For tsunami inundation, particularly for regions such as this project location where the wave would need to inundate long reaches of densely vegetated land to reach the site, inclusion of a conservative measure of bottom roughness is necessary as shown below.

East Breaks Landslide

As discussed in the Source Generator Characteristics section (2.4S.6.4.3), the excavation depth of this slide is approximately 160 m. This length provides the trough elevation (i.e. -160 m) of the hot-start initial water surface condition. The horizontal dimensions of the slide source region are ~12 km in width and 50 km in length. With this information, and knowledge of characteristic slide-generated waves taken from the literature (Lynett and Liu, 2002; Lynett and Liu, 2005), the hot-start initial condition formed from a combination of rotational and translation motions is constructed as shown in Figure 2.4S.6.4.5-6. The resulting areas (1HD) and volumes (2HD) for the excavation and deposition regions are conserved.

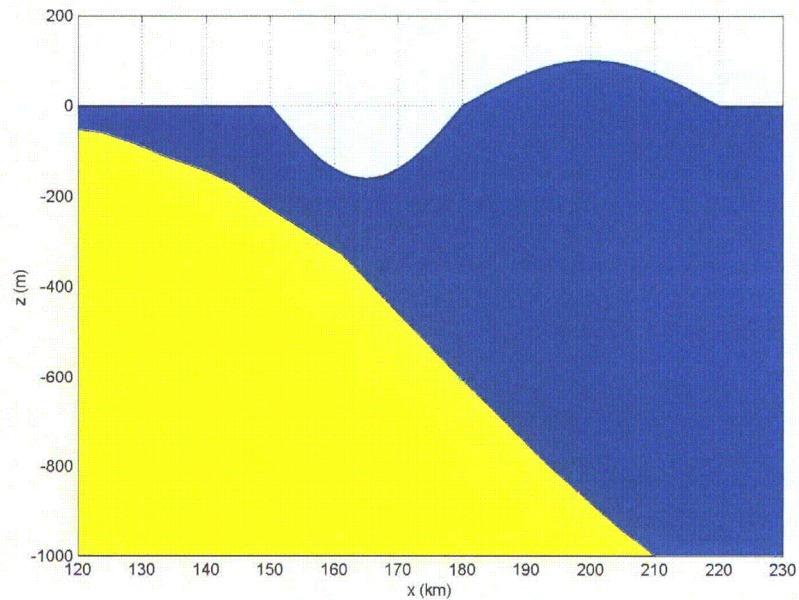


Figure 2.4S.6.4.5-6: Centerline profile of the hot-start water surface condition used for the limiting East Breaks landslide tsunami simulations.

Results: 1HD

For the East Breaks landslide, both one-horizontal-dimension (1HD) and two-horizontal-dimension (2HD) simulations are performed. The 1HD simulations require a small fraction of the CPU time of the 2HD runs, but do not include the radial spreading and refraction effects. Lack of radial spreading will lead to a conservative result in 1HD, while refraction can be either a constructive or destructive effect on the wave height, depending on the shallow water depth contours. 1HD simulations will provide information on the relative importance of overland bottom friction, while the 2HD simulations provide insight into radial spreading and refraction.

First, results from the 1HD simulations are discussed. The depth transect is taken from the source location directly to the STP site, as shown in Figure 2.4S.6.4.5-7.

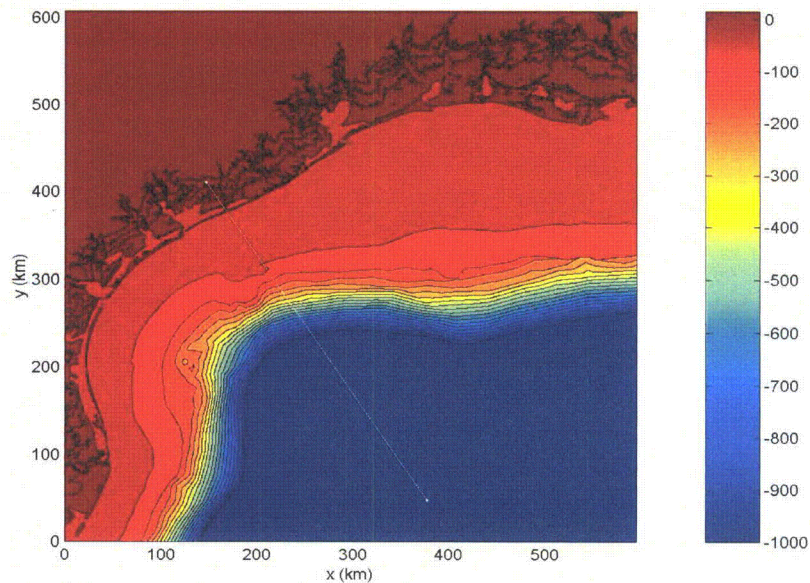


Figure 2.4S.6.4.5-7: Bathymetry/topography contour surface along the Texas coast; the white line shows the transect used for the 1HD simulations. This transect passes through the East Breaks source location as well as the STP site (Figure 2.4S.6.4.5-3).

A constant spatial grid size of 25 m is used across the transect for the 1HD cases. Predictions from three 1HD simulations are given for three cases of varying on-shore bottom friction: **A**) bottom friction due to small roughness characteristic of a very smooth, sandy ground (bottom drag coefficient, $f=0.001$), **B**) bottom friction due to small/moderate roughness characteristic of grass/turf ($f=0.01$), and **C**) bottom friction due to large roughness characteristic of the trees and dense shrub-like vegetation currently existing seaward of the STP reservoir ($f=0.05$). All of the simulations provide identical results for the tsunami prior to reaching the shoreline, as all the simulations start with the same wave, use the same bathymetry, and are frictionless offshore. The evolution of the wave in this offshore segment is shown in Figure 2.4S.6.4.5-8.

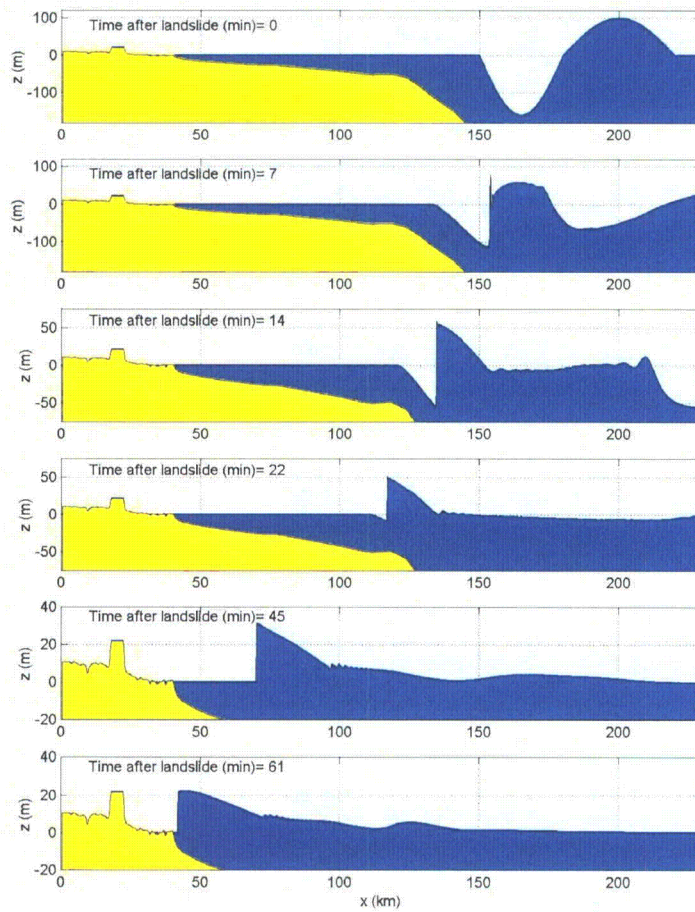


Figure 2.4S.6.4.5-8: The offshore evolution of the hot-start tsunami condition for East Breaks. The top plot is the initial condition (also shown in Figure 4) and the lower plots are at progressively later times. Note that the vertical scale changes among the plots.

As the wave starts inundating dry land, friction becomes important and the results of the three simulations diverge, shown in Figures 2.4S.6.4.5-9 through 2.4S.6.4.5-11.

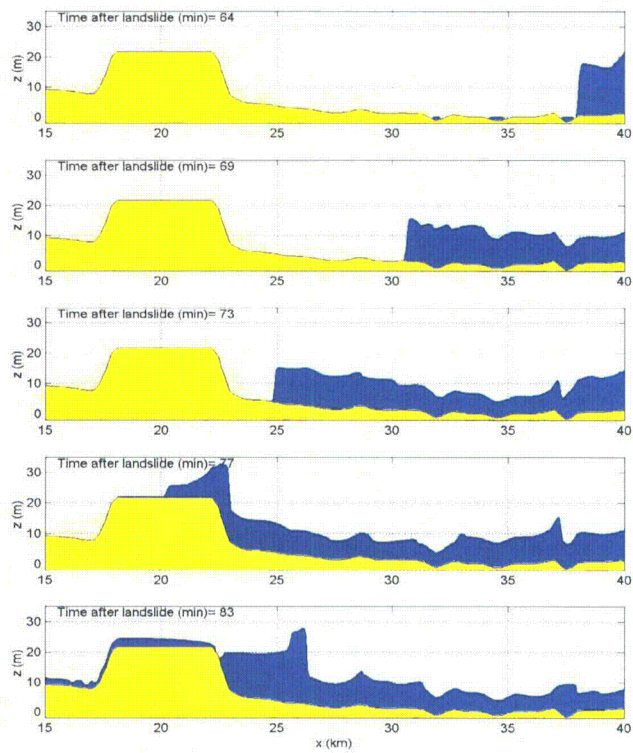


Figure 2.4S.6.4.5-9: The onshore evolution of the hot-start tsunami condition for East Breaks for the low friction case (Case A). Cross-sectional profile of the MCR is shown on the left side.

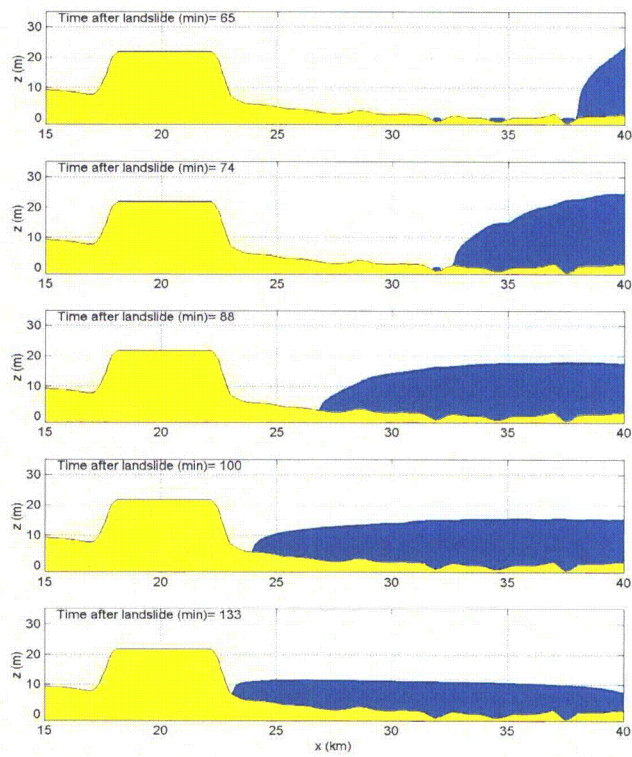


Figure 2.4S.6.4.5-10: The onshore evolution of the hot-start tsunami condition for East Breaks for the mid friction case (Case B). Cross-sectional profile of the MCR is shown on the left side.

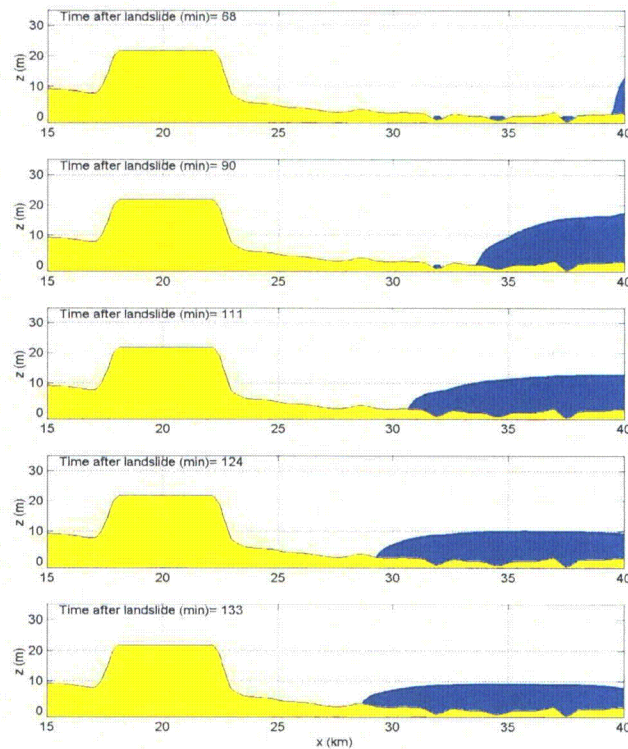


Figure 2.4S.6.4.5-11: The onshore evolution of the hot-start tsunami condition for East Breaks for the high, realistic friction case (Case C). Cross-sectional profile of the MCR is shown on the left side.

The low friction case A) shows a fast moving bore front that easily overtops the STP MCR, with maximum water surface elevations approaching +30 m. Despite the relatively low friction value used in case B), here the tsunami wave front is slowed significantly. The wave does not overtop the MCR, and maximum water elevations near STP are approximately +10 m. Finally, for case C), the large, realistic friction retards the flow considerably, and the tsunami wave front does not reach the STP site. Note that in all these figures, the horizontal and vertical scales are distorted, and that the realistic friction tsunami case (Case C) still does manage to travel 10 km inland. A conclusion of this IHD East Breaks study is that a tsunami approaching the site, with a bore height up

Technical Letter Report
South Texas Project Hydrology TER w/ OIs
Section 2.4.6

JCN Q-4151
Task Order No. 2
U.S. Geological Survey

to +30 m at the still water shoreline, will not adversely impact the site if the vegetation roughness is properly accounted for. Again, the 1HD case does not include lateral dissipation (radial spreading) of the wave from the source.

Results: 2HD

Examination of the 2HD simulation provides information about the importance of radial spreading and refraction, which can be used to correct, qualitatively, the 1HD results. A constant spatial grid size of 200 m is used in the 2HD results; use of the refined 25 m from the 1HD simulations creates an impractical, large grid. With the 200 m grid, the 2HD simulation uses 10 million grid points, and requires 20 weeks of CPU time (1 day on 144 processors).

It is most reasonable to analyze the 2HD results only to the initial shoreline. The relatively coarse grid size used in the 2HD results might cause accuracy degradation during the inundation phase due to poor resolution of shallow bathymetric and onland features. Figure 2.4S.6.4.5-12 provides a series of snapshots of the 2HD result.

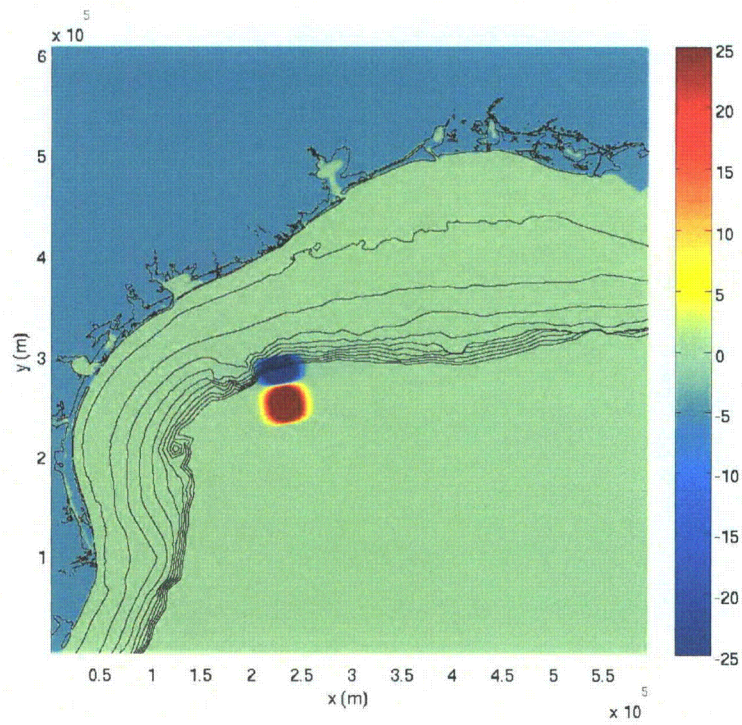


Figure 2.4S.6.4.5-12: Spatial snapshots (plan view) of the tsunami wave field from the East Breaks 2HD simulation. The time after landslide is given in the upper left corner. Location of the East Breaks landslide in relation to the STP site shown in Figure 2.4S.6.4.5-3

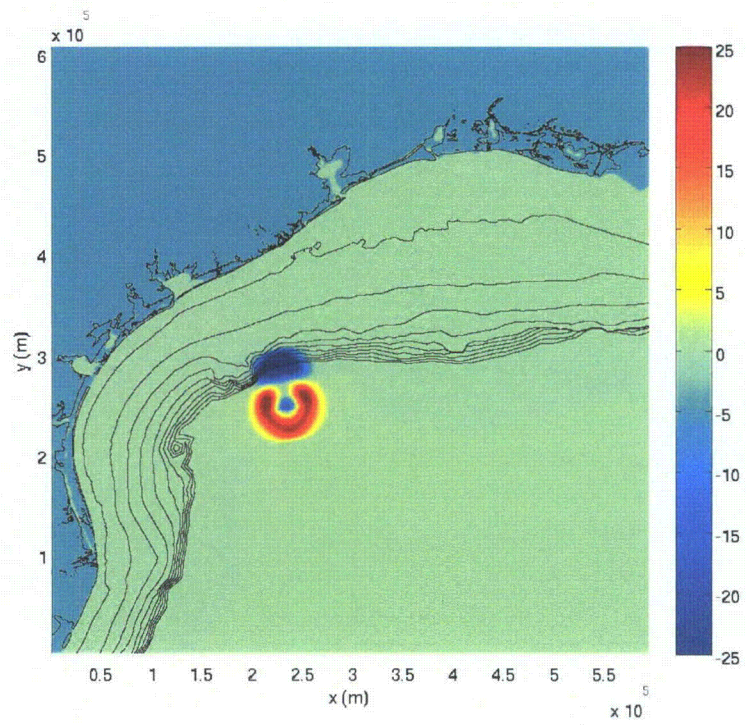


Figure 2.4S.6.4.5-12: (Cont.)

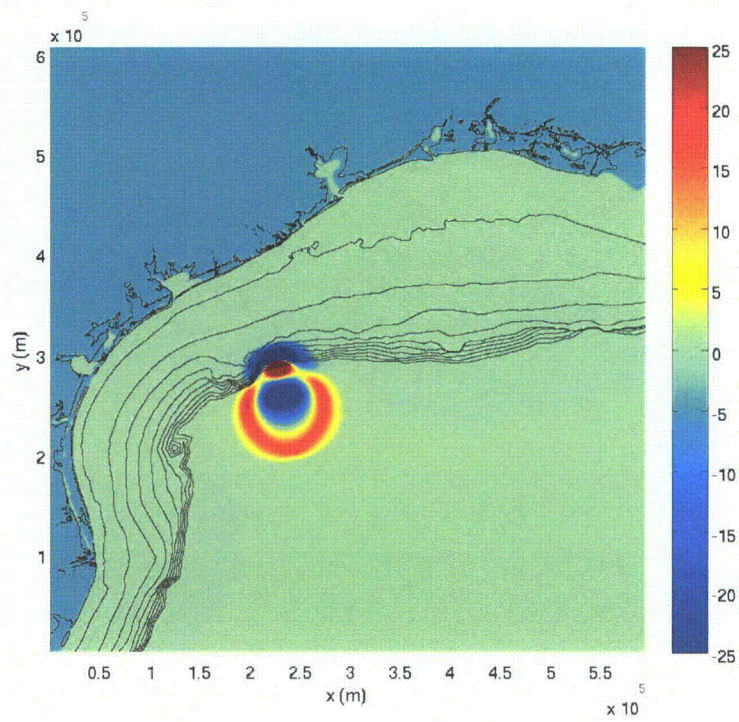


Figure 2.4S.6.4.5-12: (Cont.)

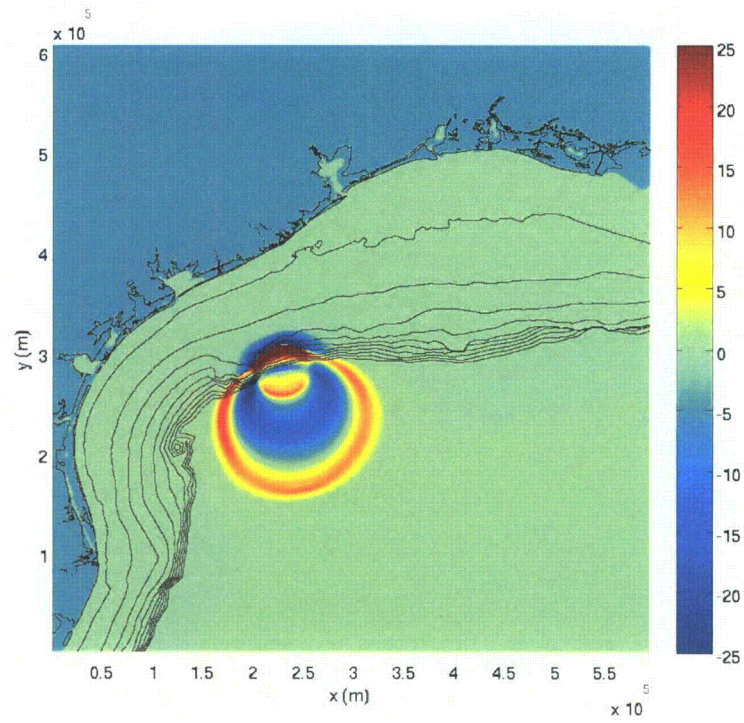


Figure 2.4S.6.4.5-12: (Cont.)

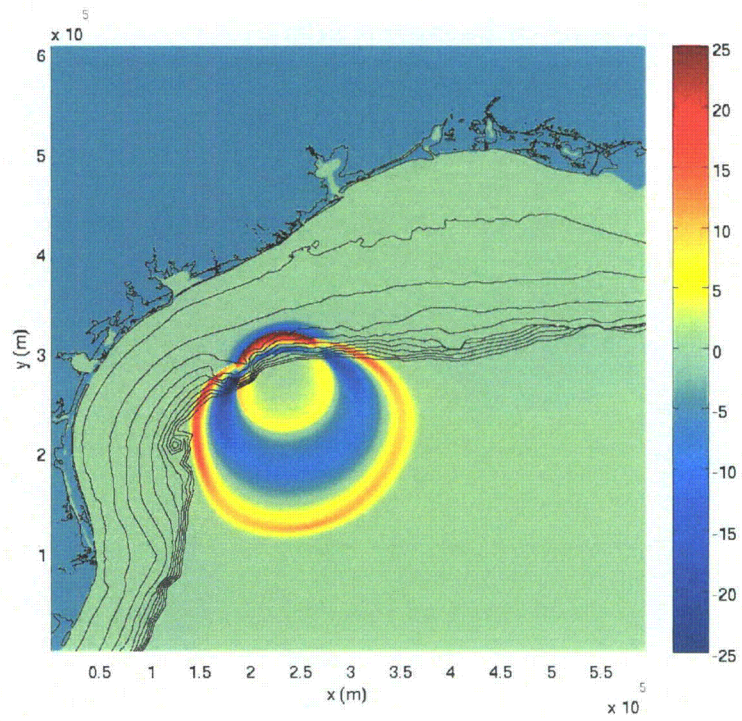


Figure 2.4S.6.4.5-12: (Cont.)

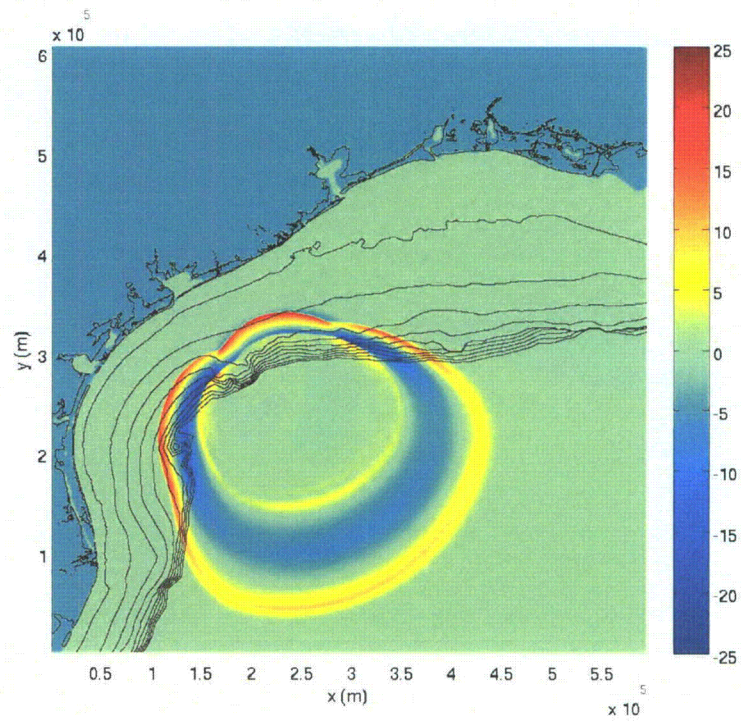


Figure 2.4S.6.4.5-12: (Cont.)

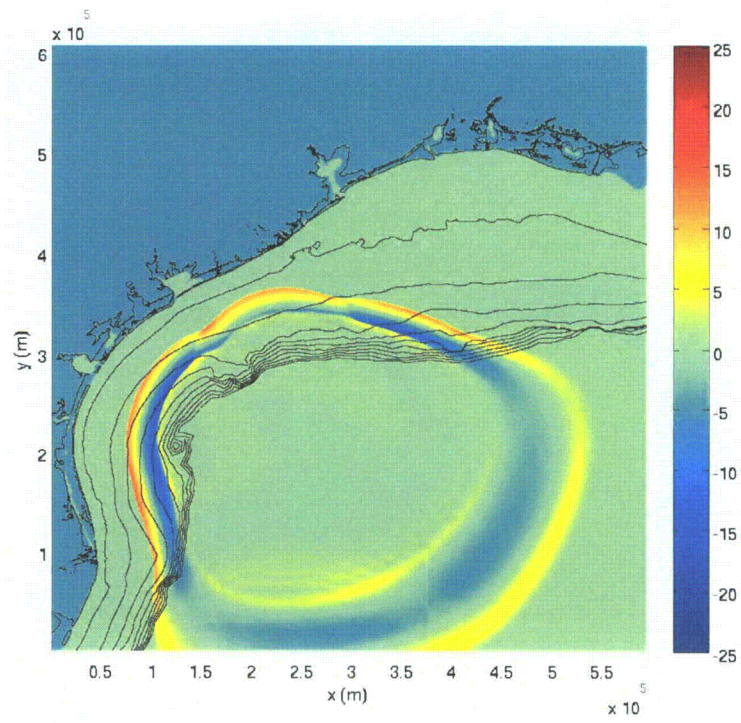


Figure 2.4S.6.4.5-12: (Cont.)

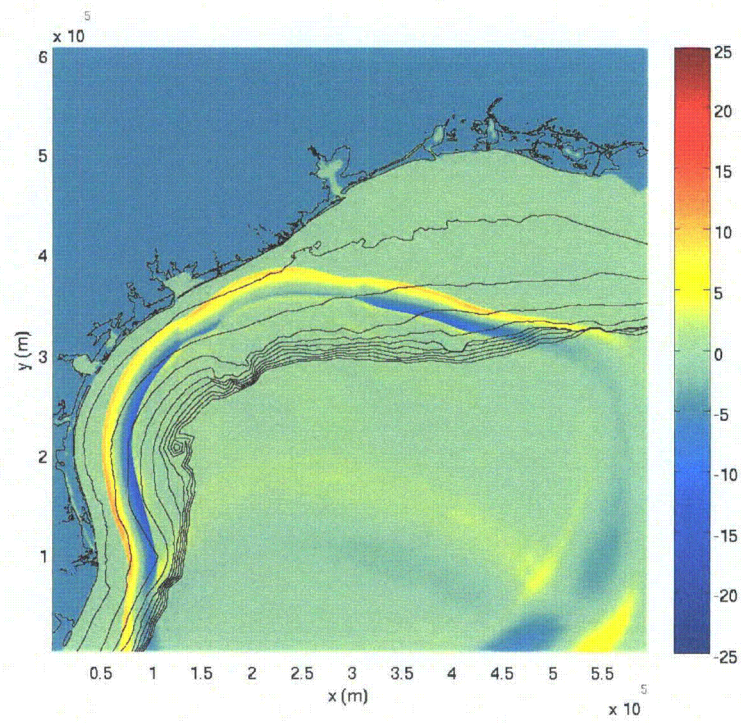


Figure 2.4S.6.4.5-12: (Cont.)

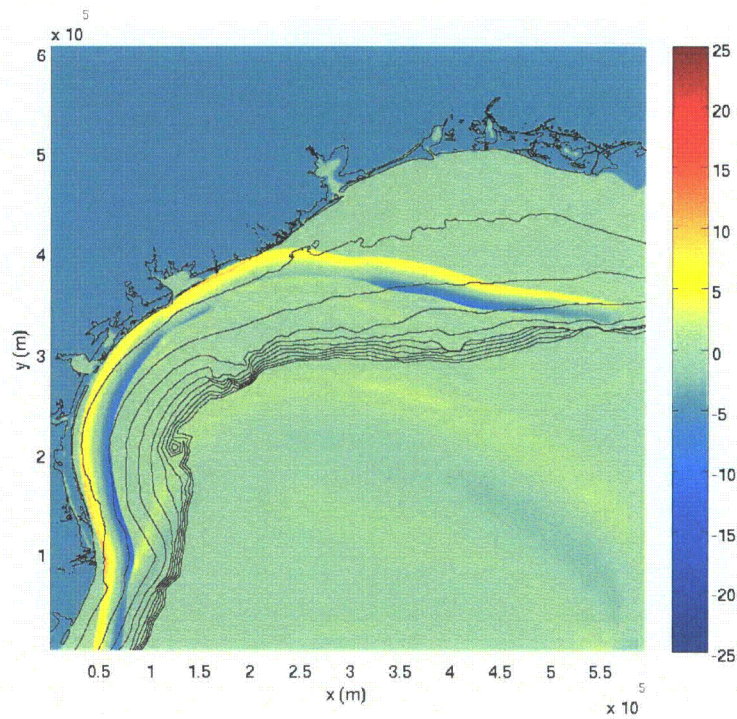


Figure 2.4S.6.4.5-12: (Cont.)

Clearly, radial spreading is important, as wave energy is propagating in all directions away from the source. The depth contours are relatively uniform seaward of STP, and there is no clear amplification due to refraction. With no refractive amplification, and significant radial spreading, it should be expected that the 2HD tsunami height prediction be less than the 1HD near the shoreline. Indeed that is the case, with the 2HD simulation yielding bore height predictions on the order of +10m at the shoreline, or 1/2 of the 1HD prediction (Figure 2.4S.6.4.5-8). Considering this 2HD spreading reduction with the 1HD inundation results and the conservative "hot-start" approach employed, it can be stated with high certainty that the tsunami from the East Breaks landslide would not impact the STP site.

Uncertainty in the primary landslide source parameters for the tsunami (excavation depth and slide length) is, to a great extent, diminished owing to depth-limiting effects on amplitude during propagation across the south Texas continental shelf (Figure 2.4S.6.4.5-8). Depth-limiting means that for a given beach profile and incident wave period, there is some ratio of wave height to shelf water depth that remains more or less constant as the wave propagates across the broad continental shelf. The leading polarity of the tsunami does appear to have a significant effect as further discussed in the Campeche Landslide results below. Landslides occurring along the south Texas continental slope will always have a leading depression polarity. With respect to uncertainty in the maximum width of a potential landslide, the IHD results effectively represents the extreme case of an infinitely wide landslide (i.e., no radial attenuation).

Campeche Landslide

One of the persistent issues during the independent confirmatory analysis is acquiring sufficient geologic information about the Campeche Escarpment with which to estimate the maximum landslide parameters as with the other Gulf of Mexico landslide provinces. Plans to conduct multibeam bathymetry surveys are pending. Presently, there is no published information showing the detailed bathymetry nor distribution of landslides on or above the Campeche Escarpment. As a provisional source for the Campeche Escarpment, we used initials conditions applicable to the maximum observed landslide along the Florida Escarpment (a similar geologic environment). This includes an initial drawdown of 150 m, with a horizontal length scale of 20 km (Figure 2.4S.6.4.5-13). The placement of this initial condition is arbitrary, but optimally oriented directly across from the STP site.

Figure 2.4S.6.4.5-13: Centerline profile of the hot-start water surface condition used for the limiting Campeche landslide tsunami simulations.

The very steep slope of the Campeche Escarpment results in the maximum depression occurring over a depth of 500 m, whereas the maximum positive wave of the initial condition occurs over a depth of 1000 m.

Results: IHD

First, results from the IHD simulations are discussed. The depth transect is taken from the source location directly to the STP site, as shown in Figure 2.4S.6.4.5-14.

Figure 2.4S.6.4.5-14: Bathymetry/topography contour surface along the Texas coast; the white line shows the transect used for the IHD simulations. This transect passes through the hypothetical Campeche escarpment source location as well as the STP site.

As with the East Breaks landslide, friction becomes important when the wave starts inundating dry land. We compare the results of the Campeche and East Breaks scenario for different bottom friction coefficients (Figures 2.4S.6.4.5-15 and 2.4S.6.4.5-16). With the conservative bottom friction (turf – East Breaks Case B), the runup is ~15 m (compared to ~7m with East Breaks). With realistic bottom friction (thick brush – East Breaks Case C), the Campeche runup is ~7 m (compared to ~3 with East Breaks).

Technical Letter Report
South Texas Project Hydrology TER w/ OIs
Section 2.4.6

JCN Q-4151
Task Order No. 2
U.S. Geological Survey

Figure 2.4S.6.4.5-15: Comparison of maximum runup for the Campeche (top) and East Breaks (bottom) landslide scenarios for the mid friction case (Case B).

Figure 2.4S.6.4.5-16: Comparison of maximum runup for the Campeche (top) and East Breaks (bottom) landslide scenarios for the realistic friction case (Case C).

Wave runup from the Campeche landslide is much larger than for the Florida Escarpment (not shown), even though the same initial conditions were used. The reason for this is that with the Florida IHD transect, the length of continental shelf that the wave must travel over is approximately two times greater than for the Campeche. With the Campeche transect, the wave is able to propagate across the narrowest section of the shelf, the same section that East Breaks is able to propagate across.

Wave runup from the Campeche landslide is also much larger than East Breaks landslide scenario (in the IHD case), even though that the wave for both cases travels over the same length of shelf and the initial wave heights are similar. The reason for this seems to be the fact that the Campeche wave is a leading elevation wave, whereas the wave from the East Breaks scenario is a leading depression wave. For East Breaks, the positive wave completely overruns the leading depression wave (Figure 2.4S.6.4.5-8), and to some degree these two components cancel one another out. The positive wave, while overrunning the negative wave, "feels" a shallower depth, and the depth-limiting dissipation (non-linear terms in the momentum equation) is stronger. Depth-limiting means that for a given beach profile and incident wave period, there is some ratio of wave height to water depth that remains more or less constant. For example, assume that this ratio is 0.8 for a particular beach. This means that in a depth of 20 m, the depth-limiting wave height will be 16m, further onshore in a depth of 10 m the height would be 8 m, etc. The discussion above implies that the leading depression acts as an effective decrease in the water depth for the following elevation wave, which will directly lead to a decrease in the elevation wave height on the order of the depression trough elevation relative to the still water level multiplied by 0.8. Since this is fundamentally a turbulent dissipation process, its mathematical origin will be in the viscous terms. Of course this process is entirely nonlinear, and without the nonlinear advection terms it would not occur physically (correctly). No such situation occurs for the Campeche slide, which in essence propagates over a shelf with water deeper than the East Breaks wave (even though, of course, this is the same shelf).

Because the propagation distance to the site for Campeche is so much larger than East Breaks (about 700 km longer), the 2D spreading effect will likely be very significant, and result in greater attenuation than for the 2HD East Breaks scenario.

Results: 2HD

Because the propagation distance for Campeche is so much larger than East Breaks (about 700 km longer), the 2D spreading effect will likely be very significant, and result in greater attenuation than for the East Breaks scenario. As a baseline 2HD (two-horizontal dimension) simulation for Campeche, initial condition parameters were taken

from the Florida Escarpment (same as for the previous 1HD slides). For the 2HD setup, the width of the slide is 20 km. Figure 2.4S.6.4.5-17 provides a series of snapshots of the 2HD result.

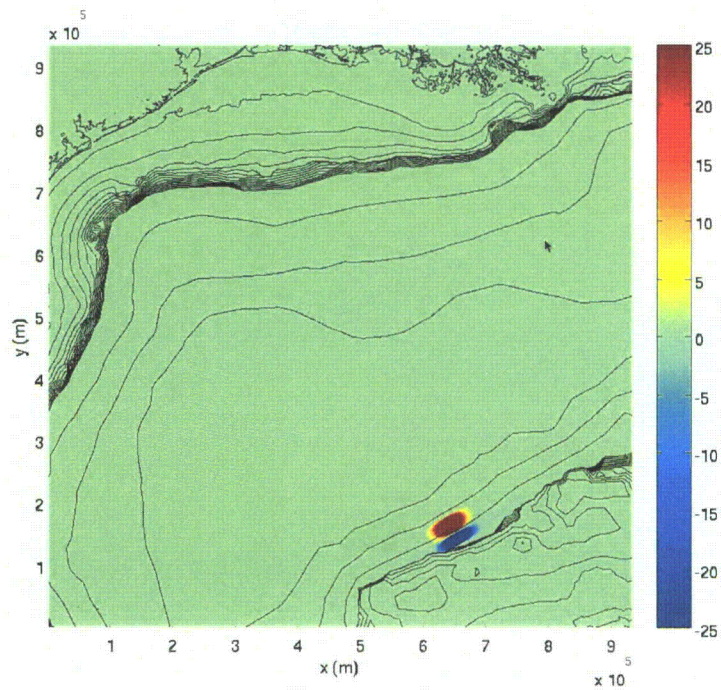


Figure 2.4S.6.4.5-17: Spatial snapshots (plan view) of the tsunami wave field from the 2HD simulation using a 20 km slide width. Start time during tsunami generation.

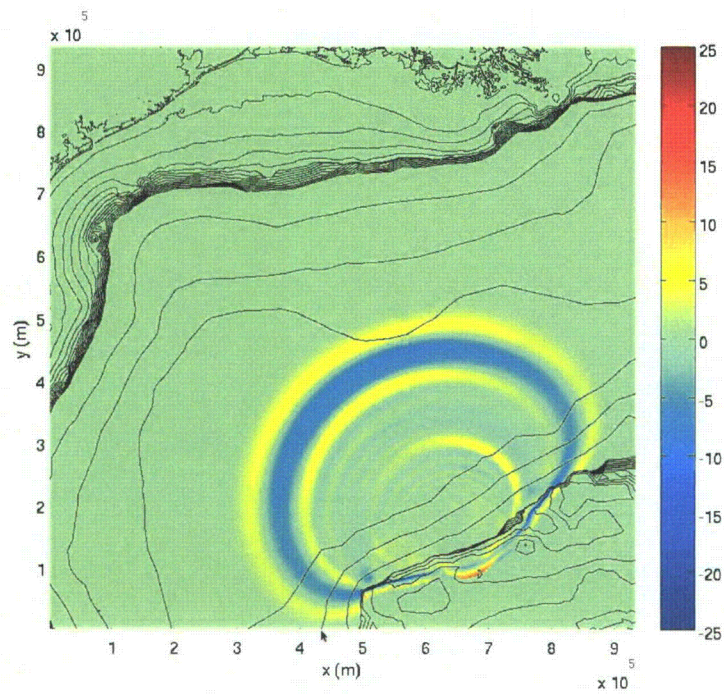


Figure 2.4S.6.4.5-17 (Cont.): Spatial snapshots (plan view) of the tsunami wave field from the 2HD simulation using a 20 km slide width. Time during propagation across the deep Gulf of Mexico.

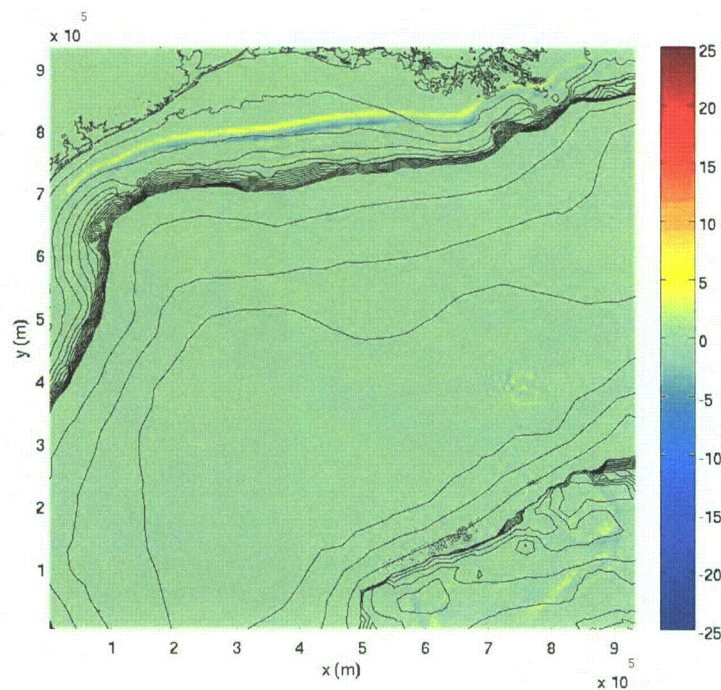


Figure 2.4S.6.4.5-17 (Cont.): Spatial snapshots (plan view) of the tsunami wave field from the 2HD simulation using a 20 km slide width. Time during propagation across the south Texas continental shelf.

Because 2HD radial attenuation for a landslide this far from site is very significant, and the fact that there is a high degree of uncertainty in the landslide width for this scenario, a second simulation with a wide slide width of 60 km was run (similar to the maximum width in the Storegga landslide complex and similar to the width for the "Monster" scenario landslide the applicant used for the south Texas continental shelf). The wave heights decrease very quickly near the source, but reach a nearly steady (slowly attenuating) condition when reaching the continental shelf off the Gulf Coast. Figure 2.4S.6.4.5-18 provides a series of snapshots of the 2HD result for the 60 km width case.

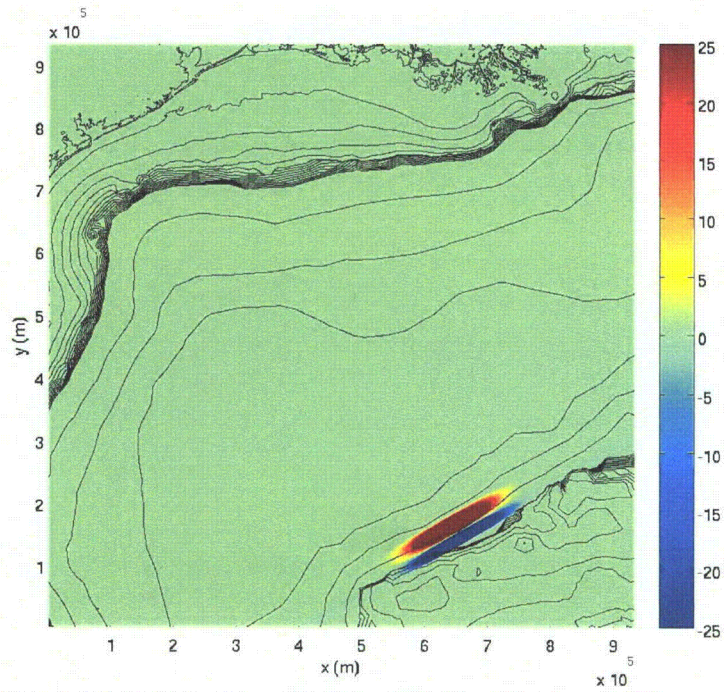


Figure 2.4S.6.4.5-18: Spatial snapshots (plan view) of the tsunami wave field from the 2HD simulation using a 60 km slide width. Start time during tsunami generation.

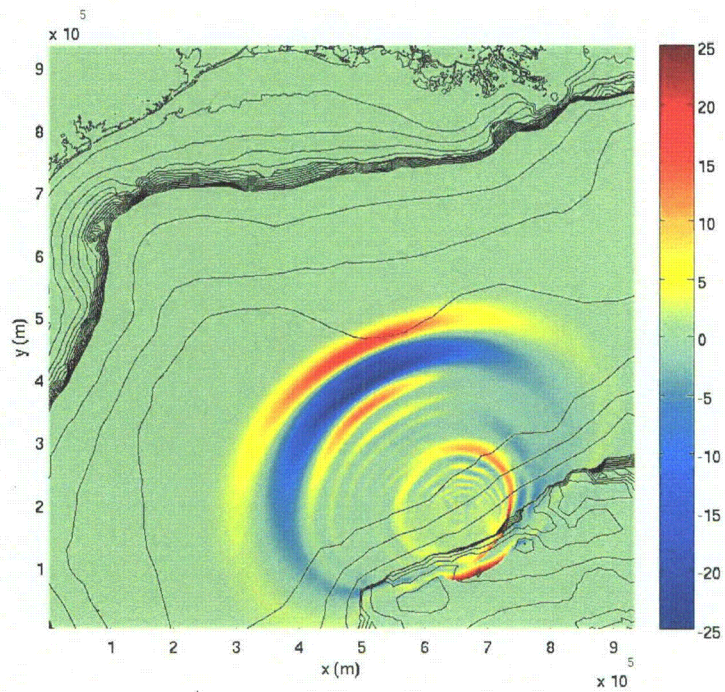


Figure 2.4S.6.4.5-18 (Cont.): Spatial snapshots (plan view) of the tsunami wave field from the 2HD simulation using a 60 km slide width. Time during propagation across the deep Gulf of Mexico.

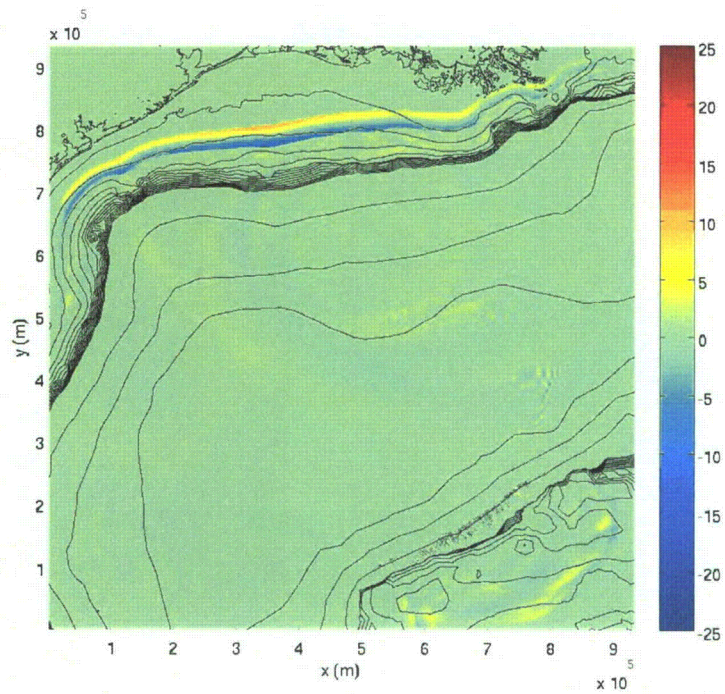


Figure 2.4S.6.4.5-18 (Cont.): Spatial snapshots (plan view) of the tsunami wave field from the 2HD simulation using a 60 km slide width. Time during propagation across the south Texas continental shelf.

Technical Letter Report
South Texas Project Hydrology TER w/ OIs
Section 2.4.6

JCN Q-4151
Task Order No. 2
U.S. Geological Survey

Figure 2.4S.6.4.5-19 plots the ocean surface elevation time series for the two slides at an offshore water depth of 50m directly across from the STP site. Of note is the larger wave with the wider source, and the fact that the Campeche event creates a leading elevation wave.

Figure 2.4S.6.4.5-19: Synthetic tsunami time series (meters) for the Campeche hypothetical landslide scenario, using two landslide widths.

Figure 2.4S.6.4.5-20 plots the ocean surface elevation time series for the offshore Campeche 20-km wide slide and the East Breaks (2HD simulations) at the same 50-m depth offshore location.

Figure 2.4S.6.4.5-20: Synthetic tsunami time series (marigrams) for the Campeche hypothetical landslide scenario and the East Breaks landslide scenario.

The general conclusion made from this comparison is that the approaching wave heights for the hypothetical Campeche scenario are comparable to that of the East Breaks scenario, unless it is found that the maximum slide width in the Campeche province is much less than 20 km. Because the properties of the incoming waves are different (leading elevation vs leading depression), and the uncertainty in the slide parameters, this analysis indicates that East Breaks and Campeche (20 km width) are equal candidates for the STP probable maximum tsunami (PMT) source.

Finally, we can see what the inundation due to the Campeche event would be. Shown in Figure 2.4S.6.4.5-21 is a cross-section, with the waves taken from the 2HD slide for the Campeche 60-km slide at the time of maximum inundation.

Figure 2.4S.6.4.5-21: Wave profile at time of maximum inundation for the Campeche 2HD 60-km slide width source scenario and for the mid friction case (Case B). (top) view across the continental shelf (bottom) view near the STP site.

This image shows detail with a resolution of ~5m, with the still water level at mean sea level, and the mid-level (conservative) bottom friction characteristic of turf. The water levels at the time of maximum runup are approximately 4 m, and the tsunami makes it about halfway to the MCR. The same conclusion is made for the 2HD East Breaks analysis. It is reasonable to conclude that either the East Breaks or Campeche scenarios represent the PMT, and neither have a significant probability of producing a wave that could reach STP.

Independent analysis of the 10% exceedance high tide was conducted for 16 years of NOAA NOS-CO-OPS data at the Freeport tide gauge station (years 1992-2007). The 10% exceedance high tide was determined to be 0.45 m relative to MSL for these years. This is consistent with the applicant's estimate of 0.46 m relative to MSL indicated in the FSAR, but inconsistent with the estimate of 1.08 m as indicated in the response to the RAI's for Section 2.4.6 (pg. 5 of 28). The long-term sea-level rise at the Freeport station is 4.35 ± 1.12 mm/yr according to NOAA NOS-CO-OPS data, as also indicated in the applicant's RAI response. The estimate given in the applicant's FSAR is 5.87 ± 0.74 mm/yr. Therefore, the PMT water level for the conservative 2HD tsunami over the next century is 4 m (max. tsunami runup) + 0.45 m (10% exceedance high tide) + 0.59 m (century sea level rise) or approximately 5.0 m (16.5 feet).

Conclusion: Results of the analysis indicates that the PMT source is a submarine landslide, either along the continental slope directly across from the site (i.e., East Breaks scenario) or along the Campeche escarpment. There is a high degree of uncertainty in the source parameters for the latter scenario. Hot-start initial conditions were used representing conservative values related to tsunami generation efficiency. In addition, several bottom friction parameters for overland flow were tested, representing realistic and conservative estimates. Analysis in one horizontal dimension (1HD) yield high values of runup that in some cases reached the base of the MCR and into the site. Realistic wave propagation in two horizontal dimensions (2HD), yielded PMT runup approximately 5 m (relative to MSL) for conservative hot-start initial conditions, and conservative values of bottom friction for overland flow, considering the effect of 10% exceedance high tide and sea level rise during the next century.

2.4S.6.4.6 Hydrography and Harbor or Breakwater Influences on Tsunami

Summary of FSAR contents: Because the maximum tsunami water level associated with the PMT is below grade elevations at the site, the applicant determines that there will be no on-site effects from breaking waves or resonance.

Technical Letter Report
South Texas Project Hydrology TER w/ OIs
Section 2.4.6

JCN Q-4151
Task Order No. 2
U.S. Geological Survey

Pending the resolution of Open Items, staff concurs that because the maximum tsunami water level associated with the PMT is below grade elevations at the site, there will be no on-site effects from breaking waves or resonance.

2.4S.6.4.7 Effects on Safety-related Facilities

Summary of FSAR contents: Because the maximum tsunami water level associated with the PMT is below grade elevations at the site, the applicant determines that there will be no on-site tsunami waves affecting safety-related facilities.

Pending the resolution of Open Items, staff concurs that because the maximum tsunami water level associated with the PMT is below grade elevations at the site, there will be no on-site tsunami waves affecting safety-related facilities.

2.4S.6.5 Post Combined License Activities

TBD - NRC staff to provide further guidance

2.4S.6.6 Conclusions

The proposed STP Units 3 & 4 site are not affected by probable maximum tsunami. There will be no on-site effects from tsunami breaking waves or resonance or on-site tsunami waves affecting safety-related facilities.

As set forth above, the applicant has presented and substantiated sufficient information pertaining to estimate the effects of probable maximum tsunami hazards at the proposed site. SRP Section 2.4.6 provides that the FSAR should address the requirements of 10 CFR Parts 52 and 100 as they relate to identifying and evaluating the effects of probable maximum tsunami hazards.

Furthermore, the applicant considered the most severe natural phenomena that have been historically reported for the site and surrounding area while describing the probable maximum tsunami hazards, with sufficient margin for the limited accuracy, quantity, and period of time in which the historical data have been accumulated. However, the applicant does not provide sufficient justification to dismiss the possibility that landslides along the Campeche Escarpment region may be a potential tsunami source that determines the PMT water levels. This is Open Item 2.4-1

In our independent confirmatory analysis of the PMT water levels, the following conservative approaches were used:

- 1) Maximum Landslide Dimensions (Section 2.4S.6.4.3, pg. 29): For the four geological provinces in the Gulf of Mexico in which potential tsunamigenic landslides can occur, the maximum landslide is determined to be the maximum single event landslide as indicated from multibeam bathymetry data. The dimensions of the landslide are determined from the pre-slide slope surface and the largest excavation region. From available dates of landslides in the Gulf of Mexico, the maximum landslide is therefore taken from geologic observations spanning tens of thousands of years.
- 2) Landslide Tsunami Initial Conditions (Section 2.4S.6.4.5, pg. 49): Conservatism was imposed by using instantaneous displacement of the sea-surface (i.e., the so-called hot-start initial conditions for tsunami generation), without taking into account the decreased efficiency of tsunami generation related to the finite process time for landslide movement. Landslide movement is generally thought to be much slower than for earthquake displacements, and therefore less efficient at generating tsunamis. However, little data exists that can be used to determine or constrain the time evolution of submarine landslide movement. Therefore, the extreme case of using instantaneous landslide displacement was used for tsunami initial conditions that maximizes tsunami generation efficiency.
- 3) Conservative Bottom Friction (Section 2.4S.6.4.5, pg. 55): Bottom roughness, and the associated energy dissipation, is assumed to be negligible in locations that are initially wet. Whereas the offshore regions are assumed to be without bottom friction, such an assumption is too physically unrealistic to accept for the inland regions where the roughness height may be the same order as the flow depth. For tsunami inundation, particularly for regions such as the project location where the wave would need to inundate long reaches of densely vegetated land to reach the site, inclusion of a conservative measure of bottom roughness is necessary.
- 4) Simulations With No Radial Spreading (Section 2.4S.6.4.5, pg. 56): One horizontal dimension (1HD) simulations were performed for the East Breaks and Campeche landslide scenarios that do not include the effect of radial spreading (in effect, an infinitely wide landslide). Lack of radial spreading will lead to a conservative result in 1HD, whereas refraction can theoretically be either a constructive or destructive effect on the wave height in 2HD, depending on the shallow water depth contours. For the site, there is no refractive amplification and significant radial spreading; thus, 2HD tsunami height predictions are less than the 1HD near the shoreline. Because the propagation distance for Campeche landslide scenario is so much larger than East Breaks (about 700 km longer) and larger than the maximum expected landslide width, the 2D radial spreading is very significant for Campeche and should be included.

2.4S.6.7 References

- Balzano, A., 1998, Evaluation of methods for numerical simulation of wetting and drying in shallow water flow models: *Coastal Engineering*, v. 34, p. 83-107.
- Barkan, R., ten Brink, U.S., and Lin, J., in press, The source of the 1755 Lisbon earthquake: Implications for tsunami hazard to the U.S. Atlantic coast: *Marine Geology*.
- Berninghausen, W.H., 1968, Tsunamis and Seismic Seiches Reported from the Western North and South Atlantic and the Coastal Waters of Northwestern Europe: Naval Oceanographic Office IR No. 68-85, 51 p. [Informal Report].
- Bird, P., and Kagan, Y.Y., 2004, Plate-tectonic analysis of shallow seismicity: apparent boundary width, beta-value, corner magnitude, coupled lithosphere thickness, and coupling in 7 tectonic settings: *Bulletin of the Seismological Society of America*, v. 94, p. 2380-2399.
- Blakey, R., 2005, Paleogeography and Geologic History of North America: Northern Arizona University, <http://jan.ucc.nau.edu/~rcb7/nam.html>.
- Bourgeois, J., Hansen, T.A., Wiberg, P.L., and Kauffman, E.G., 1988, A tsunami deposit at the Cretaceous-Tertiary boundary in Texas: *Science*, v. 241, p. 567-241.
- Capra, L., Macías, J.L., Scott, K.M., Abrams, M., and Garduño-Monroy, V.H., 2002, Debris avalanches and debris flows transformed from collapses in the Trans-Mexican Volcanic Belt, Mexico--behavior, and implications for hazard assessment: *Journal of Volcanology and Geothermal Research*, v. 113, p. 81-110.
- Chang, K.-A., Hsu, T.-J., and Liu, P.L.-F., 2001, Vortex generation and evolution in water waves propagating over a submerged rectangular obstacle. Part I. solitary waves: *Coastal Engineering*, v. 44, p. 13-36.
- Chaytor, J.D., ten Brink, U.S., Solow, A.R., and Andrews, B.D., 2009, Size distribution of submarine landslides along the U.S. Atlantic Margin: *Marine Geology*, p. 16-27.
- Chen, Q., Kirby, J.T., Dalrymple, R.A., Kennedy, A.B., and Chawla, A., 2000, Boussinesq modeling of wave transformation, breaking, and runup: Part I. 2D: *Journal of Waterway, Port, Coastal, and Ocean Engineering*, v. 126, p. 57-62.
- Cheung, K.F., Phadke, A.C., Wei, Y., Rojas, R., Douyere, Y.J.-M., Martino, C.D., Houston, S.H., Liu, P.L.-F., Lynett, P.J., Dodd, N., Liao, S., and Nakazaki, E., 2003, Modeling of storm-induced coastal flooding for emergency management: *Ocean Engineering*, v. 30, p. 1353-1386.

Technical Letter Report
South Texas Project Hydrology TER w/ OIs
Section 2.4.6

JCN Q-4151
Task Order No. 2
U.S. Geological Survey

- Coleman, J.B., Prior, D.B., and Lindsay, J.F., 1983, Deltaic influences on shelf edge instability processes, *in* Stanley, D.J., and Moore, G.T., eds., *The Shelfbreak: Critical Interface on Continental Margins: Society of Economic Paleontologists and Mineralogists, Special Publication 33*, p. 121-137.
- Dewey, J.W., and Dellinger, J.A., 2008, Location of the Green Canyon (offshore southern Louisiana) seismic event of February 10, 2006: U.S. Geological Survey, Open-File Report 2008-1184, 30 p.
- Dodd, N., 1998, Numerical model of wave run-up, overtopping, and regeneration: *Journal of Waterway, Port, Coastal, and Ocean Engineering*, v. 124, p. 73-81.
- Donn, W.L., 1964, Alaskan earthquake of 27 march 1964: Remote seiche stimulation: *Science*, v. 145, p. 261-262.
- Doyle, L.J., and Holmes, C.W., 1985, Shallow structure, stratigraphy, and carbonate sedimentary processes of West Florida Continental Slope: *American Association of Petroleum Geologists Bulletin*, v. 69, p. 1133-1144.
- Engdahl, E.R., and Villaseñor, A., 2002, Global seismicity: 1900-1999, *in* Lee, W.H.K., Kanamori, H., Jennings, P.C., and Kisslinger, C., eds., *International Handbook of Earthquake and Engineering Seismology, Part A: San Diego, Academic Press*, p. 665-690.
- Fine, I.V., Rabinovich, A.B., Bornhold, B.D., Thomson, R., and Kulikov, E.A., 2005, The Grand Banks landslide-generated tsunami of November 18, 1929: preliminary analysis and numerical modeling: *Marine Geology*, v. 215, p. 45-57.
- Gale, A.S., 2006, The Cretaceous-Palaeogene boundary on the Brazos River, Falls County, Texas: Is there evidence for impact-induced tsunami sedimentation: *Proceedings of the Geologists' Association*, v. 117, p. 173-185.
- González, F.I., Bernard, E.N., Dunbar, P., Geist, E.L., Jaffe, B.E., Kánoglu, U., Locat, J., Mofjeld, H.O., Moore, A., Synolakis, C.E., Titov, V.V., and Weiss, R., 2007, Scientific and technical issues in tsunami hazard assessment of nuclear power plant sites: NOAA Pacific Marine Environmental Laboratory NOAA Technical Memorandum OAR PMEL-136, 125 p.
- Goodwin, R.H., and Prior, D.B., 1989, Geometry and depositional sequences of the Mississippi Canyon, Gulf of Mexico: *Journal of Sedimentary Petrology*, v. 59, p. 318-329.

Technical Letter Report
South Texas Project Hydrology TER w/ OIs
Section 2.4.6

JCN Q-4151
Task Order No. 2
U.S. Geological Survey

- Gopalakrishnan, T.C., 1989, A moving boundary circulation model for regions with large tidal flats: *International Journal for Numerical Methods in Engineering*, v. 28, p. 245-260.
- Grilli, S.T., and Watts, P., 2005, Tsunami generation by submarine mass failure. I: Modeling, experimental validation, and sensitivity analyses: *Journal of Waterway, Port, Coastal, and Ocean Engineering*, v. 131, p. 283-297.
- Hansen, J.B., and Svendsen, I.A., 1979, Regular waves in shoaling water: Experimental data: Univ. of Denmark [Tech. Rep., ISVA Ser., 21].
- Heck, N.H., 1947, List of seismic sea waves: *Bulletin of the Seismological Society of America*, v. 37, p. 269-286.
- Hibberd, S., and Peregrine, D.H., 1979, Surf and run-up on a beach: *Journal of Fluid Mechanics*, v. 95, p. 323-345.
- Hildebrand, A.R., Penfield, G.T., Kring, D.A., Pilkington, M., Camargo Z., A., Jacobsen, S.B., and Boynton, W.V., 1991, Chicxulub Crater: A possible Cretaceous/Tertiary boundary impact crater on the Yucatán Peninsula, Mexico: *Geology*, v. 19, p. 867-871.
- Hsu, T.-J., Sakakiyama, T., and Liu, P.L.-F., 2002, A numerical model for wave motions and turbulence flows in front of a composite breakwater: *Coastal Engineering*, v. 46, p. 25-50.
- Hu, K., Mingham, C.G., and Causon, D.M., 2000, Numerical simulation of wave overtopping of coastal structures using the non-linear shallow water equations: *Coastal Engineering*, v. 41, p. 433-465.
- Imamura, F., 1996, Simulation of wave-packet propagation along sloping beach by TUNAMI-code, in Yeh, H., Liu, P.L.F., and Synolakis, C.E., eds., *Long-Wave Runup Models*: World Scientific, p. 25-42.
- Jiang, M.J., and Gartner, S., 1986, Calcareous nannofossil succession across the Cretaceous/Tertiary boundary in east-central Texas: *Micropaleontology*, v. 32, p. 232-255.
- Johnson, D.B., Raad, P.E., and Chen, S., 1994, Simulations of impacts of fluid free surface with solid boundary: *International Journal for Numerical Methods in Fluids*, v. 19, p. 153-174.
- Keller, G., Adatte, T., Berner, Z., Harting, M., Baum, G., Prauss, M., Tantawy, A., and Stueben, D., 2007, Chicxulub impact predates K-T boundary: New evidence from Brazos, Texas: *Earth and Planetary Science Letters*, v. 255, p. 339-356.

Technical Letter Report
South Texas Project Hydrology TER w/ OIs
Section 2.4.6

JCN Q-4151
Task Order No. 2
U.S. Geological Survey

- Kennedy, A.B., Chen, Q., Kirby, J.T., and Dalrymple, R.A., 2000, Boussinesq modeling of wave transformation, breaking and runup: I. one dimension: *Journal of Waterway, Port, Coastal, and Ocean Engineering*, v. 126, p. 39-47.
- Knight, W., 2006, Model predictions of Gulf and southern Atlantic coast tsunami impacts from a distribution of sources: *Science of Tsunami Hazards*, v. 24, p. 304-312.
- Kobayashi, N., and Wurjanto, A., 1989, Wave overtopping on coastal structures: *Journal of Waterway, Port, Coastal, and Ocean Engineering*, v. 115, p. 235-251.
- Korycansky, D.G., and Lynett, P.J., 2005, Offshore breaking of impact tsunami: The Van Dorn effect revisited: *Geophysical Research Letters*, v. 32, p. doi:10.1029/2004GL021918.
- Korycansky, D.G., and Lynett, P.J., 2007, Run-up from impact tsunami: *Geophysical Journal International*, v. 170, p. 1076-1088.
- Kowalik, Z., and Murty, T.S., 1993, Numerical simulation of two-dimensional tsunami runup: *Marine Geodesy*, v. 16, p. 87-100.
- Leendertse, J.J., 1987, Aspects of SIMSYS2D: A System for Two-Dimensional Flow Computation: The RAND Corporation R-3572-USGS, 80 p.
- Lin, P., Chang, K.-A., and Liu, P.L.-F., 1999, Runup and run-down of solitary waves on sloping beaches: *Journal of Waterway, Port, Coastal, and Ocean Engineering*, v. 125, p. 247-255.
- Lin, P., and Liu, P.L.-F., 1998a, A numerical study of breaking waves in the surf zone: *Journal of Fluid Mechanics*, v. 359, p. 239-264.
- Lin, P., and Liu, P.L.-F., 1998b, Turbulence transport, vorticity dynamics, and solute mixing under plunging breaking waves in surf zone: *Journal of Geophysical Research*, v. 103, p. 15677-15694.
- Liu, P.L.F., Cho, Y.S., Yoon, S.B., and Seo, S.N., 1995, Numerical simulations of the 1960 Chilean tsunami propagation and inundation at Hilo, Hawaii, *in* Tsuchiya, Y., and Shuto, N., eds., *Tsunami: Progress in Prediction, Disaster Prevention and Warning*: Kluwer Academic Publishers, p. 99-115.
- Lockridge, P.A., Whiteside, L.S., and Lander, J.F., 2002, Tsunamis and tsunami-like waves of the eastern United States: *Science of Tsunami Hazards*, v. 20, p. 120-157.

Technical Letter Report
South Texas Project Hydrology TER w/ OIs
Section 2.4.6

JCN Q-4151
Task Order No. 2
U.S. Geological Survey

- Lynett, P., 2007, The effect of a shallow water obstruction on long wave runup and overland flow velocity: *Journal of Waterway, Port, Coastal, and Ocean Engineering*, v. 133, p. 455-462.
- Lynett, P., Borrero, J.C., Liu, P.L.F., and Synolakis, C.E., 2003, Field survey and numerical simulations: A review of the 1998 Papua New Guinea tsunami: *Pure and Applied Geophysics*, v. 160, p. 2119-2146.
- Lynett, P., and Liu, P.L.F., 2002, A numerical study of submarine-landslide-generated waves and run-up: *Proceedings of the Royal Society of London, A*, v. 458, p. 2885-2910.
- Lynett, P., and Liu, P.L.F., 2006, Three-dimensional runup due to submerged and subaerial landslides, in Mercado, A., and Liu, P.L.F., eds., *Caribbean Tsunami Hazard*: Singapore, World Scientific Publishing Co., p. 289-307.
- Lynett, P.J., 2006, Nearshore wave modeling with high-order Boussinesq-type equations: *Journal of the Waterways and Harbors Division, A.S.C.E.*, v. 132, p. 348-357.
- Lynett, P.J., and Liu, P.L.-F., 2005, A numerical study of run-up generated by three-dimensional landslides: *Journal of Geophysical Research*, v. 10, p. doi:10.1029/2004JC002443.
- Lynett, P.J., Wu, T.-R., and Liu, P.L.-F., 2002, Modeling wave runup with depth-integrated equations: *Coastal Engineering*, v. 46, p. 89-107.
- Mader, C.L., 2001, Modeling the 1755 Lisbon tsunami: *Science of Tsunami Hazards*, v. 19, p. 93-98.
- Madsen, P.A., Sorensen, O.E., and Schaffer, H.A., 1997, Surf zone dynamics simulated by a Boussinesq-type model: Part 1. Model description and cross-shore motion of regular waves: *Coastal Engineering*, v. 32, p. 255-287.
- McGarr, A., 1965, Excitation of seiches in channels by seismic waves: *Journal of Geophysical Research*, v. 70, p. 847-854.
- Myers, E.P., and Baptista, A.M., 1995, Finite element modeling of the July 12, 1993 Hokkaido Nansei-Oki tsunami: *Pure and Applied Geophysics*, v. 144, p. 769-801.
- Nettles, M., 2007, Analysis of the 10 February 2006: Gulf of Mexico earthquake from global and regional seismic data, in 2007 Offshore Technology Conference, Houston, Texas, p. 2.
- Owen, M., 1980, Design of seawalls allowing for wave overtopping: *Hydraulics Research Rep. EX924*.

Technical Letter Report
South Texas Project Hydrology TER w/ OIs
Section 2.4.6

JCN Q-4151
Task Order No. 2
U.S. Geological Survey

- Parker, W.E., 1922, Unusual tidal registration of earthquake: *Bulletin of the Seismological Society of America*, v. 12, p. 28-30.
- Pedrozo-Acuña, A., Simmonds, D.J., Otta, A.K., and Chadwick, A.J., 2006, On the cross-shore profile change of gravel beaches: *Coastal Engineering*, v. 53, p. 335-347.
- Pelinovsky, E., Zahibo, N., Dunkley, P., Edmonds, M., Herd, R., Talipova, T., Kozelkov, A., and Nikolkina, I., 2004, Tsunami generated by the volcano eruption on July 12-13, 2003 at Montserrat, Lesser Antilles: *Science of Tsunami Hazards*, v. 22, p. 44-57.
- Peltier, W.R., and Fairbanks, R.G., 2006, Global glacial ice volume and Last Glacial Maximum duration from an extended Barbados sea level record: *Quaternary Science Reviews*, v. 25, p. 3322-3337.
- Petera, J., and Nassehi, V., 1996, A new two-dimensional finite element model for the shallow water equations using a Lagrangian framework constructed along fluid particle trajectories: *International Journal for Numerical Methods in Engineering*, v. 39, p. 4159-4182.
- Petersen, M.D., Frankel, A.D., Harmsen, S.C., Mueller, C.S., Haller, K.M., Wheeler, R.L., Wesson, R.L., Zeng, Y., Boyd, O.S., Perkins, D.M., Luco, N., Field, E.H., Wills, C.J., and Rukstales, K.S., 2008, Documentation for the 2008 update of the United States National Seismic Hazard Maps U.S. Geological Survey, 128 p. [Open-File Report 2008-1128].
- Piper, J.N., 1997, Downslope sediment transport processes and sediment distributions at the East Breaks, northwest Gulf of Mexico: Austin, University of Texas, Thesis.
- Piper, J.N., and Behrens, W.E., 2003, Downslope sediment transport processes and sediment distributions at the East Breaks, northwest Gulf of Mexico, in *Proceedings of the 23rd Annual Gulf Coast Section SEPM Research Conference*, Houston, TX, p. 359-385.
- Raubenheimer, B., 2002, Observations and predictions of fluid velocities in the surf and swash zones: *Journal of Geophysical Research*, v. 107, p. 3190.
- Rothwell, R.G., Kenyon, N.H., and McGregor, B.A., 1991, Sedimentary features of the south Texas continental slope as revealed by side-scan sonar and high-resolution seismic data: *American Association of Petroleum Geologists Bulletin*, v. 75, p. 298-312.

Technical Letter Report
South Texas Project Hydrology TER w/ OIs
Section 2.4.6

JCN Q-4151
Task Order No. 2
U.S. Geological Survey

- Saville, T., 1955, Laboratory data on wave runup and overtopping on shore structures: U.S. Army, Beach Erosion Board, Document Service Center Technical Memo. No. 64 [Technical Report].
- Schulte, P., Speijer, R., Mai, H., and Kontny, A., 2006, The Cretaceous-Paleogene (K-P) boundary at Brazos, Texas: Sequence stratigraphy, depositional events and the Chicxulub impact: *Sedimentary Geology*, v. 184, p. 77-109.
- Sielecki, A., and Wurtele, M.G., 1970, The numerical integration of the nonlinear shallow-water equations with sloping boundaries: *Journal of Computational Physics*, v. 6, p. 219-236.
- Smit, J., Roep, T.B., Alvarez, W., Montanari, A., Claeys, P., Grajales-Nishimura, J.M., and Bermudez, J., 1996, Coarse-grained, clastic sandstone complex at the K/T boundary around the Gulf of Mexico: Deposition by tsunami waves induced by the Chicxulub impact?, in Ryder, G., Fastovsky, D., and Gartner, S., eds., *The Cretaceous-Tertiary Event and Other Catastrophes in Earth History*: Boulder, Colorado, Geological Society of America, Special Paper 307, p. 151-182.
- Smith, M.S., and Shepherd, J.B., 1995, Potential Cauchy-Poisson wave generated by submarine eruptions of Kick 'em Jenny Volcano: *Natural Hazards*, v. 11, p. 75-94.
- Tao, J., 1983, Computation of wave runup and wave breaking: Danish Hydraulics Institute [Internal Report].
- Tao, J., 1984, Numerical modeling of wave runup and breaking on the beach: *Acta Oceanologica Sinica*, v. 6, p. 692-700.
- ten Brink, U.S., Twichell, D., Geist, E.L., Chaytor, J., Locat, J., Lee, H., Buczkowski, B., Barkan, R., Solow, A.R., Andrews, B.D., Parsons, T., Lynett, P., Lin, J., and Sansoucy, M., 2008, Evaluation of Tsunami Sources with the Potential to Impact the U.S. Atlantic and Gulf Coasts: An Updated Report to the Nuclear Regulatory Commission, 302 p. [U.S. Geological Survey Administrative Report].
- Ting, F.C.-K., and Kirby, J.T., 1995, Dynamics of surf-zone turbulence in a strong plunging breaker: *Coastal Engineering*, v. 24, p. 177-204.
- Titov, V.V., and Synolakis, C.E., 1995, Modeling of breaking and nonbreaking long wave evolution and runup using VTSC-2: *Journal of Waterway, Port, Coastal, and Ocean Engineering*, v. 121, p. 308-316.
- Titov, V.V., and Synolakis, C.E., 1998, Numerical modeling of tidal wave runup: *Journal of Waterway, Port, Coastal, and Ocean Engineering*, v. 124, p. 157-171.

Technical Letter Report
South Texas Project Hydrology TER w/ OIs
Section 2.4.6

JCN Q-4151
Task Order No. 2
U.S. Geological Survey

- Trabant, P., Watts, P., Lettieri, F.L., and Jamieson, A., 2001, East Breaks slump, northwest Gulf of Mexico, OTC 12960, in 2001 Offshore Technology Conference, Houston, TX, p. 231-238.
- Twichell, D., Chaytor, J.D., ten Brink, U.S., and Buczkowski, B., 2009, Morphology of late Quaternary submarine landslides along the U.S. Atlantic continental margin: *Marine Geology*, v. 264, p. 4-15.
- Twichell, D., Nelson, C.H., Kenyon, N.H., and Schwab, W.C., in press, The influence of external processes on the latest Pleistocene and Holocene evolution of the Mississippi Fan, *in* Kneller, B., McCaffrey, W., Martinsen, O., and Posamentier, H., eds., *External Controls on Deep Water Depositional Systems: SEPM Special Publication*.
- Twichell, D.C., Kenyon, N.H., Parson, L.M., and McGregor, B.A., 1991, Depositional patterns of the Mississippi Fan surface: Evidence from GLORIA II and high-resolution seismic profiles, *in* Weimer, P., and Link, M.H., eds., *Seismic Facies and Sedimentary Processes of Submarine Fans and Turbidite Systems*: New York, Springer-Verlag, p. 349-363.
- Twichell, D.C., Valentine, P.C., and Parson, L.M., 1993, Slope failure of carbonate sediment on the West Florida Slope, *in* Schwab, W.C., Lee, H.J., and Twichell, D.C., eds., *Submarine Landslides: Selected Studies in the U.S. Exclusive Economic Zone*: U.S. Geological Survey Bulletin 2002, p. 69-78.
- Van de Meer, J.W., and Janssen, J.P.F.M., 1995, Wave run-up and wave overtopping at dikes, *in* Kobayashi, N., and Demirebilek, Z., eds., *Wave Forces on inclined and Vertical Wall Structures*: ASCE, p. 1-27.
- Watts, P., Grilli, S.T., Tappin, D.R., and Fryer, G.J., 2005, Tsunami generation by submarine mass failure II: Predictive equations and case studies: *Journal of Waterway, Port, Coastal, and Ocean Engineering*, v. 131, p. 298-310.
- Wei, G., Kirby, J.T., Grilli, S.T., and Subramanya, R., 1995, A fully nonlinear Boussinesq model for surface waves. Part 1. Highly nonlinear unsteady waves: *Journal of Fluid Mechanics*, v. 294, p. 71-92.
- Wei, G., Kirby, J.T., and Sinha, A., 1999, Generation of waves in Boussinesq models using a source function method: *Coastal Engineering*, v. 36, p. 271-299.
- Woo, S.-B., and Liu, P.L.-F., 2004, A finite element model for modified Boussinesq equations. Part I: Model development: *Journal of Waterway, Port, Coastal, and Ocean Engineering*, v. 130, p. 1-16.

Technical Letter Report
South Texas Project Hydrology TER w/ OIs
Section 2.4.6

JCN Q-4151
Task Order No. 2
U.S. Geological Survey

Zelt, J.A., 1991, The runup of nonbreaking and breaking solitary waves: Coastal
Engineering, v. 15, p. 205-246.

Technical Letter Report
South Texas Project Hydrology TER w/ OIs
Section 2.4.6

JCN Q-4151
Task Order No. 2
U.S. Geological Survey

Appendix

Reprints of journal publications that form the foundation of COULWAVE are included below:

Lynett, P., and Liu, P.L.F., 2002, A numerical study of submarine-landslide-generated waves and run-up: *Proceedings of the Royal Society of London, A*, v. 458, p. 2885-2910.

Lynett, P.J., and Liu, P.L.-F., 2005, A numerical study of run-up generated by three-dimensional landslides: *Journal of Geophysical Research*, v. 10, p. doi:10.1029/2004JC002443.

Lynett, P.J., 2006, Nearshore wave modeling with high-order Boussinesq-type equations: *Journal of the Waterways and Harbors Division, A.S.C.E.*, v. 132, p. 348-357.

Lynett, P.J., Wu, T.-R., and Liu, P.L.-F., 2002, Modeling wave runup with depth-integrated equations: *Coastal Engineering*, v. 46, p. 89-107.

Lynett, P., 2006, Wave breaking velocity effects in depth-integrated models: *Coastal Engineering*, v. 53, p. 325-333.

A numerical study of submarine-landslide-generated waves and run-up

BY PATRICK LYNETT AND PHILIP L.-F. LIU

*School of Civil and Environmental Engineering,
Cornell University, Ithaca, NY 14853, USA*

Received 4 October 2001; accepted 18 February 2002; published online 30 September 2002

A mathematical model is derived to describe the generation and propagation of water waves by a submarine landslide. The model consists of a depth-integrated continuity equation and momentum equations, in which the ground movement is the forcing function. These equations include full nonlinear, but weak frequency-dispersion, effects. The model is capable of describing wave propagation from relatively deep water to shallow water. Simplified models for waves generated by small seafloor displacement or creeping ground movement are also presented. A numerical algorithm is developed for the general fully nonlinear model. Comparisons are made with a boundary integral equation method model, and a deep-water limit for the depth-integrated model is determined in terms of a characteristic side length of the submarine mass. The importance of nonlinearity and frequency dispersion in the wave-generation region and on the shoreline movement is discussed.

Keywords: landslide tsunamis; Boussinesq equations; wave run-up

1. Introduction

In recent years, significant advances have been made in developing mathematical models to describe the entire process of generation, propagation and run-up of a tsunami event (e.g. Yeh *et al.* 1996; Geist 1998). These models are based primarily on the shallow-water wave equations and are adequate for tsunamis generated by seismic seafloor deformation. Since the duration of the seismic seafloor deformation is very short, the water-surface response is almost instantaneous and the initial water-surface profile mimics the final seafloor deformation. The typical wavelength of this type of tsunami ranges from 20 to 100 km. Therefore, frequency dispersion can be ignored in the generation region. The nonlinearity is also usually not important in the generation region, because the initial wave amplitude is relatively small compared to the wavelength and the water depth. However, the frequency dispersion becomes important when a tsunami propagates for a long distance. Nonlinearity could also dominate as a tsunami enters the run-up phase. Consequently, a complete model that can describe the entire process of tsunami generation, evolution and run-up needs to consider both frequency dispersion and nonlinearity.

Tsunamis are also generated by other mechanisms. For example, submarine landslides have been documented as one of many possible sources for several destructive

tsunamis (Moore & Moore 1984; von Huene *et al.* 1989; Jiang & LeBlond 1992; Tappin *et al.* 1999; Keating & McGuire 2002). On 29 November 1975, a landslide was triggered by a 7.2-magnitude earthquake along the southeast coast of Hawaii. A 60 km stretch of Kilauea's south coast subsided 3.5 m and moved seaward 8 m. This landslide generated a local tsunami with a maximum run-up height of 16 m at Keauhou (Cox & Morgan 1977). More recently, the devastating Papua New Guinea tsunami in 1998 is thought to have been caused by a submarine landslide (Tappin *et al.* 1999, 2001; Keating & McGuire 2002). In terms of tsunami-generation mechanisms, two significant differences exist between submarine-landslide and coseismic seafloor deformation. First, the duration of a landslide is much longer and is in the order of magnitude of several minutes. Hence the time-history of the seafloor movement will affect the characteristics of the generated wave and needs to be included in the model. Secondly, the effective size of the landslide region is usually much smaller than the coseismic seafloor-deformation zone. Consequently, the typical wavelength of the tsunamis generated by a submarine landslide is also shorter, i.e. *ca.* 1–10 km. Therefore, the frequency dispersion could be important in the wave-generation region. The existing numerical models based on shallow-water wave equations may not be suitable for modelling the entire process of submarine-landslide-generated tsunami (e.g. Raney & Butler 1976; Harbitz *et al.* 1993).

In this paper, we shall present a new model describing the generation and propagation of tsunamis by a submarine landslide. In this general model, only the assumption of weak frequency dispersion is employed, i.e. the ratio of water depth to wavelength is small or $O(\mu^2) \ll 1$. Until the past decade, weakly dispersive models were formulated in terms of a depth-averaged velocity (e.g. Peregrine 1967). Recent work has clearly demonstrated that modifications to the frequency dispersion terms (Madsen & Sorensen 1992) or expression of the model equations in terms of an arbitrary-level velocity (Nwogu 1993; Liu 1994) can extend the validity of the linear-dispersion properties into deeper water. The general guideline for dispersive properties is that the 'extended' versions of the depth-integrated equations are valid for wavelengths greater than two water depths, whereas the depth-averaged model is valid for lengths greater than five water depths (e.g. Nwogu 1993). Moreover, in the model presented in this paper, the full nonlinear effect is included, i.e. the ratio of wave amplitude to water depth is of order one or $\varepsilon = O(1)$. Therefore, this new model is more general than that developed by Liu & Earickson (1983), in which the Boussinesq approximation, i.e. $O(\mu^2) = O(\varepsilon) \ll 1$, was used. In the special case where the seafloor is stationary, the new model reduces to the model for fully nonlinear and weakly dispersive waves propagating over a varying water depth (e.g. Liu 1994; Madsen & Schäffer 1998). The model is applicable for both the impulsive slide movement and creeping slide movement. In the latter case, the time duration for the slide is much longer than the characteristic wave period.

This paper is organized as follows. Governing equations and boundary conditions for flow motions generated by a ground movement are summarized in the next section. The derivation of approximate two-dimensional depth-integrated governing equations follows. The general model equations are then simplified for special cases. A numerical algorithm is presented to solve the general mathematical model. The numerical model is tested using available experimental data (e.g. Hammack 1973) for one-dimensional situations. Employing a boundary integral equation model (BIEM), which solves for potential flow in the vertical plane, a deep-water limit for waves generated by

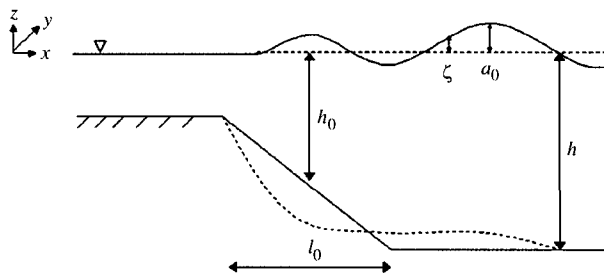


Figure 1. Basic formulational set-up.

submarine slides is determined for the depth-integrated model. The importance of nonlinearity and frequency dispersion is inferred through numerical simulation of a large number of different physical set-ups.

2. Governing equations and boundary conditions

As shown in figure 1, $\zeta'(x', y', t')$ denotes the free-surface displacement of a wave train propagating in the water depth $h'(x', y', t')$. Introducing the characteristic water depth h_0 as the vertical length-scale, the characteristic length of the submarine slide region ℓ_0 as the horizontal length-scale, $\ell_0/\sqrt{gh_0}$ as the time-scale, and the characteristic wave amplitude a_0 as the scale of wave motion, we can define the following dimensionless variables,

$$(x, y) = \frac{(x', y')}{\ell_0}, \quad z = \frac{z'}{h_0}, \quad t = \frac{\sqrt{gh_0}t'}{\ell_0},$$

$$h = \frac{h'}{h_0}, \quad \zeta = \frac{\zeta'}{a_0}, \quad p = \frac{p'}{\rho g a_0}$$

and

$$(u, v) = \frac{(u', v')}{\varepsilon \sqrt{gh_0}}, \quad w = \frac{w'}{(\varepsilon/\mu) \sqrt{gh_0}}, \quad (2.1)$$

in which (u, v) represents the horizontal velocity components, w the vertical velocity component, and p the pressure. Two dimensionless parameters have been introduced in (2.1), which are

$$\varepsilon = \frac{a_0}{h_0}, \quad \mu = \frac{h_0}{\ell_0}. \quad (2.2)$$

Assuming that the viscous effects are insignificant, the wave motion can be described by the continuity equation and Euler's equations, i.e.

$$\mu^2 \nabla \cdot \mathbf{u} + w_z = 0, \quad (2.3)$$

$$\mathbf{u}_t + \varepsilon \mathbf{u} \cdot \nabla \mathbf{u} + \frac{\varepsilon}{\mu^2} w \mathbf{u}_z = -\nabla p, \quad (2.4)$$

$$\varepsilon w_t + \varepsilon^2 \mathbf{u} \cdot \nabla w + \frac{\varepsilon^2}{\mu^2} w w_z = -\varepsilon p_z - 1, \quad (2.5)$$

where $\mathbf{u} = (u, v)$ denotes the horizontal velocity vector, $\nabla = (\partial/\partial x, \partial/\partial y)$ the horizontal gradient vector, and the subscript the partial derivative.

On the free surface, $z = \varepsilon\zeta(x, y, t)$, the usual kinematic and dynamic boundary conditions apply,

$$w = \mu^2(\zeta_t + \varepsilon\mathbf{u} \cdot \nabla\zeta) \quad \text{on } z = \varepsilon\zeta, \quad (2.6a)$$

$$p = 0. \quad (2.6b)$$

Along the seafloor, $z = -h$, the kinematic boundary condition requires

$$w + \mu^2\mathbf{u} \cdot \nabla h + \frac{\mu^2}{\varepsilon}h_t = 0 \quad \text{on } z = -h. \quad (2.7)$$

For later use, we note here that the depth-integrated continuity equation can be obtained by integrating (2.3) from $z = -h$ to $z = \varepsilon\zeta$. After applying the boundary conditions (2.6), the resulting equation reads

$$\nabla \cdot \left[\int_{-h}^{\varepsilon\zeta} \mathbf{u} \, dz \right] + \frac{1}{\varepsilon}H_t = 0, \quad (2.8)$$

where

$$H = \varepsilon\zeta + h. \quad (2.9)$$

We remark here that (2.8) is exact.

3. Approximate two-dimensional governing equations

The three-dimensional boundary-value problem described in the previous section will be approximated and projected onto a two-dimensional horizontal plane. In this section, the nonlinearity is assumed to be of $O(1)$. However, the frequency dispersion is assumed to be weak, i.e.

$$O(\mu^2) \ll 1. \quad (3.1)$$

Using μ^2 as the small parameter, a perturbation analysis is performed on the primitive governing equations. The complete derivation is given in Appendix A. The resulting approximate continuity equation is

$$\begin{aligned} \frac{1}{\varepsilon}h_t + \zeta_t + \nabla \cdot (H\mathbf{u}_\alpha) \\ - \mu^2\nabla \cdot \left\{ H \left[\left(\frac{1}{6}(\varepsilon^2\zeta^2 - \varepsilon\zeta h + h^2) - \frac{1}{2}z_\alpha^2 \right) \nabla(\nabla \cdot \mathbf{u}_\alpha) \right. \right. \\ \left. \left. + \left(\frac{1}{2}(\varepsilon\zeta - h) - z_\alpha \right) \nabla \left(\nabla \cdot (h\mathbf{u}_\alpha) + \frac{h_t}{\varepsilon} \right) \right] \right\} = O(\mu^4). \end{aligned} \quad (3.2)$$

Equation (3.2) is one of three governing equations for ζ and \mathbf{u}_α . The other two equations come from the horizontal momentum equation (2.4) and are given in vector

form as

$$\begin{aligned}
& \mathbf{u}_{\alpha t} + \varepsilon \mathbf{u}_{\alpha} \cdot \nabla \mathbf{u}_{\alpha} + \nabla \zeta \\
& + \mu^2 \frac{\partial}{\partial t} \left\{ \frac{1}{2} z_{\alpha}^2 \nabla (\nabla \cdot \mathbf{u}_{\alpha}) + z_{\alpha} \nabla \left[\nabla \cdot (h \mathbf{u}_{\alpha}) + \frac{h_t}{\varepsilon} \right] \right\} \\
& + \varepsilon \mu^2 \left\{ \left[\nabla \cdot (h \mathbf{u}_{\alpha}) + \frac{h_t}{\varepsilon} \right] \nabla \left[\nabla \cdot (h \mathbf{u}_{\alpha}) + \frac{h_t}{\varepsilon} \right] \right. \\
& \quad - \nabla \left[\zeta \left(\nabla \cdot (h \mathbf{u}_{\alpha})_t + \frac{h_{tt}}{\varepsilon} \right) \right] + (\mathbf{u}_{\alpha} \cdot \nabla z_{\alpha}) \nabla \left[\nabla \cdot (h \mathbf{u}_{\alpha}) + \frac{h_t}{\varepsilon} \right] \\
& \quad + z_{\alpha} \nabla \left[\mathbf{u}_{\alpha} \cdot \nabla \left(\nabla \cdot (h \mathbf{u}_{\alpha}) + \frac{h_t}{\varepsilon} \right) \right] + z_{\alpha} (\mathbf{u}_{\alpha} \cdot \nabla z_{\alpha}) \nabla (\nabla \cdot \mathbf{u}_{\alpha}) \\
& \quad \left. + \frac{1}{2} z_{\alpha}^2 \nabla [\mathbf{u}_{\alpha} \cdot \nabla (\nabla \cdot \mathbf{u}_{\alpha})] \right\} \\
& + \varepsilon^2 \mu^2 \nabla \left\{ -\frac{1}{2} \zeta^2 \nabla \cdot \mathbf{u}_{\alpha t} - \zeta \mathbf{u}_{\alpha} \cdot \nabla \left[\nabla \cdot (h \mathbf{u}_{\alpha}) + \frac{h_t}{\varepsilon} \right] + \zeta \left[\nabla \cdot (h \mathbf{u}_{\alpha}) + \frac{h_t}{\varepsilon} \right] \nabla \cdot \mathbf{u}_{\alpha} \right\} \\
& + \varepsilon^3 \mu^2 \nabla \left\{ \frac{1}{2} \zeta^2 [(\nabla \cdot \mathbf{u}_{\alpha})^2 - \mathbf{u}_{\alpha} \cdot \nabla (\nabla \cdot \mathbf{u}_{\alpha})] \right\} = O(\mu^4). \tag{3.3}
\end{aligned}$$

Equations (3.2) and (3.3) are the coupled governing equations, written in terms of \mathbf{u}_{α} and ζ , for fully nonlinear weakly dispersive waves generated by a seafloor movement. We reiterate here that \mathbf{u}_{α} is evaluated at $z = z_{\alpha}(x, y, t)$, which is a function of time. The choice of z_{α} is made based on the linear frequency-dispersion characteristics of the governing equations (e.g. Nwogu 1993; Chen & Liu 1995). Assuming a stationary seafloor, in order to extend the applicability of the governing equations to relatively deep water (or a short wave), z_{α} is recommended to be evaluated at $z_{\alpha} = -0.531h$. In the following analysis, the same relationship is employed. These model equations will be referred to as FNL-EXT, for fully nonlinear ‘extended’ equations.

Up to this point, the time-scale of the seafloor movement is assumed to be in the same order of magnitude as the typical period of generated water wave, $t_w = \ell_0 / \sqrt{gh_0}$ as given in (2.1). When the ground movement is creeping in nature, the time-scale of seafloor movement, t_c , could be larger than t_w . The only scaling parameter that is directly affected by the time-scale of the seafloor movement is the characteristic amplitude of the wave motion. After introducing the time-scale t_c into the time derivatives of h in the continuity equation (3.2), along with a characteristic change in water depth Δh , the coefficient in front of h_t becomes

$$\frac{\delta t_w}{\varepsilon t_c},$$

where $\delta = \Delta h / h_0$. To maintain the conservation of mass, the above parameter must be of order one. Thus

$$\varepsilon = \delta \frac{t_w}{t_c} = \frac{\delta \ell_0}{t_c \sqrt{gh_0}}. \tag{3.4}$$

The above relationship can be interpreted in the following way. During the creeping ground movement, over the time period $t < t_c$ the generated wave has propagated a distance $t\sqrt{gh_0}$. The total volume of the seafloor displacement, normalized by h_0 , is $\delta \ell_0(t/t_c)$, which should be the same as the volume of water underneath the generated

wave crest, i.e. $\varepsilon t \sqrt{gh_0}$. Therefore, over the ground-movement period, $t < t_c$, the wave amplitude can be estimated by (3.4). Consequently, nonlinear effects become important only if ε defined in (3.4) is $O(1)$. Since, by the definition of a creeping slide, the value $l_0/(t_c \sqrt{gh_0})$ is always less than one, fully nonlinear effects will be important for only the largest slides. The same conclusion was reached by Hammack (1973), using a different approach. The importance of the fully nonlinear effect when modelling creeping ground movements will be tested in §8.

4. Limiting cases

In this section, the general model is further simplified for different physical conditions.

(a) Weakly nonlinear waves

In many situations, the seafloor displacement is relatively small in comparison with the local depth, and the seafloor movement can be approximated as

$$h(x, y, t) = h_0(x, y) + \delta \bar{h}(x, y, t), \quad (4.1)$$

in which δ is considered to be small. In other words, the maximum seafloor displacement is much smaller than the characteristic water depth. Since the free-surface displacement is directly proportional to the seafloor displacement, i.e. $O(\varepsilon \zeta) = O(\delta \bar{h})$, or much less than the seafloor displacement in the case of creeping ground movements, we can further simplify the governing equations derived in the previous section by allowing

$$O(\varepsilon) = O(\delta) = O(\mu^2) \ll 1, \quad (4.2)$$

which is the Boussinesq approximation. Thus the continuity equation (3.2) can be reduced to

$$\begin{aligned} \zeta_t + \nabla \cdot (H \mathbf{u}_\alpha) + \frac{\delta}{\varepsilon} \bar{h}_t \\ - \mu^2 \nabla \cdot \left\{ h_0 \left[\left(\frac{1}{6} h_0^2 - \frac{1}{2} z_\alpha^2 \right) \nabla (\nabla \cdot \mathbf{u}_\alpha) - \left(\frac{1}{2} h_0 + z_\alpha \right) \nabla \left(\nabla \cdot (h_0 \mathbf{u}_\alpha) + \frac{\delta}{\varepsilon} \bar{h}_t \right) \right] \right\} \\ = O(\mu^4, \mu^2 \varepsilon, \delta \mu^2). \end{aligned} \quad (4.3)$$

The momentum equation becomes

$$\begin{aligned} \mathbf{u}_{\alpha t} + \varepsilon \mathbf{u}_\alpha \cdot \nabla \mathbf{u}_\alpha + \nabla \zeta + \mu^2 \frac{\partial}{\partial t} \left\{ \frac{1}{2} z_\alpha^2 \nabla (\nabla \cdot \mathbf{u}_\alpha) + z_\alpha \nabla \left[\nabla \cdot (h_0 \mathbf{u}_\alpha) + \frac{\delta}{\varepsilon} \bar{h}_t \right] \right\} \\ = O(\mu^4, \varepsilon \mu^2, \delta \mu^2). \end{aligned} \quad (4.4)$$

These model equations will be referred to as WNL-EXT, for weakly nonlinear 'extended' equations. The linear version of the above will also be used in the following analysis, and will be referred to as L-EXT, for linear 'extended' equations.

It is also possible to express the approximate continuity and momentum equations in terms of a depth-averaged velocity. The depth-averaged equations can be derived using the same method presented in Appendix A. One version of the depth-averaged

equations will be employed in future sections, which is subject to the restraint (4.2), and is given as

$$\zeta_t + \nabla \cdot (H\bar{\mathbf{u}}) + \frac{\delta}{\varepsilon} \bar{h}_t = 0 \quad (4.5)$$

and

$$\begin{aligned} \bar{\mathbf{u}}_t + \varepsilon \bar{\mathbf{u}} \cdot \nabla \bar{\mathbf{u}} + \nabla \zeta + \mu^2 \frac{\partial}{\partial t} \left\{ \frac{1}{2} h_0^2 \nabla (\nabla \cdot \bar{\mathbf{u}}) - \frac{1}{6} h_0 \nabla \left[\nabla \cdot (h_0 \bar{\mathbf{u}}) + \frac{\delta}{\varepsilon} \bar{h}_t \right] \right\} \\ = O(\mu^4, \varepsilon \mu^2, \delta \mu^2), \end{aligned} \quad (4.6)$$

where the depth-averaged velocity is defined as

$$\bar{\mathbf{u}}(x, y, t) = \frac{1}{h + \varepsilon \zeta} \int_h^{\varepsilon \zeta} \mathbf{u}(x, y, z, t) dz. \quad (4.7)$$

This set of model equations (4.5) and (4.6) will be referred to as WNL-DA, for weakly nonlinear depth-averaged equations.

(b) Nonlinear shallow-water waves

In the case that the water depth is very shallow or the wavelength is very long, the governing equations (3.2) and (3.3) can be truncated at $O(\mu^2)$. These resulting equations are the well-known nonlinear shallow-water equations in which the seafloor movement is the forcing term for wave generation. This set of equations will be referred to as NL-SW, for nonlinear shallow-water equations.

5. Numerical model

In this paper, a finite-difference algorithm is presented for the general model equations, FNL-EXT. This model has the robustness of enabling slide-generated surface waves, although initially linear or weakly nonlinear in nature, to propagate into shallow water, where fully nonlinear effects may become important. The algorithm is developed for the general two-horizontal-dimension problem; however, in this paper, only one-horizontal-dimension examples are examined. The structure of the present numerical model is similar to those of Wei & Kirby (1995) and Wei *et al.* (1995). Differences between the model presented here and that of Wei *et al.* exist in the added terms due to a time-dependent water depth and the numerical treatment of some nonlinear-dispersive terms, which is discussed in more detail in Appendix B. A high-order predictor-corrector scheme is used, employing a third order in time explicit Adams–Bashforth predictor step, and a fourth order in time Adams–Moulton implicit corrector step (Press *et al.* 1989). The implicit corrector step must be iterated until a convergence criterion is satisfied. All spatial derivatives are differenced to fourth-order accuracy, yielding a model that is numerically accurate to $(\Delta x)^4$, $(\Delta y)^4$ in space and $(\Delta t)^4$ in time. The governing equations (3.2) and (3.3) are dimensionalized for the numerical model, and all variables described in this and following sections will be in the dimensional form. Note that the dimensional equations are equivalent to the non-dimensional ones with $\varepsilon = \mu = 1$ and the addition of gravity, g , to the coefficient of the leading-order free-surface derivative in the momentum equation (i.e. the third term on the left-hand side of (3.3)). The predictor-corrector

equations are given in Appendix B, along with some additional description of the numerical scheme. Run-up and rundown of the waves generated by the submarine disturbance will also be examined. The moving-boundary scheme employed here is the technique developed by Lynett *et al.* (2002). Founded around the restrictions of the high-order numerical wave-propagation model, the moving-boundary scheme uses linear extrapolation of free surface and velocity through the shoreline, into the dry region. This approach allows for the five-point finite-difference formulae to be applied at all points, even those neighbouring dry points, and thus eliminates the need of conditional statements.

In addition to the depth-integrated-model numerical results, output from a two-dimensional (vertical-plane) BIEM model will be presented for certain cases. This BIEM model will be primarily used to determine the deep-water-accuracy limit of the depth-integrated model. The BIEM model solves for inviscid irrotational flows and converts a boundary-value problem into an integral equation along the boundary of a physical domain. Therefore, just as with the depth-integration approach, it reduces the dimension of the problem by one. The BIEM model used here solves the Laplace equation in the vertical plane (x, z), and, of course, is valid in all water depths for all wavelengths. Details of this type of BIEM model, when used to model water-wave propagation, can be found in Grilli *et al.* (1989), Liu *et al.* (1992) and Grilli (1993), for example. The BIEM model used in this work has reproduced the numerical results presented for landslide-generated waves in Grilli & Watts (1999) perfectly.

6. Comparisons with experiment and other models

As a first check of the present model, a comparison between Hammack's (1973) experimental data for an impulsive bottom movement in a constant water depth is made. The bottom movement consists of a length, $l_0 = 24.4$ water depths, which is pushed vertically upward. The change in depth for this experiment, δ , is 0.1, so nonlinear effects should play a small role near the source region. Figure 2 shows a comparison between the numerical results using FNL-EXT, experimental data and the linear theory presented by Hammack. Both the fully nonlinear model and the linear theory agree well with experiment at the edge of the source region (figure 2a). From figure 2b, a time-series taken at 20 water depths from the edge of the source region, the agreement between all data is again quite good, but the deviation between the linear theory and experiment is slowly growing. The purpose of this comparison is to show that the present numerical model accurately predicts the free-surface response to a simple seafloor movement. It would seem that if one was interested in just the wave field very near the source, linear theory is adequate. However, as the magnitude of the bed upthrust, δ , becomes large, linear theory is not capable of accurately predicting the free-surface response, even very near the source region. One such linear versus nonlinear comparison is shown in figure 2 for $\delta = 0.6$. The motion of the bottom movement is the same as in Hammack's case above. Immediately on the outskirts of the bottom movement, there are substantial differences between linear and nonlinear theory, as shown in figure 2c. Additionally, as the wave propagates away from the source, errors in linear theory are more evident.

A handful of experimental trials and analytic solutions exist for non-impulsive seafloor movements. However, for the previous work that made use of smooth obstacles, such as a semicircle (e.g. Forbes & Schwartz 1982) or a semi-ellipse (e.g. Lee *et*

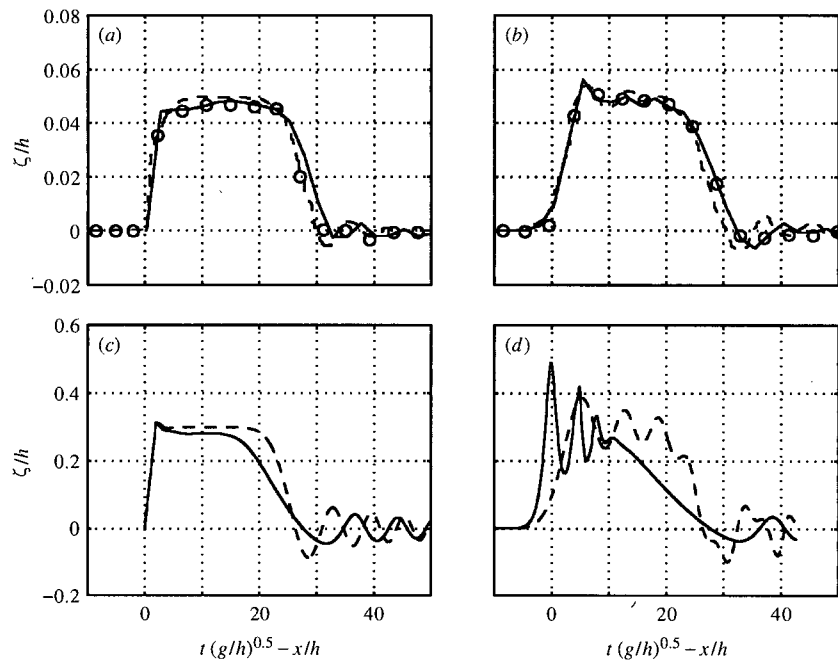


Figure 2. (a), (b) Comparison between Hammack's (1973) experimental data (dots) for an impulsive seafloor upthrust of $\delta = 0.1$, FNL-EXT numerical simulation (solid line), and linear theory (dashed line). (a) Time-series at $x/h = 0$; (b) time-series at $x/h = 20$, where x is the distance from the edge of the impulsive movement. (c), (d) FNL-EXT (solid line) and L-EXT (dashed line) numerical results for Hammack's set-up, except with $\delta = 0.6$.

al. 1989), the length of the obstacle is always less than 1.25 water depths, or $\mu \geq 0.8$. Unfortunately, these objects will create waves too short to be modelled accurately by a depth-integrated model.

Watts (1997) performed a set of experiments where he let a triangular block free fall down a planar slope. In all the experiments, the front (deep-water) face of the block was steep, and in some cases vertical. Physically, as the block travels down a slope, water is pushed out horizontally from the vertical front. Numerically, however, using the depth-integrated model, the dominant direction of water motion near the vertical face is vertical. This can be explained as follows. Examining the depth-integrated-model equations, starting from the leading-order shallow-water-wave equations, the only forcing term due to the changing water depth appears in the continuity equation. There is no forcing term in the horizontal momentum equation. Therefore, in the non-dispersive system, any seafloor bottom cannot directly create a horizontal velocity. This concept can be further illuminated by the equation describing the vertical profile of horizontal velocity,

$$\mathbf{u}(x, y, z, t) = \mathbf{u}_\alpha(x, y, t) + O(\mu^2). \quad (6.1)$$

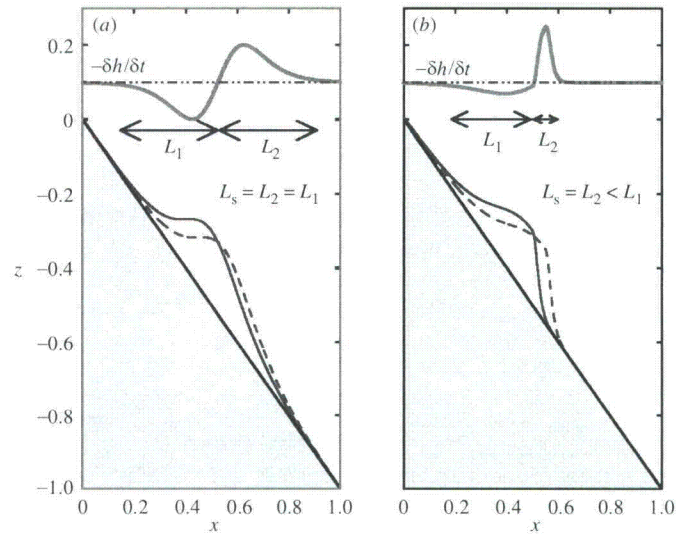


Figure 3. Graphical definition of the characteristic side length of a slide mass. The slide mass at time t_0 is shown by the solid line, while the profile at some time $t > t_0$ is shown by the dashed line. The negative of the change in water depth (or the approximate free-surface response in the non-dispersive equation model) during the increment $t - t_0$ is shown by the thick line plotted on $z = 0.1$.

Again, the changing seafloor bottom cannot directly create a horizontal velocity component for the non-dispersive system. All of the seafloor movement, whether it is a vertical or translational motion, is interpreted as strictly a vertical motion, which can lead to a very different generated wave pattern.

When adding the weakly dispersive terms, the vertical profile of the horizontal velocity becomes

$$\mathbf{u}(x, y, z, t) = \mathbf{u}_\alpha(x, y, t) - \mu^2 \left\{ \frac{1}{2} z^2 - z_\alpha^2 \nabla(\nabla \cdot \mathbf{u}_\alpha) + (z - z_\alpha) \nabla \left[\nabla \cdot (h \mathbf{u}_\alpha) + \frac{h_t}{\varepsilon} \right] \right\} + O(\mu^4). \quad (6.2)$$

Now, with the higher-order dispersive formulation, there is the forcing term, ∇h_t , which accounts for the effects of a horizontally moving body. Keep in mind, however, that this forcing term is a second-order correction, and therefore should represent only a small correction to the horizontal velocity profile. Thus, with rapid translational motion and/or steep side slopes of a submarine slide, the flow motion is strongly horizontal locally, and the depth-integrated models are not adequate. In slightly different terms, let the slide mass have a characteristic side length, L_s . A side length is defined as the horizontal distance between two points at which $\partial h / \partial t = 0$. This definition of a side length is described graphically in figure 3. Figure 3a shows a slide mass that is symmetric around its midpoint in the horizontal direction, where the back (shallow-water) and front (deep-water) side lengths are equal. Figure 3b shows a slide mass whose front side is much shorter than the back. Note that for the slide shown in figure 3b, the side lengths, measured in the

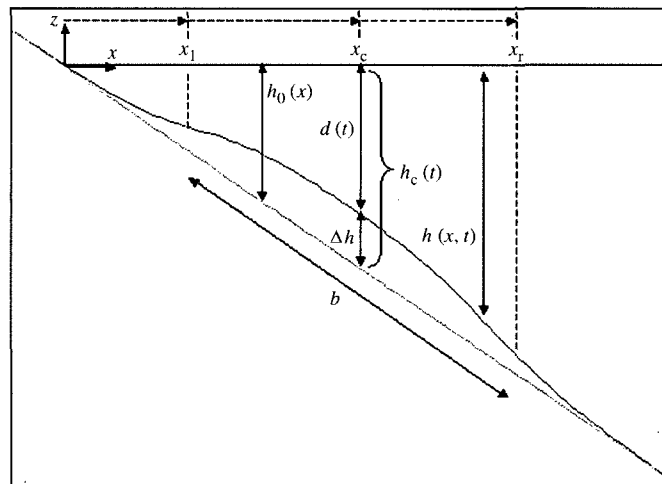


Figure 4. Set-up for submarine landslide comparisons.

direction parallel to the slope, are equal, whereas for the slide in figure 3a, the slide lengths are equal when measured in the horizontal direction. An irregular slide mass will have at least two different side lengths. In these cases, the characteristic side length, L_s , is the shortest of all sides. When L_s is small compared to a characteristic water depth, h_0 , that side is considered steep, or in deep water, and the shallow-water-based depth-integrated model will not be accurate. For the vertical face of Watts's experiments, $L_s = 0$, and therefore $L_s/h_0 = 0$, and the situation resembles that of an infinitely deep ocean. The next section will attempt to determine a limiting value of L_s/h_0 where the depth-integrated model begins to fail.

7. Limitations of the depth-integrated model

Before using the model for practical applications, the limits of accuracy of the depth-integrated model must be determined. As illustrated above, just as there is a short-wave accuracy limit (wave should be at least two water depths long when applying the 'extended' model), it is expected that there is also a slide length-scale limitation. By comparing the outputs of this model to those of the BIEM model, a limiting value of L_s/h_0 can be inferred. The high degree of BIEM model accuracy in simulating wave propagation is well documented (e.g. Grilli 1993; Grilli *et al.* 1995).

The comparison cases will use a slide mass travelling down a constant slope. The slide mass moves as a solid body, with velocity described following Watts (1997). This motion is characterized by a decreasing acceleration until a terminal velocity is reached. All of the solid-body motion coefficients used in this paper are identical to those employed by Grilli & Watts (1999). Note that all of the submarine landslide simulations presented in this paper are non-breaking.

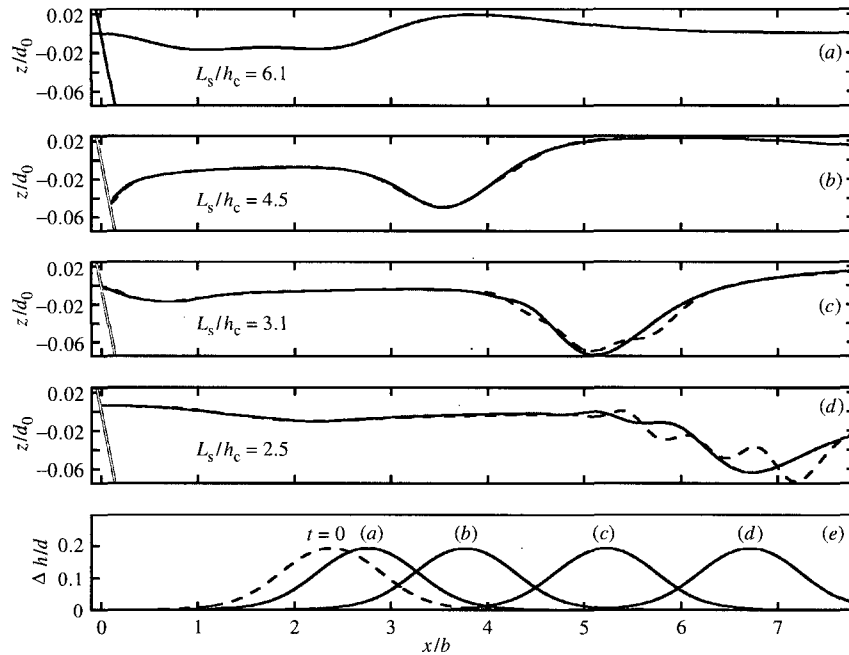


Figure 5. Free-surface snapshots for BIEM (solid line) and depth-integrated (dashed line) results at $t(g/d_0)^{1/2}$ values of (a) 10.6, (b) 21, (c) 31.6 and (d) 41. (e) The location of the slide mass in each of the four snapshots above.

The set-up of the slide mass on the slope is shown in figure 4. The time-history of the seafloor is described by

$$h(x, t) = h_0(x) - \frac{1}{2}\Delta h \left[1 + \tanh\left(\frac{x - x_1(t)}{S}\right) \right] \left[1 - \tanh\left(\frac{x - x_r(t)}{S}\right) \right], \quad (7.1)$$

where Δh is the maximum vertical height of the slide, x_1 is the location of the tanh inflection point of the left side of the slide, x_r is the location of the inflection point on the right side, and S is a shape factor, controlling the steepness of the slide sides. The left and right boundaries and steepness factor are given by

$$x_1(t) = x_c(t) - \frac{1}{2}b \cos(\theta), \quad x_r(t) = x_c(t) + \frac{1}{2}b \cos(\theta), \quad S = \frac{0.5}{\cos(\theta)},$$

where x_c is the horizontal location of the centre point of the slide, and is determined using the equations governing the solid body motion of the slide. The angle of the slope is given by θ . The thickness of the 'slideless' water column, or the baseline water depth, at the centre point of the slide is defined by $h_c(t) = h_0(x_c(t)) = \Delta h + d(t)$. With a specified depth above the initial centre point of the slide mass, $d_0 = d(t=0)$, the initial horizontal location of the slide centre, $x_c(t=0)$, can be found. The length along the slope between x_1 and x_r is defined as b , and all lengths are scaled by b .

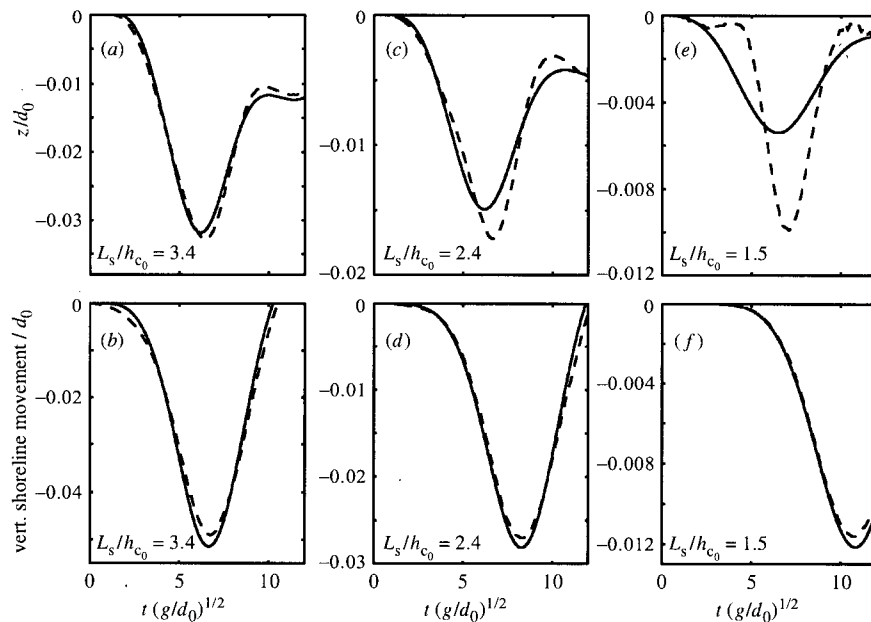


Figure 6. Time-series above the initial centre point of the slide ((a), (c), (e)) and vertical movement of the shoreline ((b), (d), (f)) for a 20° slope and a slide mass with a maximum height $\Delta h = 0.1$. BIEM results are shown by the solid line, depth-integrated results by the dashed line. (a), (b) $d_0/b = 0.4$; (c), (d) $d_0/b = 0.6$; and (e), (f) $d_0/b = 1.0$.

For the first comparison, a slide with the parameter set $\theta = 6^\circ$, $d_0/b = 0.2$ and $\Delta h/b = 0.05$ is modelled with FNL-EXT and BIEM. With these parameters, the characteristic horizontal side length of the slide mass, L_s/b , is 1.7. L_s is defined as in figure 3 or, specifically, the horizontal distance between two points at which $\partial h/\partial t$ is less than 1% of the maximum $\partial h/\partial t$ value. Note that a 6° slope is roughly $\frac{1}{10}$. Figure 5 shows four snapshots of the free-surface elevation from both models. The lowest panel in the figure shows the initial location of the slide mass, along with the locations corresponding to the four free-surface snapshots. Initially, as shown in figure 5a, b, where $L_s/h_c = 6.1$ and 4.5 respectively, the two models agree, and thus are still in the range of acceptable accuracy of the depth-integrated model. In figure 5c, as the slide moves into deeper water, where $L_s/h_c = 3.1$, the two models begin to diverge over the source region, and by figure 5d, the free-surface responses of the two models are quite different. These results indicate that in the vicinity of $x/b = 5$, the depth-integrated model becomes inaccurate. At this location, $h_c/b = 0.5$ and $L_s/h_c = 3.4$.

Numerous additional comparison tests were performed, and all indicated that the depth-integrated model becomes inaccurate when $L_s/h_c < 3$ –3.5. One more of the comparisons is shown here. Examining a 20° slope and a slide mass with a maximum height $\Delta h/b = 0.1$, the initial depth of submergence, d_0/b , will be successively increased from 0.4 to 0.6 to 1.0. The corresponding initial L_s/h_c values are 3.4, 2.4

and 1.5, respectively. Time-series above the initial centre point of the slide masses and vertical shoreline movements are shown in figure 6. The expectation is that the first case ($L_s/h_c = 3.4$ initially) should show good agreement, the middle case ($L_s/h_c = 2.4$ initially) marginal agreement, and the last case ($L_s/h_c = 1.5$ initially) bad agreement. The time-series above the centre, figure 6*a, c, e*, clearly agree with the stated expectation. Various different z_α levels were tested in an attempt to better the agreement with the BIEM-model results for the deeper water cases, but $z_\alpha = -0.531h$ provided the most accurate output. Rundown, as shown in figure 6*b, d, f*, shows good agreement for all the trials. The explanation is that the wave that creates the rundown is generated from the back face of the slide mass. This wave sees a characteristic water depth that is less than h_c , and thus this back face wave remains in the region of accuracy of the depth-integrated model, whereas the wave motion nearer to the front face of the slide is inaccurate. This feature is also clearly shown in figure 5. Thus, if one was solely interested in the leading wave approaching the shoreline, the characteristic water depth should be interpreted as the average depth along the back face of the slide, instead of h_c . The inaccurate elevation waves created by the front face of the moving mass could be absorbed numerically, such as with a sponge layer, so that they do not effect the simulation.

A guideline that the depth-integrated 'extended' model will yield accurate results for $L_s/h_c > 3.5$ is accepted. This restriction would seem to be more stringent than the 'extended' model frequency-dispersion limitation, which requires that the free-surface wave be at least two water depths long. In fact, the slide length-scale limitation is more in line with the dispersion limitations of the depth-averaged (conventional) model. The limitations of the various model formulations, i.e. 'extended' and depth averaged, are discussed in the next section.

8. Importance of nonlinearity and frequency dispersion

Another useful guideline would be to know when nonlinear effects begin to play an important role. This can be determined by running numerous numerical trials, employing the FNL-EXT, WNL-EXT and L-EXT equation models. These three equation sets share identical linear-dispersion properties, but have varying levels of nonlinearity. The linear-dispersion limit of these 'extended' equations, for the rigid bottom case, is near $kh = 3$, where k is the wavenumber. Nonlinearity, however, is only faithfully captured to near $kh = 1.0$ for the FNL-EXT model, and to an even lesser value for WNL-EXT (Gobbi *et al.* 2000). The source-generation accuracy limitation of the model is such that the side length of the landslide over the depth must be greater than 3.5. If the slide is symmetric in the horizontal direction, which is the only type of slide examined in this section, then the wavelength of the generated wave will be $2 \times 3.5 \times h$, or roughly $kh = 1$. Thus, up to the accuracy limit found in the previous section, nonlinearity is expected to be well captured. The FNL-EXT model will be considered correct, and any difference in output compared to the other models with lesser nonlinearity would indicate that full nonlinear effects are important.

The importance of nonlinearity will be tested through examination of various $\Delta h/d_0$ combinations, using the slide mass described in the previous section. The value of $\Delta h/d_0$ can be thought of as an impulsive nonlinearity, as this value represents the magnitude of the free-surface response if the slide motion was entirely vertical and instantaneous. The procedure will be to hold the value $h_{c_0} = h_c(t = 0) = \Delta h + d_0$

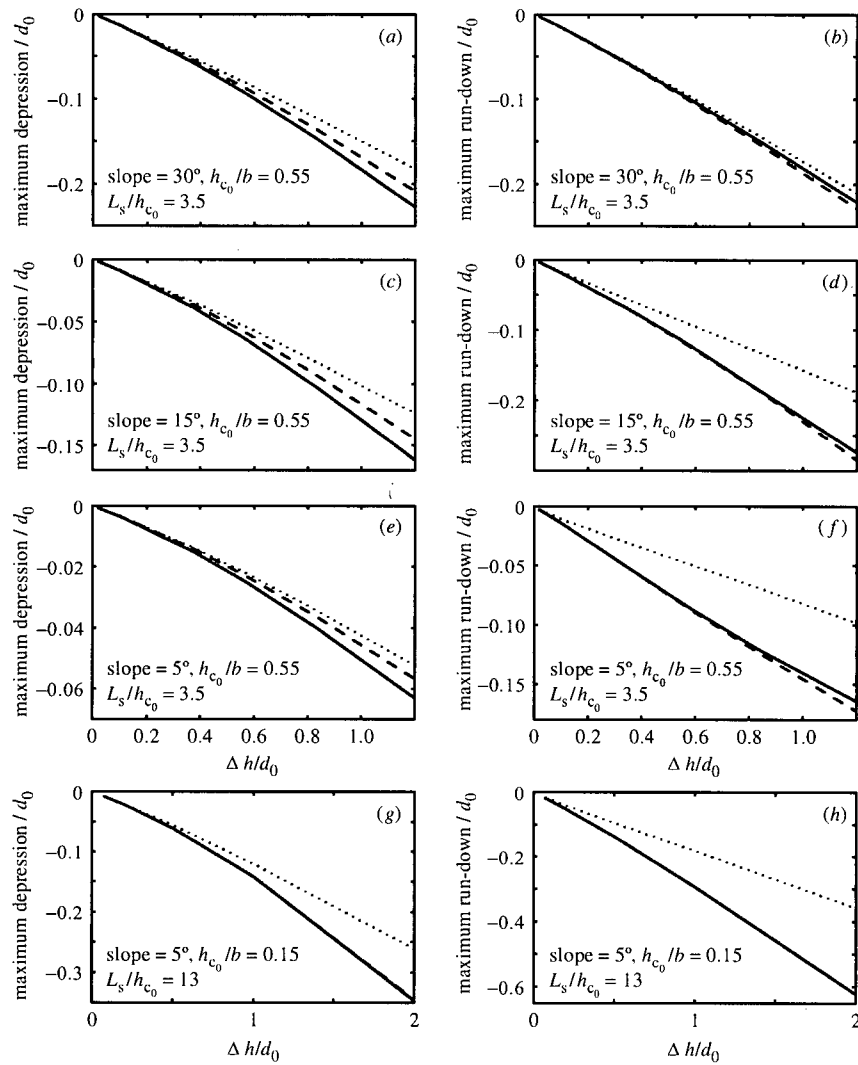


Figure 7. Maximum depression above the initial centre point of the slide mass and maximum rundown for four different trial sets. FNL-EXT results indicated by the solid line, WNL-EXT by the dashed line and L-EXT by the dotted line.

constant for a given slope angle, while altering Δh and d_0 . Two output values will be compared between all the simulations: maximum depression above the initial centre point of the slide and maximum rundown. For all simulations presented in this section, $\Delta x/b = 0.003$ and $\Delta t \sqrt{gh_{c_0}}/b = 0.0003$.

Table 1. Characteristics of the simulations performed for the nonlinearity test

set no.	slope (deg)	h_{c_0}/b	L_s/h_{c_0}
1	30	0.55	3.5
2	15	0.55	3.5
3	5	0.55	3.5
4	5	0.15	13

Figure 7 shows the output from four sets of comparisons, whose characteristics are given in table 1. Figure 7*a, b* show the depression above the centre point and the rundown for set 1, figure 7*c, d* for set 2, figure 7*e, f* for set 3 and figure 7*g, h* for set 4. Examining the maximum depression plots for sets 1–3, it is clear that the trends between the three sets are very similar, with FNL-EXT predicting the largest depression and L-EXT predicting the smallest. The difference between FNL-EXT and WNL-EXT is solely due to nonlinear-dispersive terms, which are of $O(\varepsilon\mu^2)$, while the difference between WNL-EXT and L-EXT is caused by the nonlinear-divergence term in the continuity equation and the convection term in the momentum equation, which are of $O(\varepsilon)$. The relative differences in the maximum depression predicted between FNL-EXT and WNL-EXT are roughly the same as the differences between WNL-EXT and L-EXT for sets 1, 2 and 3. Therefore, in the source region, for L_s/h_{c_0} values near the accuracy limit of the ‘extended’ model (near 3.5), the nonlinear-dispersive terms are as necessary to include in the model as the leading order nonlinear terms. As the L_s/h_c value is increased, the slide produces an increasingly longer (shallow-water) wave. Frequency dispersion plays a lesser role, and thus the nonlinear-dispersive terms become expectedly less important. This can be seen in the maximum depression plot for set 4. For this set, $L_s/h_{c_0} = 13$, and the FNL-EXT and WNL-EXT results are nearly indistinguishable.

Inspecting the maximum rundown plots for sets 1, 2 and 3, it seems that the trends between the three different models have changed. Now, WNL-EXT predicts the largest rundown, while L-EXT predicts the smallest. It is hypothesized that the documented over-shoaling of WNL-EXT (Wei *et al.* 1995) cancels out the lesser wave height generated in the source region compared to FNL-EXT, leading to rundown heights that agree well between the two models. As the slope is decreased, the error in the L-EXT rundown prediction increases. This is attributed to a longer distance of shoaling before the wave reaches the shoreline. As the slope is decreased, while h_{c_0} is kept constant, the horizontal distance from the shoreline to the initial centre point of the slide increases. The slide length is roughly the same for the three sets, therefore the generated wavelength is roughly the same. Thus, with a lesser slope, the generated wave shoals for a greater number of wave periods. During this relatively larger distance of shoaling, nonlinear effects, and in particular the leading-order nonlinear effects, accumulate and yield large errors in the linear (L-EXT) simulations. This trend is also evident in the rundown plot for set 4. Also note that in set 4, where the nonlinear-dispersive terms are very small, the FNL-EXT and WNL-EXT rundowns are identical.

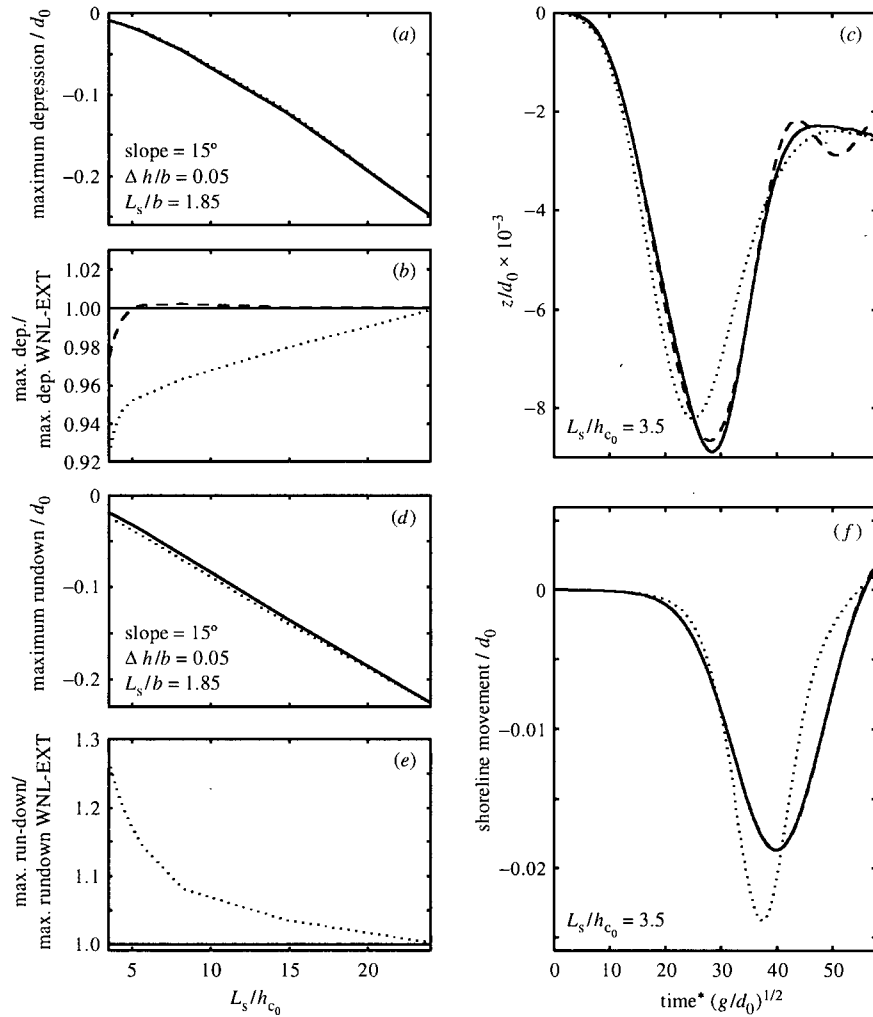


Figure 8. Maximum depression above the initial centre point of the slide mass (a) and maximum rundown (d) for a set of numerical simulations on a 15° slope. (b), (e) The maximum depression and maximum rundown scaled by the corresponding values from the WNL-EXT model. Time-series comparisons for $L_s/h_{c0} = 3.5$ showing the free-surface elevation above the centre point (c) and vertical shoreline movement (f) are given on the right. WNL-EXT results indicated by the solid line, WNL-DA by the dashed line and NL-SW by the dotted line.

A deep-water limit has been determined for the 'extended' model ($L_s/h_c > 3.5$), but it would also be interesting to know the limits of applicability of the depth-averaged (WNL-DA) and shallow-water (NL-SW) models. The only differences

between these three models (the weakly nonlinear ‘extended’, weakly nonlinear depth averaged and nonlinear shallow water) are found in the frequency-dispersion terms—the nonlinear terms are the same. The testing method to determine the deep-water limits of the various model types will be to fix both a slope of 15° and a slide mass, with $\Delta h/b = 0.05$ and $L_s/b = 1.85$, while incrementally increasing the initial water depth above the centre point of the slide, d . Figure 8 shows a summary of the comparisons of the three models. Figure 8*a, d* show the maximum free-surface depression measured above the initial centre point of the slide and the maximum rundown for various L_s/h_{c_0} combinations. WNL-EXT solutions are indicated by solid lines, WNL-DA by dashed lines and NL-SW by the dotted lines. Also shown in figure 8*b, e* are the maximum depression and rundown results from WNL-DA and NL-SW relative to the results from WNL-EXT, thereby more clearly depicting the differences between the models. These figures show WNL-EXT and WNL-DA agreeing nearly exactly, while the errors in NL-SW decrease with increasing L_s/h_{c_0} . The NL-SW results do not converge with the WNL-EXT results until $L_s/h_{c_0} \gtrsim 15$. Figure 8*c, f* are time-series of the free-surface elevation above the initial centre point of the slide and the vertical movement of the shoreline for the case of $L_s/h_{c_0} = 3.5$, respectively. Differences between NL-SW and WNL-EXT are clear, with NL-SW under-predicting the free surface above the slide, but over-predicting the rundown due to over shoaling in the non-dispersive model. The only significant difference between the WNL-EXT and WNL-DA results come after the maximum depression in figure 8*c*, where WNL-DA predicts an oscillatory train following the depression. These results indicate that to the deep-water limit that WNL-EXT was shown to be accurate, WNL-DA is accurate as well. As mentioned previously, altering the level on which z_α is evaluated in the ‘extended’ model does not increase the deep-water accuracy limit for slide-generated waves.

In summary, the nonlinear-dispersive terms are important for slides near the deep-water limit ($L_s/h_c = 3.5$) whose heights, or $\Delta h/d_0$ values, are large (greater than 0.4). For shallow-water slides ($L_s/h_c > 10$), the nonlinear-dispersive terms are not important near the source, even for the largest slides. The ‘extended’ formulation of the depth-integrated equations does not appear to offer any benefits over the depth-averaged formulation in regards to modelling the generation of waves in deeper water. The ‘extended’ model would be useful if one was interested in modelling the propagation of shallow-water slide-generated waves into deeper water, which is not the focus of this paper. The shallow-water-wave equations are only valid for slides in very shallow water, where $L_s/h_{c_0} \gtrsim 15$.

9. Conclusions

A model for the creation of fully nonlinear long waves by seafloor movement, and their propagation away from the source region, is presented. The general fully nonlinear model can be truncated, so as to only include weakly nonlinear effects, or model a non-dispersive wave system. Rarely will fully nonlinear effects be important above the landslide region, but the model has the advantage of allowing the slide-generated waves to become fully nonlinear in nature, without requiring a transition among governing equations.

A high-order finite-difference model is developed to numerically simulate wave generation by seafloor movement. The numerical generation of waves by both impulsive and creeping movements agrees with experimental data and other numerical models. A deep-water accuracy limit of the model, $L_s/h_c > 3.5$, is adopted. Within this limitation, the 'extended' formulation of the depth-integrated equations shows no benefit over the 'conventional' depth-averaged approach near the source region. Leading-order nonlinear effects were shown to be important for prediction of shoreline movement, and the fully nonlinear terms are important for only the thickest slides with relatively short length-scales. Although only one-horizontal-dimension problems are examined in this paper, slides in two horizontal dimensions have been analysed by the authors, but, due to paper length limitations, will be presented in a future publication. As a final remark, it is noted that prediction of landslide tsunamis in real cases is subject to the large uncertainty inherent in knowing the time-evolution of a landslide. Extensive field research of high-risk sites is paramount to reducing this uncertainty.

The research reported here is partly supported by grants from the National Science Foundation (CMS-9528013, CTS-9808542 and CMS 9908392) and a subcontract from the University of Puerto Rico. The authors thank Ms Yin-yu Chen for providing the numerical results based on her BIEM model.

Appendix A. Derivation of approximate two-dimensional governing equations

In deriving the two-dimensional depth-integrated governing equations, the frequency dispersion is assumed to be weak, i.e.

$$O(\mu^2) \ll 1. \quad (\text{A } 1)$$

We can expand the dimensionless physical variables as power series of μ^2 ,

$$f = \sum_{n=0}^{\infty} \mu^{2n} f_n \quad (f = \zeta, p, \mathbf{u}), \quad (\text{A } 2)$$

$$w = \sum_{n=1}^{\infty} \mu^{2n} w_n. \quad (\text{A } 3)$$

Furthermore, we will assume the flow is irrotational. Zero horizontal vorticity yields the following conditions:

$$\frac{\partial}{\partial z} \mathbf{u}_0 = 0, \quad (\text{A } 4)$$

$$\frac{\partial}{\partial z} \mathbf{u}_1 = \nabla w_1. \quad (\text{A } 5)$$

Consequently, from (A 4), the leading-order horizontal velocity components are independent of the vertical coordinate, i.e.

$$\mathbf{u}_0 = \mathbf{u}_0(x, y, t). \quad (\text{A } 6)$$

Substituting (A 2) and (A 3) into the continuity equation (2.3) and the boundary condition (2.7), we collect the leading-order terms as

$$\nabla \cdot \mathbf{u}_0 + w_{1z} = 0, \quad -h < z < \varepsilon\zeta, \quad (\text{A } 7)$$

$$w_1 + \mathbf{u}_0 \cdot \nabla h + \frac{h_t}{\varepsilon} = 0 \quad \text{on } z = -h. \quad (\text{A } 8)$$

Integrating (A 7) with respect to z and using (A 8) to determine the integration constant, we obtain the vertical profile of the vertical velocity components,

$$w_1 = -z\nabla \cdot \mathbf{u}_0 - \nabla \cdot (h\mathbf{u}_0) - \frac{h_t}{\varepsilon}. \quad (\text{A } 9)$$

Similarly, integrating (A 5) with respect to z , with information from (A 8), we can find the corresponding vertical profiles of the horizontal velocity components,

$$\mathbf{u}_1 = -\frac{1}{2}z^2\nabla(\nabla \cdot \mathbf{u}_0) - z\nabla \left[\nabla \cdot (h\mathbf{u}_0) + \frac{h_t}{\varepsilon} \right] + \mathbf{C}_1(x, y, t), \quad (\text{A } 10)$$

in which \mathbf{C}_1 is a unknown function to be determined. Up to $O(\mu^2)$, the horizontal velocity components can be expressed as

$$\begin{aligned} \mathbf{u} = & \mathbf{u}_0(x, y, t) \\ & + \mu^2 \left\{ -\frac{1}{2}z^2\nabla(\nabla \cdot \mathbf{u}_0) - z\nabla \left[\nabla \cdot (h\mathbf{u}_0) + \frac{h_t}{\varepsilon} \right] + \mathbf{C}_1(x, y, t) \right\} + O(\mu^4), \\ & -h < z < \varepsilon\zeta. \end{aligned} \quad (\text{A } 11)$$

Now, we can define the horizontal velocity vector, $\mathbf{u}_\alpha(x, y, z_\alpha(x, y, t), t)$, evaluated at $z = z_\alpha(x, y, t)$, as

$$\mathbf{u}_\alpha = \mathbf{u}_0 + \mu^2 \left\{ -\frac{1}{2}z_\alpha^2\nabla(\nabla \cdot \mathbf{u}_0) - z_\alpha\nabla \left[\nabla \cdot (h\mathbf{u}_0) + \frac{h_t}{\varepsilon} \right] + \mathbf{C}_1(x, y, t) \right\} + O(\mu^4). \quad (\text{A } 12)$$

Subtracting (A 12) from (A 11), we can express \mathbf{u} in terms of \mathbf{u}_α as

$$\mathbf{u} = \mathbf{u}_\alpha - \mu^2 \left\{ \frac{1}{2}z^2 - z_\alpha^2\nabla(\nabla \cdot \mathbf{u}_\alpha) + (z - z_\alpha)\nabla \left[\nabla \cdot (h\mathbf{u}_\alpha) + \frac{h_t}{\varepsilon} \right] \right\} + O(\mu^4). \quad (\text{A } 13)$$

Note that $\mathbf{u}_\alpha = \mathbf{u}_0 + O(\mu^2)$ has been used in (A 13).

The exact continuity equation (2.8) can be rewritten approximately in terms of ζ and \mathbf{u}_α . Substituting (A 13) into (2.8), we obtain

$$\begin{aligned} \frac{1}{\varepsilon}H_t + \nabla \cdot (H\mathbf{u}_\alpha) - \mu^2\nabla \cdot \left\{ H \left[\left(\frac{1}{6}(\varepsilon^2\zeta^2 - \varepsilon\zeta h + h^2) - \frac{1}{2}z_\alpha^2 \right) \nabla(\nabla \cdot \mathbf{u}_\alpha) \right. \right. \\ \left. \left. + \left(\frac{1}{2}(\varepsilon\zeta - h) - z_\alpha \right) \nabla \left(\nabla \cdot (h\mathbf{u}_\alpha) + \frac{h_t}{\varepsilon} \right) \right] \right\} = O(\mu^4), \end{aligned} \quad (\text{A } 14)$$

in which $H = h + \varepsilon\zeta$.

Equation (A 14) is one of three governing equations for ζ and \mathbf{u}_α . The other two equations come from the horizontal momentum equation (2.4). However, we must

find the pressure field first. This can be accomplished by approximating the vertical momentum equation (2.5) as

$$\varepsilon p_z = -1 - \mu^2(\varepsilon w_{1t} + \varepsilon^2 \mathbf{u}_0 \cdot \nabla w_1 + \varepsilon^2 w_1 w_{1z}) + O(\mu^4), \quad -h < z < \varepsilon \zeta. \quad (\text{A } 15)$$

We can integrate the above equation with respect to z to find the pressure field as

$$\begin{aligned} p = & \left(\zeta - \frac{z}{\varepsilon} \right) \\ & + \mu^2 \left\{ \frac{1}{2} (z^2 - \varepsilon^2 \zeta^2) \nabla \cdot \mathbf{u}_{0t} + (z - \varepsilon \zeta) \left[\nabla \cdot (h\mathbf{u})_{0t} + \frac{h_{tt}}{\varepsilon} \right] \right. \\ & + \frac{1}{2} \varepsilon (z^2 - \varepsilon^2 \zeta^2) \mathbf{u}_0 \cdot \nabla (\nabla \cdot \mathbf{u}_0) + \varepsilon (z - \varepsilon \zeta) \mathbf{u}_0 \cdot \nabla \left[\nabla \cdot (h\mathbf{u}_0) + \frac{h_t}{\varepsilon} \right] \\ & \left. + \frac{1}{2} \varepsilon (\varepsilon^2 \zeta^2 - z^2) (\nabla \cdot \mathbf{u}_0)^2 + \varepsilon (\varepsilon \zeta - z) \left[\nabla \cdot (h\mathbf{u}_0) + \frac{h_t}{\varepsilon} \right] \nabla \cdot \mathbf{u}_0 \right\} \\ & + O(\mu^4) \end{aligned} \quad (\text{A } 16)$$

for $-h < z < \varepsilon \zeta$. We remark here that (A 11) has been used in deriving (A 16). To obtain the governing equations for \mathbf{u}_α , we first substitute (A 13) and (A 16) into (2.4) and obtain the following equation, up to $O(\mu^2)$,

$$\begin{aligned} & \mathbf{u}_{\alpha t} + \varepsilon \mathbf{u}_\alpha \cdot \nabla \mathbf{u}_\alpha + \nabla \zeta \\ & + \mu^2 \left\{ \frac{1}{2} z_\alpha^2 \nabla (\nabla \cdot \mathbf{u}_{\alpha t}) + z_\alpha \nabla \left[\nabla \cdot (h\mathbf{u}_\alpha)_t + \frac{h_{tt}}{\varepsilon} \right] \right\} \\ & + \mu^2 z_{\alpha t} \left\{ z_\alpha \nabla (\nabla \cdot \mathbf{u}_\alpha) + \nabla \left[\nabla \cdot (h\mathbf{u}_\alpha) + \frac{h_t}{\varepsilon} \right] \right\} \\ & + \varepsilon \mu^2 \left\{ \left[\nabla \cdot (h\mathbf{u}_\alpha) + \frac{h_t}{\varepsilon} \right] \nabla \left[\nabla \cdot (h\mathbf{u}_\alpha) + \frac{h_t}{\varepsilon} \right] \right. \\ & \quad - \nabla \left[\zeta \left(\nabla \cdot (h\mathbf{u}_\alpha)_t + \frac{h_{tt}}{\varepsilon} \right) \right] + (\mathbf{u}_\alpha \cdot \nabla z_\alpha) \nabla \left[\nabla \cdot (h\mathbf{u}_\alpha) + \frac{h_t}{\varepsilon} \right] \\ & \quad + z_\alpha \nabla \left[\mathbf{u}_\alpha \cdot \nabla \left(\nabla \cdot (h\mathbf{u}_\alpha) + \frac{h_t}{\varepsilon} \right) \right] + z_\alpha (\mathbf{u}_\alpha \cdot \nabla z_\alpha) \nabla (\nabla \cdot \mathbf{u}_\alpha) \\ & \quad \left. + \frac{1}{2} z_\alpha^2 \nabla [\mathbf{u}_\alpha \cdot \nabla (\nabla \cdot \mathbf{u}_\alpha)] \right\} \\ & + \varepsilon^2 \mu^2 \nabla \left\{ -\frac{1}{2} \zeta^2 \nabla \cdot \mathbf{u}_{\alpha t} - \zeta \mathbf{u}_\alpha \cdot \nabla \left[\nabla \cdot (h\mathbf{u}_\alpha) + \frac{h_t}{\varepsilon} \right] \right. \\ & \quad \left. + \zeta \left[\nabla \cdot (h\mathbf{u}_\alpha) + \frac{h_t}{\varepsilon} \right] \nabla \cdot \mathbf{u}_\alpha \right\} \\ & + \varepsilon^3 \mu^2 \nabla \left\{ \frac{1}{2} \zeta^2 [(\nabla \cdot \mathbf{u}_\alpha)^2 - \mathbf{u}_\alpha \cdot \nabla (\nabla \cdot \mathbf{u}_\alpha)] \right\} = O(\mu^4). \end{aligned} \quad (\text{A } 17)$$

Equations (A 14) and (A 17) are the coupled governing equations, written in terms of \mathbf{u}_α and ζ , for fully nonlinear weakly dispersive waves generated by a submarine landslide.

Appendix B. Numerical scheme

To simplify the predictor-corrector equations, the velocity time derivatives in the momentum equations are grouped into the dimensional form,

$$U = u + \frac{1}{2}(z_\alpha^2 - \zeta^2)u_{xx} + (z_\alpha - \zeta)(hu)_{xx} - \zeta_x[\zeta u_x + (hu)_x], \quad (\text{B } 1)$$

$$V = v + \frac{1}{2}(z_\alpha^2 - \zeta^2)v_{yy} + (z_\alpha - \zeta)(hv)_{yy} - \zeta_y[\zeta v_y + (hv)_y], \quad (\text{B } 2)$$

where subscripts denote partial derivatives. Note that this grouping is different from that given in Wei *et al.* (1995). The grouping given above in (B 1) and (B 2) incorporates nonlinear terms, which is not done in Wei *et al.* These nonlinear time derivatives arise from the nonlinear-dispersion terms $\nabla[\zeta(\nabla \cdot (hu)_t + h_{tt}/\varepsilon)]$ and $\nabla(\frac{1}{2}\zeta^2\nabla \cdot \mathbf{u}_{\alpha t})$, which can be reformulated using the relation

$$\begin{aligned} & \nabla \left[\zeta \left(\nabla \cdot (hu)_t + \frac{h_{tt}}{\varepsilon} \right) \right] \\ &= \nabla \left[\zeta \left(\nabla \cdot (hu)_t + \frac{h_{tt}}{\varepsilon} \right) \right]_t - \nabla \left[\zeta_t \left(\nabla \cdot (hu)_t + \frac{h_{tt}}{\varepsilon} \right) \right] \nabla (\frac{1}{2}\zeta^2\nabla \cdot \mathbf{u}_{\alpha t}) \\ &= \nabla (\frac{1}{2}\zeta^2\nabla \cdot \mathbf{u}_{\alpha t})_t - \nabla (\zeta \zeta_t \nabla \cdot \mathbf{u}_{\alpha t}). \end{aligned}$$

The authors have found that this form is more stable and requires less iterations to converge for highly nonlinear problems, as compared to the Wei *et al.* formulation. The predictor equations are

$$\eta_{i,j}^{n+1} = \eta_{i,j}^n + \frac{1}{12}\Delta t(23E_{i,j}^n - 16E_{i,j}^{n-1} + 5E_{i,j}^{n-2}), \quad (\text{B } 3)$$

$$U_{i,j}^{n+1} = U_{i,j}^n + \frac{1}{12}\Delta t(23F_{i,j}^n - 16F_{i,j}^{n-1} + 5F_{i,j}^{n-2}) + 2(F_1)_{i,j}^n - 3(F_1)_{i,j}^{n-1} + (F_1)_{i,j}^{n-2}, \quad (\text{B } 4)$$

$$V_{i,j}^{n+1} = V_{i,j}^n + \frac{1}{12}\Delta t(23G_{i,j}^n - 16G_{i,j}^{n-1} + 5G_{i,j}^{n-2}) + 2(G_1)_{i,j}^n - 3(G_1)_{i,j}^{n-1} + (G_1)_{i,j}^{n-2}, \quad (\text{B } 5)$$

where

$$\begin{aligned} E &= -h_t - [(\zeta + h)u]_x - [(\zeta + h)v]_y \\ &\quad + \{(h + \zeta)[\frac{1}{6}(\zeta^2 - \zeta h + h^2) - \frac{1}{2}z_\alpha^2]S_x + (\frac{1}{2}(\zeta - h) - z_\alpha)T_x\}_x \\ &\quad + \{(h + \zeta)[\frac{1}{6}(\zeta^2 - \zeta h + h^2) - \frac{1}{2}z_\alpha^2]S_y + (\frac{1}{2}(\zeta - h) - z_\alpha)T_y\}_y, \quad (\text{B } 6) \end{aligned}$$

$$\begin{aligned} F &= -\frac{1}{2}[(u^2)_x + (v^2)_x] - g\zeta_x - z_\alpha h_{xtt} - z_{\alpha t}h_{xt} + (\zeta h_{tt})_x - [E(\zeta S + T)]_x \\ &\quad - [\frac{1}{2}(z_\alpha^2 - \zeta^2)(uS_x + vS_y)]_x - [(z_\alpha - \zeta)(uT_x + vT_y)]_x - \frac{1}{2}[(T + \zeta S)^2]_x, \quad (\text{B } 7) \end{aligned}$$

$$F_1 = \frac{1}{2}(\zeta^2 - z_\alpha^2)v_{xy} - (z_\alpha - \zeta)(hv)_{xy} + \zeta_x[\zeta v_y + (hv)_y], \quad (\text{B } 8)$$

$$\begin{aligned} G &= -\frac{1}{2}[(u^2)_y + (v^2)_y] - g\zeta_y - z_\alpha h_{ytt} - z_{\alpha t}h_{yt} + (\zeta h_{tt})_y - [E(\zeta S + T)]_y \\ &\quad - [\frac{1}{2}(z_\alpha^2 - \zeta^2)(uS_x + vS_y)]_y - [(z_\alpha - \zeta)(uT_x + vT_y)]_y - \frac{1}{2}[(T + \zeta S)^2]_y, \quad (\text{B } 9) \end{aligned}$$

$$G_1 = \frac{1}{2}(\zeta^2 - z_\alpha^2)u_{xy} - (z_\alpha - \zeta)(hu)_{xy} + \zeta_y[\zeta u_x + (hu)_x] \quad (\text{B } 10)$$

and

$$S = u_x + v_y, \quad T = (hu)_x + (hv)_y + h_t. \quad (\text{B } 11)$$

All terms are evaluated at the local grid point (i, j) , and n represents the current time-step, when values of ζ , u and v are known. The above expressions (B 6)–(B 11) are for the fully nonlinear problem; if a weakly nonlinear or non-dispersive system is to be examined, the equations should be truncated accordingly. The fourth-order implicit corrector expressions for the free-surface elevation and horizontal velocities are

$$\eta_{i,j}^{n+1} = \eta_{i,j}^n + \frac{1}{24}\Delta t(9E_{i,j}^{n+1} + 19E_{i,j}^n - 5E_{i,j}^{n-1} + E_{i,j}^{n-2}), \quad (\text{B } 12)$$

$$U_{i,j}^{n+1} = U_{i,j}^n + \frac{1}{24}\Delta t(9F_{i,j}^{n+1} + 19F_{i,j}^n - 5F_{i,j}^{n-1} + F_{i,j}^{n-2}) + (F_1)_{i,j}^{n+1} - (F_1)_{i,j}^n, \quad (\text{B } 13)$$

$$V_{i,j}^{n+1} = V_{i,j}^n + \frac{1}{24}\Delta t(9G_{i,j}^{n+1} + 19G_{i,j}^n - 5G_{i,j}^{n-1} + G_{i,j}^{n-2}) + (G_1)_{i,j}^{n+1} - (G_1)_{i,j}^n. \quad (\text{B } 14)$$

The system is solved by first evaluating the predictor equations, then u and v are solved via (B 1) and (B 2), respectively. Both (B 1) and (B 2) yield a diagonal matrix after finite differencing. The matrices are diagonal, with a bandwidth of five (due to five-point finite differencing), and an efficient LU decomposition can be used. At this point in the numerical system, we have predictors for ζ , u and v . Next, the corrector expressions are evaluated, and again u and v are determined from (B 1) and (B 2). The relative errors in each of the physical variables is found, in order to determine if the implicit correctors need to be reiterated. This relative error is given as

$$\frac{w^{n+1} - w_*^{n+1}}{w^{n+1}}, \quad (\text{B } 15)$$

where w represents ζ , u and v , and w_* is the previous iterations value. The correctors are recalculated until all errors are less than 10^{-4} . Note that, inevitably, there will be locations in the numerical domain where values of the physical variables are close to zero, and applying the above error calculation to these points may lead to unnecessary iterations in the corrector loop. Thus it is required that

$$\left| \frac{\zeta}{a} \right|, \left| \frac{u, v}{\epsilon\sqrt{gh}} \right| > 10^{-4}$$

for the corresponding error calculation to proceed, where a is determined from equation (3.4) for a creeping slide. For the model equations, linear stability analysis gives that $\Delta t < \Delta x/2c$, where c is the wave celerity in the deepest water. Note that when modelling highly nonlinear waves, a smaller Δt is usually required for stability. In this analysis, $\Delta t = \Delta x/4c$ produced stable and convergent results for all trials.

For the numerical exterior boundaries, two types of conditions are applied: reflective and radiation. The reflective, or no-flux, boundary condition for the Boussinesq equations has been examined by previous researchers (Wei & Kirby 1995), and their methodology is followed here. For the radiation, or open, boundary condition, a sponge layer is used. The sponge layer is applied in the manner recommended by Kirby *et al.* (1998). Run-up and rundown are modelled with the ‘extrapolation’ moving-boundary algorithm described in Lynett *et al.* (2002).

Nomenclature

a	wave amplitude
b	length along the slope between x_l and x_r for the tanh slide
c	wave celerity
d	depth of water above the centre point of the slide, function of time
d_0	initial depth of water above the centre point of the slide, i.e. at $t = 0$
g	gravity
h_0	characteristic water depth or baseline water depth, function of space
h	water depth profile, function of space and time
\bar{h}	the changing part of the water depth profile $((h - h_0)/\delta)$
h_c	baseline water depth at the centre point of the slide $(\Delta h + d)$
h_{c0}	initial baseline water depth at the centre point of the slide $(\Delta h + d_0)$
H	total water depth $(h + \varepsilon\zeta)$
l_0	characteristic horizontal length-scale of the submarine slide
L_s	characteristic horizontal side length of the submarine slide
p	depth-dependent pressure
S	shape factor for tanh slide
t	time
t_c	time-scale of seafloor motion
t_w	typical period of wave generated by a specified seafloor motion
u, v, w	depth-dependent components of velocity in x, y, z
u_α, v_α	magnitude of horizontal velocity components u, v evaluated on z_α
\bar{u}, \bar{v}	depth-averaged horizontal velocity components
\mathbf{u}	horizontal velocity vector, (u, v)
x_c, y_c	horizontal coordinates of the midpoint of the seafloor movement
x_l, x_r	locations of the left and right inflection points for the tanh slide profile
z_α	arbitrary level on which the 'extended' equations are derived
δ	scaled characteristic change in water depth due to seafloor motion $(\Delta h/h_0)$
Δh	characteristic, or maximum, change in water depth due to seafloor motion
Δt	time-step in numerical model
$\Delta x, \Delta y$	space steps in numerical model
ε	nonlinearity parameter (a/h_0)
∇	horizontal gradient vector
ρ	density of water
θ	slope angle
μ	frequency-dispersion parameter (h_0/l_0)
ζ	free-surface displacement

References

- Chen, Y. & Liu, P. L.-F. 1995 Modified Boussinesq equations and associated parabolic model for water wave propagation. *J. Fluid Mech.* **228**, 351–381.
- Cox, D. C. & Morgan, J. 1977 Local tsunamis and possible local tsunamis in Hawaii. Report no. HIG 77-14, Hawaii Institute of Geophysics, University of Hawaii.
- Forbes, L. K. & Schwartz, L. W. 1982 Free-surface flow over a semicircular obstruction. *J. Fluid Mech.* **114**, 299–314.
- Geist, E. L. 1998 Local tsunami and earthquake source parameters. *Adv. Geophys.* **39**, 117–209.
- Gobbi, M., Kirby, J. T. & Wei, G. 2000 A fully nonlinear Boussinesq model for surface waves. Part 2. Extension to $O(kh^4)$. *J. Fluid Mech.* **405**, 181–210.
- Grilli, S. T. 1993 Modeling of nonlinear wave motion in shallow water. In *Computational methods for free and moving boundary problems in heat and fluid flows* (ed. I. C. Wrobel & C. A. Brebbia), ch. 3, pp. 37–65. Elsevier.
- Grilli, S. T. & Watts, P. 1999 Modeling of waves generated by a moving submerged body. Applications to underwater landslides. *Engng Analysis Bound. Elem.* **23**, 645–656.
- Grilli, S. T., Skourup, J. & Svendsen, I. A. 1989 An efficient boundary element method for nonlinear waves. *Engng Analysis Bound. Elem.* **6**, 97–107.
- Grilli, S. T., Subramanya, R., Svendsen, I. A. & Veeramony, J. 1995 Shoaling of solitary waves on plane beaches. *J. Watway Port Coastal Ocean Engng* **120**, 74–92.
- Hammack, H. L. 1973 A note on tsunamis: their generation and propagation in an ocean of uniform depth. *J. Fluid Mech.* **60**, 769–799.
- Harbitz, C. B., Pedersen, G. & Gjevik, B. 1993 Numerical simulation of large water waves due to landslides. *J. Hydraul. Engng* **119**, 1325–1342.
- Jiang, L. & LeBlond, P. H. 1992 The coupling of a submarine slide and the surface waves which it generates. *J. Geophys. Res.* **97**, 12731–12744.
- Keating, B. H. & McGuire, W. J. 2002 Island edifice failures and associated hazards. In *Pure and applied geophysics, special issue: landslide and tsunamis*. (In the press.)
- Kirby, J. T., Wei, G., Chen, Q., Kennedy, A. B. & Dalrymple, R. A. 1998 *FUNWAVE 1.0: fully nonlinear Boussinesq wave model documentation and user's manual*. Newark, DE: University of Delaware.
- Lee, S.-J., Yates, G. T. & Wu, T. Y. 1989 Experiments and analyses of upstream-advancing solitary waves generated by moving disturbances. *J. Fluid Mech.* **199**, 569–593.
- Liu, P. L.-F. 1994 Model equations for wave propagations from deep to shallow water. In *Advances in coastal and ocean engineering* (ed. P. L.-F. Liu), vol. 1, pp. 125–158. World Scientific.
- Liu, P. L.-F. & Earickson, J. 1983 A numerical model for tsunami generation and propagation. In *Tsunamis: their science and engineering* (ed. J. Iida & T. Iwasaki), pp. 227–240. Harpenden: Terra Science.
- Liu, P. L.-F., Hsu, H.-W. & Lean, M. H. 1992 Applications of boundary integral equation methods for two-dimensional non-linear water wave problems. *Int. J. Numer. Meth. Fluids* **15**, 1119–1141.
- Lynett, P., Wu, T.-W. & Liu, P. L.-F. 2002 Modeling wave runup with depth-integrated equations. *Coastal Engng* **46**, 89–107.
- Madsen, P. A. & Schäffer, H. A. 1998 Higher-order Boussinesq-type equations for surface gravity waves: derivation and analysis. *Phil. Trans. R. Soc. Lond. A* **356**, 2123–3184.
- Madsen, P. A. & Sorensen, O. R. 1992 A new form of the Boussinesq equations with improved linear dispersion characteristics. Part II. A slowly varying bathymetry. *Coastal Engng* **18**, 183–204.
- Moore, G. & Moore, J. G. 1984 Deposit from giant wave on the island of Lanai. *Science* **222**, 1312–1315.

- Nwogu, O. 1993 Alternative form of Boussinesq equations for nearshore wave propagation. *J. Wtrwy Port Coastal Ocean Engng* **119**, 618–638.
- Peregrine, D. H. 1967 Long waves on a beach. *J. Fluid Mech.* **27**, 815–827
- Press, W. H., Flannery, B. P. & Teukolsky, S. A. 1989 *Numerical recipes: the art of scientific computing*, pp. 569–572. Cambridge University Press.
- Raney, D. C. & Butler, H. L. 1976 Landslide generated water wave model. *J. Hydraul. Div.* **102**, 1269–1282.
- Tappin, D. R. (and 18 others) 1999 Sediment slump likely caused 1998 Papua New Guinea tsunami. *Eos* **80**, 329.
- Tappin, D. R., Watts, P., McMurtry, G. M., Lafoy, Y. & Matsumoto, T. 2001 The Sissano, Papua New Guinea tsunami of July 1998—offshore evidence on the source mechanism. *Mar. Geol.* **175**, 1–23.
- von Huene, R., Bourgois, J., Miller, J. & Pautot, G. 1989 A large tsunamigenic landslide and debris flow along the Peru trench. *J. Geophys. Res.* **94**, 1703–1714.
- Watts, P. 1997 Water waves generated by underwater landslides. PhD thesis, California Institute of Technology.
- Wei, G. & Kirby, J. T. 1995 A time-dependent numerical code for extended Boussinesq equations. *J. Wtrwy Port Coastal Ocean Engng* **120**, 251–261.
- Wei, G., Kirby, J. T., Grilli, S. T. & Subramanya, R. 1995 A fully nonlinear Boussinesq model for surface waves. Part 1. Highly nonlinear unsteady waves. *J. Fluid Mech.* **294**, 71–92.
- Yeh, H., Liu, P. L.-F. & Synolakis, C. (eds) 1996 Long-wave runup models. In *Proc. 2nd Int. Workshop on Long-wave Runup Models*. World Scientific.

As this paper exceeds the maximum length normally permitted,
the authors have agreed to contribute to production costs.

A numerical study of the run-up generated by three-dimensional landslides

Patrick Lynett

Department of Civil Engineering, Texas A&M University, College Station, Texas, USA

Philip L.-F. Liu

School of Civil and Environmental Engineering, Cornell University, Ithaca, New York, USA

Received 18 March 2004; revised 20 October 2004; accepted 19 January 2005; published 8 March 2005.

[1] A large set of numerical experiments are designed to examine the maximum run-up generated by three-dimensional (3-D) submerged and subaerial, solid body landslides. A depth-integrated numerical model is utilized, allowing for the efficient simulation of landslides in shallow and intermediate water. Six dimensionless parameters are introduced: the slide thickness, the slide wave number, a slide shape parameter, the horizontal aspect ratio of the slide, the specific gravity of the slide mass, and the slope of the beach. Six sets of simulations are first presented, wherein one of the six dimensionless parameters are singularly varied. This allows for the identification of parameter dependence on maximum run-up. After combining the dependencies a number of relationships appear. Most notably, a very clear division between the near and far field is observed, where here the far field is defined as the region displaced from the projection of the landslide, on the nearby beach, where edge waves may dominate the wave pattern. For submerged slides a nondimensional estimation of the maximum run-up just landward of the slide is found as well as the location and magnitude of the secondary run-up peak. This secondary peak is due to the propagation of edge waves and is in some cases larger than the peak immediately landward of the slide. The results presented in this paper may be useful for preliminary hazard assessment, where a simple and quick estimation of the maximum run-up height and locations are required. Additionally, the formulas developed will be particularly beneficial to those developing 3-D landslide experiments.

Citation: Lynett, P., and P. L.-F. Liu (2005), A numerical study of the run-up generated by three-dimensional landslides, *J. Geophys. Res.*, 110, C03006, doi:10.1029/2004JC002443.

1. Introduction

[2] Interest in landslide generated tsunamis has risen in the last decade, due in large part to the devastating slump-induced tsunamis of Papua New Guinea (PNG) in 1998 [e.g., Synolakis et al., 2002]. Additionally, in parts of the United States, mainly on the west coast, significant efforts have been recently undertaken to assess landslide tsunami hazards. Landslide tsunamis tend to be local, although possibly extreme, in their effects. Recorded on-land water elevations for the PNG tsunami exceed 10 m, but this large wave height was restricted to a shoreline length of roughly 15 km.

[3] Landslide tsunamis require a different characterization than earthquake tsunamis due to the fact that the length scale of a landslide, and the resulting tsunami, is typically much less than that of an earthquake. The physical implication of this fact is that, although described by the long wave descriptor tsunami, landslide tsunamis are not necessarily best characterized as long waves. Recent numerical

work has shown that for typical submarine landslide setups, frequency dispersion can play an important role in determining both the offshore wave field and the shoreline movement [e.g., Lynett and Liu, 2002; Lynett et al., 2003].

[4] To date, very few studies of landslide generated tsunamis include two horizontal dimension (2HD) effects. Numerically, although there are numerous 2HD landslide model presentations [e.g., Jiang and LeBlond, 1994; Grilli et al., 2002] there is little in the way of model application for tsunami characterization. One such recent effort to look at 2HD slide tsunamis is that of Okal and Synolakis [2004], who used run-up distributions to infer characteristics of the source. The work to be presented here is similar in nature, although the focus is on a more complete landslide model, while the work of Okal and Synolakis [2004] also consider dislocation sources.

[5] 2HD landslide tsunami studies are particularly daunting, because of difficulty in minimizing reflection off three tank walls, such that uncontaminated run-up measurements can be obtained. Despite this hurdle, recent experiments [Synolakis and Raichlen, 2002] have been performed with a tank width of four slide widths. This type of experiment

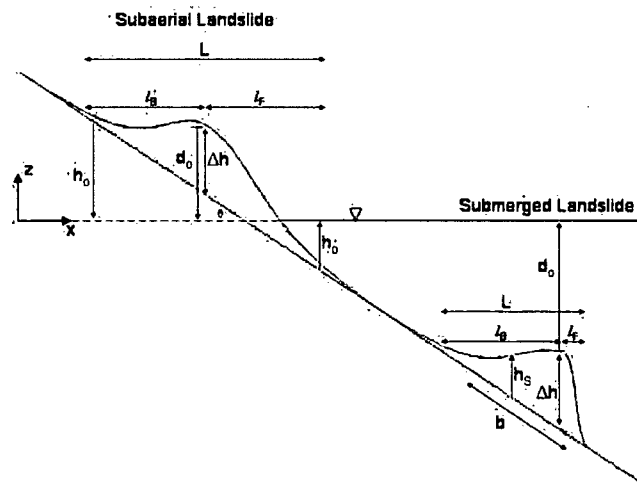


Figure 1. Definitions for a (left) subaerial and (right) submerged sliding mass. Note that the subaerial slide is symmetric in the horizontal plane ($\kappa = l_F/l_B = 1$), while the submerged slide is not ($\kappa \approx 0.15$).

allows for detailed physical study of the leading tsunami waves, but wall reflections quickly contaminate secondary behavior. Without examination of the secondary behavior, it becomes possible to miss one of the important phenomena controlling landslide tsunami run-up: edge waves.

[6] Edge waves have been studied by coastal engineers and scientists for many decades, largely motivated by Ursell's [1952] analytical solution for edge waves on a constant slope. Edge waves, while rarely observed directly in typical coastal environments [Schaffer and Jonsson, 1992], can be easily discriminated for transient disturbances, such as tsunamis [Gonzalez *et al.*, 1995]. It seems reasonable to expect that submerged landslide tsunamis, and especially subaerial landslide tsunamis, with their fair amount of oblique wave energy, would generate shore-trapped, edge wave modes. In fact, this expectation has already been observed in experimental testing [e.g., Liu *et al.*, 1994; Chang, 1995] and numerical simulation of landslide tsunamis [e.g., Tinti *et al.*, 1999].

[7] This paper is organized as follows. First, a description of the theoretical model to be used is presented, followed by the method of numerical simulation. Next, the landslide geometry and motion profiles are given. It is in this section that the nondimensional parameters governing the physical slide characteristics are developed. After the setup description, results from the numerical simulations are examined. For each of the six nondimensional parameters, a subset of simulations is run, varying that parameter while holding the other five constant. Finally, all of the scaling laws extracted

from the six subsets of simulations are combined, yielding global scalings.

2. Model Equations

[8] The model to be applied here is the 2HD, depth-integrated, multilayer model. The multilayer concept represents a different approach to developing a depth-integrated model with high-order dispersive properties. The multilayer derivation consists of a piecewise integration of the primitive equations of motion through N constant-density layers of arbitrary thickness. Within each layer, an independent velocity profile is determined. With N separate velocity profiles, matched at the interfaces of the layers, the resulting set of equations have $N + 1$ free parameters, allowing for an optimization with known analytical properties of water waves. The optimized two-layer model equations, which are used in the study presented here, show good linear wave characteristics up to $kh \approx 8$, while the second-order nonlinear behavior is well captured to $kh \approx 6$. Details of the multilayer approach can be found in the work of Lynett [2002] (see <http://ceprofs.tamu.edu/plynett/publications/publications.htm>) and Lynett and Liu [2004a, 2004b], while applications can be found in the work of Basterretxea *et al.* [2004] and Ryu *et al.* [2003]. The layer interface and the characteristic velocity elevations are specified as functions of the water depth, and thus these elevations change in time with the moving seafloor. On initially dry land, all of the layer elevations converge on $z = -h$ and are not allowed to exist below the beach. Thus on initially dry land, the two-

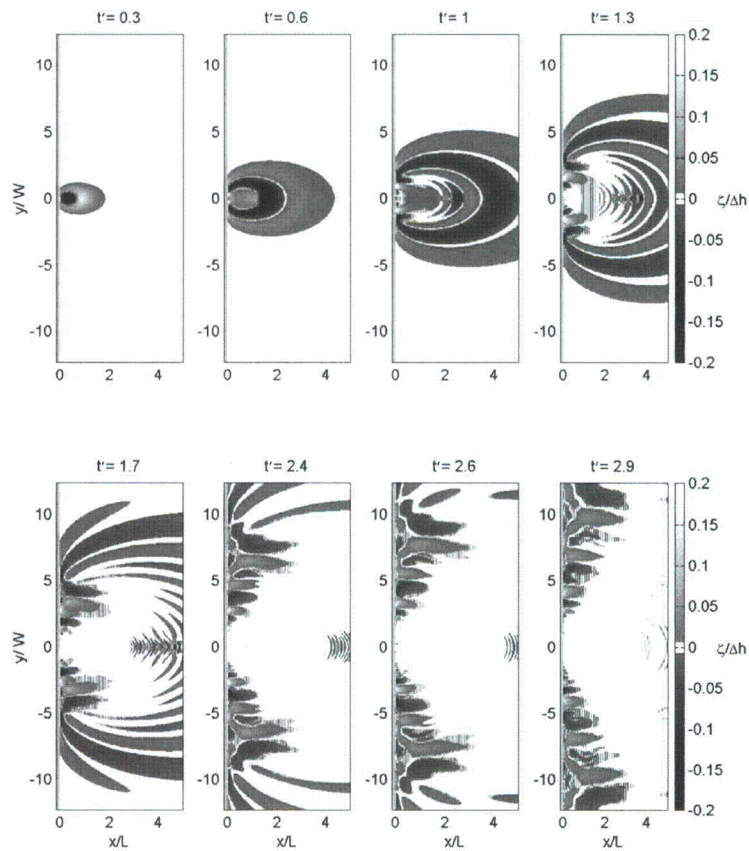


Figure 2. Spatial snapshots of the free surface.

layer model reduces to the one-layer model with the velocity evaluation level at the seabed.

[9] The simplest of the multilayer models is the one-layer model, which is equivalent to the model of Liu [1994] and the fully nonlinear extension of Nwogu's [1993] model presented by Wei *et al.* [1995]. An analysis of the one-layer model's ability to predict the waves created by submarine landslides was done by Lynett and Liu [2002]. All of the accuracy restrictions given in that paper, in the form of minimum initial slide length scale to depth of submergence ratios, were closely followed in this study.

[10] As the one-layer accuracy restrictions are enforced in all the simulations performed, the obvious question of "why use the two-layer model" arises. The answer is that the two-

layer model is required to overcome the practical and numerical challenges of these simulations. The primary difference between the one- and two-layer model is that the two-layer model is accurate into much deeper water, in both the linear and nonlinear sense. It was found from numerical testing that if the landslide was stopped, slowed, allowed to exit the numerical domain, or travel onto a milder slope, waves would be generated by this change. These waves would affect the run-up patterns, essentially contaminating the results with a small, but unknown error. Thus for the desired outcome of run-up generated by a slide traveling down a slope, the slope and the slide motion needed to be continuous and uninterrupted for the entire duration of each numerical simulation. While this objective may seem trivial or obvious from a numerical setup point of

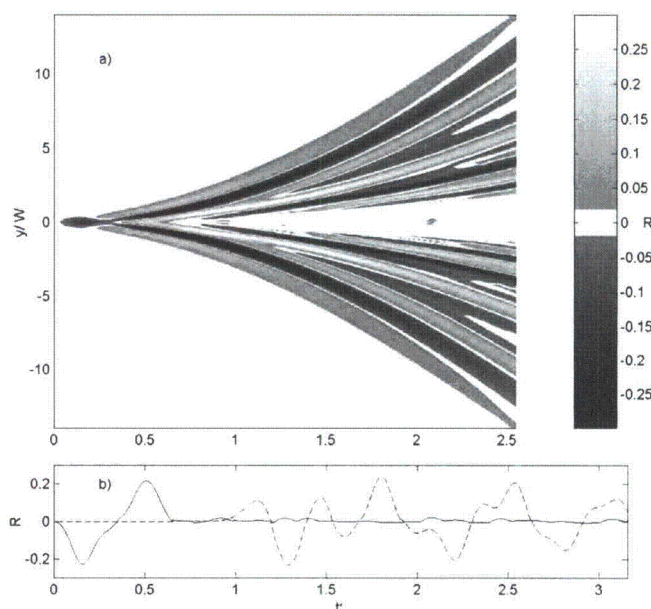


Figure 3. (a) Shoreline elevation as a function of time and transverse coordinate. (b) Run-up time series at $y/W = 0$ (solid line) and $y/W = 3$ (dashed line).

view, it is in fact not. The one-layer (Boussinesq) model, applied to deep water, tends to become unstable, predicting very large, rapidly (and unphysically) propagating short waves. These short waves will typically lead to numerical instability. When attempting to simulate a slide mass traveling down a long slope into deep water, large deep water (short) waves often are generated, and simulations crashed. The solution to this problem was use of the two-layer model. The two-layer model has accuracy into much deeper water than the one-layer, and proved to be stable, without production of unrealistic, large short waves. Therefore while the two-layer model is not strictly required for accuracy in the run-up region for any of the simulations presented here, it is required for accuracy/stability in the deep water region, without which the simulations will not successfully complete.

3. Numerical Model

[11] The finite difference algorithm presented by *Lynett and Liu* [2002, 2004a] is used to solve the model equations. A high-order predictor-corrector scheme is utilized, employing a third order in time explicit Adams-Bashforth predictor step, and a fourth order in time Adams-Moulton implicit corrector step [Press *et al.*, 1989]. Spatial derivatives are differenced to fourth-order accuracy, yielding a model

which is numerically accurate to $(\Delta x)^4$, $(\Delta y)^4$ in space and $(\Delta t)^4$ in time.

[12] Run-up and run-down of the waves generated by the landslide disturbance will be examined. The moving boundary scheme employed here is the technique developed by *Lynett et al.* [2002]. Founded around the restrictions of the high-order numerical wave propagation model, the moving boundary scheme utilizes linear extrapolation of free surface and velocity through the shoreline, into the dry region. This approach allows for the five-point finite difference formulas to be applied at all points, even those neighboring dry points, and thus eliminates the need of conditional statements.

4. Landslide Description

4.1. Slide Motion

[13] All of the simulations undertaken for this study use a solid slide mass traveling down an infinite slope. When fully submerged, the slide motion is described by the formulation given by *Watts* [1997]. This formulation requires the specification of a number of coefficients, and those used in this paper are identical to the set employed by *Grilli and Watts* [1999].

[14] Many of the simulations performed, however, are for initially subaerial slides. The expression for slide velocity must be altered to include the aerial acceleration. The

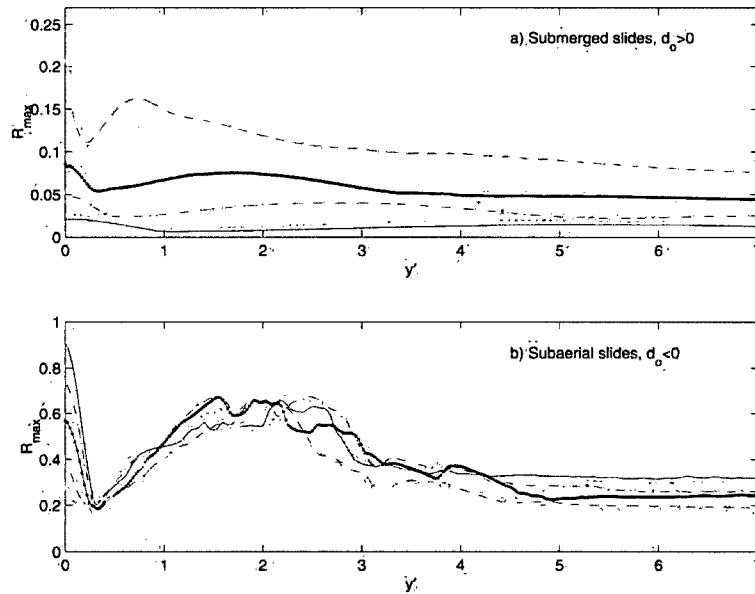


Figure 4. Maximum shoreline elevation at a function of distance from slide centerline for slides with variable c values. The different line types correspond to different c values: [0.125, -0.125] (solid line); [0.15, -0.15] (dotted line); [0.25, -0.25] (dash-dotted line); [0.4, -0.4] (dark bold line); [0.75, -0.75] (dashed line); and [1.0, -1.0] (light bold line). See color version of this figure in the HTML.

approach taken here is to formulate the slide velocity as a weighted average of the aerial and submerged velocity, where the weighting is based on the fraction of the landslide submerged. Thus the slope-parallel velocity of the slide is given by

$$f_s u_s + f_a g t \sin \theta, \quad (1)$$

where g is gravity, t is the time, and θ is the slope angle. The coefficients f_s and f_a represent the volume fractions of the landslide submerged and aerial, respectively, and of course must fall between 0 and 1, summing to 1. The time-dependent velocity of a submerged landslide, u_s , is calculated as by *Grilli et al.* [2002]:

$$u_s = u_t \tanh\left(\frac{t}{t_0}\right), \quad (2)$$

where

$$u_t = \sqrt{gb \frac{\pi(\gamma - 1)}{2C_d} \sin \theta}, \quad (3)$$

$$t_0 = u_t \frac{\gamma + C_m}{g(\gamma - 1) \sin \theta}, \quad (4)$$

$C_d = C_m = 1$ are the drag and added mass coefficients, respectively, γ is the specific gravity of the slide material, and b is the slope-parallel slide length.

4.2. Landslide Geometry

[15] The graphical definitions of the variables described in this section are shown in Figure 1. The spatial profile of the time-variable seafloor can be given in the general form

$$h(x, y, t) = h_b(x) - h_S(x, t)G(y), \quad (5)$$

where h_b is the planar “baseline” profile with slope angle θ , h_S is the shore-normal profile of the sliding mass, and G is a specified transverse (shore-parallel) profile. The shore-normal profile is similar to that proposed by *Lynett and Liu* [2002]:

$$h_S(x, t) = \Delta h \frac{\left[1 + \tanh\left(\frac{x - x(t)}{S}\right)\right] \left[1 - \tanh\left(\frac{x - x(t)}{S}\right)\right]}{\left[1 + \tanh\left(\frac{h \cos \theta}{2S}\right)\right] \left[1 - \tanh\left(-\frac{h \cos \theta}{2S}\right)\right]}, \quad (6)$$

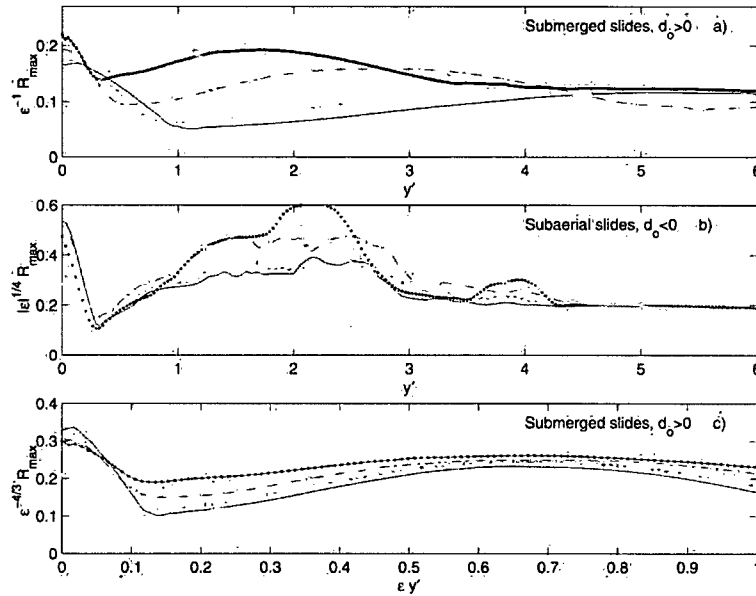


Figure 5. Various trends of the maximum run-up for slides with variable c values. Figure setup is the same as in Figure 4. See color version of this figure in the HTML.

where Δh is the maximum vertical height of the slide, x_l is the location of the tanh inflection point of the left side of the slide, x_r is the location of the inflection point on the right side, b is the constant in time, slope-parallel distance between the inflection points, and S_l, S_r are shape factors controlling the steepness of the left and right slide sides. The right and left boundaries, and steepness factors are given by

$$x_l(t) = x_c(t) - \frac{b}{2} \cos \theta, \quad x_r(t) = x_c(t) + \frac{b}{2} \cos \theta, \quad (7)$$

where x_c is the horizontal location of the center point of the slide, determined using (1). Shown in Figure 1 are typical slide shapes created by the above formulation. It is remarked that the slightly awkward form of (6) is employed so that the effects of slide asymmetry, which can be altered through S_l and S_r , can be examined.

[16] For the transverse profile, a Gaussian is employed:

$$G(y) = \exp \left[-\frac{(y - y_0)^2}{0.23W^2} \right], \quad (8)$$

where y_0 is the centerline coordinate of the slide, W is the width of the slide, defined as the distance between locations where the vertical slide thickness is 1% of the maximum thickness. For the simulations to be presented in the following sections, there are eight parameters to be varied.

(1) Parameter Δh is the maximum vertical thickness of the slide. (2) Parameter d_0 is the vertical distance from the center point of the slide to $z = 0$ at time $t = 0$; positive for the submerged slides and negative for the subaerial slides presented here. (3) Parameters l_F, l_B are the horizontal length of the front slide side (forward facing) and the back slide side, respectively, in the shore-normal direction; defined as the distance from the location of maximum vertical slide thickness, Δh , to the location where vertical slide thickness is $0.01\Delta h$. These lengths are varied through changing S_l and S_r . (4) Parameter $L = l_F + l_B$ are the total horizontal length of the slide in the shore-normal direction. Additionally, we define a wave number for the slide, k_S , such that $k_S = 2\pi/L$. (5) Parameter W is the horizontal width of the slide in the shore-parallel direction. Defined as the distance between locations where the vertical slide thickness is $0.01\Delta h$. (6) Parameter ρ_S is the density of the landslide material. (7) Parameter θ is the slope angle of the "baseline" depth profile. Within this dimensional set, six characteristic dimensionless parameters are defined. (1) Parameter $c = \Delta h/d_0$ is the dimensionless slide thickness. This parameter is related to the dimensionless amplitude of the generated wave, and thus is an indicator of the importance of shallow water nonlinearity. (2) Parameter $\kappa = l_F/l_B$ is the ratio of the front and back slide lengths. Within this value is a measure of the shape, or symmetry of the slide mass, where a value of 1 represents a symmetric slide in the horizontal plane.

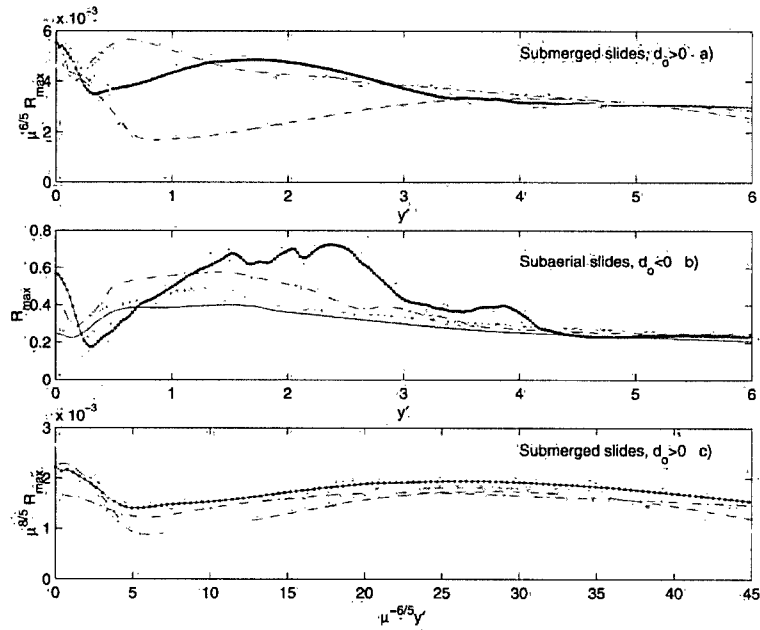


Figure 6. Scaled maximum shoreline elevation at a function of distance from slide centerline for slides with variable μ values. The different line types correspond to different μ values: [0.01] (solid line); [0.025] (dotted line); [0.05] (dash-dotted line); [0.10] (dark bold line); [0.20] (dashed line); and [0.25] (light bold line). Note that each subplot does not contain all line types. See color version of this figure in the HTML.

(3) Parameter $\mu = k_S \Delta h$ is a measure of the steepness of the slide. Constructed as such to carry a relevance to the steepness of a water wave, ka , (4) Parameter $A = L/W$ is the aspect ratio of the slide. (5) Parameter $\gamma = \rho_S / \rho_{\text{water}}$ is the specific gravity of the landslide material. (6) Parameter $S = \tan \theta$ is the slope of planar beach. Each of these dimensionless parameters will first be varied independently, and the individual effects of each on the 2HD run-up profile will be discussed. The accuracy restrictions given by *Lynett and Liu* [2002] can be expressed in terms of the above parameters, and require

$$\mu \left(\max \left[\kappa, \frac{1}{\kappa} \right] + 1 \right) \left(\frac{1}{\epsilon} + 1 \right) \leq \frac{4\pi}{7}. \quad (9)$$

Additionally, slides with large c (relatively small d_o) are not simulated. These are submerged slides that are initially nearly penetrating the still water surface, and numerical simulations indicated that turbulent effects were likely very important. Note that for this analysis, all of the slides denoted "subaerial" are characterized by $d_o < 0$, while all "submerged" slides have $d_o > 0$. The large c slides represent

a transitional class of slides between the submerged and subaerial slides simulated in this paper.

5. Two Horizontal Dimension Run-Up Created by Submerged and Subaerial Landslides

[17] Before analyzing the individual effects of the dimensionless parameters through groups of simulations, a single simulation is examined with

$$\epsilon = 0.4, \quad \kappa = 1.0, \quad \mu = 0.01, \quad A = 1.0, \quad \gamma = 2.0, \quad S = 1/10.$$

The above ϵ indicates that nonlinear effects are likely important, μ tells that this slide is thin (or long), and the slope is relatively steep, although still in the validity range of the depth-integrated model used here. This simulation, as well as all to be discussed, employed a spatial domain that was large enough such that reflections off the side walls do not affect any of the results presented. Eight spatial snapshots of the free surface elevation, ζ , are plotted in Figure 2. As the slide motion initiates, at $t\sqrt{gd_o}/L = t' = 0.3$,

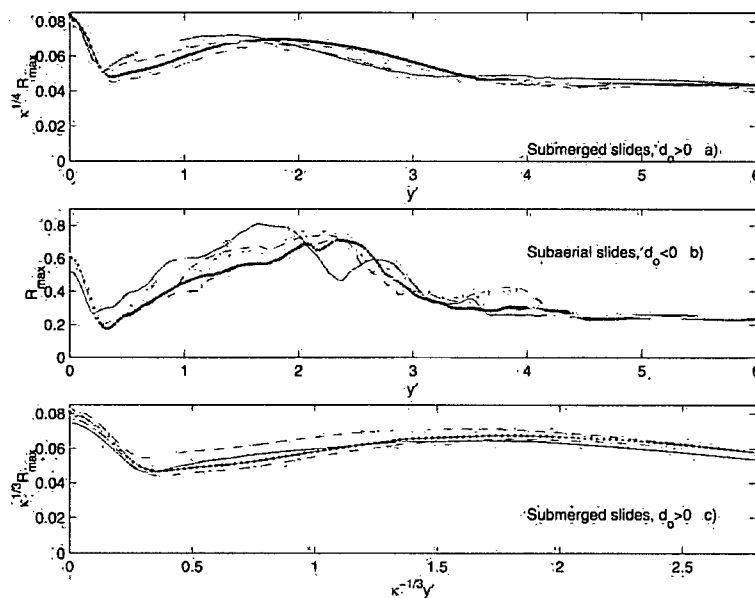


Figure 7. Scaled maximum shoreline elevation at a function of distance from slide centerline for slides with variable κ values. The different line types correspond to different κ values: [1.7] (solid line); [1.2] (dotted line); [1.1] (dash-dotted line); [0.90] (dark bold line); [0.83] (dashed line); and [0.73] (light bold line). See color version of this figure in the HTML.

an elevation wave is generated and traveling offshore, while the depression wave created by the landward slide face is already interacting with the shoreline. As the slide continues into deeper water, the offshore directed waves develop into an oscillatory train, trailed by short waves resembling a "V." By $t' = 1.0$, edge waves begin to dominate the wave field near the shoreline. These trapped waves exhibit their characteristic dispersive behavior, as the longer waves travel away from $y = 0$ quickly, leaving a dispersive tail of shorter waves behind. It is clear from this simulation that 2HD effects can be extremely important to the accurate prediction of landslide generated shoreline movement.

[18] The complete picture of shoreline motion for this simulation is shown in Figure 3. This figure gives the shoreline elevation as a function of time for all y' shoreline locations. At the earliest times, $t' < 0.2$, the only section of shoreline experiencing water motion is that directly landward of the slide due to the back face-generated depression wave. The front face elevation wave quickly wraps around the depression such that immediately outside of the slide centerline (i.e., $y' > 0.5$), shoreline motion is characterized by a leading elevation wave. Progressing further in time, the edge waves lead to numerous significant oscillations of the

shoreline, for example there are a series of large run-up maxima near $y' = 3$, with the third being the largest (run-up time series are also shown in Figure 3). This is in interesting contrast to the location where one might expect the motion to be most extreme; at $y' = 0$ there is only a single elevation peak, with a magnitude less than that for $1 < y' < 5$. Again, 2HD effects, in particular edge wave formation, drive maximum run-up patterns.

[19] The occurrence of trapped energy in edge waves will lead to a division of the near and far fields. Here, the far field is defined as the region displaced from the projection of the landslide, on the nearby beach, where edge waves become important. The near field is the region where the wave field is dominated by source-specific waves. These source-specific waves are those which, if the landslide was away from the beach, would radiate out from the source and decay rapidly due to amplitude spreading. Radially spreading source waves are expected to exhibit amplitude decay proportional to $1/r^{4/3}$ [Mei, 1983], where r is the scaled radial distance from the source. As edge waves are trapped with little decay, it is expected that the near-far field division occurs around $r \approx 5$, or five slide widths from the source, where the near field amplitude has decreased to approximately 10% of its

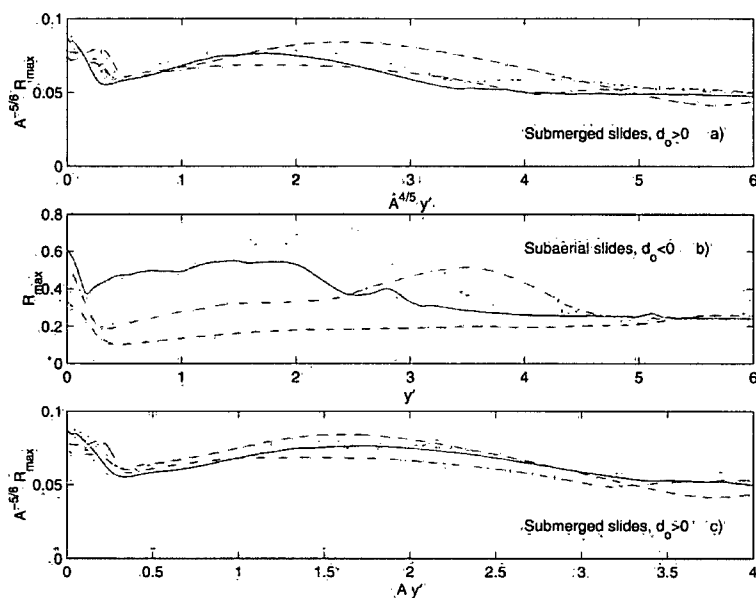


Figure 8. Scaled maximum shoreline elevation at a function of distance from slide centerline for slides with variable A values. The different line types correspond to different A values: [1] (solid line); [2] (dotted line); [5] (dash-dotted line); and [10] (dashed line). See color version of this figure in the HTML.

maximum. It will be demonstrated in this paper that the division does in fact occur roughly five length scales from the source.

[20] In the following subsections, the 2HD dependance on six dimensionless parameters is examined.

5.1. Variable $\epsilon = \Delta h/d_0$: Dimensionless Slide Thickness

[21] Here ϵ is varied through the range $0.125 < |\epsilon| < 1.0$, for both positive and negative ϵ values. The parameters which are constant for all of these simulations are

$$\kappa = 1.0, \quad \mu = 0.1, \quad A = 1.0, \quad \gamma = 2.0, \quad S = 1/10.$$

The dimensionless maximum shoreline elevations or run-ups, R_{\max} , as a function of distance from the slide centerline for both submerged and subaerial landslides are given in Figures 4a and 4b, respectively. The dimensional run-up has been scaled by Δh to yield R_{\max} . For the submerged slides, there is a clear trend of decreasing R_{\max} with decreasing ϵ . This is not the case for the subaerial slides, as from roughly $y' = 0.5$ to 4.0, the curves fall very close together. The secondary maximum in run-up, which is due to edge wave formation, occurs between $y' = 1.5$ to 2.5 with a magnitude $0.55 < R_{\max} < 0.65$ for the subaerial slide range tested here.

[22] Now, trends within the run-up profiles are sought. As there is only one variable parameter, ϵ , for all the simulations in Figure 4, it must be used in any attempt to condense the data into single trends. First, the submerged run-up profiles in Figure 4a were multiplied by the factor $1/\epsilon$; this modified plot is given as Figure 4a. While no unique trend could be achieved across the range $0.1 < y' < 4.5$, it is evident that the maximum run-up directly landward of the slide ($y' \approx 0$) falls in the range $0.18 < R_{\max}/\epsilon < 0.21$. Perhaps more interesting is that all of the run-up profiles condense into a single trend for $y' > 4.5$. This trend is very slowly decreasing, with a mean value of $R_{\max}/\epsilon \approx 0.11$. The subaerial slide run-up can also be condensed for $y' > 4.5$. Shown in Figure 4b is R_{\max} multiplied by $\epsilon^{1/4}$. The result is a very high correlation trend for $y' > 4.5$ such that $R_{\max}\epsilon^{1/4} = 0.2$. These two data manipulations strongly indicate that there is a transition near $y' = 4.5$, where for lesser values an accurate description of the source is extremely important, but for values larger, not important at all. Thus $y' \approx 4.5$, or 4.5 slide widths from the centerline, likely divides the near and far fields.

[23] For a final analysis of these simulations, the submerged slide profiles are once more examined. By multiplying y' by ϵ , all of the secondary run-up peaks, a result of the edge waves, occur at the same location of $\epsilon y' \approx 0.7$, with a magnitude $0.22 < R_{\max}/\epsilon^{4/3} < 0.26$. This data is shown in Figure 5c. This result indicates that even in the very near

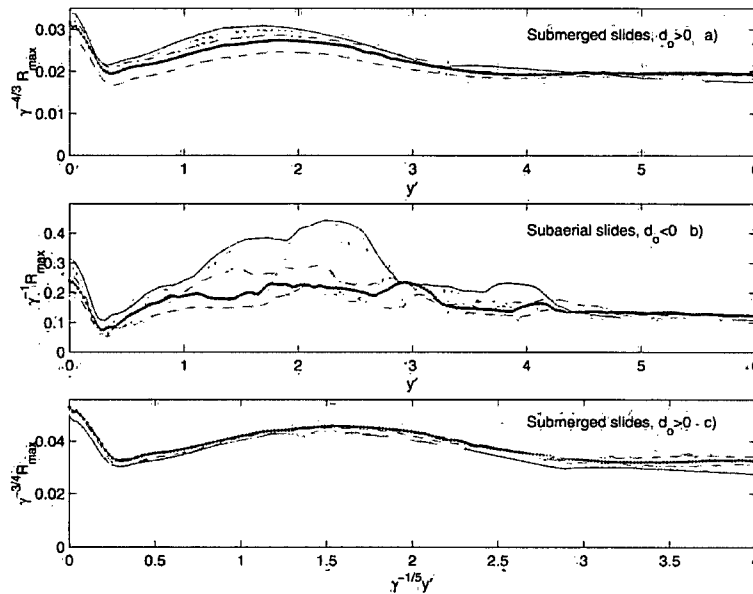


Figure 9. Scaled maximum shoreline elevation at a function of distance from slide centerline for slides with variable γ values. The different line types correspond to different γ values: [1.8] (solid line); [2.0] (dotted line); [2.2] (dash-dotted line); [2.4] (dark bold line); [2.8] (dashed line); and [3.2] (light bold line). See color version of this figure in the HTML.

field area, where nonlinear and dispersive effects are important, certain aspects of the slide behavior will follow simple scaling laws.

5.2. Variable $\mu = k_s \Delta h$: Slide Steepness

[24] Now μ is varied through the range $0.01 < \mu < 0.25$. The parameters which are constant for all of these simulations are

$$\epsilon = \mp 0.4, \quad \kappa = 1.0, \quad A = 1.0, \quad \gamma = 2.0, \quad S = 1/10.$$

The μ range for submerged slides is $0.05 < \mu < 0.25$, due to the fact that $x_s/L < 0.5$ for lesser values. For subaerial slides the range is $0.01 < \mu < 0.1$; larger μ values tended to generate very steep waves which one would expect to break in a physical setup. The scaled dimensionless maximum shoreline elevations or run-ups, R_{max} , as a function of distance from the slide centerline for both submerged and subaerial landslides are given in Figure 6. Note that this figure is constructed in an identical fashion as Figure 5. Again, there is a far field collapse of the run-up curves for $y' > 4.5$ for both submerged and subaerial slides, shown in Figures 6a and 6b, where the submerged run-up has been scaled by $\mu^{6/5}$. There is no factor required for the subaerial

run-up, indicating that far field run-up has no dependence on μ . In Figure 6c, the submerged run-up is scaled by $\mu^{8/5}$ and the distance by $\mu^{-6/5}$, yielding the relationship that the secondary run-up peak occurs near $y' \approx 28\mu^{6/5}$ with a magnitude of $R_{max} \approx 0.0018 \mu^{-8/5}$.

5.3. Variable $\kappa = l_F/l_B$: Symmetry of Slide Shape

[25] In this section, κ is varied through the range $0.7 < \kappa < 1.7$. Note that a small κ value indicates a relatively steeper front face, which is a situation commonly found with deformable landslide flows. The parameters which are constant for all of these simulations are

$$\epsilon = \mp 0.4, \quad \mu = 0.1, \quad A = 1.0, \quad \gamma = 2.0, \quad S = 1/10.$$

The dimensionless maximum shoreline elevations or run-ups, R_{max} , as a function of distance from the slide centerline for both submerged and subaerial landslides are given in Figure 7. Although there is a clear dependency on κ , the relatively low powers of scalings indicate that the dependency is weak over the range tested. The far field collapse of the run-up for both submerged and subaerial slides is evident again.

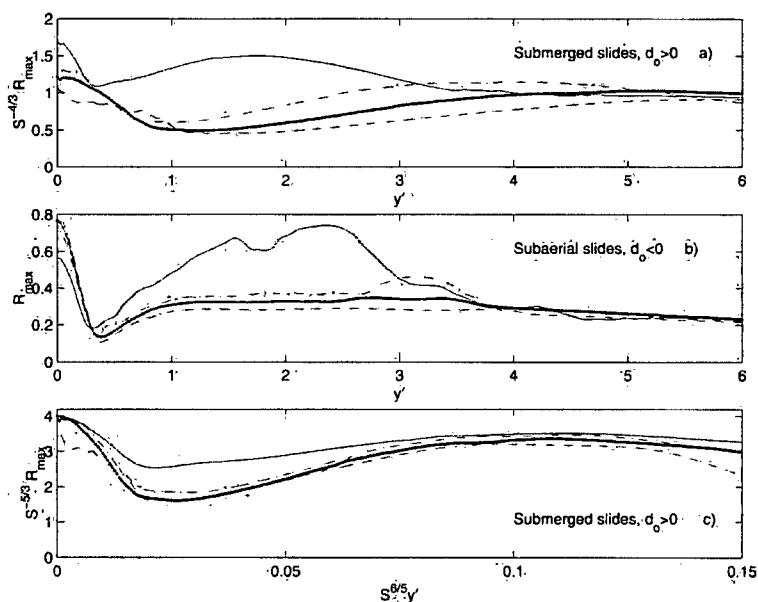


Figure 10. Scaled maximum shoreline elevation at a function of distance from slide centerline for slides with variable S values. The different line types correspond to different S values: [1/10] (solid line); [1/20] (dash-dotted line); [1/25] (dark bold line); and [1/30] (dashed line). See color version of this figure in the HTML.

5.4. Variable $A = L/W$: Aspect Ratio of Slide

[26] Here A is varied through the range $1 < A < 10$. Only values of $A \geq 1$ are tested due to the fact that physical landslides tend to have large A more frequently than small A . Additionally, there is practical limitation, in terms of computer time, on the number of numerical simulations which could be run for very large or small A . This limitation arises from the imposed requirement of a minimum of 20 grid points across the shortest horizontal slide dimension, and thus large or small A simulations require more grid points. The parameters which are constant for all of these simulations are

$$\epsilon = \mp 0.4, \quad \kappa = 1.0, \quad \mu = 0.1, \quad \gamma = 2.0, \quad S = 1/10.$$

The dimensionless maximum shoreline elevations or run-ups, R_{\max} , as a function of distance from the slide centerline for both submerged and subaerial landslides are given in Figure 8. The far field collapse of the run-up curves for $y' > 4.5$ for both submerged and subaerial slides is shown in Figures 8a and 8b, where the submerged run-up has been scaled by $A^{-3/5}$. There is no factor required for the subaerial run-up, indicating that far field run-up has no dependence on A .

5.5. Variable $\gamma = \rho_s/\rho_{\text{water}}$: Specific Gravity of Slide Material

[27] Next, γ is varied through the range $1.8 < \gamma < 3.2$. The parameters which are constant for all of these simulations are

$$\epsilon = \mp 0.4, \quad \kappa = 1.0, \quad \mu = 0.1, \quad A = 1.0, \quad S = 1/10.$$

The dimensionless maximum shoreline elevations or run-ups, R_{\max} , as a function of distance from the slide centerline for both submerged and subaerial landslides are given in Figure 9. Trends from both submerged and subaerial slides converge with a high degree of precision. Of note is that far field subaerial run-up is dependent on γ , which is just the second parameter found to influence this run-up, the other being ϵ .

5.6. Variable $S = \tan \theta$: Beach Slope

[28] Finally, S is varied through the range $1/30 < S < 1/10$. The parameters which are constant for all of these simulations are

$$\epsilon = \mp 0.4, \quad \kappa = 1.0, \quad \mu = 0.1, \quad A = 1.0, \quad \gamma = 2.0.$$

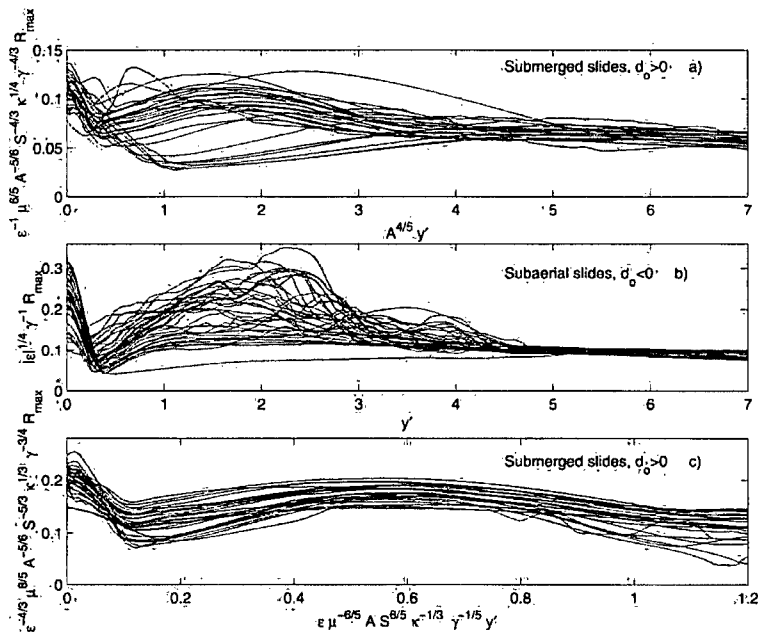


Figure 11. Scaled maximum shoreline elevation as a function of distance from slide centerline for all slides. See color version of this figure in the HTML.

The dimensionless maximum shoreline elevations or run-ups, R_{\max} , as a function of distance from the slide centerline for both submerged and subaerial landslides are given in Figure 10. The far field collapse of the run-up curves is again evident, where the submerged run-up has been scaled by $S^{-4/3}$. There is no factor required for the subaerial run-up, indicating that far field run-up has no dependence on S , as was the case of all the parameters except c and γ . In Figure 10c, the submerged run-up is scaled by $S^{-5/3}$ and the distance by $S^{6/5}$, yielding the relationship that the secondary run-up peak occurs near $y' \approx 0.11 S^{-6/5}$ with a magnitude of $R_{\max} \approx 3.0 S^{5/3}$.

5.7. Combined Trends

5.7.1. Far Field

[29] With the parameter dependencies for each of the six sets of numerical experiments described above, we can combine these dependencies to determine global trends. In addition, 18 more simulations were run with dimensionless parameters lying within the ranges examined above, and are included in the plots discussed now. Looking first to the far field behavior of submerged landslide run-up, the scalings shown in Figures 5a, 6a, 7a, 8a, 9a, and 10a are combined, and the resulting plot

is given in Figure 11a. For far-field, submerged landslide run-up, the important parameter is

$$C_1 = \epsilon^{1/4} \mu^{-6/5} A^{5/6} S^{4/3} \kappa^{-1/4} \gamma^{4/3}. \quad (10)$$

Examination of Figure 11a shows that C_1 influences the far field aspects of submerged landslide run-up. Looking to the far field, which is reasonably defined as $y' > 5A^{-4/5}$, we see the convergence of run-up curves. This convergence starts with a maximum run-up of $R_{\max} = 0.07 \pm 0.015 C_1$ and decreases slowly, exhibiting decreasing scatter within the trend, reaching $R_{\max} = 0.06 \pm 0.01 C_1$ by $y' = 7A^{-4/5}$.

[30] For far-field, subaerial landslide run-up, the parameter of interest is

$$C_2 = \epsilon^{-1/4} \gamma. \quad (11)$$

An extremely clear confluence of subaerial run-up curves for $y' > 5$ is shown in Figure 11b. This is an interesting result, indicating that for subaerial slides, the far field run-up can be very closely estimated with only knowledge of the thickness, initial location, slide width, and density. The maximum run-up is $R_{\max} = 0.10 \pm 0.01 C_2$ at $y' = 5$, slowly decreasing to $R_{\max} = 0.09 \pm 0.01 C_2$ at $y' = 7$.

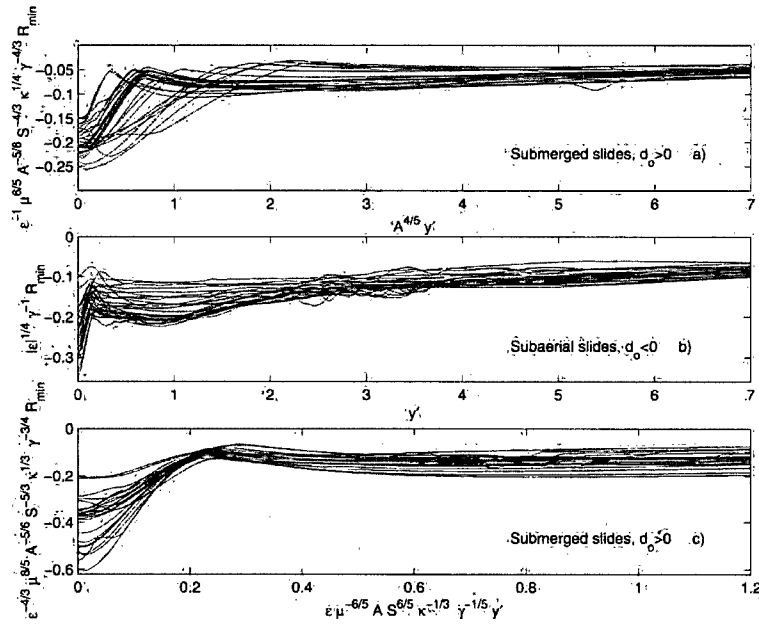


Figure 12. Scaled minimum shoreline elevation as a function of distance from slide centerline for all slides. See color version of this figure in the HTML.

[31] Finally, the secondary run-up peak, due to edge wave propagation, is checked for submerged slides. Here, the important parameters impacting the properties of secondary run-up are

$$C_3 = \epsilon^{4/3} \mu^{-8/5} A^{5/6} S^{5/3} \kappa^{-1/3} \gamma^{3/4} \quad (12)$$

$$C_4 = \epsilon^{-1} \mu^{6/5} A^{-1} S^{-6/5} \kappa^{1/3} \gamma^{-1/5}. \quad (13)$$

With these parameters, the secondary run-up peak can be described approximately as being located at $y' = 0.60 \mp 0.1C_4$, with a magnitude of $R_{\max} = 0.17 \mp 0.03C_3$. In general, the error for the predictions presented in this section is roughly $\mp 15\%$.

[32] While the entire focus of this paper up to now has been on run-up, run-down can be an equally important, and destructive, aspect of the waves generated by landslides. Applying the scalings found above for run-up, the run-down is given in Figure 12, presented in the same form as Figure 11. Just as with the run-up, we see the far field collapse of the submerged and subaerial run-down, shown in Figures 12a and 12b, at roughly the same shoreline locations. This is an indication that the scalings are in fact a good basic representation of the physical aspects of the landslide problem; they were determined for run-up, but work equally well for run-down.

5.7.2. Near Field

[33] All of the previous analysis examined far field scalings, and the search for asymptotic run-up trends. The entire analysis can easily be repeated in an attempt to uncover the proper run-up scalings for a specific location in the near field. In particular, dimensionless expressions are sought for run-up and run-down at $y' \approx 0$, which for many slide setups will be the location of the largest shoreline movement. Additionally, these $y' \approx 0$ run-up/run-down scalings will allow for comparisons with existing experimental data, and validation of the trend-finding approach utilized here.

[34] Repeating the analysis of sections 5.1–5.6, the run-up at $y' \approx 0$ for submerged slides can be given by $R_{\max} \approx 0.30 \mp 0.05C_5$, where

$$C_5 = \epsilon^{1.16} \mu^{-1.40} A^{0.83} S^{1.71} \kappa^{-0.015} \gamma^{0.80}. \quad (14)$$

Run-down for submerged slides is described by $R_{\min} \approx -0.23 \mp 0.04C_6$, where

$$C_6 = \epsilon \mu^{-1.19} A^{0.87} S^{1.14} \kappa^{-0.23} \gamma^{0.62}. \quad (15)$$

It is reiterated here that the dimensional run-up and run-down has been scaled by Δh to yield R_{\max} and R_{\min} . Figure 13 shows the excellent fit for the run-up and run-

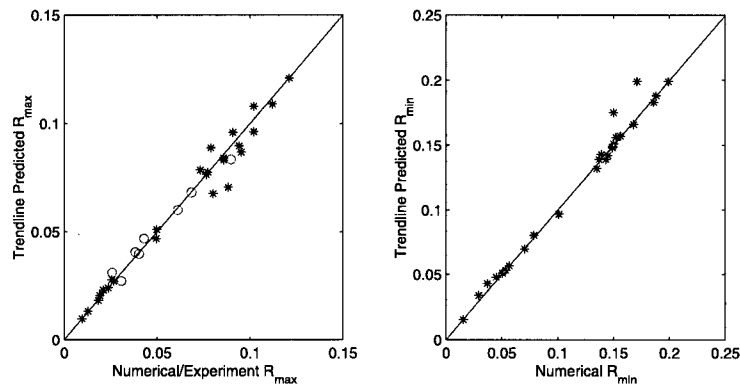


Figure 13. Accuracy of predicted submerged slide run-up/run-down versus results obtained by numerical simulation (asterisks) and experiment (circles). See color version of this figure in the HTML.

down predictions. Also included in the plots are experimental data, discussed in the next section.

6. Comparison With Experimental Data

[35] Owing to the experimental constraints on measuring the three-dimensional (3-D) waves created by landslides, such as accurate measurement of the slide time history and the extremely long and wide tanks required to eliminate reflection effects, very little data exists. Only recently has some data been presented, for example the sliding body experiments of *Synolakis and Raichlen* [2002]. In this paper, some of the data from the *Synolakis and Raichlen* [2002] experiments, where shoreline location was measured, will be employed. For these cases, a spherical hemisphere slid down a 1:2 slope. The hemisphere had a radius of 1.5 ft; the initial depth of submergence and the density of the mass were varied. To be consistent with the work done in this paper, when calculating the length scales of the slide, we look at the horizontal projection of the slide when on the slope. When examining the projection, $L \approx 2.6$ ft, $\delta h \approx 1.5$ ft, $l_B \approx 1.8$ ft, and $l_F \approx 0.8$ ft.

[36] Table 1 summarizes both the predicted run-up and the measured experimental run-up. Experiment runs 8, 22, and 33 were not included in the comparison, as these cases exhibited significant breaking and turbulence in the laboratory. The predicted run-up is calculated from the scalings developed in this paper: $R_{\max} \approx 0.30C_5$. The accuracy of the predictions is very good. For the $\gamma = 2.0$ and 2.3 runs, the predictions are excellent. For the $\gamma = 3.2$ runs, the predictions are not quite as good, and are indicative of the error range of the run-up prediction formula. Possible explanations for the decrease in accuracy for larger γ is increased slide bottom friction, or increased level of turbulence due to faster slide motion. These physical aspects are not considered in the numerical model. It should also be noted that the experimental ϵ , μ , κ , and S values are all outside of the range

examined numerically in this paper, yet good agreement is still achieved.

[37] Examination of this experimental data provides a good basis for a coefficient and exponent sensitivity analysis. It is reiterated here that, when choosing the exponent values in sections 5.1–5.6, the exponent which provided the least trend line spread was the chosen exponent, thereby pushing the uncertainty into the leading coefficient. For completeness, however, a brief exponent sensitivity analysis will be given now. Looking to the independent parameter analyses (Figures 5–10), the maximum coefficient spread is on the order of $\pm 10\%$. It is reasonable to assume an exponent spread of the same order for this analysis. Looking to run 9 given in Table 1, the predicted run-up is recalculated, now with all the exponents in C_5 increased and decreased by 10%. Increasing all exponents yields a run-up prediction of 2.7 cm, while decreasing all exponents gives 3.6 cm. This spread is similar to the coefficient uncertainty, $\pm 15\%$. It is reasonable to state, now, that the maximum possible spread is on the order of $\pm 30\%$, accounting for possible errors in the leading coefficient and exponents. However, it is expected that much of the

Table 1. Comparison of Maximum Run-Up at $y = 0^a$

Run	ϵ	γ	Predicted R_{\max} , cm	Measured R_{\max} , cm	% Error
9	2.3	2.3	3.1	3.1	0
10	1.5	2.3	2.0	2.1	-5
11	1.1	2.3	1.4	1.2	15
23	2.3	3.2	4.1	3.8	10
25	0.8	3.2	1.2	1.4	-15
26	1.1	3.2	1.8	1.8	0
34	2.3	2.0	2.8	2.7	5
35	1.5	2.0	1.8	1.8	0

^aPredicted data is from the formula $R_{\max} \approx 0.30C_5$, and experimental data is from *Liu et al.* [2005]. Constant parameters are $\mu = 3.6$, $A = 0.87$, $S = 0.5$, and $\kappa = 0.45$.

spread will be located in the leading coefficient, with an uncertainty of $\pm 15\%$.

[38] In addition to the hemisphere slide experiments compared above, Liu *et al.* [2005] also present wave data for tsunamis generated by triangular block shaped slides. Owing to the sharp corners and very large slopes of these shapes, the Boussinesq-type numerical model is incapable of simulating the triangular block slide. Additionally, comparison of the experimental triangular block slide run-up at $\gamma = 0$ with (14) shows very poor agreement with errors on the order of 100%. As with the hemisphere experiments, ϵ , μ , κ , and S values for the triangular slide are all outside of the range examined numerically in this paper. It must therefore be stated that the trends developed in this paper may only be applicable for smooth shaped slides. In order to simulate these experiments more exactly, a vertically resolving model is required, such as a Navier-Stokes model.

7. Conclusions

[39] A comprehensive set of numerical experiments, including over 75 numerical simulations requiring more than 100 days of desktop CPU time, has been undertaken. The submerged and subaerial slides examined here created nonbreaking waves in shallow to intermediate water. Through analysis of the run-up from these slides, a number of dimensionless relationships have been determined. For submerged slides, the maximum run-up immediately landward of the slide, as well as the magnitude and location of the secondary run-up peak, can now be reasonably estimated. For both subaerial and submerged slides, the division between near and far field has been shown, along with maximum run-up at these locations. In dimensional form, the key relationships are summarized as follows.

(1) Submerged slides:

Maximum run-up immediately landward of slide centerline

$$R/\Delta h \approx 0.30\epsilon^{-1.16}\mu^{-1.40}A^{0.83}S^{1.71}\kappa^{-0.015}\gamma^{0.80}, \quad (16)$$

Maximum run-down immediately landward of slide centerline

$$R/\Delta h \approx -0.23\epsilon\mu^{-1.19}A^{0.87}S^{1.14}\kappa^{-0.23}\gamma^{0.62}, \quad (17)$$

Near-far field division

$$y/W \approx 5A^{-4/5}; \quad (18)$$

Run-up at near-far field division

$$R/\Delta h \approx 0.07\epsilon\mu^{-6/5}A^{5/6}S^{4/3}\kappa^{-1/4}\gamma^{4/3}, \quad (19)$$

Location of secondary run-up peak due to edge waves

$$y/W \approx 0.6\epsilon^{-1}\mu^{6/5}A^{-1}S^{-6/5}\kappa^{1/3}\gamma^{-1/5}, \quad (20)$$

Secondary peak run-up

$$R/\Delta h \approx 0.17\epsilon^{4/3}\mu^{-8/5}A^{5/6}S^{5/3}\kappa^{-1/3}\gamma^{3/4}. \quad (21)$$

(2) Subaerial slides:

Near-far field division

$$y/W \approx 5; \quad (22)$$

Run-up at near-far field division

$$R/\Delta h \approx 0.1\epsilon^{-1/4}\gamma. \quad (23)$$

[40] These prediction equations can be expected to have errors bounds of 15%. Comparisons with experiment show that the scaling relationships yield reasonable predictions. These relationships may be useful for preliminary hazard assessment, where a simple and quick estimation of the maximum run-up height and locations are required. Additionally, the formulas developed in this paper will be particularly beneficial to those developing 3-D landslide experiments. Finally, it should be noted that the simulations performed for this paper all make use of a simple planar slope, and do not take into account irregular bathymetry effects. It is known from PNG, as well as from many tsunami events, that bathymetric focusing can greatly impact the shoreline run-up profiles [e.g., Matsuyama *et al.*, 1999], and thus one must always be mindful of site specific seafloor contours when estimating run-up.

[41] **Acknowledgment.** The research reported here is partially supported by grants from the National Science Foundation (CMS-9528013, CTS-9808542, and CMS 9908392).

References

- Basterretxea, G., A. Orfila, A. Jordi, B. Casas, P. Lynett, P. L.-F. Liu, C. M. Duarte, and J. Tintoré (2004), Seasonal dynamics of a microtidal pocket beach with Posidonia Oceanica seabeds (Mallorca, Spain), *J. Coastal Res.*, **20**, 1155–1164.
- Chang, K. T. (1995), Evolution of landslide-generated edge wave packet, Ph.D. thesis, Univ. of Wash., Seattle.
- Gonzalez, F., K. Satake, E. Boss, and H. Mofjeld (1995), Edge wave and non-trapped modes of the 25 April 1992 Cape-Mendocino tsunami, *Pure Appl. Geophys.*, **144**, 409–426.
- Grilli, S. T., and P. Watts (1999), Modeling of waves generated by a moving submerged body: Applications to underwater landslides, *Eng. Anal. Boundary Elem.*, **23**, 645–656.
- Grilli, S. T., S. Vogelmann, and P. Watts (2002), Development of a 3D numerical wave tank for modeling tsunami generation by underwater landslides, *Eng. Anal. Boundary Elem.*, **26**, 301–313.
- Jiang, L., and P. H. LeBlond (1994), Three-dimensional modeling of tsunami generation due to a submarine landslide, *J. Phys. Oceanogr.*, **24**, 559–572.
- Liu, P. L.-F. (1994), Model equations for wave propagation from deep to shallow water, in *Advances in Coastal Engineering*, vol. 1, edited by P. L.-F. Liu, pp. 125–157, World Sci., Hackensack, N. J.
- Liu, P. L.-F., H. Yeh, P. Lin, K. Chang, and Y.-S. Cho (1994), Generation and evolution of edge-waves packets, *Phys. Fluids*, **10**, 1635–1657.
- Liu, P. L.-F., T.-R. Wu, F. Raichlen, C. E. Synolakis, and J. Borrero (2005), Runup and rundown from three-dimensional sliding masses, *J. Fluid Mech.*, in press.
- Lynett, P. (2002), A multi-layer approach to modeling nonlinear, dispersive waves from deep water to the shore, Ph.D. thesis, Cornell Univ., Ithaca, N. Y.
- Lynett, P., and P. L.-F. Liu (2002), A numerical study of submarine landslide generated waves and runup, *Proc. R. Soc. London. Ser. A*, **458**, 2885–2910.
- Lynett, P., and P. L.-F. Liu (2004a), A two-layer approach to water wave modeling, *Proc. R. Soc. London. Ser. A*, **460**, 2637–2669.
- Lynett, P., and P. L.-F. Liu (2004b), Linear analysis of the multi-layer model, *Coastal Eng.*, **51**, 439–454.
- Lynett, P., T.-R. Wu, and P. L.-F. Liu (2002), Modeling wave runup with depth-integrated equations, *Coastal Eng.*, **46**, 89–107.
- Lynett, P., J. Borrero, P. L.-F. Liu, and C. E. Synolakis (2003), Field survey and numerical simulations: A review of the 1998 Papua New Guinea tsunamis, *Pure Appl. Geophys.*, **160**, 2119–2146.

- Matsuyama, M., J. P. Walsh, and H. Yeh (1999), The effect of bathymetry on tsunami characteristics at Sisanu Lagoon, Papua New Guinea, *Geophys. Res. Lett.*, *26*, 3513–3516.
- Mei, C. C. (1983), *The Applied Dynamics of Ocean Surface Waves*, Wiley-Interscience, Hoboken, N. J.
- Nwogu, O. (1993), Alternative form of Boussinesq equations for nearshore wave propagation, *J. Waterw. Port Coastal Ocean Eng.*, *119*, 618–638.
- Okal, E., and C. Synolakis (2004), Source discriminants for near-field tsunamis, *Geophys. J. Int.*, *158*, 899–912.
- Press, W. H., B. P. Flannery, and S. A. Teukolsky (1989), *Numerical Recipes: The Art of Scientific Computing*, Cambridge Univ. Press, New York.
- Ryu, S., M. H. Kim, and P. Lynett (2003), Fully nonlinear wave-current interactions and kinematics by a BEM-based numerical wave tank, *J. Comput. Mech.*, *32*, 336–346.
- Schaffer, H., and I. Jonsson (1992), Edge waves revisited, *Coastal Eng.*, *16*, 349–368.
- Synolakis, C. E., and F. Raichlen (2002), Wave and run-up generated by a three-dimensional sliding mass, paper 299 presented at the 28th International Conference on Coastal Engineering, Cardiff, Wales, 7–12 July.
- Synolakis, C., J. Bardet, J. Borrero, H. Davies, E. Okal, E. Silver, S. Sweet, and D. Tappin (2002), The slump origin of the 1998 Papua New Guinea tsunami, *Proc. R. Soc. London, Ser. A*, *458*, 763–789.
- Tinti, S., E. Bortolucci, and A. Armigliato (1999), A numerical simulation of the landslide-induced tsunami of 1988 on Vulcano Island, Italy, *Bull. Volcanol.*, *61*, 121–137.
- Ursell, F. (1952), Edge waves on a sloping beach, *Proc. R. Soc. London, Ser. A*, *214*, 79–97.
- Watts, P. (1997), Water waves generated by underwater landslides, Ph.D. thesis, Calif. Inst. of Technol., Pasadena.
- Wei, G., J. T. Kirby, S. T. Grilli, and R. Subramanya (1995), A fully nonlinear Boussinesq model for surface waves. part 1. Highly nonlinear unsteady waves, *J. Fluid Mech.*, *294*, 71–92.

P. L.-F. Liu, School of Civil and Environmental Engineering, Cornell University, Ithaca, NY 14853, USA. (p113@cornell.edu)
P. Lynett, Department of Civil Engineering, Texas A&M University, College Station, TX 77843-3136, USA. (plynett@tamu.edu)

Nearshore Wave Modeling with High-Order Boussinesq-Type Equations

Patrick J. Lynett¹

Abstract: The accuracy of using high-order Boussinesq-type models as compared to the typical order models is examined in this paper. The high-order model used is the two-layer model of Lynett and Liu in 2004, which captures both linear and nonlinear wave evolution up to $kh \approx 6$. The physical situations examined all involve nearshore breaking, and an eddy-viscosity type breaking model is adopted for the two-layer model. One-horizontal dimension setups are the focus of this paper. It is shown that high-order models show significant benefit very near to the breaker line. For regular incident waves, the overshooting seen in the one-layer ("fully nonlinear" extended Boussinesq) model is due to rapid increase of energy in the fifth and higher harmonics. These high-order nonlinear components are captured well in the two-layer model. The two-layer model also exhibits a noticeable accuracy increase for cnoidal waves breaking on a slope. For regular wave evolution over a bar, the high-order models are in good agreement with experiment, correctly modeling the free short waves behind the step. Under irregular wave conditions, it is likewise shown that high-order nonlinearity is important near the breaker line and the outer surf zone. Using SwashX field data, spectral comparisons are made and discussed.

DOI: 10.1061/(ASCE)0733-950X(2006)132:5(348)

CE Database subject headings: Breaking waves; Boussinesq equations; Nearshore; Hydrologic models.

Introduction

Due to present computational constraints, time-domain modeling of large-scale wave evolution in the nearshore zone requires approximate equations. Boussinesq-type equations are becoming increasingly popular for this task. In the past decade, these equations have been used to accurately predict wave evolution across large basins (Basterretxea et al. 2004), wave breaking over irregular topography, wave-structure interaction (Lynett et al. 2000), and wave-induced current patterns (Chen et al. 2003) among many others.

Initial formulations, based on the depth-averaged velocity, were somewhat limited in their description of wind waves in the nearshore. These models generally had good linear accuracy to $kh \approx 1$, but could not yield accurate predictions in the intermediate water regime. Manipulations of the Boussinesq derivation, initiated by Madsen and Sorensen (1992) and Nwogu (1993), led to final model equations with good accuracy through intermediate water. Further nonlinear improvements (e.g., Liu 1994; Wei et al. 1995; Kennedy et al. 2001) made the model even more useful for coastal modeling. However, as noted in Beji and Battjes (1994) and others, even these equations sometimes yielded incorrect predictions, in particular in highly nonlinear situations where, due to bathymetry changes, locked nonlinear components become free. For these scenarios, and in general for a more robust prediction, higher-order accuracy is needed.

A handful of high-order Boussinesq-type models exist. Madsen et al. (2002), based on the approach of Agnon et al. (1999), developed a model with excellent linear and nonlinear accuracy in very deep water ($kh \approx 40$). Gobbi et al. (2000) expanded Nwogu's approach to the next order in $(kh)^2$, creating a model with linear accuracy into deep water and nonlinear accuracy throughout intermediate water. Lynett and Liu (2004a) presented the multilayer concept, where the water column is divided into same-fluid "layers" or segments of the water column governed by matched, but unique polynomials describing the horizontal flow field. The two-layer version shows linear and nonlinear accuracy to $kh \approx 6$, while the three and four layer models have good linear accuracy to $kh \approx 17$ and 30, respectively (Lynett and Liu 2004b). Simulations with these high-order models indicate that many nearshore setups benefit from the increased accuracy. High-order model applications involving wave breaking have not been examined to a substantial degree; one such investigation is reported in Sorensen et al. (1999).

In the first section of this paper, the theoretical and numerical aspects of the two-layer model are presented and discussed. Experimental comparisons of wave breaking on a constant slope are given, with the purpose of validating the wave breaking model in both the typical and high-order models. Wave height and setup profiles are examined. Next, one-horizontal-dimension (1HD) wave breaking over a bar is compared. Concluding the comparisons is a recreation of a field experiment.

Two-Layer Model

The high-order simulations presented in this paper employ the two-layer model of Lynett and Liu (2004a). The water column is divided into two same fluid layers, where velocity and pressure are matched at the interface. Within each layer, a unique quadratic polynomial is used to describe the vertical profile of the

¹Professor, Dept. of Civil Engineering, Texas A&M Univ., College Station, TX 77843-3136. E-mail: plynett@tamu.edu

Note. Discussion open until February 1, 2007. Separate discussions must be submitted for individual papers. To extend the closing date by one month, a written request must be filed with the ASCE Managing Editor. The manuscript for this paper was submitted for review and possible publication on February 18, 2005; approved on August 4, 2005. This paper is part of the *Journal of Waterway, Port, Coastal, and Ocean Engineering*, Vol. 132, No. 5, September 1, 2006. ©ASCE, ISSN 0733-950X/2006/5-348-357/\$25.00.

horizontal velocity. The multi-layer concept is described as a piecewise matching of polynomials through the water column, where the matching location represents the "interface" between two "layers." The resulting equation model consists of a continuity equation, a momentum equation for the upper layer, and a matching equation for the velocity in the lower layer. These equations are given below

$$\begin{aligned} \frac{\partial \zeta}{\partial t} + \nabla \cdot [(\zeta - \eta)\mathbf{u}_1 + (\eta + h)\mathbf{u}_2] - \nabla \cdot \left\{ \left[\frac{\eta^3 + h^3}{6} - \frac{(\eta + h)\kappa_2}{2} \right] \right. \\ \left. \times \nabla S_2 + \left[\frac{\eta^2 - h^2}{2} - (\eta + h)\kappa_2 \right] \nabla T_2 \right\} \\ - \nabla \cdot \left\{ \left[\frac{\zeta^3 - \eta^3}{6} - \frac{(\zeta - \eta)\kappa_1}{2} \right] \nabla S_1 \right. \\ \left. + \left[\frac{\zeta^2 - \eta^2}{2} - (\zeta - \eta)\kappa_1 \right] \nabla T_1 \right\} = 0 \end{aligned} \quad (1)$$

$$\begin{aligned} \frac{\partial \mathbf{u}_1}{\partial t} + \frac{1}{2} \nabla (\mathbf{u}_1 \cdot \mathbf{u}_1) + g \nabla \zeta + \frac{\partial}{\partial t} \left[\frac{\kappa_1}{2} \nabla S_1 + \kappa_1 \nabla T_1 - \nabla \left(\frac{\zeta^2}{2} S_1 \right) \right. \\ \left. - \nabla (\zeta T_1) \right] + \nabla \left\{ \frac{\partial \zeta}{\partial t} (T_1 + \zeta S_1) + (\kappa_1 - \zeta)(\mathbf{u}_1 \cdot \nabla) T_1 \right. \\ \left. + \frac{1}{2} (\kappa_1^2 - \zeta^2)(\mathbf{u}_1 \cdot \nabla) S_1 + \frac{1}{2} [(T_1 + \zeta S_1)^2] \right\} \\ - \mathbf{R}_b + \mathbf{R}_f + \nu_T \left[\nabla S_1 - \nabla^2 \mathbf{u}_1 - \nabla^2 \left(\frac{\kappa_1}{2} \nabla S_1 + \kappa_1 \nabla T_1 \right) \right. \\ \left. + \nabla \left(\frac{\zeta^2}{2} \nabla^2 S_1 + \zeta \nabla^2 T_1 \right) \right] = 0 \end{aligned} \quad (2)$$

$$\begin{aligned} \mathbf{u}_2 + \frac{\kappa_2 - \eta^2}{2} \nabla S_2 + (\kappa_2 - \eta) \nabla T_2 = \mathbf{u}_1 + \frac{\kappa_1^2 - \eta^2}{2} \nabla S_1 \\ + (\kappa_1 - \eta) \nabla T_1 \end{aligned} \quad (3)$$

where

$$S_2 = \nabla \cdot \mathbf{u}_2, \quad T_2 = \nabla \cdot (h\mathbf{u}_2)$$

$$S_1 = \nabla \cdot \mathbf{u}_1, \quad T_1 = \eta(S_2 - S_1) + T_2 \quad (4)$$

\mathbf{R}_b =breaking-related dissipation term; \mathbf{R}_f accounts for bottom friction; ν_T =constant eddy viscosity; $\nabla^2=(\partial^2/\partial x^2+\partial^2/\partial y^2)$; $\kappa_1=-0.127h$ =evaluation level for the velocity \mathbf{u}_1 ; $\eta=-0.266h$ =layer interface elevation; $\kappa_2=-0.618h$ =evaluation level for the velocity \mathbf{u}_2 ; and ζ =free surface elevation. It is noted that with the choice of $\kappa_1=-0.531h$ and $\eta=\kappa_2=-h$, the resulting two equation model becomes equivalent to the highly nonlinear Boussinesq-type model presented by Liu (1994). Also derived by Wei et al. (1995), this highly nonlinear model will be referred to as the one-layer model in this paper. For clarity, the two-layer model is the high-order model, and the one-layer model is the typical-order model.

The two-layer equation model was analyzed in depth in Lynett and Liu (2004a), and will not be repeated here. The resulting linear properties of the two-layer model are shown in Fig. 1, as are the properties of the one-layer model. The numerical scheme used to solve the equation system is a fourth-order, predictor-corrector method for the time integration, with spatial derivatives

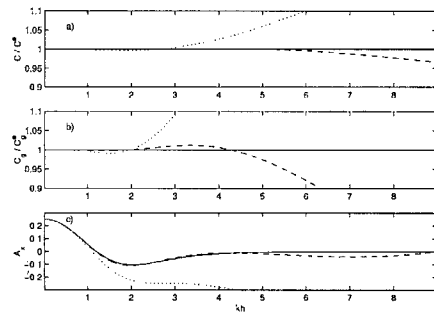


Fig. 1. Linear accuracy of two-layer model. In each plot, solid line is linear theory, dotted line is one-layer model, and dashed line is two-layer model. Subplot (a) shows comparison of phase velocity; (b) group velocity; and (c) shoaling gradient as given by $a_x/a=A_x h_x/h$, where a =wave amplitude and h =water depth.

finite differenced to fourth-order accuracy on a regular grid. Complete details of the numerical model can be found in Lynett and Liu (2004a).

As can be seen in Eq. (2), there are three sources of dissipation: bottom friction, breaking, and constant eddy viscosity dissipation. Bottom friction is calculated with the quadratic friction equation

$$\mathbf{R}_f = \frac{f}{h + \zeta} \mathbf{u}_b |\mathbf{u}_b| \quad (5)$$

where \mathbf{u}_b =velocity evaluated at the seafloor; and f =bottom friction coefficient, typically in the range of 10^{-3} – 10^{-2} . As noted in Lynett et al. (2002), maximum runup is sensitive to the value of f , particularly for very large, breaking waves: a conservative value of 10^{-3} is used for all simulations here. To simulate the effects of wave breaking, the eddy viscosity model of Kennedy et al. (2000) is used here with some modification. The first modification regards the manner in which a breaking event is initiated. A range of breaking simulations were undertaken including regular wave breaking on a planar slope (Hansen and Svendsen 1979), cnoidal wave breaking on a planar slope (Ting and Kirby 1995), and wave breaking over a submerged breakwater (Dingemans 1994). All of these simulations have experimental data indicating the breaking locations. To determine the best breaking indicator in the numerical model, a number of possible IHD threshold parameters were investigated, including ζ_x/c , ζ_x/u_s , H^2/c , and u_x/c , where u_s =free surface speed (as evaluated from the extended-Boussinesq vertical profile of horizontal velocity); c =local nonlinear long wave speed= \sqrt{gH} ; H =total water depth= $\zeta+h$; and the subscripts x and t indicate partial derivatives with respect to time and space. Note that simulations using the linear phase speed and the local depth as scaling factors were attempted as well. The results of this analysis are that ζ_x is the least sensitive breaking threshold, with the correct breaking location predicted by $\zeta_x=0.6 \pm 0.02$ using the two-layer model. The other results showed correct breaking initialization as $\zeta_t/c=0.55 \pm 0.06$, $u_s H^2/c=0.62 \pm 0.05$, and $u_x/c=0.40 \pm 0.06$. Therefore, wave slope should be used as the breaking model trigger, as has been commonly employed (e.g., Schäffer et al. 1993). It must be noted

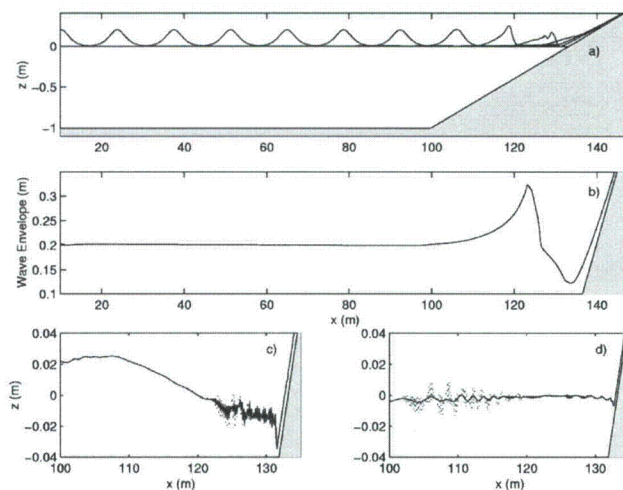


Fig. 2. Solitary wave breaking and runup. Subplot (a) shows waveform at various times; (b) gives wave envelope from simulation with viscosity (solid line) and simulation without viscosity (dotted line); and (c) and (d) are closeups near beach, where two simulations are given as in subplot (b). Subplot (c) is at earlier time than (d), and both are during rundown phase. Positive wave shown in (c) is reflection moving away from beach, and has left frame by (d). Solid seafloor is gray.

here, however, that these coefficients will be specific to the nonlinear-dispersive properties of a given model (here the two-layer model), and care must be taken when employing these thresholds in alternative models.

Through testing with various dissipation models, it was found that, in terms of stability and lack of numerical noise generation, the eddy viscosity model of Kennedy et al. (2000) was preferred for this particular numerical scheme. For the dissipation under a breaking event, modifications to Kennedy et al. are concerned primarily with reformulating the model thresholds in terms of the total water depth, H . In Kennedy et al. thresholds are given in terms of h , making the simulation of breaking uprush, where h is negative, unclear. The structure of the dissipation formulation is identical to Kennedy et al. although the calibrated threshold values are modified. The complete formulation for R_b is given in Appendix II.

The final dissipation term in Eq. (2), with the leading coefficient ν_T , has not explicitly been included in Boussinesq-type models to date. This term arises when including eddy viscosity in the Navier–Stokes equations, which are the primitive equations used to derive the Boussinesq. A brief Boussinesq model derivation, showing the inclusion of the eddy viscosity, is given in Appendix I. Leading-order dissipation from this term exists for 2HD simulations only and is related to the horizontal gradient of vertical vorticity, which due to the irrotational foundations of the Boussinesq derivation, should be small. However, with the inclusion of bottom friction and wave breaking, this is not necessarily the case. The second-order terms in this expression are related to the fourth-order spatial derivatives of velocity, which should also be small. It is interpreted that this term accounts for the eddy dissipation that is not included in the breaking and bottom friction

models. Through simulation testing, an eddy viscosity of $\nu_T = 0.001 h_0 \sqrt{g h_0}$ is used here, where h_0 is a characteristic water depth of the initial condition. This value was found to not have significant impact on the wave field when numerical short waves are not present.

To show the effectiveness of this dissipation term an example simulation is given here. In the numerical model, when a large amplitude solitary wave breaks and runs up a slope, it is common for a small amount of numerical noise to be generated during the rundown phase when bottom friction is not included or small. The reason for this is a very steep, nearly stationary hydraulic jump at the base of the rundown, which propagates out short waves as numerical dispersive errors. For this example simulation, a bottom friction coefficient of $f = 0.0001$ is used. Fig. 2 gives four subplots of the solitary wave runup, showing spatial profiles from simulations with $\nu_T = 0$ and $\nu_T = 0.003 \text{ m}^2/\text{s}$ (as calculated from the recommended equation with $h_0 = 1 \text{ m}$). Properties of the simulation are nondimensional wave height = 0.2, beach slope = 1/35, and $\Delta x/h_0 = 0.1$. The added dissipation has no effect on the wave propagation and runup [Fig. 2(b)], however the rapid damping of the rundown-created short waves is clear as shown in Figs. 2(c) and (d). Essentially, this new dissipation model represents a somewhat physical means of filtering out unwanted short wave energy.

Experimental Comparisons and Discussion

In this section, a range of 1HD simulations are compared. The focus is on wave characteristics near the breakpoint and through the surf zone. The nearshore impact of using a model with good

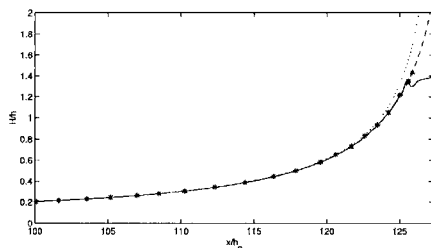


Fig. 3. Shoaled solitary wave height, H , scaled by local water depth, h , versus horizontal location, where h_0 =depth at base of slope. Dotted line is one-layer model without breaking; dashed line is two-layer model without breaking; solid line is two-layer model with breaking; and stars are potential flow results as presented in Wei et al. (1995). Last shown star (at $x/h_0=125.9$) is break point predicted by potential flow model.

short wave properties will be discussed. The numerical grid and time steps for all simulations are given in Appendix III, "Numerical Simulation Parameters."

1HD Wave Breaking on Constant Slope

For an initial comparison, the solitary wave of Fig. 2 is examined more closely. Solitary wave shoaling, up to the break point, was investigated with a potential flow model by Grilli et al. (1994) and then compared with the fully nonlinear Boussinesq model of Wei et al. (1995), a one-layer model. In general, the Boussinesq model predicted shoaling correctly, in agreement with the potential flow model, until very near the break point where the wave overshoots. The two-layer model is compared with the potential flow results, as given in Wei et al. (1995), in Fig. 3. The two-layer model predicts the near-break point shoaling better, however the break point is a bit early. This example provides some confidence that the two-layer model very accurately captures shoaling to near the break point.

Regular wave breaking up a planar slope is examined now. The setup here is taken from Hansen and Svendsen (1979). The depth near the wavemaker from these trials is 0.36 m, leading to a beach slope of 1:34.26. Five cases will be compared, with varying wave period and amplitude. Both wave height and mean water level data is available from the experiments. Fig. 4 gives the results from the one- and two-layer models, as well as the experimental data. A very clear trend appears: the one-layer model overshoots the wave near the breakpoint, while the two-layer model shoals at a rate more consistent with the experimental data. The overshooting of the one-layer model has been noted previously (e.g. Kennedy et al. 2000), and is an expected property of the one-layer model.

With the two-layer model exhibiting very good accuracy for these cases, we have a mechanism for determining how the one-layer model overshoots the wave. By plotting the behavior of the various harmonics in the wave train, the source of the error becomes apparent. Fig. 5 gives the trends of various harmonics from the one- and two-layer models. In this figure are given three curves for each simulation, showing the combined spectral amplitudes in three harmonic groups: the first harmonic (A_1), the second through fourth harmonics (A_{2-4}), and the fifth and higher

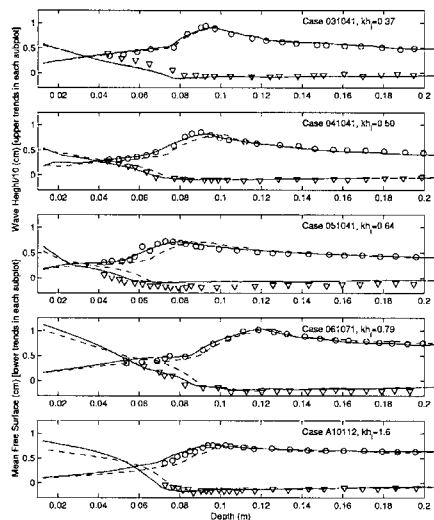


Fig. 4. Wave height and setup comparisons with regular wave breaking experiments of Hansen and Svendsen (1979). Each figure gives kh value of wave at wavemaker, symbols are experimental data, dashed line is one-layer model, and solid line is two-layer model. Top trends in each subplot are wave height and lower trends are mean water level.

harmonics (A_{5+}). These harmonics are grouped as such because the harmonics in each group behaved similarly. Interestingly, both models show significant spectral energy into the tenth harmonic, particularly in the inner surf.

Evident from this comparison is that the overshooting in the one-layer model is due to over amplification of the fifth and higher harmonics (note that $kh \approx 2$ for the fifth harmonic near the break point). The very high order nonlinear interactions creating these harmonics are, expectedly, not described properly in the one-layer model. Additionally, the break point appears to be controlled by the fifth and higher harmonics, which exhibit an rapid increase in amplitude near the break point, while A_1 shows a nearly linear decrease and A_{2-4} show a linear increase before breaking. To achieve excellent hydrodynamic predictions near the breaking point, a model with correct high-order nonlinear behavior is needed.

Next, cnoidal wave breaking over a constant slope is examined. The data by Ting and Kirby for plunging (1995) and spilling (1996) is used here. This data have been used most frequently to test turbulence generation in numerical models more sophisticated than the one used here (e.g., Lin and Liu 1998; Zhao et al. 2004). However, the wave height data obtained during the experiments are also an excellent benchmark for depth-integrated models in the surf zone (Bredmose et al. 2004). It is noted that, for the cnoidal wave cases, the location of the numerical wavemaker (internal source wave generator), does play a role in the break point location. The reason for this is that, due to the high nonlinearity of the incident wave condition, free waves tended to be generated

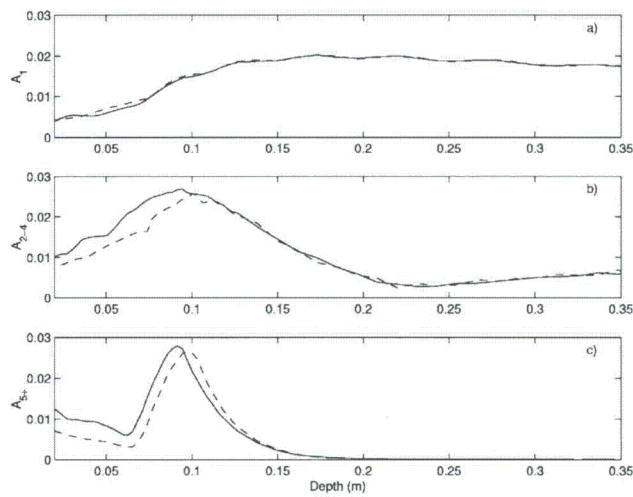


Fig. 5. Amplitudes in harmonic bins as predicted by one-layer (dashed line) and two-layer (solid line) model for case 041041 shown in Fig. 4. In (a) is first harmonic amplitude, A_1 , in (b) is sum of second through fourth, $A_{2-4} = \sum_{n=2}^4 A_n$, and in (c) sum of fifth and higher harmonics, $A_{5+} = \sum_{n=5}^{\infty} A_n$.

with the cnoidal wave train, which would then interact in a nonlinear manner. Depending on the interaction time possible for the wave components, which is controlled by the wavemaker location, the breakpoint could be shifted. Care was taken to ensure that the numerical wavemaker was at the same location as the experimental. The numerical-experimental comparisons for the spilling and plunging breakers are given in Figs. 6 and 7, respectively. Shown in these comparisons is a trend similar to that already mentioned: the one-layer model shoals much more rapidly

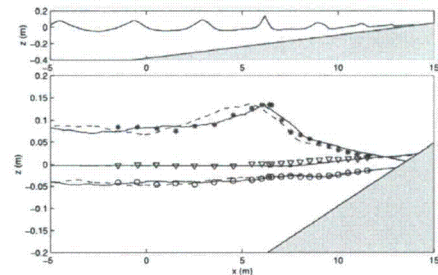


Fig. 6. Comparisons with experimental data from Ting and Kirby spilling breaker. In top subplot, snapshot of numerical simulation is given. Below experimental crest level (stars), trough level (circles), and mean water level (triangles) are shown, as well as corresponding values from one-layer model (dashed line) and two-layer model (solid line).

near the break point, and apparently much less realistically. This is the case in particular for the plunging breaker, where the one-layer model predicts substantially different crest levels near the break point and the outer surf zone. Interestingly, the mean water level and the trough level as predicted by the one-layer model is quite good, in agreement with both the two-layer model and the experiment. This is an indication that, at least for these cnoidal wave cases, the mean water level and the trough level are not sensitive to high-order nonlinear and dispersion accuracy, while the crest level is. Also worthy of note is that in the inner surf zone, the numerical predictions converge, which is a likely sign that breaking is becoming a depth-limited process in this region.

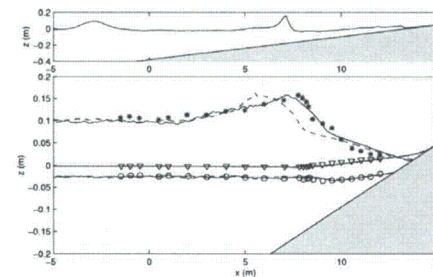


Fig. 7. Comparisons with experimental data from Ting and Kirby plunging breaker. Figure setup same as in Fig. 6.

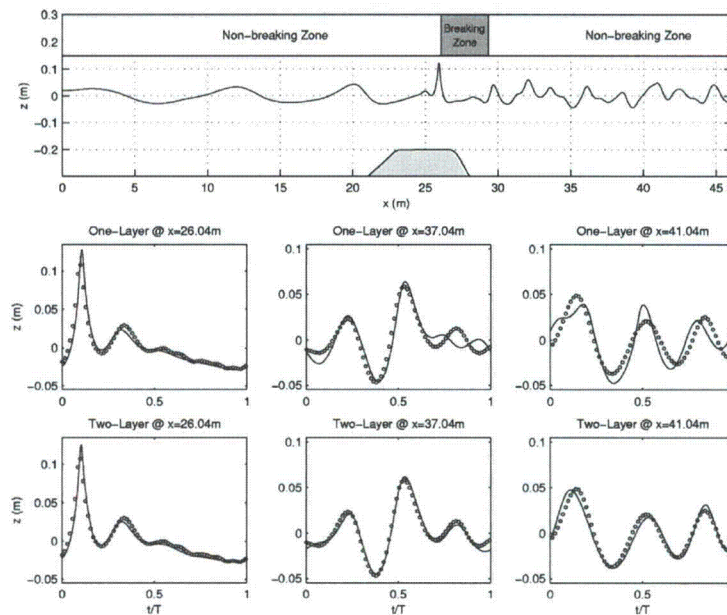


Fig. 8. Comparison with experimental data from Dingemans submerged step. Top subplot gives snapshot of numerical free surface, as well as breaking region. Middle row gives one-layer comparisons and last row gives two-layer comparisons. One- and two-layer results are given with solid lines and experimental data with circles.

1HD Wave Breaking over Bar

As described in Kennedy et al. (2000), the breaking initiation criteria for the eddy viscosity breaking model, stated in terms of η_b , depends on whether the wave is breaking on a constant slope (as discussed above) or breaking over a bar-type feature. With the modifications given in this paper, including the breaking initiation given in terms of local free surface slope, this does not appear to be the case. The single recommended value works for both slope and bar tests. Here, the numerical models are compared with the submerged step experiments presented by Dingemans (1994). Note that this is the same setup as reported in Luth et al. (1994). The bathymetry is composed of a wavemaker depth of 0.86 m leading to a step with a front side slope of 1/20, a back slope of 1/10, and a minimum depth above the step of 0.2 m. The incident wave condition is $kh=0.55$ with a nondimensional amplitude of $a/h=0.072$.

For this case, both the one- and two-layer models are run. Fig. 8 summarizes the results and gives the experimental comparisons. The top subplot shows a snapshot of the free surface, and also gives the breaking region. The experimentally observed breaking region between $x=26$ and 29 m matches the numerically predicted region very well. Note that for the numerical models to reach convergence, an extremely fine grid was required: 400 points per wave at the wavemaker, or $dx=0.024$ m. The reason for this required very fine grid is that, for this case, the breaking

threshold is just barely met, requiring a very precise evaluation of the wave slope. Using a more practical resolution, 100 points per incident wave (which gives roughly 10 points in the crest immediately before breaking), similar accuracy is achieved with the breaking initiation reduced to $\xi_1=0.5$.

Looking to the free surface comparisons in Fig. 8, the two-layer model shows higher agreement with experiment behind the bar. This increase in agreement is related to the release of locked higher harmonics after the wave breaks and passes into the deep water behind the bar. Once free, these higher harmonics travel according to the linear dispersion relation, which the one-layer model predicts inaccurately for the third and higher harmonics (third harmonic has $kh=2.5$ behind the bar).

Random Wave Breaking

In this section, the numerical model is compared with field data obtained during the SwashX experiments (Raubenhier 2002). The beach profile is shown in the top plot of Fig. 9. Here, the spectral transformation as well as the wave height through the surf zone are examined. A 15 min segment of the recorded field data is recreated numerically. The numerical recreation uses as input the spectral decomposition of the field data, which is a linear superposition of many frequencies with varying amplitude.

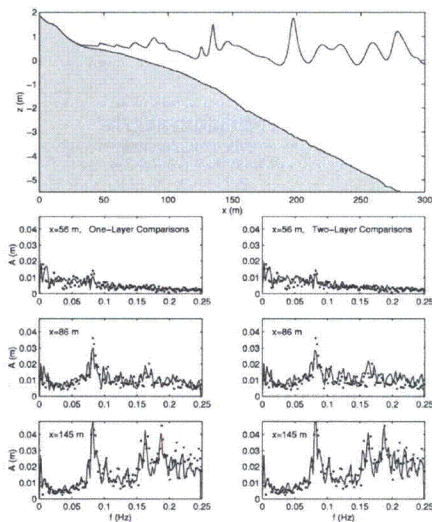


Fig. 9. Comparison with SwashX field data. Top plot shows spatial snapshot from two-layer model, where measured beach profile is given in grey. Lower subplots compare discrete amplitude spectrums at different locations from numerics (solid line) and measured data (dots), where one-layer comparisons are on left and two-layer are on right. All spectrums use identical frequency spacings and are filtered.

Thus, the numerical recreation suffers with this linear superposition, as most certainly some of the field energy is locked.

In the lower subplots of Fig. 9, spectral comparisons with the numerical and field data are made, for both the one- and two-layer models. Two items become evident: (1) the Boussinesq-type model with the employed breaking scheme does a very good job at capturing the spectral transformation through the surf zone including infragravity wave energy, and (2) the one- and two-layer models show equivalent agreement in light of the accuracy of the field data and the uncertainty in the numerical wave input condition.

While the above discussion looks at the detail of the wave field, it is also useful to examine the mean quantities. Fig. 10 compares mean surface and significant wave height. Again both models do a reasonable job at recreating the field site. The trends in wave height mimic previously analyzed data, with the two-layer model predicting larger values in the outer surf, due to better shoaling representation and a break point in shallower water. While the differences between the model results are clear and arguably significant, this comparison indicates that the errors in the one-layer model are likely on the order of those associated with the ability to recreate field conditions and in the measured field data itself. However, the two-layer model has a demonstrated higher accuracy, and preference should be given to its use when practical.

Conclusions

A slightly modified version of the eddy viscosity breaking model (Kennedy et al. 2000) is employed here in a high-order Boussinesq-type model: the two-layer model of Lynett and Liu (2004a). Numerous simulations are run and compared with the highly nonlinear Boussinesq-type model, or the one-layer model.

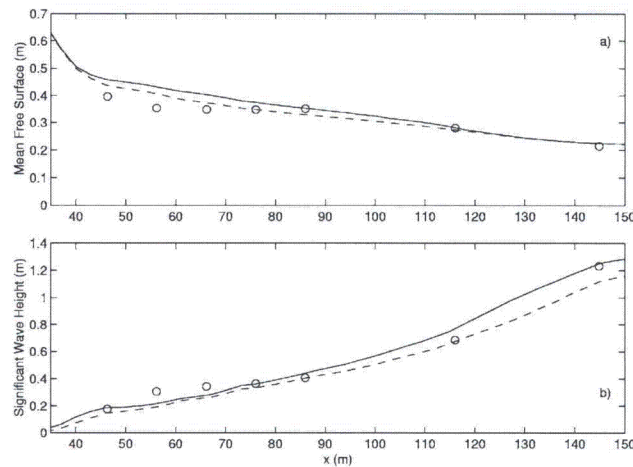


Fig. 10. Numerical-field comparisons between mean free surface (a) and wave height (b). Measured data are given by circles; one-layer model by dashed line; and two-layer model by solid line. x coordinate is same as shown in Fig. 9.

The documented over-shoaling of the one-layer model for regular waves is shown to be due to an overamplification of the fifth and higher harmonics in a region immediately seaward of breaking. These high-order nonlinear components are better captured in the two-layer model, which exhibits closer agreement with experimental data for both monochromatic and cnoidal waves. With wave breaking over a step, breaking does start using a single initiation threshold parameter for both step and slope breaking. Better accuracy is seen in the two-layer model behind the step, where high kh waves propagate as free waves. Finally, the SwashX field conditions are recreated approximately, and the Boussinesq-type model shows its ability to capture the spectral transformation of a wave field through the surf zone, without favoring the higher-order model.

Acknowledgments

The writer would like to thank Dr. Britt Raubenhiemer for providing the raw data from the SwashX experiments, which were funded by the Office of Naval Research. The research presented here was partially supported by a grant from the National Science Foundation (Grant No. CTS-0427115).

Appendix I. Inclusion of Viscosity Terms in Boussinesq Derivation

The goal of this section is to derive a set of equations by integrating the primitive equations of motion in the vertical direction. The sole difference between this derivation, and that given in Lynett and Liu (2004a), is that the viscosity term is not truncated in the momentum equations. It is noted that although the derivation presented here employs just two layers, the procedure is directly extendable to any arbitrary number of layers (Lynett and Liu 2004b). The flow region is divided by an interface, $z' = \eta'$. The resulting upper layer has a characteristic thickness d_1 (all variables contained entirely in this layer will be denoted with the subscript "1"), while the lower layer has a thickness d_2 (variables in this layer denoted by the subscript "2"). The determination of the location of the interface constitutes a part of the formulation of the model equations. Utilizing the layer thicknesses d_1 and d_2 as the vertical length scales in the upper and lower layer, respectively, the characteristic length of the wave l_0 as the horizontal length scale, h_0 as the characteristic water depth, $l_0/\sqrt{gh_0}$ as the time scale, and the characteristic wave amplitude a_0 as the scale of wave motion, we can define the following dimensionless variables:

$$(x, y) = (x', y')/l_0, \quad z_n = z'/d_n, \quad t = \sqrt{gh_0}t'/l_0$$

$$h = h'/h_0, \quad \zeta = \zeta'/a_0, \quad \eta = \eta'/d_1$$

$$(U_n, V_n) = (U'_n, V'_n)/(\epsilon_n \sqrt{gh_0}), \quad W_n = W'_n/(\epsilon_n \mu_n \sqrt{gh_0})$$

$$p_n = p'/\rho g a_0 \quad (6)$$

in which the subscript $n=1, 2$ indicates the layer index; (U_n, V_n) represent the horizontal velocity components in the different layers; W_n =vertical velocity component; and p_n =pressure. Note that the vertical coordinate, z_n , is scaled differently in each layer. Two dimensionless parameters have been introduced in Eq. (6), i.e.

$$\epsilon_n = a_0/h_0, \quad \mu_n = h_0/l_0 \quad (7)$$

Assuming that the viscous effects are not insignificant, the wave motion can be described by the continuity equation and the Navier–Stokes equation, i.e.

$$\frac{d_n}{h_0} \nabla \cdot \mathbf{U}_n + \frac{\partial W_n}{\partial z_n} = 0 \quad (8)$$

$$\frac{\partial \mathbf{U}_n}{\partial t} + \epsilon_n \mathbf{U}_n \cdot \nabla \mathbf{U}_n + \epsilon_n W_n \frac{\partial \mathbf{U}_n}{\partial z_n} = -\nabla p_n + \nu_n \nabla_n^2 \mathbf{U}_n \quad (9)$$

$$\begin{aligned} & \mu_n^2 \left(\frac{\partial W_n}{\partial t} + \epsilon_n \mathbf{U}_n \cdot \nabla W_n \right) + \epsilon_n \mu_n^2 W_n \frac{\partial W_n}{\partial z_n} \\ & = - \left(\frac{\partial p_n}{\partial z_n} + \frac{1}{\epsilon_n} \right) + \mu_n^2 \nu_n \nabla_n^2 W_n \end{aligned} \quad (10)$$

where $\mu_n^2 = d_n h_0 / l_0^2$; $\epsilon_n = a_0 / d_n$; $\mathbf{U}_n = (U_n, V_n)$ denotes horizontal velocity vector; $\nabla = (\partial/\partial x, \partial/\partial y)$ =horizontal gradient vector; $\nabla_n^2 = (\partial^2/\partial x^2 + \partial^2/\partial y^2 + \partial^2/\partial z_n^2)$; and ν_n =dimensionless, layer dependent viscosity equal to $\nu'_n / (l_0 \sqrt{gh_0})$; where ν'_n =dimensional viscosity. It is remarked here that ν'_n will eventually be specified through an eddy viscosity type formulation.

Derivation of the vertical profiles of velocity and the approximate continuity equation are based only on Eq. (8) and boundary conditions, and are thus unchanged from that given in Lynett and Liu (2004a). The eddy viscosity included in the primitive equations above is interpreted as acting in the body of the fluid, away from the boundaries. The bottom friction model given in Eq. (5) is expected to approximately include bottom boundary layer dissipation. It is not sought here to modify the bottom boundary condition such that the velocity profile in this region is better modeled, as done in Liu and Orfila (2004).

Working through the perturbation Boussinesq derivation, with the assumption of a constant eddy viscosity in space, the pressure profile in the upper layer is modified to

$$\begin{aligned} p_1 = & \zeta - \frac{z_1}{\epsilon_1} + \mu_1^2 \{ \dots \} \\ & + \mu_n^2 \nu_n \left\{ \frac{1}{2} (\epsilon_1^2 \zeta^2 - z_1^2) \nabla^2 S_1 + (\epsilon_1 \zeta - z_1) \nabla^2 T_1 \right\} \\ & + O(\mu_n^2 \mu_n^2, \mu_n^4), \quad \eta < z_1 < \epsilon_1 \zeta \end{aligned} \quad (11)$$

where $\nabla^2 = (\partial^2/\partial x^2 + \partial^2/\partial y^2)$. This pressure profile leads to the new momentum equation

$$\begin{aligned} \frac{\partial \mathbf{u}_1}{\partial t} + \frac{\epsilon_n}{2} \nabla (\mathbf{u}_1 \cdot \mathbf{u}_1) + \nabla \zeta + \mu_1^2 \{ \dots \} \\ + \nu_n \left[\frac{h_0}{d_1} \nabla S_1 - \nabla^2 \mathbf{u}_1 - \mu_n^2 \nabla^2 \left(\frac{\kappa_1^2}{2} \nabla S_1 + \kappa_1 \nabla T_1 \right) \right. \\ \left. + \mu_n^2 \nabla \left(\frac{1}{2} \epsilon_1^2 \zeta^2 \nabla^2 S_1 + \epsilon_1 \zeta \nabla^2 T_1 \right) \right] = O(\mu_n^3 \mu_1^2) \end{aligned} \quad (12)$$

In the above equations the neglected terms in the $\{ \dots \}$ can be found in Lynett and Liu (2004a), or any highly nonlinear extended Boussinesq derivation.

Appendix II. Wave Breaking Formulation

The breaking term in the momentum equation is given by $\mathbf{R}_b = [R_{bx}, R_{by}]$, where

$$R_{bx} = \frac{1}{H} \{ [v(Hu_x)]_x + 0.5[v(Hu_x)]_y + v(Hu_x)_{xx} \} \quad (13)$$

$$R_{by} = \frac{1}{H} \{ [v(Hu_y)]_y + 0.5[v(Hu_y)]_x + v(Hu_y)_{yy} \} \quad (14)$$

The viscosity, ν , is

$$\nu = B\delta^2 H \zeta_t \quad (15)$$

where

$$B = \begin{cases} 1, & \zeta_t \geq 2\zeta_t^* \\ \zeta_t/\zeta_t^* - 1, & \zeta_t^* < \zeta_t \leq 2\zeta_t^* \\ 0, & \zeta_t \leq \zeta_t^* \end{cases}$$

and

$$\zeta_t^* = \begin{cases} \zeta_t^F, & t - t_0 \geq T^* \\ \zeta_t^F + \frac{t - t_0}{T^*} (\zeta_t^I - \zeta_t^F), & 0 \leq t - t_0 < T^* \end{cases}$$

To this point, the formulation, as given by the above equations, is identical to that presented by Kennedy et al. (2000). For the two-layer model, the following parameter values are found to yield the best agreement with experiment:

$$\begin{aligned} \delta &= 10, \quad T^* = 10\sqrt{H/g} \\ \zeta_t^I &= 0.5\sqrt{gH}, \quad \zeta_t^F = 0.05\sqrt{gH} \end{aligned} \quad (16)$$

Furthermore, breaking cannot initiate unless

$$\sqrt{\zeta_x^2 + \zeta_y^2} \geq 0.60 \quad (17)$$

This criteria is enforced by first checking if the wave in question is already breaking; if it is not, the slope threshold must be met for any further breaking model calculations to be performed. The breaking model is utilized in a semiexplicit manner, meaning that the viscosity at time level $n+1$ is calculated with ζ values from time level n . The remaining terms in \mathbf{R}_b are calculated in an implicit manner. It is reiterated here that the above parameter set is tuned for the two-layer model, and transference of these parameters into a different model with different nonlinear properties will likely yield different results.

Appendix III. Numerical Simulation Parameters

Table 1 provides the incident water depth (h_0), wavelength (L_0), constant grid length (Δx), and time step (Δt) for all results presented in this paper.

Table 1. Numerical Simulation Parameters.

	h_0 (m)	L_0 (m)	Δx (m)	Δt (s)
Solitary wave (Fig. 2)	1.0	≈ 7	0.10	0.020
H-S 031041 (Fig. 4)	0.36	6.1	0.012	0.0035
H-S 041041 (Fig. 4)	0.36	4.5	0.012	0.0035
H-S 051041 (Fig. 4)	0.36	3.5	0.012	0.0035
H-S 061071 (Fig. 4)	0.36	2.9	0.012	0.0035
H-S A10112 (Fig. 4)	0.36	1.4	0.012	0.0035
T-K spiller (Fig. 6)	0.40	5.3	0.026	0.0067
T-K plunger (Fig. 7)	0.40	15	0.030	0.0077
Submerged step (Fig. 8)	0.86	9.9	0.024	0.0043
SwashX (Fig. 9)	6.7	≈ 70	0.34	0.021

References

- Agnon, Y., Madsen, P. A., and Schäffer, H. (1999). "A new approach to high order Boussinesq models." *J. Fluid Mech.*, 399, 319–333.
- Basterretxea, G., Orfila, A., Jordi, A., Casas, B., Lynett, P. L., P. L.-F., Duarte, C. M., and Tintor, J. (2004). "Seasonal dynamics of a microtidal pocket beach with posidonia oceanica seabeds (Mallorca, Spain)." *J. Coastal Res.*, 20(4), 1155–1164.
- Beji, S., and Battjes, J. A. (1994). "Numerical simulation of nonlinear waves propagation over a bar." *Coastal Eng.*, 23, 116.
- Bredmose, H., Schäffer, H. A., and Madsen, P. A. (2004). "Boussinesq evolution equations: numerical efficiency, breaking and amplitude dispersion." *Coastal Eng.*, 51(11–12), 1117–1142.
- Chen, Q., Kirby, J. T., Dalrymple, R. A., Shi, F., and Thornton, E. B. (2003). "Boussinesq modeling of longshore currents." *J. Geophys. Res.*, 108(C11), 3362.
- Dingemans, M. (1994). "Comparison of computations with Boussinesq-like models and laboratory measurements." *Mast-G&M Note No H1684*, Delft Hydraulics, Delft, The Netherlands.
- Gobbi, M. F., Kirby, J. T., and Wei, G. (2000). "A fully nonlinear Boussinesq model for surface waves. Part II: Extension to $O(kh^4)$." *J. Fluid Mech.*, 405, 182–210.
- Grilli, S. T., Subramanya, R., Svendsen, I. A., and Veeramony, J. (1994). "Shoaling of solitary waves on plane beaches." *J. Waterw., Port, Coastal, Ocean Eng.*, 120(6), 609–628.
- Hansen, J. B., and Svendsen, I. A. (1979). "Regular waves in shoaling water: Experimental data." *Tech. Rep. ISVA Ser. 21*, Technical Univ. of Denmark, Denmark.
- Kennedy, A. B., Chen, Q., Kirby, J. T., and Dalrymple, R. A. (2000). "Boussinesq modeling of wave transformation, breaking and runup. I: 1D." *J. Waterw., Port, Coastal, Ocean Eng.*, 126(1), 39–47.
- Kennedy, A. B., Kirby, J. T., Chen, Q., and Dalrymple, R. A. (2001). "Boussinesq-type equations with improved nonlinear behaviour." *Wave Motion*, 33, 225–243.
- Lin, P., and Liu, P. L.-F. (1998). "A numerical study of breaking waves in the surf zone." *J. Fluid Mech.*, 359, 239–264.
- Liu, P. L.-F. (1994). "Model equations for wave propagation from deep to shallow water." *Advances in coastal engineering* P. L.-F. Liu, ed., Vol. 1, World Scientific, Singapore, 125–157.
- Liu, P. L.-F., and Orfila, A. (2004). "Viscous effects on transient long wave propagation." *J. Fluid Mech.*, 520, 83–92.
- Luth, H. R., Klopman, G., and Kitou, N. (1994). "Project 13G: Kinematics of waves breaking partially on an offshore bar; LDV measurements for wave with and without net onshore current." *Delft Hydraulics Rep. H1573*, Delft, The Netherlands.
- Lynett, P., and Liu, P. L.-F. (2004a). "A two-layer approach to water wave modeling." *Proc. R. Soc. London, Ser. A*, 460, 2637–2669.
- Lynett, P., and Liu, P. L.-F. (2004b). "Linear analysis of the multi-layer model." *Coastal Eng.*, 51(6), 439–454.
- Lynett, P., Liu, P. L.-F., Losada, I., and Vidal, C. (2000). "Solitary wave interaction with porous breakwaters." *J. Waterw., Port, Coastal,*

- Ocean Eng.*, 126(6), 314–322.
- Lynch, P. Wu, T.-R., and Liu, P. L.-F. (2002). "Modeling wave runup with depth-integrated equations." *Coastal Eng.*, 46(2), 89–107.
- Madsen, P. A., Bingham, H. B., and Liu, H. (2002). "A new Boussinesq method for fully nonlinear waves from shallow to deep water." *J. Fluid Mech.*, 462, 1–30.
- Madsen, P. A., and Sorensen, O. R. (1992). "A new form of the Boussinesq equations with improved linear dispersion characteristics. Part II: A slowly varying bathymetry." *Coastal Eng.*, 18, 183–204.
- Nwogu, O. (1993). "Alternative form of Boussinesq equations for near-shore wave propagation." *J. Waterw., Port, Coastal, Ocean Eng.*, 119(6), 618–638.
- Raubenheimer, B. (2002). "Observations and predictions of fluid velocities in the surf and swash zones." *J. Geophys. Res.*, 107, 3190.
- Schäffler, H. A., Madsen, P. A., and Deigaard, R. (1993). "A Boussinesq model for waves breaking in shallow water." *Coastal Eng.*, 20, 185–202.
- Sorensen, O. R., Madsen, P. A., and Schäffler, H. A. (1999). "Nearshore wave dynamics simulated by Boussinesq-type models." *Proc., ICCE'98, ASCE, Reston, Va.*, 272–285.
- Ting, F. C.-K., and Kirby, J. T. (1995). "Dynamics of surf-zone turbulence in a strong plunging breaker." *Coastal Eng.*, 24, 177–204.
- Ting, F. C. K., and Kirby, J. T. (1996). "Dynamics of surf-zone turbulence in a spilling breaker." *Coastal Eng.*, 27, 131–160.
- Wei, G., Kirby, J. T., Grilli, S. T., and Subramanya, R. (1995). "A fully nonlinear Boussinesq model for surface waves. Part I. Highly nonlinear unsteady waves." *J. Fluid Mech.*, 294, 71–92.
- Zhao, Q., Armfield, S., and Tanimoto, K. (2004). "Numerical simulation of breaking waves by a multi-scale turbulence model." *Coastal Eng.*, 51, 53–80.



Modeling wave runup with depth-integrated equations

Patrick J. Lynett, Tso-Ren Wu, Philip L.-F. Liu*

*Joseph DeFrees Hydraulics Lab., School of Civil and Environmental Engineering, Cornell University,
223 Hollister Hall, Ithaca, NY 14853, USA*

Received 13 June 2001; received in revised form 14 March 2002; accepted 27 March 2002

Abstract

In this paper, a moving boundary technique is developed to investigate wave runup and rundown with depth-integrated equations. Highly nonlinear and weakly dispersive equations are solved using a high-order finite difference scheme. An eddy viscosity model is adopted for wave breaking so as to investigate breaking wave runup. The moving boundary technique utilizes linear extrapolation through the wet–dry boundary and into the dry region. Nonbreaking and breaking solitary wave runup is accurately predicted by the proposed model, yielding a validation of both the wave breaking parameterization and the moving boundary technique. Two-dimensional wave runup in a parabolic basin and around a conical island is investigated, and agreement with published data is excellent. Finally, the propagation and runup of a solitary wave in a trapezoidal channel is examined. © 2002 Elsevier Science B.V. All rights reserved.

Keywords: Wave runup; Breaking waves; Boussinesq equations

1. Introduction

The past decade saw the advent and widespread applications of Boussinesq-type equation models for studying wave propagation in one and two horizontal dimensions. The conventional Boussinesq equations (Peregrine, 1967) had two major limitations: (1) The depth-averaged model poorly described the frequency dispersion of wave propagation in intermediate depths, and (2) the weakly nonlinear assumption limited the largest wave height that could accurately be modeled. The dispersion properties of the conventional Boussinesq equation model have been improved by modifying the dispersive terms (Madsen and Sorensen, 1992) or using a reference velocity at a specified depth (Nwogu, 1993). These techniques yield a set of equa-

tions whose linear dispersion relation can be adjusted such that the resulting intermediate-depth dispersion characteristics are close to the true linear solution. Liu (1994) and Wei et al. (1995) presented a set of highly nonlinear Boussinesq-type equations that not only can be applied to intermediate water depth but also are capable of simulating wave propagation with strong nonlinear interaction. Wei et al. (1995) have also developed a high-order numerical scheme to solve these equations. All of these efforts successfully extended the usage of the Boussinesq-type equation model, such that wave evolution from relatively deep water to the breaking point could be accurately captured.

Wave propagation using Boussinesq-type equations is now well simulated and understood, but the process of runup and rundown is not. Shoreline boundaries may move significantly under the temporal influence of incident waves. A numerical model should be able

* Corresponding author.

E-mail address: pl3@cornell.edu (P.L.-F. Liu).

to take into account such variations correctly in order to obtain realistic flow patterns.

Researchers generally use a fixed grid, finite difference or finite element method to solve the Boussinesq-type equations. Using a fixed grid numerical model to solve a moving boundary problem can lead to difficulties related to the loss of mass conservation and instabilities in the computations (Leendertse, 1987) as a result of imposing discrete fixed increments to the extent of wetting and drying areas (Balzano, 1998). To reduce the computational instabilities near the wet–dry interface, some researchers added bottom friction into the momentum equations. However, a numerical model should be stable even without using bottom friction dissipation.

Zelt (1991) used a Lagrangian form of the Boussinesq-type equations to simulate shoreline movement. This model produced maximum runup values that compared well with experimental values, but the shape of the wave as it traveled up the slope did not compare as favorably. A handful of others have utilized Lagrangian techniques with depth-integrated equation models to simulate a moving shoreline (e.g., Petera and Nassehi, 1996; Gopalakrishnan, 1989). Another treatment of moving boundary problem is employing a slot or permeable-seabed technique (Tao, 1983, 1984). The first application of the permeable slot with a Boussinesq-type model (Madsen et al., 1997) yielded runup errors on the order of 10% of the maximum. Modifications have been made to this permeable slot technique (Kennedy et al., 2000), increasing the accuracy, but it was also shown that the empirical coefficients that govern the technique cannot be universally determined, due to numerical stability problems (Chen et al., 2000).

In this paper, we present a new moving boundary treatment for wave propagation models. The moving boundary algorithm is conceptually simple, easy to implement, and can be employed by different numerical schemes (i.e., finite difference and finite element) utilizing depth-integrated equations. The moving boundary technique utilizes linear extrapolation near the wet–dry boundary, thereby allowing the real boundary location to exist in-between nodal points. The model is compared with the classic Carrier and Greenspan (1958) solution for monochromatic long wave runup on a constant slope. As another one horizontal dimension test, the solitary wave runup

experiments of Synolakis (1986, 1987), which range from nonbreaking to breaking waves, are recreated numerically. To test the accuracy of two horizontal dimension moving boundary problems, three cases are examined: wave oscillations in a parabolic basin, solitary wave interaction with a conical island, and wave evolution in a trapezoidal channel.

2. Model equations and numerical scheme

The model equations to be utilized in this paper are the highly nonlinear, weakly dispersive wave equations, given in dimensional form (e.g., Liu, 1994):

$$\zeta_t + E = 0, \quad \mathbf{u}_{xt} + \mathbf{F} = 0 \quad (1)$$

where

$$E = \nabla \cdot \{ (h + \zeta) \mathbf{u}_x \} - \nabla \cdot \left\{ (h + \zeta) \times \left[\left(\frac{1}{6} (\zeta^2 - \zeta h + h^2) - \frac{1}{2} z_x^2 \right) \nabla (\nabla \cdot \mathbf{u}_x) + \left[\frac{1}{2} (\zeta - h) - z_x \right] \nabla [\nabla \cdot (h \mathbf{u}_x)] \right] \right\} \quad (2)$$

$$\begin{aligned} \mathbf{F} = & \mathbf{u}_x \cdot \nabla \mathbf{u}_x + g \nabla \zeta \\ & + \left\{ \frac{1}{2} z_x^2 \nabla (\nabla \cdot \mathbf{u}_{xt}) + z_x \nabla [\nabla \cdot (h \mathbf{u}_{xt})] \right\} \\ & + \{ [\nabla \cdot (h \mathbf{u}_x)] \nabla [\nabla \cdot (h \mathbf{u}_x)] - \nabla [\zeta (\nabla \cdot (h \mathbf{u}_{xt}))] \\ & + (\mathbf{u}_x \cdot \nabla z_x) \nabla [\nabla \cdot (h \mathbf{u}_x)] \} \\ & + \left\{ z_x \nabla [\mathbf{u}_x \cdot \nabla (\nabla \cdot (h \mathbf{u}_x))] \right. \\ & \left. + z_x (\mathbf{u}_x \cdot \nabla z_x) \nabla (\nabla \cdot \mathbf{u}_x) + \frac{z_x^2}{2} \nabla [\mathbf{u}_x \cdot \nabla (\nabla \cdot \mathbf{u}_x)] \right\} \\ & + \nabla \left\{ -\frac{\zeta^2}{2} \nabla \cdot \mathbf{u}_{xt} - \zeta \mathbf{u}_x \cdot \nabla [\nabla \cdot (h \mathbf{u}_x)] + \right. \\ & \left. + \zeta [\nabla \cdot (h \mathbf{u}_x)] \nabla \cdot \mathbf{u}_x \right\} \\ & + \nabla \left\{ \frac{\zeta^2}{2} [(\nabla \cdot \mathbf{u}_x)^2 - \mathbf{u}_x \cdot \nabla (\nabla \cdot \mathbf{u}_x)] \right\} \quad (3) \end{aligned}$$

where ζ is the free surface elevation, h is the local water depth, and $\mathbf{u}_x = (u_x, v_x)$ is the reference horizontal

velocity. The velocity is evaluated at the elevation $z_x = -0.531h$, as recommended by Nwogu (1993), based on optimum agreement of the governing equations with the linear dispersion relation. Wherever h is negative (initially dry land), this relationship is set to $z_x = -h$, so as to avoid the evaluation of u_x under the seafloor. Two dimensionless, characteristic coefficients can be given as

$$\varepsilon = a/h, \quad \mu = h/\lambda \quad (4)$$

where a is the wave amplitude and λ is the horizontal length scale. ε is indicative of the importance of nonlinearity and is assumed to be $O(1)$ in Eqs. (1)–(3); μ represents frequency dispersion and $O(\mu^2) \ll 1$. The order of magnitude of accuracy of these equations is $O(\mu^4)$. Note that the above momentum equation, Eq. (3), is slightly different from that presented by Wei et al. (1995). This difference is caused by the omission of some $O(\mu^2)$ terms in Wei et al. in their conversion of $1/2 \nabla(\mathbf{u}_x^2)$ to $\mathbf{u}_x \cdot \nabla \mathbf{u}_x$. These neglected terms vanish only if $\nabla \times \mathbf{u}_x = 0$, which, however, does not imply the irrotationality of the flow field. In fact, $\nabla \times \mathbf{u}_x$ is of $O(\mu^2)$. A more mathematically detailed explanation can be found in Hsiao and Liu (in press).

The parameterizations, R_f and R_b , account for the effects of bottom friction and wave breaking, respectively. Bottom friction is described in the quadratic form:

$$R_f = \frac{f}{h + \zeta} \mathbf{u}_x |\mathbf{u}_x| \quad (5)$$

where f is a bottom friction coefficient, typically in the range of 10^{-3} – 10^{-2} , depending on the Reynolds number and seafloor condition. To simulate the effects of wave breaking, the eddy viscosity model (Zelt, 1991; Kennedy et al., 2000) is used here. Readers are directed to Kennedy et al. (2000) for a thorough description and validation of the breaking model, and the coefficients and thresholds given therein are used for all the simulations presented in this paper.

The model used for all the simulations in this paper is nicknamed COULWAVE, for Cornell University Long and Intermediate Wave Modeling Package. This model has the ability to simulate a wide range of long wave problems, including interaction with porous coastal structures (Lynett et al., 2000), wave gener-

ation by seafloor movements such as landslides (Lynett and Liu, in press (a)), and internal wave propagation and evolution (Lynett and Liu, in press (b)). The numerical model utilizes a predictor–corrector time-stepping scheme, accurate to $(\Delta t)^4$, where Δt is the time step. Similar numerical schemes have been successfully employed by Wei et al. (1995) for modeling surface wave phenomena. Assume now that the numerical simulation is at time n , where all physical values (free surface and velocity) at time n , and previous times, are known. To determine the physical values at the next time step $n+1$, the explicit predictor is first applied:

$$\zeta_{i,j}^{n+1} = \zeta_{i,j}^n - \frac{\Delta t}{12} (23E_{i,j}^n - 16E_{i,j}^{n-1} + 5E_{i,j}^{n-2}) \quad (6)$$

$$\begin{aligned} (\mathbf{u}_x)_{i,j}^{n+1} = & (\mathbf{u}_x)_{i,j}^n - \frac{\Delta t}{12} (23\mathbf{F}_{i,j}^n - 16\mathbf{F}_{i,j}^{n-1} \\ & + 5\mathbf{F}_{i,j}^{n-2}) \end{aligned} \quad (7)$$

where n represents the time index, i the x -space index, and j the y -space index (x and y make up the horizontal plane). Thus, in order to start a simulation, initial conditions from three time levels are required. Now, with an initial estimate of the physical values at the new time level, the implicit corrector equations can be applied:

$$\begin{aligned} \zeta_{i,j}^{n+1} = & \zeta_{i,j}^n - \frac{\Delta t}{24} (9E_{i,j}^{n+1} + 19E_{i,j}^n - 5E_{i,j}^{n-1} \\ & + E_{i,j}^{n-2}) \end{aligned} \quad (8)$$

$$\begin{aligned} (\mathbf{u}_x)_{i,j}^{n+1} = & (\mathbf{u}_x)_{i,j}^n - \frac{\Delta t}{24} (9\mathbf{F}_{i,j}^{n+1} + 19\mathbf{F}_{i,j}^n \\ & - 5\mathbf{F}_{i,j}^{n-1} + \mathbf{F}_{i,j}^{n-2}) \end{aligned} \quad (9)$$

These equations are solved with Jacobi iteration, so the calculation of E^{n+1} and \mathbf{F}^{n+1} is performed with the free surface and velocity values from the previous iteration. To implement the algorithm, an additional grouping of the mixed space and time derivatives in the dispersive terms is required. Wei et al.'s (1995) paper gives a good description and justification of this grouping procedure.

Spatial differencing in the numerical model employs centered finite differences. All first-order spatial derivatives are differenced with fourth-order ($\Delta x^4 = \Delta y^4$) accurate equations, which are five-point differences. Second-order spatial derivatives are approximated with three-point centered finite difference equations, which are second-order accurate. The second-order spatial derivatives are taken to lower-order accuracy because these derivatives only appear in dispersive terms. The “combined” dispersive-numerical error for the second-order derivatives is $O(\Delta x^2 \mu^2)$, which is less than the error associated with first-order spatial derivatives, $O(\Delta x^4)$, for all the grid spacings and wavelengths modeled in this paper.

3. Moving boundary algorithm

The development of the moving boundary algorithm presented in this paper began with a search for a scheme that allows for the wet–dry boundary to exist at any location, not restrictively at a node on a fixed grid. One method of achieving this is through dynamic regridding, using a Lagrangian approach. Methods such as this have been used in finite difference and finite element nonlinear shallow water (NLSW) and Boussinesq equation models (e.g., Petera and Nassehi, 1996; Zelt, 1991). Lagrangian moving boundary techniques require numerical flexibility, in terms of utilizing constantly changing space and time steps, to be implemented in conjunction with a Eulerian-type model. This flexibility is not present in the current numerical scheme, and is difficult to achieve due to the nature of the required high-order derivatives, and so a different approach is developed in this paper.

Owing to the significant number of derivatives calculated by the numerical model (~ 50 in 2D), it would be advantageous if the moving boundary scheme did not require any sort of special treatment of the derivatives near the wet–dry boundary (i.e., forward, backward, or low-order finite differences). To require, for example, directional differences at the boundary leads to abundant conditional statements, making the programming tedious and the runtime longer. Therefore, the five-point centered finite differences that are employed in the numerical model are desired to be used at all locations, including those

points near the shoreline, where neighboring nodes may be dry. With this in mind, the moving boundary scheme will employ a linear extrapolation of free surface displacement, ζ , and velocity components, u_x and v_x , from the fluid domain, through the wet–dry boundary, and into the dry region. Kowalik and Bang (1987) presented a similar approach of employing a linear extrapolation into the dry region, based on Sielecki and Wurtele’s (1970) earlier developments. Their model uses a leapfrog scheme to approximate the NLSW equations, and is limited to one-dimensional, nonbreaking problems. This paper will attempt to extend this idea to two horizontal dimension-breaking problems, using a high-order numerical model.

An extrapolation through the wet–dry boundary permits this boundary to exist in-between nodal points. Fig. 1 gives a numerical example of how the extrapolation is performed in a one-dimensional problem, showing a solitary wave interacting with a 1:20 slope. The free surface locations that are determined using the governing Eqs. (1)–(3) are shown by the solid line, whereas the linearly extrapolated points are shown by the dots. With extrapolated values of ζ and velocity components in the dry region, solving the model equations at wet nodes can proceed. When solving the model equations, five-point centered differences are employed to approximate the spatial derivatives. Although no derivatives are calculated at dry (extrapolated) points, the physical values of free surface and velocity at these points are used to evaluate derivatives at neighboring wet points. The determination of the location of the wet–dry boundary is performed once per time step, immediately after the predictor step. The moving boundary technique is numerically stable, and does not require any additional dissipative mechanisms.

The first step in the extrapolation boundary method is to determine a nodal boundary dividing an area where the model equations are to be solved (i.e., the wet region) and an area to be extrapolated (i.e., the dry region). The criteria employed to determine this dividing point is dependant on the total water depth, \mathcal{H} , where $\mathcal{H} = h + \zeta$. If $\mathcal{H} > \delta$, where δ is some threshold, the model equations will be applied at the node; otherwise, the physical variables at the node will be extrapolated from a neighboring node. The value of δ should be small; a value of $a_0/50$, where a_0

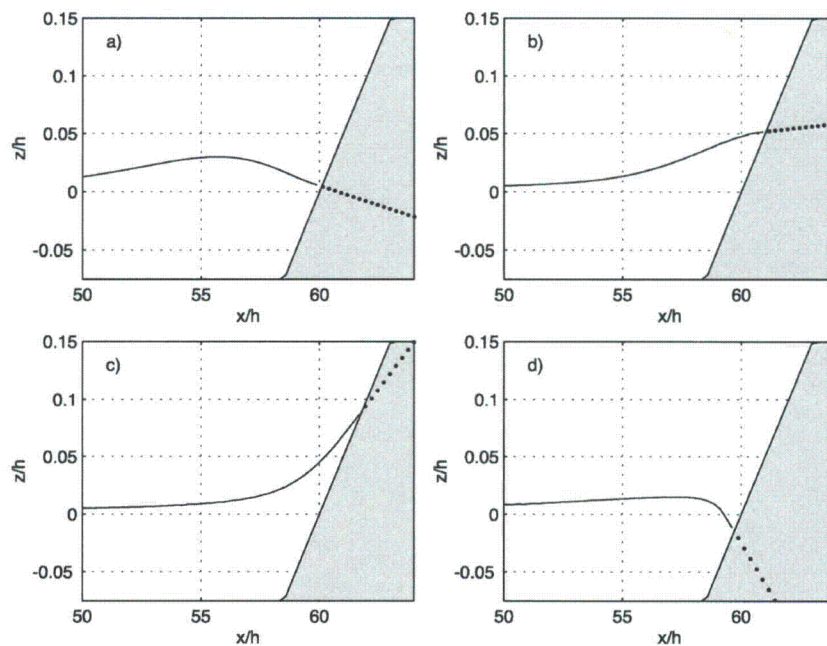


Fig. 1. Runup and rundown of a solitary wave, where extrapolated nodes are shown by the dots.

is the incident wave amplitude, was used for all simulations presented in this paper. This value is chosen based on stability. It was found that decreasing this value could occasionally cause stability problems, especially for simulations with strong wave breaking or ones that include bottom friction. The instability problems associated with these two parameterizations are due to the fact that they are inversely proportional to the total water depth. A very small total water depth may create an equally large dissipative momentum flux, which can lead to an overflow in the iterative numerical scheme. However, for nonbreaking simulations without bottom friction, a δ value of $a_0/5000$ could be stably employed. A convergence check, by changing δ , will be discussed briefly in the next section.

For the simple one-dimensional problem shown in Fig. 1, the extrapolation procedure is straightforward. Using the two wet points (where $\mathcal{H} > \delta$) nearest to the wet–dry boundary, a linear extrapolation into the dry (where $\mathcal{H} < \delta$) region is performed. For the two-dimensional case, the procedure is slightly more complex, but the logic is identical. The 2D extrapolation is performed by checking the surrounding eight points of a dry node. For each surrounding node that is wet, a 1D linear extrapolation is used to estimate the free surface at the dry node. Since more than one surrounding node can be wet, the free surface value at the dry node is taken to be the average of the 1D extrapolations. This procedure is simply repeated for the second layer of dry nodes, extrapolating from the just-extrapolated first layer of dry nodes. For both

1D and 2D cases, a four-point filter is passed over the extrapolated region, smoothing ζ , u_x , and v_x and eliminating possible slope discontinuities in the extrapolation. Additionally, there is one possible arrangement of wet and dry nodes that cannot be allowed to exist. When a wet node is grouped with dry nodes on both sides, i.e., if node i is wet and both $i-1$ and $i+1$ are dry, the extrapolation is impossible for both dry nodes. When this situation is developed, the wet node is no longer considered to be in the fluid domain, and its value will be extrapolated.

As the shoreline moves up and down the slope, the number of wet and dry points changes. For example, at time $n-1$, node $i-1$ is wet and node i is dry, and its free surface value has been extrapolated. Now, at time n , the new extrapolation for node i yields a total water depth greater than δ . Node i is therefore now a wet node, and its value is no longer extrapolated, but calculated by Eqs. (1)–(3).

As the extrapolated, dry points are solely a function of the neighboring wet points, the finite differences that incorporate these dry points cannot truly be thought of as centered finite differences. Let us consider a one horizontal dimension problem, and focus on six grid points, numbered from $i=-3$ to $i=2$. At the time that we take a snapshot, the shoreline exists somewhere between points $i=0$ and $i=1$. Points to the left of this point are wet ($i=-3, -2, -1, 0$), and points to the right are dry ($i=1, 2$). At the wet points, the governing equations, using the predictor–corrector scheme, are solved. At the dry points, the free surface and velocity are linearly extrapolated, and can be given as:

$$P_1 = 2P_0 - P_{-1} \quad (10)$$

$$P_2 = 3P_0 - 2P_{-1} \quad (11)$$

where P represents both ζ and u_x , and the subscripts represent the i -index. Substituting the extrapolated values of points $i=1$ and $i=2$ into the fourth-order first derivative difference equation:

$$\frac{\partial P_0}{\partial x} = \frac{P_{-2} - 8P_{-1} + 8P_1 - P_2}{12\Delta x} \quad (12)$$

yields, after some manipulation:

$$\frac{\partial P_0}{\partial x} = \frac{1}{6} \left[\frac{\partial P_0}{\partial x} \right]_{2B} + \frac{5}{6} \left[\frac{\partial P_0}{\partial x} \right]_{1B} \quad (13)$$

where $2B$ stands for the second-order backward (or upwind) finite difference:

$$\left[\frac{\partial P_0}{\partial x} \right]_{2B} = \frac{P_{-2} - 4P_{-1} + 3P_0}{2\Delta x} \quad (14)$$

and $1B$ stands for the first-order backward (or upwind) finite difference:

$$\left[\frac{\partial P_0}{\partial x} \right]_{1B} = \frac{-P_{-1} + P_0}{\Delta x} \quad (15)$$

Using the same approach, the derivative at $i=-1$ can be rewritten as:

$$\frac{\partial P_{-1}}{\partial x} = \frac{1}{2} \left[\frac{\partial P_0}{\partial x} \right]_{3T} + \frac{1}{3} \left[\frac{\partial P_0}{\partial x} \right]_{2C} + \frac{1}{6} \left[\frac{\partial P_0}{\partial x} \right]_{1B} \quad (16)$$

where $3T$ stands for the third-order tilted (in the backward direction) finite difference:

$$\left[\frac{\partial P_{-1}}{\partial x} \right]_{3T} = \frac{P_{-3} - 6P_{-2} + 3P_{-1} + 2P_0}{6\Delta x} \quad (17)$$

and $2C$ stands for the second-order centered finite difference:

$$\left[\frac{\partial P_{-1}}{\partial x} \right]_{2C} = \frac{-P_{-2} + P_0}{2\Delta x} \quad (18)$$

So clearly, hidden within the linear extrapolation, is leading order dissipation associated with the upwind differencing, even though a fourth-order centered difference is being taken. Note that the extrapolations are done for both free surface and velocity, so the moving boundary scheme will dissipate both momentum and mass.

The same analysis can be done for the second-order in space derivatives. At the point $i=0$, the curvature is given as

$$\frac{\partial^2 P_0}{\partial x^2} = \frac{P_{-1} - 2P_0 + P_1}{\Delta x^2} \quad (19)$$

which is, with the linear extrapolation of P_1 , exactly zero at this point. Therefore, at the first wet point, all second-order differences disappear, and the governing Eqs. (1)–(3) reduce to the nonlinear shallow water wave equations. Now, looking at the whole picture of first- and second-order spatial derivatives, we see that numerical dissipation is not as great as it might

appear. It was shown that the first spatial derivative at the first wet point, $\partial P_0/\partial x$, is in large part approximated by the first-order upwind finite difference, $[\partial P_0/\partial x]_{i,B}$. The leading numerical truncation error of the upwind difference is $(\Delta x/2)(\partial^2 P_0/\partial x^2)$, which is the source of the numerical dissipation in upwind schemes. However, at this first wet point, the second spatial derivative, $\partial^2 P_0/\partial x^2$, is forced to zero in the numerical model. The leading numerical truncation error of the second spatial derivative taken with a second-order centered difference formula is $(\Delta x^2/12)(\partial^4 P_0/\partial x^4)$. Therefore, the leading order, dissipative truncation error of the upwind difference at the first wet point is actually $(\Delta x/2)(\Delta x^2/12)(\partial^4 P_0/\partial x^4)$. At the second wet point, the first spatial derivative, $\partial P_{-1}/\partial x$, also incorporates upwind differencing (although its importance is five times less here as compared to the first wet point). As the second spatial derivative at this point is non-zero, there will at this point occur dissipation proportional to the second spatial derivative, equal to $(\Delta x/10)(\partial^2 P_{-1}/\partial x^2)$.

It is worth noting that these issues with leading order numerical dissipation associated with the linear extrapolation could be avoided by utilizing a higher-polynomial extrapolation. Unfortunately, these higher-order extrapolations created stability problems with breaking and near-breaking wave runup. As these waves approach the beach, typically the curvature of the free surface is large very near the shoreline. The large curvature created rapidly varying extrapolated values, which then led to numerical roundoff problems.

It would seem to be unnecessary to perform the linear extrapolation in the numerical model, as one could simply code a couple conditional statements, where if the current calculation node in the model is near the wet–dry boundary, use upwind differencing, instead of centered differencing. This too was attempted, but always resulted in $2\Delta x$ waves. It was found, through trial and error, that stability comes from the prediction of velocity in the dry region. In this numerical scheme:

$$(u_x)^{n+1} = f[(u_x)^{n+1}, (u_x)^n, (u_x)^{n-1}, (u_x)^{n-2}] \quad (20)$$

as well as a function of numerous other parameters. Let us say that at time n , the point i was dry. Now, at time $n+1$, the point i is wet. What are the previous values of velocity, at times $n-2$, $n-1$, and n , to use

in the predictor–corrector scheme? An answer of zero velocity would be most obvious, because physically, there was no fluid. Using a zero velocity at these times in the numerical model led to $2\Delta x$ waves. So for this type of model, a zero velocity at previous times does not work. Using the linearly extrapolated velocities at the previous times of $n-2$, $n-1$, and n works well. It could be argued that the velocities at the previous “dry” times should not be zero, in fact they should not be anything—they are undefined. Thus, this model is simply taking a reasonable guess at what the undefined velocity should be in order to yield a stable and accurate numerical model. The linear spatial extrapolation is not just important as a spatial extrapolation (which is equivalent to some combination of upwind differencing)—it is especially important as a temporal extrapolation.

As a primary check of the algorithm, its ability to conserve mass is analyzed. Mass is defined as the integral of the free surface elevation, not the integral of the total water depth. A range of solitary waves, from $0.01 < \epsilon < 0.4$ propagating up one-dimensional slopes of 1:10, 1:20, and 1:50 were checked for conservation of mass. Note that when referencing solitary waves, $\epsilon = H/h$, where H is the solitary wave height. The solitary wave is generated using the analytic formulas presented in Wei and Kirby (1995), which are derived from the weakly nonlinear, “extended” Boussinesq equations. Fig. 2 summarizes the conservation properties of these cases. Shown in this figure is the fractional change in mass of the soliton, after completely exiting the nearshore region. Thus, these fractions represent the change in mass, scaled by the initial mass, after interaction with the shoreline is over. There are two clear trends: (1) for a given slope, the error in conservation is larger with larger wave heights and (2) for a given wave height, the error is larger with milder slopes. Both of these trends are consistent with the expectation that the numerical error is larger when the curvature near the shoreline is larger.

A question that arises with examination of Fig. 2 is whether the small conservation errors will accumulate during a regular wave simulation, destroying the simulation accuracy. A test case with a sine-wave shoaling up a 1/10 slope was simulated, and is summarized in Fig. 3. The incident wave has a wave height/water depth = 0.1 and a wavelength/water

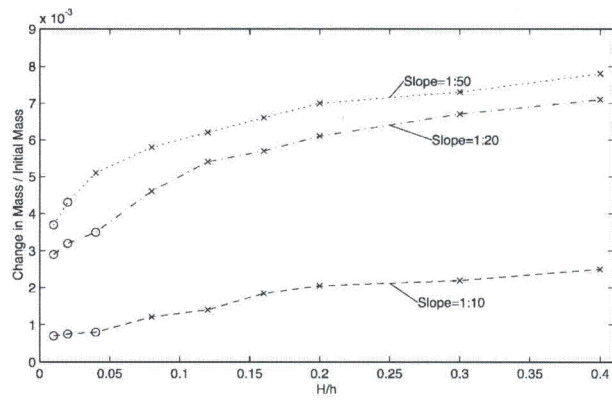


Fig. 2. Fractional change in mass for breaking and nonbreaking solitary waves interacting with three different planar slopes. Simulations where breaking occurs are indicated by the \times 's, nonbreaking results by the \circ 's.

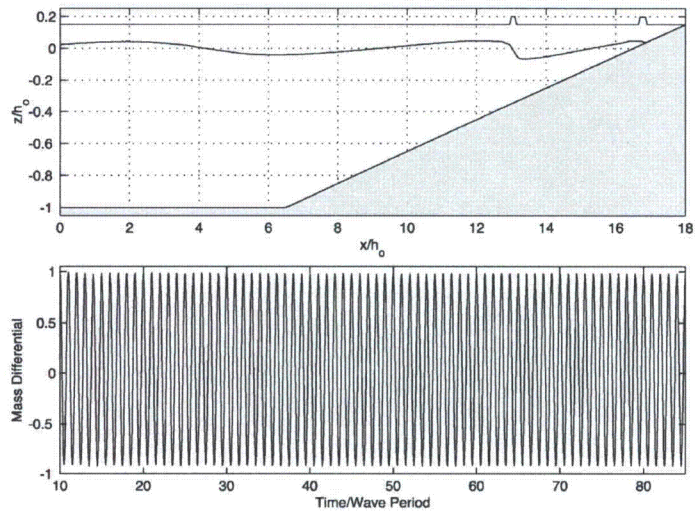


Fig. 3. Mass conservation check for a breaking period wave. The top subplot shows a spatial snapshot of the free surface, roughly 80 wave periods into the simulation, where the locations of breaking are given by the steps in the line plotted on $z/h_0 = 0.15$. The bottom plot gives the total mass fluctuation in the numerical domain as a function of time.

depth = 10, and breaks strongly while approaching the shoreline. The top plot of Fig. 3 is a snapshot of the free surface and also indicates the breaking locations. Note that a sponge layer is used as the left boundary. The bottom plot of the same figure shows the oscillation of mass in the entire numerical domain through 80 wave periods of time. The oscillation is due to the constant addition/subtraction of mass by the internal source wave generator. Clearly, no accumulation of errors occurs, as the oscillation remains regular for a large number of periods. In regard to this periodic, breaking simulation, numerical filtering was required for long-term stability. Each time a wave breaking event initiated, a small amount of noise was generated immediately behind the breaker. Eventually, this noise accumulated and caused the simulation to become unstable. This statement is not restricted to simulations that contain a shoreline, any simulation with periodic wave breaking suffers from this difficulty. For the setup used in Fig. 3, the simulation would overflow after 15 wave periods. To eliminate this

noise and the associated instability, a nine-point filter (see Kirby et al., 1998) was passed over the domain, filtering both the free surface and velocity, once every two wave periods. The use of the filter has very little effect on conservation, but gives a huge boost to numerical stability, allowing the simulation to run indefinitely. Filtering is only needed for periodic, breaking waves, and thus for all simulation results presented in this paper, except of course for those given in Fig. 3, no filtering is used.

4. Validation in one horizontal dimension

4.1. Sine wave runoff

As a first check of the moving boundary model, a monochromatic wave train is let to runup and rundown a plane beach. This situation has an analytic solution derived by Carrier and Greenspan (1958). Their derivation makes use of the NLSW equations,

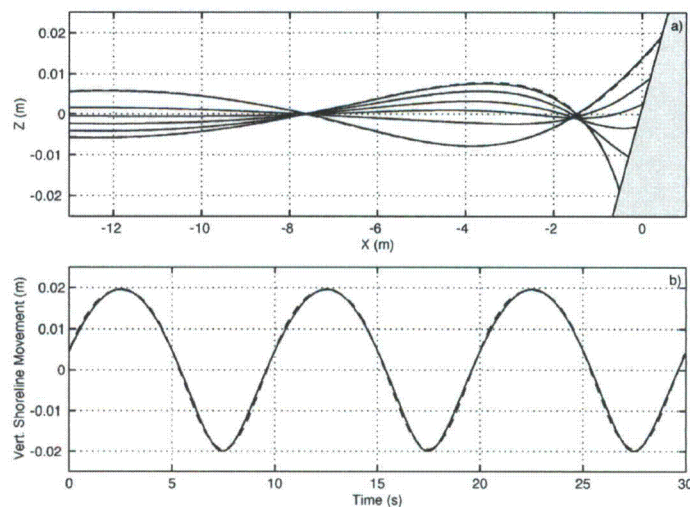


Fig. 4. Sine wave runoff on a planar beach. (a) Numerical free surface at various times, analytic free surface is shown by the dashed line (— —), and is only compared for the maximum and minimum shoreline movement profiles. (b) Comparison between analytical (— —) and numerical (—) shoreline movement.

and thus for consistency the dispersive (μ^2) terms will be ignored in the numerical simulations for this comparison. The wave and slope parameters for this test case are identical to those used by Madsen et al. (1997) and Kennedy et al. (2000). A wave train with height 0.006 m and period of 10 s travels in a one-dimensional channel with a depth of 0.5 m and a slope of 1:25. For the numerical simulation, a grid size of 0.045 m and a time step 0.01 s are used; bottom friction is not included and the wave does not break. It should be noted that the grid size is an order of magnitude smaller than what is required for a convergent solution. This small grid size is used only to make certain that the boundary location travels a significant number of grid points (>10) during runup and rundown.

The results of the numerical simulation are shown in Fig. 4. Fig. 4a shows the numerical free surface at various times, along with two profiles of the analytic free surface. The comparison between analytic and

numerical horizontal shoreline movement is shown as Fig. 4b. The agreement is good. Also, as a check on the convergence properties of δ , an additional simulation with $\delta = a_0/5000$ was run. A comparison between the $\delta = a_0/50$ shows little difference, and is not given in this paper. The maximum deviation in shoreline at any time between the two δ runs is on the order of 0.01% of the maximum excursion.

4.2. Nonbreaking and breaking solitary wave runup

Solitary wave runup and rundown was investigated experimentally by Synolakis (1986, 1987). In his work, dozens of experimental trials were performed, encompassing two orders of magnitude of solitary wave height. The beach slope was kept constant at 1:19.85. Many researchers have used this data set to validate numerical models (e.g., Zelt, 1991; Lin et al., 1999). To compare with this data, solitary waves with heights in the range of $0.005 < \epsilon < 0.5$ are made to

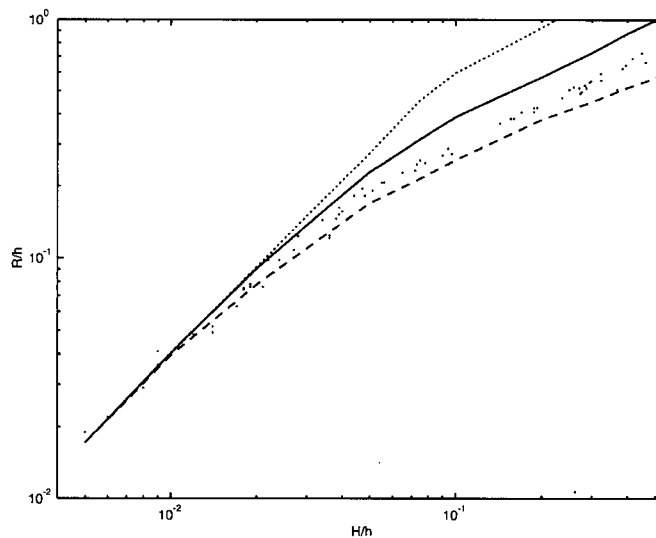


Fig. 5. Nondimensional maximum runup of solitary waves on a 1:19.85 beach versus nondimensional wave height. The points experimental data taken from Synolakis (1986), the dotted line is the numerical result with no bottom friction, the solid line is the numerical result with a bottom friction coefficient, f_b , of 10^{-3} , and the dashed line with $f_b = 10^{-2}$.

runup and rundown a slope and the maximum vertical runup is calculated. Note that this range includes both nonbreaking and breaking waves. For all simulations, $\Delta x/h = 0.3$ and $\Delta t\sqrt{g/h} = 0.03$. As a test of the sensitivity of wave runup to bottom friction, three sets of simulations were undertaken with different bottom friction coefficients, f . Set 1 was run with no

bottom friction, Set 2 with $f = 10^{-3}$, and Set 3 with $f = 10^{-2}$.

The numerical results are compared with the experimental data in Fig. 5, where maximum vertical runup is scaled by the water depth. For the smallest solitary waves ($\epsilon < 0.01$) bottom friction does not affect the runup, as maximum runup is identical for

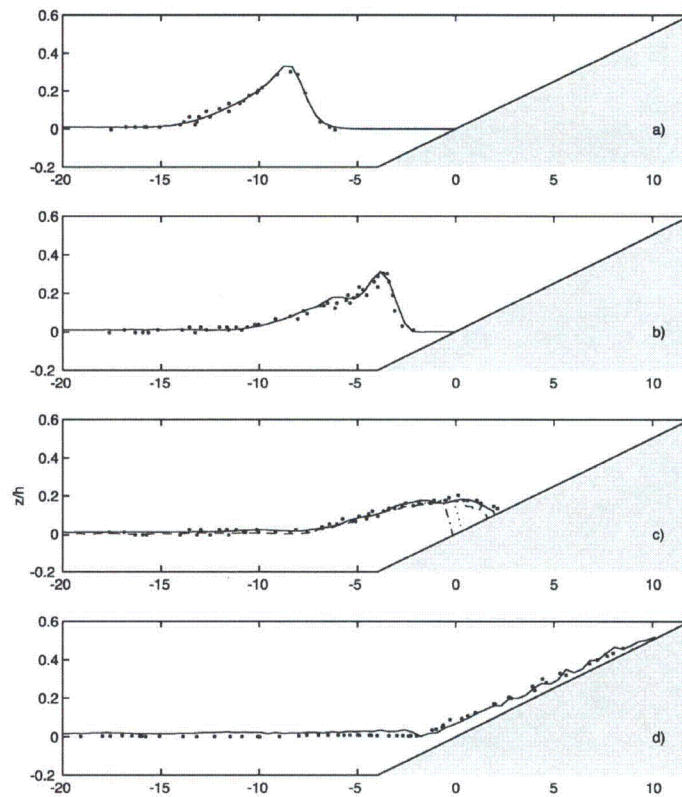


Fig. 6. Breaking solitary wave runup and rundown on a planar beach at $t(g/h)^{1/2} =$ (a) 15, (b) 20, (c) 25, (d) 45. The solid line represents the numerical results and the points represent the experimental data. In (c), the dashed line represents numerical results by Lin et al. (1999) (closest to experiment and numerical results presented in this paper), the dotted line represents results by Zelt (1991), and the dashed-dotted line results by Titov and Synolakis (1995).

all three numerical sets. This is consistent with previous research (e.g., Liu et al., 1995), where it is shown that bottom friction effects are minor for non-breaking waves, and will typically alter the runup by <0.5% of the maximum. For larger wave heights, breaking is initiated, both experimentally and numerically, near $\epsilon=0.04$. It is at this point that the numerical runup for Set 1 and Set 2 begins to diverge. Note that due to the log–log scale used in Fig. 5, the deviation in maximum runup may not be apparent. As an example, for $\epsilon=0.3$, scaled runup with no bottom friction is 1.21, with $f=10^{-3}$ runup is 0.73, and with $f=10^{-2}$ is 0.45, which are significantly different. Use of $f=5 \times 10^{-3}$ yields the best agreement with experimental data for this particular case.

It would seem that inclusion of an accurate bottom friction parameterization becomes increasingly important with increasing degree of wave breaking. The probable reason is that as a broken wave runs up a mild slope, it travels up the slope as a fairly thin layer of water. As can be seen from Eq. (5), the smaller the total water depth, the more important bottom friction becomes.

Synolakis (1986) also photographed the waves during runup and rundown. One set of these snap-

shots, for $\epsilon=0.28$, was digitized and compared with the numerical prediction, shown in Fig. 6. The numerical simulation shown in this figure uses $f=10^{-3}$. The wave begins to break between Fig. 6c and b, and the runup/rundown process is shown in Fig. 6c–d. In Fig 6c, numerical snapshots from three other models are plotted. The comparisons indicate a significant improvement over weakly nonlinear Boussinesq equation results of Zelt (1991) and the NLSW results of Titov and Synolakis (1995). Additionally, the numerical results presented in this paper compare favorably to the two dimensional (vertical plane) results of Lin et al. (1999), which makes use of a complex turbulence model.

5. Validation in two horizontal dimensions

5.1. Long wave resonance in a parabolic basin

Analytic solutions exist for few nonlinear, two horizontal dimension problems. One such solution is that for a long wave resonating in a circular parabolic basin. Thacker (1981) presented a solution to the

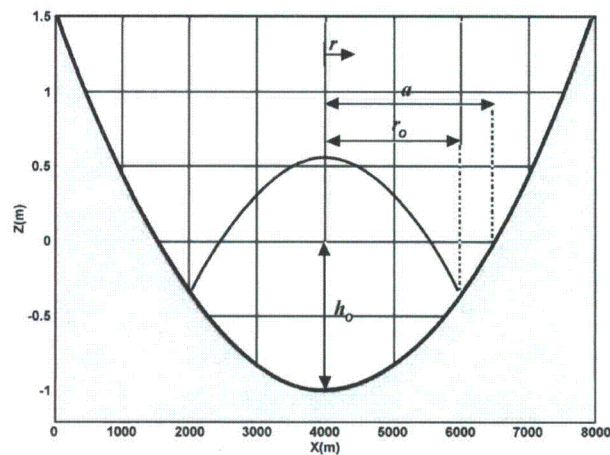


Fig. 7. Initial free surface and depth profile for parabolic basin test.

NLSW equations, where the initial free surface displacement is given as:

$$\zeta(r, t = 0) = h_0 \left[\frac{(1 - A^2)^{1/2}}{1 - A} - 1 - \frac{r^2}{a^2} \left\{ \frac{1 - A^2}{(1 - A^2)^2} - 1 \right\} \right] \quad (21)$$

and the basin shape is given by:

$$h(r) = h_0 \left(1 - \frac{r^2}{a^2} \right) \quad (22)$$

where

$$A = \frac{a^4 - r_0^4}{a^4 + r_0^4}, \quad (23)$$

h_0 is the center point water depth, r is the distance from the center point, a is the distance from the center point to the zero elevation on the shoreline, and r_0 is the distance from the center point to the point where the total water depth is initially zero. The numerical values used for this test are: $h_0 = 1.0$ m, $r_0 = 2000$ m, and $a = 2500$ m. The centerline initial condition and depth profile is shown in Fig. 7. Thacker showed the solution to this problem to be:

$$\zeta(r, t) = h_0 \left[\frac{(1 - A^2)^{1/2}}{1 - A \cos \omega t} - 1 - \frac{r^2}{a^2} \left\{ \frac{1 - A}{(1 - A \cos \omega t)^2} - 1 \right\} \right] \quad (24)$$

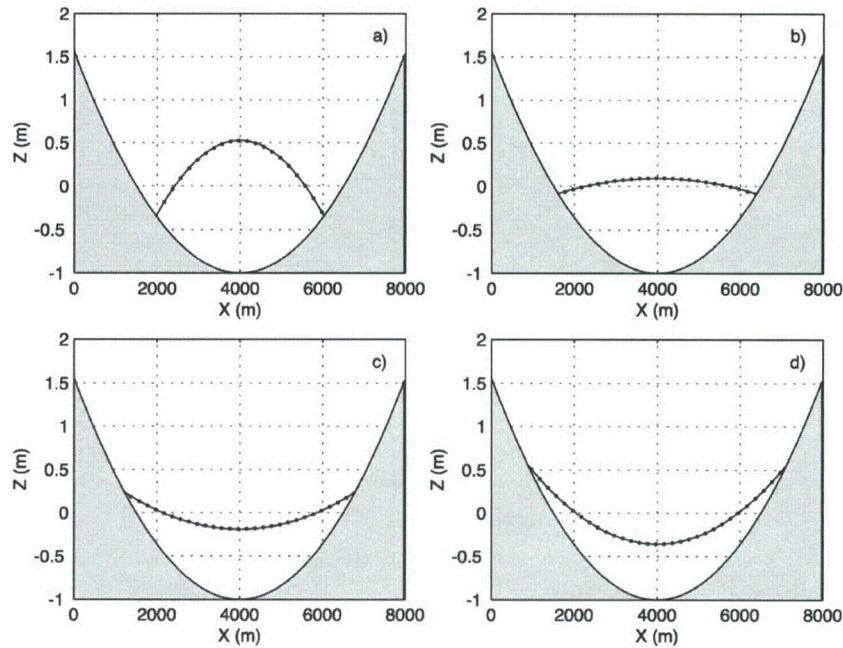


Fig. 8. Centerline free surface profiles for numerical (---) and analytical (···) bowl oscillation solutions at $t=(a) 5T$, (b) $1/6T$, (c) $1/3T$, (d) $5/12T$, where T is the oscillation period.

where

$$w = \frac{1}{a} (8gh_0)^{1/2} \quad (25)$$

and g is gravity. Cho (1995) also used this solution as a test for his NLSW moving boundary model. Cho's model, an explicit leap-frog finite-difference scheme which includes numerical frequency dispersion, reproduced the analytical solution very well for roughly one-half of an oscillation, but began to deviate soon after. A simulation using the extrapolation boundary technique presented in this paper was undertaken, truncating the dispersive terms in Eqs. (2) and (3) to be consistent with the NLSW solution, and using $\Delta x = 28$ m and $\Delta t = 0.9$ s. Bottom friction is not included and the wave does not break. The comparison between the numerical and analytic results is shown in Fig. 8. The numerical free surfaces shown in Fig. 8a–d are from the fifth oscillation, and show excellent agreement with the analytic solution. Additionally, a test using the full equations (Eqs. (2) and (3)), with dispersive terms, was performed. Interestingly, the wave field in this situation becomes chaotic after the first oscillation, and shows a similar pattern of divergence from the analytical solution as Cho's results. Therefore, this parabolic basin comparison would appear to be an ideal test for NLSW models, as the effects of numerical dispersion or dissipation become evident rapidly.

5.2. Runup on a conical island

Briggs et al. (1994) presented a set of experimental data for solitary wave interaction around a conical island. The slope of the island is 1:4 and the water depth is 0.32 m. Three cases were simulated, corresponding to solitary wave heights of 0.013 m ($\epsilon = 0.04$), 0.028 m ($\epsilon = 0.09$), and 0.058 m ($\epsilon = 0.18$). In addition to recording free surface elevation at a half dozen locations, maximum wave runup around the entire island was measured. This data set has been used by several researchers to validate numerical runup models (e.g., Liu et al., 1995; Titov and Synolakis, 1998; Chen et al., 2000). In this paper, free surface elevation is compared at the locations shown in Fig. 9. Gages #6 and #9 are located near the front face of the island, with #9 situated very near the initial shoreline position. Gages

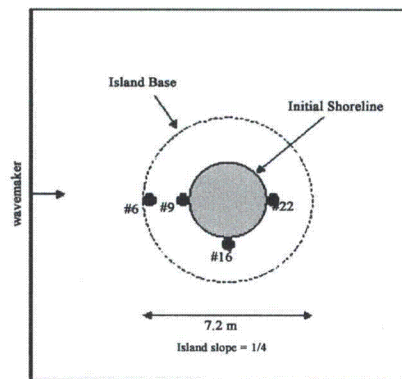


Fig. 9. Conical island setup. The gage locations are shown by the dots, and the wave approaches the island from the left.

#16 and #22 are also located at the initial shoreline, where #16 is on the side of the island and #22 on the back face.

Simulations were performed using $\Delta x = 0.15$ m and $\Delta t = 0.02$ s; bottom friction is neglected for these numerical tests. A soliton is placed in the numerical domain, as an initial condition. Numerical–experimental time series comparisons are shown in Fig. 10. Fig. 10a–d is for Case A ($\epsilon = 0.04$), Fig. 10e–h is for Case B ($\epsilon = 0.09$), and Fig. 10i–l is for Case C ($\epsilon = 0.18$). The gage number is shown in the upper left of each subplot. For all comparisons, the lead wave height and shape is predicted very well with the current model. Also, for all comparisons, the secondary depression wave is not predicted well. The numerical results show less of a depression following the main wave than in the experiments. This deviation is consistent with other runup model tests (e.g., Liu et al., 1995; Chen et al., 2000). The agreement of Case C is especially notable, as the soliton breaks along the backside of the island as the trapped waves intersect. This breaking occurs both experimentally, as discussed in Liu et al. (1995), and numerically.

As mentioned, maximum runup was also experimentally recorded. The vertical runup heights are converted to horizontal runups, scaled by the initial shoreline radius, and plotted in Fig. 11. The crosshairs represents the experimental data, where Fig. 11a is for

Case A, Fig. 11b is for Case B, and Fig. 11c is for Case C. The numerical maximum inundation is also plotted, given by the solid line. The agreement for all cases is very good.

5.3. Soliton evolution in a trapezoidal channel

Peregrine (1969) presented laboratory experiments wherein solitary waves propagated through a trapezoidal channel. To experimentally create the solitons,

a piston wavemaker was cut to fit the channel and could slide horizontally along the trapezoidal channel. In the numerical simulations, as it is difficult to implement a piston wavemaker in a trapezoidal channel, the solutions of solitary waves in rectangular channels are used as an initial condition everywhere in the channel.

Once a solitary wave enters a trapezoidal channel, it deforms. Eventually, in certain channels, the leading wave will reach a quasi steady state, and the wave-

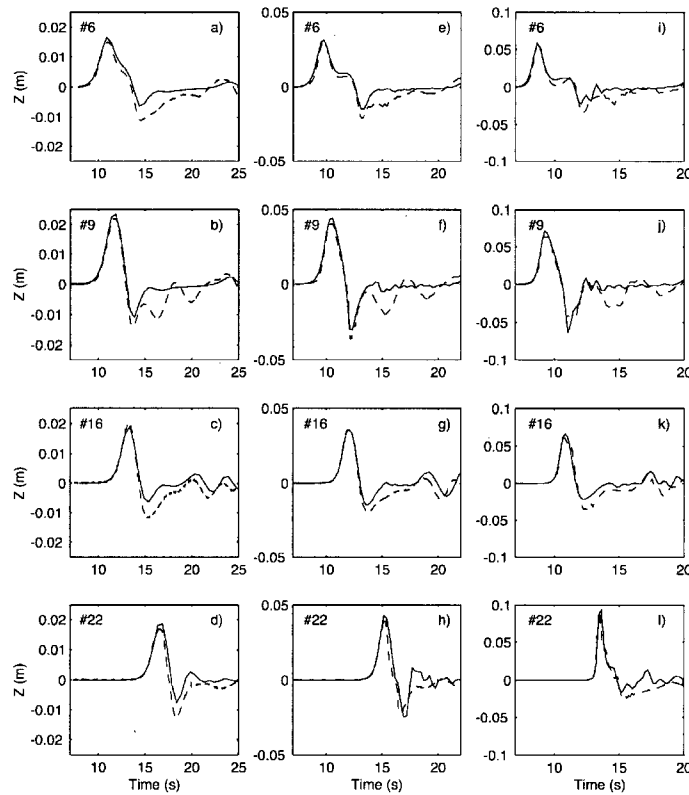


Fig. 10. Experimental (---) and numerical (—) time series for solitary wave interaction with a conical island. (a–d) are for Case A, (e–h) are for Case B, and (i–l) are for Case C. The gage number is shown in the upper left.

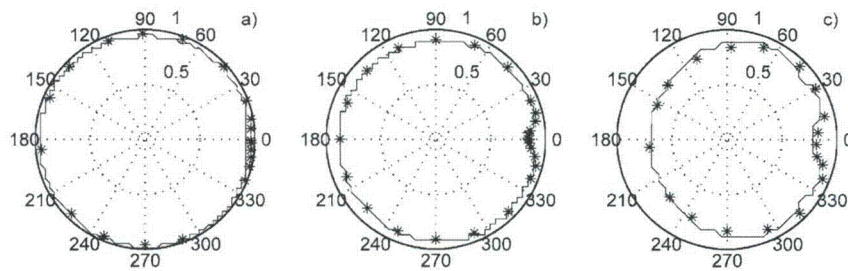


Fig. 11. Maximum horizontal runup, scaled by the initial shoreline radius, for Case A (a), Case B (b), and Case C (c). Experimental values are shown by the stars and the numerical results are shown by the solid line.

form will not change in time. After reaching this quasi steady state, numerical results of the lead wave height are compared with Peregrine's experimental results. The comparisons are shown in Fig. 12. For this comparison, a trapezoidal half-channel (one vertical wall and one sloping side wall) with constant depth width of $1.5h_0$, where h_0 is the depth at the non-sloping part of the channel, and a side-wall slope of 1:1

is employed. Three different amplitude solitary waves ($a = 0.08h_0$, $a = 0.12h_0$, and $a = 0.18h_0$) are simulated and compared with experimental results. The numerical results show reasonably good agreement with laboratory data, although there is a clear trend of under prediction of wave height near the shoreline.

An interesting property of wave evolution in certain trapezoidal channels is the successive regenera-

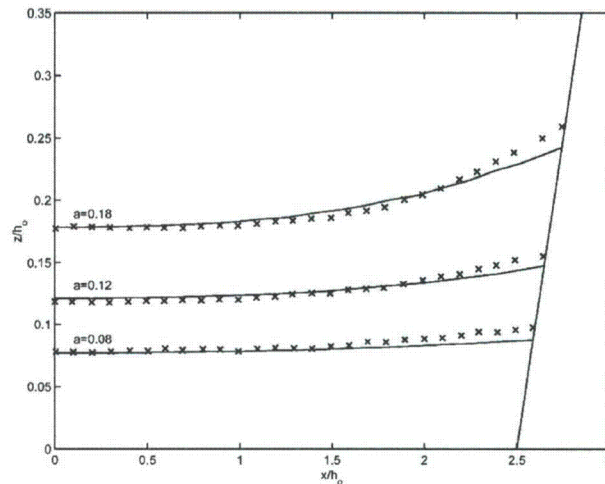


Fig. 12. The transverse profile of a solitary wave in a trapezoidal channel. The continuous line shows the numerical result; the crosses indicate the measured profile digitized from Peregrine's (1969) paper.

tion of the wave front. When the channel is wide enough, with respect to the wavelength, and the side-wall slope is gradual enough, the wave energy that is reflected off the side walls does not resituate in the original wave. This occurs in the Peregrine (1969) experiments discussed above, but forms a distinct wave behind the original wave front. Wave energy is continually transferred from the original wave front into the new wave behind, until the original wave front virtually disappears. The new front has a smaller height, and a slightly longer wavelength than the original.

One example of the phenomenon is discussed in this section. A half channel is created (one vertical wall at $y=0$, one sloping side wall), with a constant water depth width of $9h_0$ and a length of $250h_0$, where h_0 is the constant water depth along the center of the

channel. The side wall is sloped at 1:5. A solitary wave, with wave height $0.1h_0$ is placed in the channel as an initial condition. The wave does not break, and bottom friction is not included. For this simulation, $\Delta x/h_0=0.14$ and $\Delta t\sqrt{g/h_0}=0.05$ are used.

Fig. 13 shows four snapshots, in plan view, of the wave propagating through the part of channel. The dashed line plotted across the channel is the $x-ct=0$ line, where c is the linear long wave speed, $\sqrt{gh_0}$. Seafloor elevation contours are also shown on each plot. Fig. 13a shows the wave soon after the simulation has begun, and the front is beginning to arc, due to slower movement in the shallower water. By the time shown in Fig. 13b, wave energy has reflected off the slope, and has formed a second, trailing, wave crest behind the original wave. As this slope-reflected wave crest interacts with the vertical wall (or center-

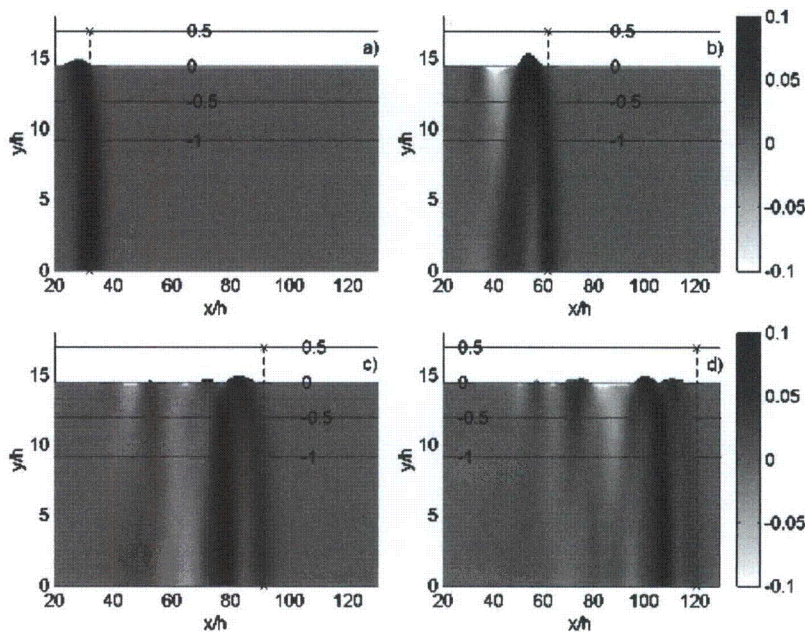


Fig. 13. Evolution of a solitary wave in a trapezoidal channel (half channel shown), at $t/(g/h)^{1/2}=(a) 7.5, (b) 35, (c) 65, (d) 93$. Seafloor elevation contours are shown at increments of $0.5h_0$, by the solid lines. The line of $x-ct=0$ is shown by the dashed line.

line of channel), a Mach stem forms at the vertical wall, and virtually no wave energy is reflected off the vertical wall. Also at this time, an oscillatory train, trailing the leading wave, forms along the slope. At time = 65, shown in Fig. 13c, most of the wave energy has transferred from the original wave front, to the secondary crest. In the last plot, Fig. 13d, the process has started to repeat itself, evidenced by the lobe growing behind the second front, near a depth of 0.9.

This process can be examined from a different perspective with Fig. 14. This figure shows numerous time series, taken along the centerline of the channel ($y=0$). Also shown are three characteristic lines. Following the first characteristic, we can see that the lead wave as nearly disappeared by $x=140h_0$, whereas the secondary wave is clearly defined by this point. The process repeats; at $x=230h_0$, the secondary wave is vanishing, and a third wave front is beginning to take shape. The phenomenon shown in Figs. 13 and 14 is an interesting one, although not wholly unexpected, and is a demonstration of the interaction between nonlinearity and refraction.

6. Conclusion

A moving boundary algorithm is developed for use with depth integrated equations. Used here in conjunction with a fixed grid finite difference model, the moving boundary algorithm could also be employed by a finite element scheme. Founded around the restrictions of the high-order numerical wave propagation model, the moving boundary scheme employs linear extrapolation of free surface and velocity through the wet–dry boundary, into the dry region. The linear extrapolation is simple to implement and can be straightforwardly incorporated into a numerical model. The technique is numerically stable, does not require any sort of additional dissipative mechanisms or filtering, and conserves mass.

The moving boundary is tested for accuracy using one- and two-dimensional analytical solutions and experimental data sets. Nonbreaking and breaking solitary wave runup is accurately predicted, yielding a validation of both the eddy viscosity breaking parameterization and the runup model. For strongly

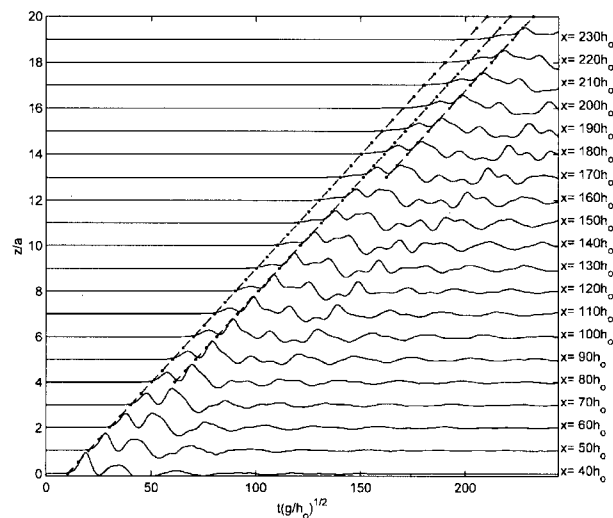


Fig. 14. Time series along the centerline of the channel ($y=0$); location of each time series is noted along the right border of the figure. Characteristics are shown by the dashed–dotted lines.

breaking waves, the proper numerical estimation of bottom friction is shown to be important. Two-dimensional wave runup in a parabolic basin and around a conical island is investigated, and comparisons with published data show excellent agreement. Also, solitary wave evolution in a trapezoidal channel is simulated, and an interesting phenomenon is examined.

Acknowledgements

This research has been supported in part by National Science Foundation grants to Cornell University (CMS-9908392, CTS-9808542).

References

- Balzano, A., 1998. Evaluation of methods for numerical simulation of wetting and drying in shallow water flow models. *Coast. Eng.* 34, 83–107.
- Briggs, M.J., Synolakis, C.E., Harkins, G.S., 1994. Tsunami runup on a conical island. *Proc. Waves—Physical and Numerical Modeling*. University of British Columbia, Vancouver, Canada, pp. 446–455.
- Carrier, G.F., Greenspan, H.P., 1958. Water waves of finite amplitude on a sloping beach. *J. Fluid Mech.* 4, 97–109.
- Chen, Q., Kirby, J.T., Dalrymple, R.A., Kennedy, A.B., Chawla, A., 2000. Boussinesq modeling of wave transformation, breaking, and runup: Part I. 2D. *J. Waterw. Port Coast. Ocean Eng.* 126 (1), 57–62.
- Cho, Y.-S., 1995. Numerical simulations of tsunami propagation and run-up. PhD Thesis, Cornell University, 264 pp.
- Gopalakrishnan, T.C., 1989. A moving boundary circulation model for regions with large tidal flats. *Int. J. Numer. Methods Eng.* 28, 245–260.
- Hsiao, S.-C., Liu, P.L.-F., 2002. Permeable effects on nonlinear water waves. *Proc. R. Soc. Lond.* in press.
- Kennedy, A.B., Chen, Q., Kirby, J.T., Dalrymple, R.A., 2000. Boussinesq modeling of wave transformation, breaking, and runup. Part I: 1D. *J. Waterw. Port Coast. Ocean Eng.* 126 (1), 39–47.
- Kirby, J.T., Wei, G., Chen, Q., Kennedy, A.B., Dalrymple, R.A., 1998. "FUNWAVE 1.0. Fully nonlinear Boussinesq wave model. Documentation and user's manual." Report CACR-98-06, Center for Applied Coastal Research, Department of Civil and Environment Engineering, University of Delaware.
- Kowalik, Z., Bang, I., 1987. Numerical computation of tsunami runup by the upstream derivative method. *Sci. Tsunami Hazards* 5 (2), 77–84.
- Leendertse, J.J., 1987. "Aspects of SIMSYS2D, a system for two-dimensional flow computation." R-3752-USGS. Rand, Santa Monica, CA, 80.
- Lin, P., Chang, K.-A., Liu, P.L.-F., 1999. Runup and rundown of solitary waves on sloping beaches. *J. Waterw. Port Coast. Ocean Eng.* 125 (5), 247–255.
- Liu, P.L.-F., 1994. Model equations for wave propagation from deep to shallow water. In: Liu, P.L.-F. (Ed.), *Advances in Coastal Engineering*, vol. 1, pp. 125–157.
- Liu, P.L.-F., Cho, Y.-S., Briggs, M.J., Kanoglu, U., Synolakis, C.E., 1995. Runup of solitary waves on a circular island. *J. Fluid Mech.* 302, 259–285.
- Lynett, P., Liu, P.L.-F., 2002a. A numerical study of submarine landslide generated waves and runup. *Proc. R. Soc. Lond.* in press.
- Lynett, P., Liu, P.L.-F., 2002b. A two-dimensional, depth-integrated model for internal wave propagation. *Wave Motion* in press.
- Lynett, P., Liu, P.L.-F., Losada, I., Vidal, C., 2000. Solitary wave interaction with porous breakwaters. *J. Waterw. Port Coast. Ocean Eng.* 126 (6), 314–322.
- Madsen, P.A., Sorensen, O.R., 1992. A new form of the Boussinesq equations with improved linear dispersion characteristics: Part II. A slowly varying bathymetry. *Coast. Eng.* 18, 183–204.
- Madsen, P.A., Sorensen, O.R., Schaffer, H.A., 1997. Surf zone dynamics simulated by a Boussinesq-type model: Part I. Model description and cross-shore motion of regular waves. *Coast. Eng.* 32, 255–287.
- Nwogu, O., 1993. Alternative form of Boussinesq equations for nearshore wave propagation. *J. Waterw. Port Coast. Ocean Eng.* 119 (6), 618–638.
- Peregrine, D.H., 1967. Long waves on a beach. *J. Fluid Mech.* 27, 815–827.
- Peregrine, D.H., 1969. Solitary waves in trapezoidal channels. *J. Fluid Mech.* 35, 1–6.
- Petera, J., Nassehi, V., 1996. A new two-dimensional finite element model for the shallow water equations using a Lagrangian framework constructed along fluid particle trajectories. *Int. J. Numer. Methods Eng.* 39, 4159–4182.
- Sielecki, A., Wurtele, M.G., 1970. The numerical integration of the nonlinear shallow-water equations with sloping boundaries. *J. Comput. Phys.* 6, 219–236.
- Synolakis, C.E., 1986. The runup of long waves. PhD thesis, California Institute of Technology, Pasadena, CA.
- Synolakis, C.E., 1987. The runup of solitary waves. *J. Fluid Mech.* 185, 523–545.
- Tao, J., 1983. Computation of wave runup and wave breaking. Internal Report, Danish Hydraulics Institute, Denmark.
- Tao, J., 1984. Numerical modeling of wave runup and breaking on the beach. *Acta Oceanol. Sin.* 6 (5), 692–700 (in Chinese).
- Thacker, W.C., 1981. Some exact solutions to the nonlinear shallow water wave equations. *J. Fluid Mech.* 107, 499–508.
- Titov, V.V., Synolakis, C.E., 1995. Modeling of breaking and non-breaking long wave evolution and runup using VTCS-2. *J. Waterw. Port Coast. Ocean Eng.* 121, 308–316.
- Titov, V.V., Synolakis, C.E., 1998. Numerical modeling of tidal wave runup. *J. Waterw. Port Coast. Ocean Eng.* 124 (4), 157–171.
- Wei, G., Kirby, J.T., 1995. A time-dependent numerical code for extended Boussinesq equations. *J. Waterw. Port Coast. Ocean Eng.* 120, 251–261.
- Wei, G., Kirby, J.T., Grilli, S.T., Subramanya, R., 1995. A fully nonlinear Boussinesq model for surface waves: Part I. Highly nonlinear unsteady waves. *J. Fluid Mech.* 294, 71–92.
- Zelt, J.A., 1991. The runup of nonbreaking and breaking solitary waves. *Coast. Eng.* 15, 205–246.



Available online at www.sciencedirect.com



Coastal Engineering 53 (2006) 325–333

**Coastal
Engineering**
An International Journal for Coastal,
Harbour and Offshore Engineers

www.elsevier.com/locate/coastaleng

Wave breaking velocity effects in depth-integrated models

Patrick J. Lynett

Department of Civil Engineering, Texas A&M University, College Station, TX 77843-3136, United States

Received 11 May 2005; received in revised form 25 August 2005; accepted 12 October 2005
Available online 21 November 2005

Abstract

A simple model for predicting the velocities under breaking waves in depth-integrated models is developed. A velocity modification due to wave breaking is formulated based on a specific exponential profile, which is then added to the numerically predicted, depth-integrated velocity profile. This modification is superficial in that it does not directly change the hydrodynamic calculations inside the depth-integrated model. The modifications can be employed in any of the numerous Boussinesq-type models, and is not dependant on the use of a particular breaking dissipation scheme. Horizontal velocity profiles, both mean and instantaneous, are compared with experimental data in the surf zone. The comparisons show good agreement, markedly better than the un-modified results, and on par with published numerical results from sophisticated models.

© 2005 Elsevier B.V. All rights reserved.

Keywords: Boussinesq; Undertow; Currents; Wave breaking

1. Introduction

For the near future, depth-integrated models will likely dominate nearshore, wave-resolving simulation, in particular when large spatial domains are considered. These models, primarily the shallow water and Boussinesq-type variety, predict the 3D wave field with 2D equations and so can simulate large basins in a practical length of computational time. While these properties seem to lead to great opportunities for nearshore hydrodynamic predictions, the depth-integrated derivation creates a set of equations for which some of the most important nearshore physics are approximated, or left out entirely.

Shallow-water-based depth-integrated models typically assume that the vertical profile of velocity can be represented by a polynomial, wherein the order of the polynomial is proportional to the accuracy of the resulting model. For non-breaking waves, this polynomial predicts the vertical profile of velocity very well, even for strongly nonlinear waves (e.g., Wei et al., 1995; Ryu et al., 2003), provided the wave is not in deep water. Implicit with this velocity profile, and often a direct inviscid assumption, is a lack of ability to simulate turbulence.

To simulate nearshore hydrodynamics, some method must be employed to approximate breaking, bottom friction, etc.

The depth-integrated model, in general, consists of one continuity equation, solved for the free surface elevation, and one vector momentum equation, solved for some characteristic velocity. To simulate the effects of breaking, the most common approach is to add a dissipation submodel to the momentum equation. This is an ad hoc addition, as common depth-integrated derivations start with an inviscid assumption, either implicitly or explicitly. There are two primary classes of breaking models: the roller model (e.g., Madsen et al., 1997) and the eddy viscosity model (e.g., Kennedy et al., 2000). The two models can be roughly equated, although the parameters controlling the dissipations are based on different physical thresholds.

Through a calibration of the parameters inherent in these models, very good agreement in wave height and mean water level can be achieved for wave transformation through the surf zone. Due to the success in applying the Boussinesq-type model through the surf, the natural progression is to employ these models for transport calculations. Transport calculations become very sensitive to accurate representation of the mean horizontal velocity, or undertow if below the mean trough level. It was immediately recognized that the raw Boussinesq model yielded very poor predictions of this undertow. For

E-mail address: plynett@tamu.edu.

example, when using a Boussinesq-type model, here the two-layer model of Lynett (in press), to predict the undertow of the Cox et al. (1995) experiment, the results prove poor. Shown in Fig. 1 are the numerical-experimental predictions. The numerical profiles are the wave-averaged horizontal velocities. As the numerical profiles are taken throughout the water column, the undertow (below the trough) must be balanced by the crest flux (above the trough). This should be the case with any finite amplitude wave theory — some undertow must be predicted.

Shown in the subplots at $x=3.5$ m and $x=5.8$ m, the numerical undertow agrees very well with the experimental. The reason for this is that at these locations, breaking has not yet initiated or has just barely initiated, and thus the impact on the profile due to breaking is minimal. These two plots are another demonstration of the ability of the Boussinesq model to simulate nearshore hydrodynamics accurately. Looking to the other four profiles shown, located throughout the surf zone, it is clear that the undertow is not predicted correctly in either magnitude or vertical variation. The Boussinesq profiles are always uniform below the trough, due to the Boussinesq-*interpreted* long wave, inviscid nature of the breaking wave.

Using the "raw" Boussinesq velocity profiles to predict the undertow leads to significant errors.

To work around this obstacle within the Boussinesq framework, researchers have developed solutions across a range of physical complexity. On the sophisticated end are the approaches similar to Veeramony and Svendsen (2000), who solved a coupled set of Boussinesq and vorticity models. This approach does involve the inevitable vorticity generation calibration, as well as a relatively complex equation model (compared to the standard Boussinesq), but yields very good agreement when compared to the undertow data of Cox et al. (1995).

Much of the work in examining Boussinesq velocity profiles in the surf zone employs the surface roller breaking model, used with the improved Boussinesq equations of Madsen et al. (1997). This particular model is somewhat limited in its ability to predict the vertical profile of velocity due to the manipulations of the model equations, rather than the velocity profile used to derive said equations (e.g., Nwogu, 1993). Due to these manipulations, a velocity profile consistent with the solved equations does not exist. However, in the surf zone, where Boussinesq predicted velocities are close to uniform in the

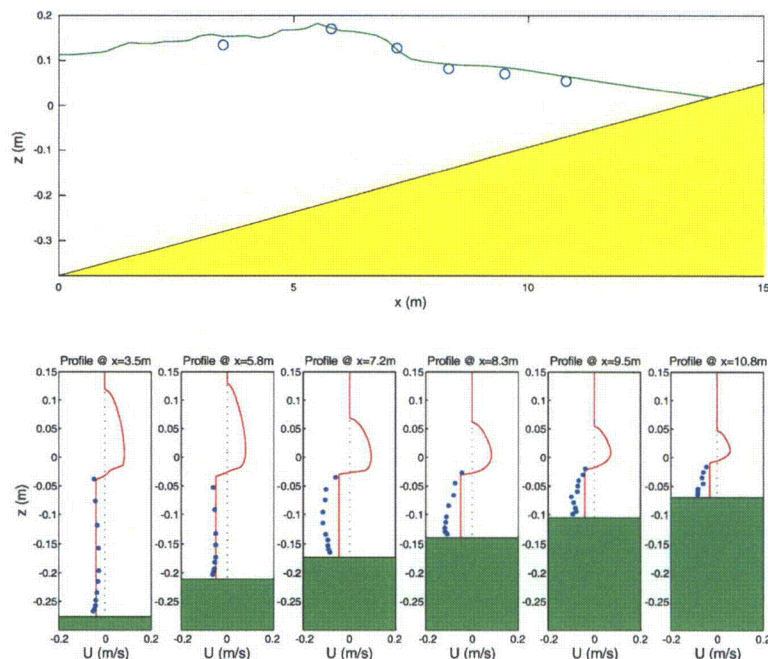


Fig. 1. Comparison with the data of Cox et al. (1995). Top plot is the numerical wave height profile (line) and the experimental (circles). The bottom row of plots are the time-averaged horizontal velocities at various locations, given in the subplot titles. The experimental values are shown with the dots, and the "unmodified" Boussinesq results by the solid line.

vertical, this limitation will not impact the results greatly. When using the roller breaking model, the horizontal velocity profile under a breaking wave is modified such that in the roller region, the velocity is assumed to be a large value related to the local long wave speed, while the velocity under the roller is set to a uniform value. This uniform value is determined such that the modified flux is equal to the Boussinesq-predicted flux. While this approach has been shown to yield reasonable results, it is not possible for this concept to predict a vertically varying undertow, as is measured in many experiments, without additional hydrodynamic submodels.

2. Breaker effect on depth-integrated velocity profile

A consistent modification to the velocity profile due to breaking is sought. In its foundation, the procedure given in this section is similar to the roller approach used to modify the vertical velocity profile, discussed above. Here, however, properties of the velocity modifications will be taken from the extended-Boussinesq theory.

Following the conventional perturbation derivation for Boussinesq equations, the vertical profile of the vertical velocity, W , is given in dimensionless form as:

$$W = -zS - T + O(\mu^2) \tag{1}$$

where

$$S = \nabla \cdot U, \quad T = \nabla \cdot (hU), \tag{2}$$

z is the vertical coordinate, U is the vertically-varying horizontal velocity vector, and h is the local water depth. To include the impact of breaking induced velocity profile changes, a fundamental modification is made to the above velocity profile:

$$W = -zS - T + A(x, y, t)f(x, y, z, t) + O(\mu^2) \tag{3}$$

where A and f comprise some arbitrary function which is meant to approximately account for breaking effects. Using this modified vertical velocity, the horizontal velocity vector, as referenced to a velocity at an arbitrary elevation, is given by:

$$U = u - \mu^2 \left\{ \frac{z^2 - z_\alpha^2}{2} \nabla S + (z - z_\alpha) \nabla T \right\} + \mu^2 \left\{ \nabla A \left[\int f(z) dz - \int f(z_\alpha) dz \right] + A \left[\int \nabla f(z) dz - \int \nabla f(z_\alpha) dz \right] \right\} + O(\mu^4) \tag{4}$$

where u is the horizontal velocity evaluated at some arbitrary elevation z_α . The purpose of the additional terms in the horizontal velocity profile will be to allow velocities near the free surface to be larger when breaking is occurring, to better represent the fast moving breaking region. It is desired that

$U(x, y, \zeta, t) = C(x, y, t)$ where C is some prescribed free surface breaking velocity and ζ is the free surface elevation. Further, let us define the Boussinesq predicted free surface velocity

$$u_s = u - \mu^2 \left\{ \frac{\zeta^2 - z_\alpha^2}{2} \nabla S + (\zeta - z_\alpha) \nabla T \right\} + O(\mu^4). \tag{5}$$

Therefore, a solution to the following expression is desired:

$$\mu^2 \nabla A \left[\int f(\zeta) dz - \int f(z_\alpha) dz \right] + \mu^2 A \left[\int \nabla f(\zeta) dz - \int \nabla f(z_\alpha) dz \right] = C - u_s \tag{6}$$

Using the assumption that $\nabla f(z) = O(\mu^2)$, employing $f(z_\alpha) = f(z_B) + O(\mu^2)$ where z_B is some elevation in the water column, and the substitution $g = \int f dz$, a relatively simple equations results

$$g(\zeta) - g(z_B) = 1 \tag{7}$$

where ∇A has been set equal to $\frac{\delta}{\mu^2} (C - u_s)$, and $\delta = 1$ when breaking is occurring and is 0 otherwise. As the initial modifications to the vertical velocity profile are ad hoc in nature, there is no guidance contained directly in the depth-integrated derivation as to what form $g(z)$ should take. Since the Boussinesq-model should capture the velocities correctly if the phenomenon is of the shallow- or intermediate-water type, we chose here to give g a deep-water based form, an exponential:

$$g = B e^{k(z - \zeta)} \tag{8}$$

where B is a coefficient and k is some vertical wave number. Substituting this form into (7) gives the solution for B :

$$B = \frac{1}{1 - e^{k(z_B - \zeta)}} \tag{9}$$

and we are left with the wave number, k , and the elevation, z_B , as unknowns. From this point on, all terms will be discussed in their dimensional form. To summarize, the modified horizontal velocity profile is given as:

$$U = U_O + U_B \tag{10}$$

where

$$U_O = u - \left\{ \frac{z^2 - z_\alpha^2}{2} \nabla S + (z - z_\alpha) \nabla T \right\} \tag{11}$$

$$U_B = \nabla A [g(z) - g(z_B)] \tag{12}$$

$$\nabla A = \delta (C - u_s) \tag{13}$$

It is noted that (10) is written in a more generic form using U_O . While the derivation up to this point has looked at the “extended” Boussinesq model, it is completely applicable to any Boussinesq-type of model, for example depth-averaged or multi-layer. In these cases, only the expression for U_O in (11) would change.

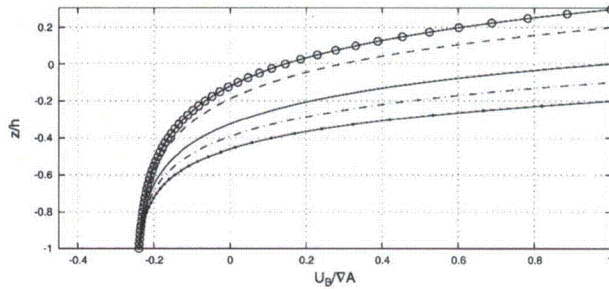


Fig. 2. Horizontal velocity modifications due to breaking, where the line with open circles is for $\zeta = 0.3 h$, the dashed line for $\zeta = 0.2 h$, the solid line for $\zeta = 0$, the dashed-dotted line for $\zeta = -0.1 h$, and the solid dotted line for $\zeta = -0.2 h$.

With any modification of the velocity profiles comes a modification to the resulting depth-integrated continuity and momentum equations. The additional flux terms in the continuity equation are

$$\int_{-h}^{\zeta} \nabla A [g(z) - g(z_B)] dz = B \nabla A \left[\frac{1}{k} (1 - e^{-kH}) - H e^{k(z_B - \zeta)} \right] \quad (14)$$

where $H = \zeta + h$. Now, to solve the continuity equation, some value for k must be given. There are a few possibilities here, for

example, k can be related somehow to the total water depth, i.e., $k = 2\pi/H$, or based on some other instantaneous wave property, i.e., $k = \sqrt{|\zeta_{xx}/\zeta|}$ where x is the direction of propagation of the breaker. A value of k will be chosen that yields good agreement with experiment — it will be the empirical parameter of the breaking velocity modifications. With a given k , we are left with z_B as the remaining unspecified variable. Here, a choice is made for z_B based on experience when using the Boussinesq model for breaking wave studies. It is seen that the “unmodified” model, when using either a roller or eddy-viscosity breaker submodel in the momentum equation, reproduces mean quantities (wave height, mean free surface, etc.) in the surf

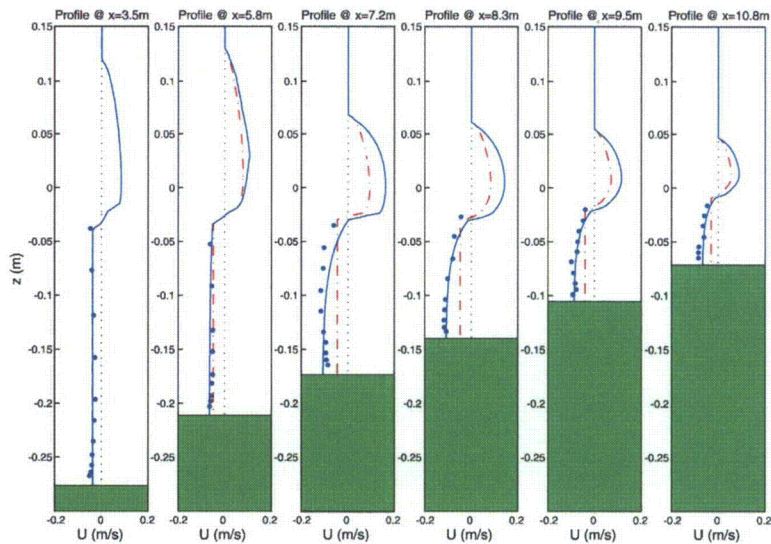


Fig. 3. Comparison with the data of Cox et al. (1995), using the same setup as in Fig. 1. The experimental values are shown with the dots, the breaking-enhanced Boussinesq by the solid line, and the unmodified Boussinesq results by the dashed-dotted line.

accurately. Thus the flux predicted by the “unmodified” model is already well predicted. We will chose z_B such that the new terms do not change the flux, i.e.,

$$\int_{-h}^{\zeta} \nabla A [g(z) - g(z_B)] dz = 0 \tag{15}$$

or

$$e^{-kH} + kHe^{k(z_B - \zeta)} = 1 \tag{16}$$

The above equation is readily solved for z_B :

$$z_B = -h + \frac{\ln[\frac{1}{kH}(e^{kH} - 1)]}{k} \tag{17}$$

Therefore, with a specified value of k , z_B is given and the breaking modifications to the velocity profile in (10) can be calculated. In the limit of very small k (long wave), the modifications resemble a linear trend going from a velocity addition at the free surface to a velocity subtraction near the bed, with z_B approaching $-h + H/2$, the midpoint of the instantaneous water column. For large k , the modification is a

velocity addition highly localized at the surface and a small velocity subtraction in the remaining water column, with z_B approaching ζ .

Looking to the momentum equation, additional terms will also be present when carrying through the modified velocity profiles. The assumption is made that the breaking submodels have already taken these terms in account in some approximate form. Thus, it can be concluded that the modifications given by (10) are in fact the implied velocity profile changes associated with the use of a breaking submodel, here the eddy viscosity model. In addition, since the changes presented here do not affect the governing equations, all previous free surface benchmarks and calibrations remain unchanged, and, in essence, the velocity profile changes in (10) are a post-processing modification.

3. Comparison with experimental data

The modified velocity profile under breaking waves will be compared with the available experimental data in this section. The data of Cox et al. (1995) and Ting and Kirby (1995, 1996), for both mean flows (undertoe) and phase-averaged velocities,

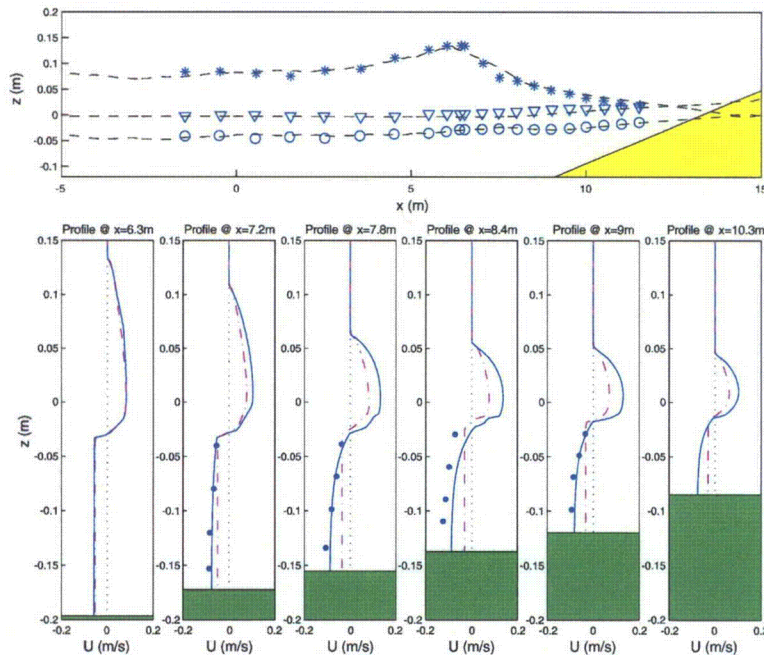


Fig. 4. Comparison with the data of Ting and Kirby spiller. The top plot shows the mean crest level (stars), mean water level (triangles), and mean trough level (circles) for the experiment as well as the numerical simulation. The lower subplots are the time-averaged horizontal velocities, where the experimental values are shown with the dots, the breaking-enhanced Boussinesq by the solid line, and the unmodified Boussinesq results by the dashed-dotted line.

is used. To achieve the best possible agreement with the data, the following value of k is specified:

$$k = \frac{5}{H} \quad (18)$$

The solutions are not strongly sensitive to this choice, with numerator values ranging from 4 to 6 yielding similar results. Note that the numerator value, as well as the chosen form of k , are chosen based on the model employed here, and may be different for other Boussinesq-type models. To elucidate how the added terms to (10) will modify the profile, Fig. 2 gives U_B for various free surface elevation values. At the free surface, an addition is made such that the velocity is equal to C , where

$$C = \frac{u_s}{|u_s|} \sqrt{\text{gravity} * H + \bar{U}}, \quad (19)$$

the nonlinear long wave speed corrected for the depth-averaged current, \bar{U} . Downward through the water column, the velocity addition decreases until the modifications act to reduce the velocity. Note that these curves will collapse if plotted against $(z - \zeta)/H$ instead of z/h , following the $\zeta=0$ curve given in Fig. 2.

For the Boussinesq simulations, the highly-nonlinear, extended Boussinesq model is used for all simulations. A close variation of the eddy-viscosity model is employed to approximate wave breaking, as described in Lynett (in press). As a first experimental comparison, the data of Cox et al. (1995) is examined. Remember that this data has already been compared with the "unmodified" model, as shown in Fig. 1. The unmodified model, while capturing the mean velocity correctly near the trough level, shows significant errors below the trough. With the breaking velocity "enhancements", the mean velocities are predicted very well, as shown in Fig. 3. Both the magnitude and the vertical variation of undertow are captured throughout the surf zone. For this case, the breaking enhancements are large, leading to big differences in the two results, and indicating that for this wave, the Boussinesq predicted free surface velocity is much less than the nonlinear long wave speed. The agreement shown here is on par with published comparisons, based on more physically robust and computationally expensive formulations (e.g., Veeramony and Svendsen, 2000).

Next, the data of Ting and Kirby, for spilling (1995) and plunging (1996) breakers, is compared. These experiments

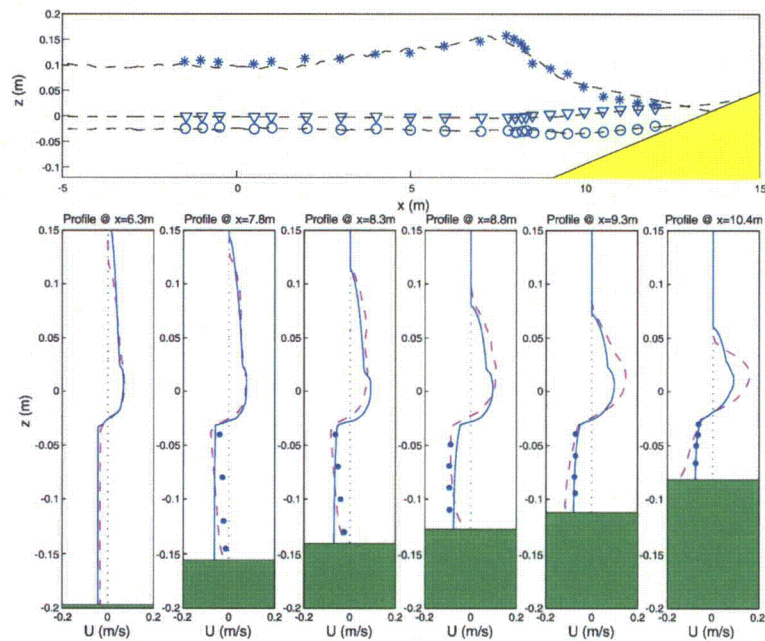


Fig. 5. Comparison with the data of Ting and Kirby plunger. The top plot shows the mean crest level (stars), mean water level (triangles), and mean trough level (circles) for the experiment as well as the numerical simulation. The lower subplots are the time-averaged horizontal velocities, where the experimental values are shown with the dots, the breaking-enhanced Boussinesq by the solid line, and the results of a VOF RANS model (COBRAS, provided by Dr. P. Lin) by the dashed line.

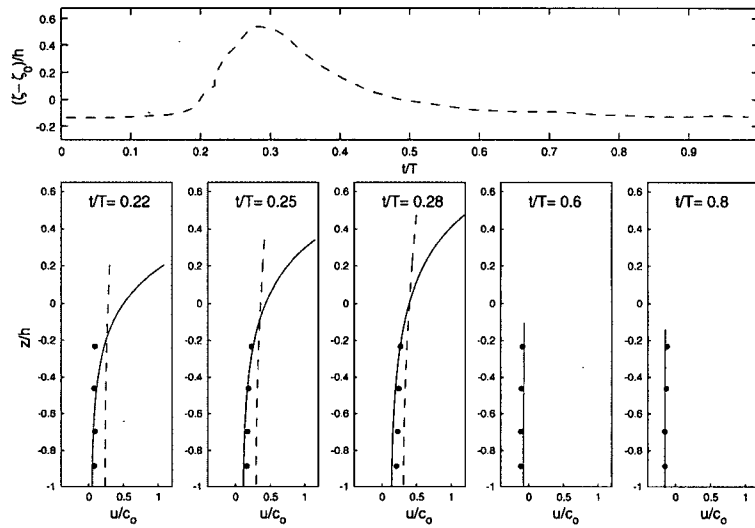


Fig. 6. Comparisons of the vertical profile of phase-averaged horizontal velocity at different wave phases for the Ting and Kirby spiller at $x = 7.2$ m. The top plot shows the experimental phase-averaged free surface. In the lower subplots are the velocity profiles at different points under the wave, where the dots are the experiment, the breaking-enhanced Boussinesq by the solid line, and the unmodified Boussinesq results by the dashed line. Velocity in the lower plots is scaled by c_0 , the linear long wave speed.

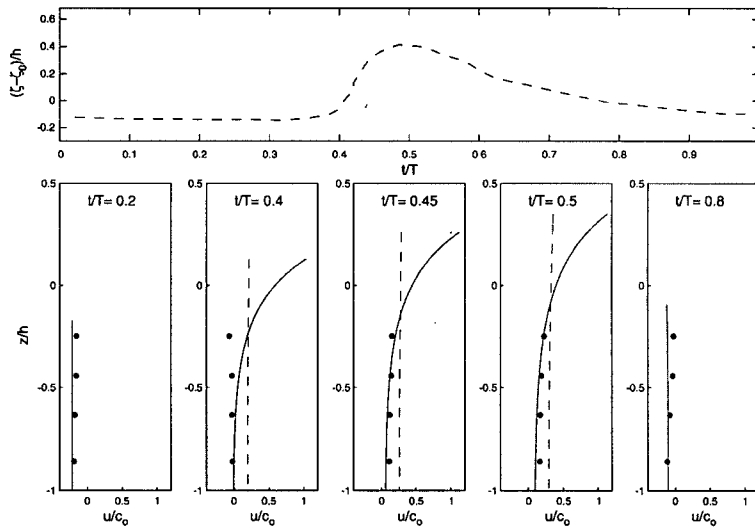


Fig. 7. Comparisons of the vertical profile of phase-averaged horizontal velocity at different wave phases for the Ting and Kirby spiller at $x = 7.8$ m. Figure setup same as Fig. 6.

look at cnoidal wave breaking on a 1/35 slope. First, mean velocity profiles are discussed. In Fig. 4 are comparisons at four locations along the slope. As with the Cox et al. data, velocity measurements below the trough are available. The breaking enhanced model does a much better job at representing the undertow profile, including the vertical variation. The agreement at $x=8.4$ m is poor, although equal to the agreement achieved in other models (e.g., Lin and Liu, 2004). As with the data of Cox et al., the breaking enhanced model predicts a very different undertow profile as compared to the unmodified model.

A physical setup that does not show much difference between the breaking enhanced and unmodified models is that of Ting and Kirby (1996) for plunging cnoidal waves. For this comparison, shown in Fig. 5, the breaking enhanced model is compared with the experimental and the numerical results from a RANS VOF model, COBRAS (Lin and Liu, 1998). Before breaking, at $x=6.3$ m, the predictions of the two numerical models through the entire water column are in agreement. In the outer surf zone, the RANS model predicts the undertow better, capturing the vertical variation. Also note that at these locations, the positive mass flux, above the trough level, as predicted by the two models are in very close agreement. Moving towards the inner surf, the Boussinesq breaking enhanced model yields a much better prediction of the undertow, with excellent agreement at the two innermost measurement locations. The breaking enhanced impact for this case is in fact rather small, as can be inferred from the small vertical variation of the undertow predicted by this model. This

implies that the Boussinesq prediction of the free surface velocity of the breaker is near the nonlinear long wave speed.

While examination of the undertow profiles indicates that the breaking enhancements are correctly modifying the velocity profiles in the mean sense, it does not necessary require that the instantaneous profiles are being altered reasonably. To investigate this point, the data of Ting and Kirby (1995), for the spiller, is re-examined. The experimental velocity profiles are phase-averaged, which is the equivalent of the instantaneous Boussinesq velocity profile, where turbulent fluctuations are not modelled. Figs. 6–8 give comparisons at three locations, $x=7.2$, 7.8, and 9 m, respectively. In the top plot of each of these figures is the free surface elevation (waveform) for one wave period.

Looking to the vertical profiles of horizontal velocity, given in the lower subplots of the figures, it becomes clear that while the breaking enhancements have been shown to predict undertow well, they also capture the phase-averaged velocities below the mean trough level. Given in each figure are three profiles under the breaking part of the wave, and two elsewhere. Note that the unmodified profiles are close to vertically invariant at all locations under the wave. Only at the trough of the wave, however, is this a good approximation. The breaking enhancements show a large improvement over the unmodified predictions, with the vertical variation and the velocity magnitude very well modelled. It is also evident that below the trough level, the proposed modification will act to reduce the horizontal velocity under the breaker, thereby generally decreasing the skewness (and asymmetry) of the

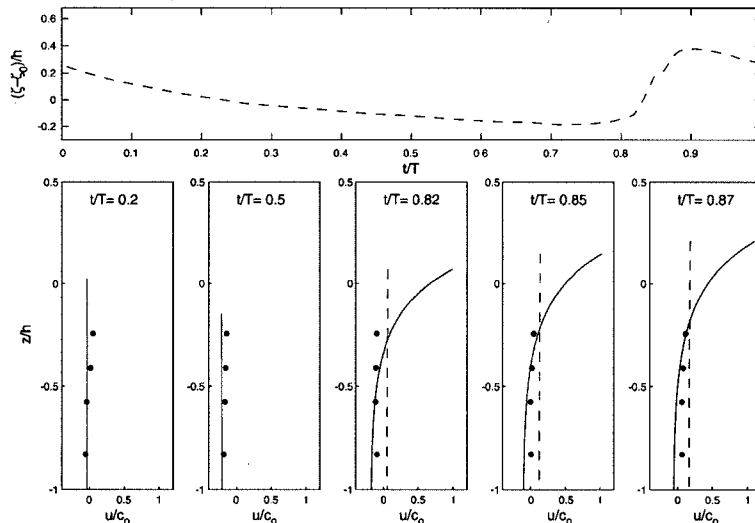


Fig. 8. Comparisons of the vertical profile of phase-averaged horizontal velocity at different wave phases for the Ting and Kirby spiller at $x=9.0$ m. Figure setup same as Fig. 6.

under-trough velocity. The effect is opposite above the trough. This incorrect under-trough prediction in the unmodified Boussinesq model has been recognized previously; for example see the “roller” velocity modification in some Boussinesq models (commonly in the Madsen et al. (1997) type Boussinesq models, see developments by Rakha (1998)). To reiterate, the unmodified Boussinesq model is capturing the depth-averaged velocity well at all locations — but the vertical variation is missing under the breaking portion. This observation served as the spark for the research presented here.

4. Conclusions

A simple model for predicting the velocities under breaking waves in depth-integrated models is developed. Under the non-breaking portions of the wave, no modification is made to the Boussinesq vertical profiles of velocity. The velocity modification is formulated based on a specific exponential profile, which is then added to the numerically predicted velocity profile under a breaking wave. This modification is superficial in that it does not directly change any of the hydrodynamic calculations inside the depth-integrated model. However, if one were to employ these modifications in a model that used the velocity for transport predictions through the surf and swash, the predictions would be different. The modifications can be employed in any of the numerous Boussinesq-type models, and is not dependant on the use of any of the existing breaking dissipation schemes. It is reiterated here that much of the benefit of this “breaking enhancement” comes from its simplicity and ability to be seamlessly integrated into existing models.

While the established experimental data with which to compare these modifications is limited, the results are promising in both the average and instantaneous sense. The approach presented here could be extended to the boundary layer as well, or, alternatively, one could use a more physically detailed approach (e.g., Liu and Orfila, 2004). Extension of this approach to 2HD is also straightforward, although additional and ongoing research into the inclusion of vertical vorticity evolution is equally important for velocity profile modeling. With accurate velocity profiles both in magnitude and vertical

variation, such as those given here, using established Boussinesq-type models, without additional viscous sub-models, to simulate transport in the surf zone becomes a more promising endeavor.

Acknowledgement

The research presented here was partially supported by a grant from the National Science Foundation (CTS-0427115).

References

- Cox, D.T., Kobayashi, N., Okayasu, A., 1995. Experimental and numerical modeling of surf zone hydrodynamics. Technical Report CACR-95-07. Center for Applied Coastal Research, University of Delaware.
- Kennedy, A.B., Chen, Q., Kirby, J.T., Dalrymple, R.A., 2000. Boussinesq modeling of wave transformation, breaking and runup: I. One dimension. *Journal of Waterway, Port, Coastal, and Ocean Engineering* 126, 39–47.
- Lin, P., Liu, P.L.-F., 1998. A numerical study of breaking waves in the surf zone. *Journal of Fluid Mechanics* 359, 239–264.
- Lin, P., Liu, P.L.-F., 2004. Discussion of vertical variation of the flow across the surf zone. *Coastal Engineering* 50, 161–164.
- Liu, P.L.-F., Orfila, 2004. Viscous effects on transient long wave propagation. *Journal of Fluid Mechanics* 520, 83–92.
- Lynett, P., in press. Nearshore wave modeling with high-order Boussinesq-type equations. *Journal of Waterway, Port, Coastal and Ocean Engng.*
- Madsen, P.A., Sorensen, O.R., Schaffer, H.A., 1997. Surf zone dynamics simulated by a Boussinesq-type model. Part I. Model description and cross-shore motion of regular waves. *Coastal Engineering* 32, 255–287.
- Nwogu, O., 1993. Alternative form of Boussinesq equations for nearshore wave propagation. *Journal of Waterway, Port, Coastal, and Ocean Engineering* 119 (6), 618–638.
- Rakha, K.A., 1998. A quasi-3D phase-resolving hydrodynamic and sediment transport model. *Coastal Engineering* 34, 277–311.
- Ryu, S., Kim, M.H., Lynett, P., 2003. Fully nonlinear wave-current interactions and kinematics by a BEM-based numerical wave tank. *Computational Mechanics* 32, 336–346.
- Ting, F.C.-K., Kirby, J.T., 1995. Dynamics of surf-zone turbulence in a strong plunging breaker. *Coastal Engineering* 24, 177–204.
- Ting, F.C.K., Kirby, J.T., 1996. Dynamics of surf-zone turbulence in a spilling breaker. *Coastal Engineering* 27, 131–160.
- Veeramony, J., Svendsen, I., 2000. The flow in surf zone waves. *Coastal Engineering* 39, 93–122.
- Wei, G., Kirby, J.T., Grilli, S.T., Subramanya, R., 1995. A fully nonlinear Boussinesq model for surface waves: Part I. Highly nonlinear unsteady waves. *Journal of Fluid Mechanics* 294, 71–92.